



---

Publicly Accessible Penn Dissertations


---

2021

## Imaging Glutamate In The Human Brain At Ultra-High Magnetic Field: Advances And Applications

Abigail Talya Jordan Cember  
*University of Pennsylvania*

Follow this and additional works at: <https://repository.upenn.edu/edissertations>

 Part of the [Biomedical Commons](#), [Biophysics Commons](#), and the [Neuroscience and Neurobiology Commons](#)

---

### Recommended Citation

Cember, Abigail Talya Jordan, "Imaging Glutamate In The Human Brain At Ultra-High Magnetic Field: Advances And Applications" (2021). *Publicly Accessible Penn Dissertations*. 3694.  
<https://repository.upenn.edu/edissertations/3694>

This paper is posted at ScholarlyCommons. <https://repository.upenn.edu/edissertations/3694>  
For more information, please contact [repository@pobox.upenn.edu](mailto:repository@pobox.upenn.edu).

---

# Imaging Glutamate In The Human Brain At Ultra-High Magnetic Field: Advances And Applications

## Abstract

Glutamate is one of the primary neurotransmitters in the human brain, and many unanswered questions in neuroscience, psychiatry and medicine revolve around this molecule: its production, transport, conversion or degradation, regulation and effects. Yet, to date, methods for actually measuring glutamate within the human body are extremely limited. Amongst the few options in the medical imaging toolbox are magnetic resonance spectroscopy (MRS) and a recently introduced specialized form of magnetic resonance imaging (MRI) known as glutamate-weighted chemical exchange saturation transfer imaging, or gluCEST. MRS, while providing good specificity at high field strengths, lacks spatial or temporal resolution. GluCEST has the potential to provide excellent spatial resolution, but has generally been limited to single-slice acquisitions with sub-optimal B1 correction, precluding its wider application to volumetric measurements of brain structures. In this thesis, we present a novel way to correct gluCEST for B1 inhomogeneity, yielding higher quality images. We then demonstrate expansion of single-slice gluCEST imaging to volumetric 'slab' imaging, greatly expanding our ability to capture specific structures within the brain. We apply gluCEST in both two and three dimensions to investigate healthy brain physiology as well as the response of healthy subjects to transcranial magnetic stimulation (TMS). We were able to detect elevated gluCEST in the dentate gyrus in the brains of healthy subjects, the first non invasive measurement of its kind pertaining to this small but vital structure. We also detected, for the first time, a change in glutamate concentration in the brains of subjects who have received TMS. Finally, we present work in the area of spectroscopy, presenting a technique in which –in sharp contrast to existing methodologies requiring non-standard hardware– metabolic dynamics of glutamate can be detected using only proton-based chemical shift imaging (CSI) in conjunction with oral ingestion of deuterium labeled glucose. While itself limited in spatial resolution, this ability to detect and visualize the dynamic neural metabolism of glucose to glutamate provides a deeply complimentary source of information to gluCEST. In the future, qCSI and gluCEST could be used in tandem to provide next-generation precision diagnostics for patients suffering from neurological maladies of metabolic origin.

## Degree Type

Dissertation

## Degree Name

Doctor of Philosophy (PhD)

## Graduate Group

Biochemistry & Molecular Biophysics

## First Advisor

Ravinder Reddy

## Keywords

brain, CEST, glutamate, imaging, MRI, spectroscopy

## Subject Categories

Biomedical | Biophysics | Neuroscience and Neurobiology

IMAGING GLUTAMATE IN THE HUMAN BRAIN AT ULTRA-HIGH MAGNETIC FIELD: ADVANCES

AND APPLICATIONS

Abigail Talya Jordan Cember

A DISSERTATION

in

Biochemistry and Molecular Biophysics

Presented to the Faculties of the University of Pennsylvania

in

Partial Fulfillment of the Requirements for the

Degree of Doctor of Philosophy

2021

***Supervisor of Dissertation***

Ravinder Reddy, PhD., Professor of Radiology

***Graduate Group Chairperson***

Kim A. Sharp, PhD., Associate Professor of Biochemistry and Biophysics

***Dissertation Committee***

Despina Kontos, PhD., Associate Professor of Radiology

David R. Roalf, PhD., Research Assistant Professor of Behavioral Neuroscience in Psychiatry

Walter R. Witschey, PhD., Associate Professor of Radiology

## Dedication

*Эта работа посвящается всем физикам-светоносцам XXого века -- и в особенности, как здесь  
годится, Завойскому – которые не сходили с святого пути опознания структуры и свойств  
физической реальности, даже как наш мир, их окружающий, горел пламями самой глубины  
человеческой темноты.*

*And also to the biologists and chemists who, in the face of the crisis which gripped the world as I wrote,  
worked tirelessly to preserve human life from the relentless aggression of nature against our kind.*

*Here is my one pebble for our temple and our fortress.*



## Acknowledgements

First and foremost, everyone knows that credit for the fact that I am at long last earning a PhD goes to my thesis advisor, Dr. Ravinder Reddy. I am a personal beneficiary of Ravi's approach of giving everyone a chance, of encouraging his group to act as a team while highlighting individual strengths and achievements, to act upon curiosity without losing sight of practicality, and to work diligently and carefully without wasting energy in the pursuit of perfection. I have always been particularly in awe of his patience and sense of humor in the face of myriad sources of unreasonable behavior in this world. When reviewer comments made me want to cry, I tried to imagine the day when I couldn't focus on what I was doing in Matlab because Ravi and Hari were laughing loudly all afternoon at some kind of "criticism" that someone had received on a grant or paper. I don't think there is any one bit of technical information I have learned in all of graduate school that was a more important lesson than this scene of how to handle apparent adversity or hostility.

Amongst finite groups of people, there could hardly be a more complete package of support and expertise than at CMROI. Mark answers all of my questions about Linux and imaging data, Neil answers all of my questions about sequences and spectroscopy, Ravi Nanga's knowledge of biochemistry is ready like a textbook when I don't actually know things I'm supposed to have learned, and Dushyant is armed with mathematical techniques like a sorcerer might be with spells. Hari was always ready to answer all my questions about MR physics –no matter how much they veered into the realm of the philosophical-- and even offered up wisdom regarding spiritual approaches to life itself. For pretty much anything else earthly, I think it's safe to assume that between them, Ari and Susan would have it covered. Likewise, our "research specialists" have hardly turned out to be "specialists" at all, but jacks-of-all-trades with a staggeringly broad repertoire of skills. Kevin has repaired my devices, Deepa has cut my hair, Blake has paced me on the track and Ryan has changed the battery in my car. Dr. Laurie Rich, a very upstanding fellow, has done at least two very lovely things for me. One of them was walking me home all the way across downtown Montreal in the middle of the night after he drank a certain renowned in vivo NMR expert under the table, rendering the latter unable to do so...

I am deeply indebted to Dr. Puneet Bagga in particular for friendship and support in innumerable forms, including keeping me company up and down the 14 flights of stairs of Blockley Hall when I needed to lower my bloodsugar, patiently teaching me to read Devanagari when we were the last ones in the lab, and apparently never tiring of receiving text messages to the effect of "देखो, मैंने बैंगन बनाया!". His usual response that I "can already speak Hindi like a pro!" is typical of his routine exaggerations of my abilities and accomplishments, for which I could not be more thankful, despite knowing that they need to be taken with even more salt than he puts into my favorite dal.

Like Neil and Puneet, there were quite a number of older students and post-docs whose presence and guidance during my graduate school saga made an enormous – sometimes

completely vital-- difference. Drs. Mirna El Khatib, Dmitry Andrianov, Catherine deBrosse, Christopher Bialas, Joseph Jordan and, of course, the infamous Ian D. Rowe are amongst those whose names cannot go unmentioned. Likewise for several professors from the BMB and Chemistry Departments here at Penn, in particular those whom I took courses or rotated with, including Kim Sharp (who wears many hats, all of them excellently), Paul Axelsen, Feng Gai, Joe Subotnik, and, of course, Sergei Vinogradov. As for latter, few things in life have made as deep of an impression on me as the opportunity to see Sergei in action day in and day out. I have rarely encountered anyone who I think so completely embodied the maximum possible capability of the variable type known as 'human being' and I would not have given up this experience for anything. Before this, the unofficial 'biophysics department' at the University of Maryland 'raised me' in an unparalleled nurturing environment. I think the word 'encouragement' does not do the situation justice: my undergraduate professors, research mentor and academic advisors -- Dr. Sukharev, Dr. Fushman, Dr. Dayie, Dr. Beckett, and even the graduate students I had as TAs -- nearly *infected* me and a few of my friends with the idea that we should and would become excellent scientists.

Lastly, life is both extraordinarily non-linear and extraordinarily dependent on initial conditions. You don't need a fancy statistical package to observe that children who grow up thinking that graduated cylinders are normal things to have in the kitchen are more likely to earn PhDs in science. There is not a single aspect of my tendencies, priorities or abilities that has not been overwhelmingly influenced by my parents - -I think much more so than they realize. From them I inherited (or was made to inherit) the habits of measuring things, of keeping records, of near-obsessive personal organization, extreme literacy and numeracy, ever-present inquisitiveness, appreciation and fascination with both the natural and human worlds, the study of foreign languages, and the pursuit of athletics. More abstractly and importantly: the conviction to care for and respect others without letting their opinion influence your own approach to anything, to follow your own path, and to never to arrive at a point in life where the adventure has ended, the questions have all been answered, or the goals have all been met -- because that would mean that the second law of thermodynamics has vanquished you, and that's not what we're about. When contemplating the challenging practice of compiling a thesis, I sometimes thought of the fact that my mother wrote hers while an infant me was probably routinely clamoring for her attention, and I realized, "Jeez, I really have it easy". And if you were to take a vector sum, this has basically been true about everything.

Thank you again to everyone who made it so. I got darn lucky.

# ABSTRACT

## IMAGING GLUTAMATE IN THE HUMAN BRAIN AT ULTRA-HIGH MAGNETIC FIELD: ADVANCES AND APPLICATIONS

**Abigail Talya Jordan Cember**

**Ravinder Reddy**

Glutamate is one of the primary neurotransmitters in the human brain, and many unanswered questions in neuroscience, psychiatry and medicine revolve around this molecule: its production, transport, conversion or degradation, regulation and effects. Yet, to date, methods for actually measuring glutamate within the human body are extremely limited. Amongst the few options in the medical imaging toolbox are magnetic resonance spectroscopy (MRS) and a recently introduced specialized form of magnetic resonance imaging (MRI) known as glutamate-weighted chemical exchange saturation transfer imaging, or gluCEST. MRS, while providing good specificity at high field strengths, lacks spatial or temporal resolution. GluCEST has the potential to provide excellent spatial resolution, but has generally been limited to single-slice acquisitions with sub-optimal  $B_1$  correction, precluding its wider application to volumetric measurements of brain structures. In this thesis, we present a novel way to correct gluCEST for  $B_1$  inhomogeneity, yielding higher quality images. We then demonstrate expansion of single-slice gluCEST imaging to volumetric 'slab' imaging, greatly expanding our ability to capture specific structures within the brain. We apply gluCEST in both two and three dimensions to investigate healthy brain physiology as well as the response of healthy subjects to transcranial magnetic stimulation (TMS). We were able to detect elevated gluCEST in the dentate gyrus in the brains of healthy subjects, the first non invasive measurement of its kind pertaining to this small but vital structure. We also detected, for the first time, a change in glutamate concentration in the brains of subjects who have received TMS. Finally, we present work in the area of spectroscopy, presenting a technique in which –in sharp contrast to existing methodologies requiring non-standard hardware-- metabolic dynamics of glutamate can be detected using only proton-based chemical shift imaging (CSI) in conjunction with oral ingestion of deuterium labeled glucose. While itself limited in spatial resolution, this ability to detect and visualize the dynamic neural metabolism of glucose to glutamate provides a deeply complimentary source of information to gluCEST. In the future, qCSI and gluCEST could be used in tandem to provide next-generation precision diagnostics for patients suffering from neurological maladies of metabolic origin.

## Table of Contents

Dedication .....	ii
Acknowledgements.....	iii
Abstract.....	v
List of Tables.....	ix
List of Figures.....	x
Preface .....	xiii
Chapter 1: Introduction.....	1
<b>1a) Magnetic Resonance Imaging and Spectroscopy: Overview of Physical Underpinnings ...</b>	<b>1</b>
1a.1 Magnetic resonance and the intrinsic property ‘spin’ .....	1
1a.2 The external field $B_0$ breaks the degeneracy of spin eigenstates and induces precession .....	3
1a.3 Physical and chemical factors mediating net magnetization $M_0$ and Larmor frequency $\omega_0$ .....	8
1a.4 Expressing $H_0$ (and subsequent calculations) in the rotating frame of reference .....	10
1a.5 The applied radio frequency (RF) field: $B_1$ .....	13
1a.6 Additional useful formalisms .....	15
1a.7 Relaxation (as per Bloch) .....	18
1a.8 Exploiting variations in $B_{0, local}$ to perform imaging and spectroscopy .....	22
<b>1b: The Chemical Exchange Saturation Transfer Experiment.....</b>	<b>35</b>
1b.1 Overview and strategy of the experiment.....	35
1b.2 Generation and analysis of the Z-spectrum.....	38
1b.3 The challenge of specificity in the CEST experiment .....	40
1b.4 The saturation pulse .....	42
1b.5 Effect of exchange rate .....	45
1b.6 Transfer of saturation from one species to another .....	48
1b.7 Other forms of CEST.....	49
1b.8 Other effects which appear in the Z- spectrum.....	51
1b.9 Phenomenological modeling of the CEST experiment: Bloch-McConnell equations....	52
1b.10 The CEST experiment in practice .....	57
<b>1c: <i>In vivo</i> glutamate measurement: biochemical significance and current state of the art .</b>	<b>67</b>

1c.1 Neurobiological context of glutamate .....	67
1c.2 MR-based detection of glutamate .....	71
1c.3 Summary of human and animal gluCEST applications to date .....	73
1c.4 Summary of advances presented in this thesis.....	74
<b>Chapter 2: An improved method for post-processing correction of <math>B_1</math> inhomogeneity in gluCEST images of the human brain.....</b>	<b>81</b>
2.1 Introduction .....	81
2.2 Methods.....	84
2.3 Theory: Simple Parameterization of the Functional Form of $M_z/M_0(B_{1, sat})$ .....	85
2.4 Acquisition and Use of Calibration Data .....	88
2.5 Results.....	92
2.6 Discussion.....	102
2.7 Supplementary Information .....	107
<b>Chapter 3: GluCEST measurements of the aging brain .....</b>	<b>124</b>
<b>3A. Age-dependent variation in CEST signal at low <math>B_1</math> may reflect contribution of lipids ...</b>	<b>124</b>
<b>3B. Glutamate Weighted Imaging (GluCEST) as a Biomarker of Cognitive Function: Preliminary Findings from GluCEST MRI in Older Adults.....</b>	<b>128</b>
3B.1 MCI and AD: Additional Background .....	128
3B.2 Analysis .....	129
3B.3 Results and Discussion.....	129
3B.4 Limitations of the Study.....	135
3B.5 Conclusions .....	135
<b>Chapter 4: Using gluCEST to probe the mechanism of transcranial magnetic stimulation (TMS) .....</b>	<b>139</b>
4.1 Introduction .....	139
4.2 Materials and Methods.....	142
4.3 Results.....	146
4.4 Discussion.....	149
4.5 Conclusions .....	153
<b>Chapter 5: Volumetric (3D) gluCEST enables <i>in vivo</i> detection of metabolic differences between human hippocampal subfields .....</b>	<b>157</b>
5.1 Introduction .....	157
5.2 Methods.....	159

5.4 Discussion.....	170
5.5 Supplementary Information and Appendices to Chapter 5.....	176
<b>Chapter 6: Integrating <sup>1</sup>H MRS and deuterium labeled glucose for mapping the dynamics of neural metabolism in humans .....</b>	<b>189</b>
<i>Preface</i> .....	189
6.1 Introduction .....	189
6.2 Materials and Methods.....	192
6.3 Results.....	196
6.4 Discussion.....	203
6.5 Supplementary Figures and Information .....	206
Appendices .....	<b>214</b>
<b>Appendix A: Bloch-McConnell simulations of the CEST experiment.....</b>	<b>215</b>
<b>Appendix B: GluCEST post-processing in Matlab.....</b>	<b>247</b>

### Summary of Publications and Abstracts

The material in this thesis comprises in part of material that has been previously published or presented, as well as material included in manuscripts currently in preparation. The following table summarizes where the results may have been previously communicated.

Chapter 2	<i>Cember et al, NMR in Biomedicine 2021</i>
Chapter 3	Poster presentation, ISMRM 2019 Oral presentation, ISMRM 2020 (summa cum laude abstract)
Chapter 4	Poster presentation, ISMRM 2019 Oral presentation, CEST symposium 2020 <i>Cember, Deck, et al, in preparation</i>
Chapter 5	Oral presentation, WMIC 2020 <i>Cember et al, in preparation</i>
Chapter 6	Oral presentation, ISMRM 2021 <i>Cember, Wilson, Rich, et al, under review</i>

ISMRM: Annual Meeting of the International Society for Magnetic Resonance in Medicine

WMIC: World Molecular Imaging Congress

## **List of Tables**

Table 1a.1: Properties of selected nuclei

Table 2.S1. Bloch-McConnell Simulation parameters

Tables 2.S2, A-E. Tables relating to fitting and generation of correction surfaces

Table 4.1 Results of unpaired T-tests of gluCEST by cortical segment (TMS)

Table 5.1. GluCEST means and standard deviations by medial temporal lobe subfield

Table 5.S1 Pulse sequence parameters (2D and 3D gluCEST)

Table 6.1 qCSI results from all subjects, white matter

Table 6.2 qCSI results from all subject, gray matter

## List of Figures

### Chapter 1. Introduction

Figure 1a.1: Basic gradient-echo pulse sequence

Figure 1a.2 semi-LASER pulse sequence

Figure 1b.1. Illustration of CEST phenomenon

Figure 1b.2 The Z-spectrum:  $B_1$  dependence and Lorentzian fitting

Figure 1b.3. Electronic structures give rise to chemical exchange phenomena

Figure 1b.4. Matrix representations of the Bloch-McConnell differential equations

Figure 1b.5. Acquisition and post-processing of a gluCEST measurement (also Figure 2.2)

Figure 1b.6. Schematic of ‘image synthesis’ approach to  $B_0$  correction.

Figure 1b.7. Illustration of inaccurate CEST asymmetry calculation due to uncorrected  $B_0$  shift.

Figure 1c.1 Glutamate and related metabolites in the nervous system

Figure 1c.2: NMR spectra of glutamate and glutamine

### Chapter 2. An improved method for post-processing correction of $B_1$ inhomogeneity in gluCEST images of the human brain

Figure 2.1. Origin and application of Equation 2.1

Figure 2.2 Full schematic of gluCEST acquisition and post-processing using  $B_1$  correction based on  $M_z(B_1, T_1)$  surfaces.

Figure 2.3: Image comparison with previous correction method.

Figure 2.4. Example histogram-based comparison of performance of ‘Old’ and ‘New’  $B_1$  correction methods in areas of high and low  $B_1$

Figure 2.5. Evaluation of  $M_z(B_1, T_1)$  surface-based correction for varying  $B_1$  strength; comparison with simulation.

Figure 2.S1. Introduction to the problem of correcting GluCEST for  $B_1$  inhomogeneity.

Figure 2.S2. Simulations of contrast as a function of saturation  $B_1$ , comparing gluCEST and APT CEST.

Figure 2.S3. Schematic: generating  $M_z(B_1, T_1)$  correction surfaces from calibration data.

Figure 2.S4: Fitting performance of Equation 2.1 and dependence on number of  $T_1$  bins

Figure 2.S5. Fitting parameters vary smoothly with both simulated physical parameters and with real  $T_1$  values



Figure 2.S6: Comparison of surface-based  $B_1$  correction on different slices indicates that limiting factor is flip angle  $B_1$ , rather than saturation  $B_1$ power.

Figure 2.S7, A-C : Expanded histogram-based analysis of correction performance in example slices

### **Chapter 3. GluCEST measurements of the aging brain**

Figure 3A.1. Coronal gluCEST images of healthy subjects of three different ages

Figure 3A.2. CEST contrast surfaces derived from subjects of differing ages

Figure 3A.3 Histogram of  $T_1$  values at 7T for white matter of healthy younger and older individuals

Figure 3B.1: GluCEST maps of selected control and MCI subjects

Figure 3B.2. High-resolution structural segmentation of medial temporal lobe structures

Figure 3A.3: Plot of anatomical volume v. gluCEST values in MCI subjects

Figure 3A.4 Graphical representations of average gluCEST values of MTL subfields in older adults

Figure 3A.5. Histograms of gluCEST in the entorhinal cortex of younger and older adults

### **Chapter 4. Using gluCEST to probe the mechanism of transcranial magnetic stimulation (TMS)**

Figure 4.1: TMS/CEST basics

Figure 4.2. Illustration of CEST slice placement and regional analysis in the TMS/CEST experiment.

Figure 4.3: Sample CEST maps and histograms for gluCEST in the left precentral gyrus of stimulated subjects

Figure 4.4. Segmentwise gluCEST maps of stimulated v. control group

Figure 4.5: Barplot of gluCEST changes by segment: 99% confidence intervals

### **Chapter 5: Volumetric (3D) gluCEST enables *in vivo* detection of metabolic differences between human hippocampal subfields**

Figure 5.1. The Human Hippocampus.

Figure 5.2 Schematic of 3D CEST sequence.

Figure 5.3: Individual slices of 3D gluCEST volume of MTL, shown with segmentation and  $B_1$  maps.

Figure 5.4. Box plots of gluCEST values by subfield of the medial temporal lobe

Figure 5.5: Comparison of gluCEST values in left and right hippocampal subfields.

Figure 5.6. T-test for statistically significant difference in gluCEST between subfields: confidence interval colormaps

Figure 5.7: Segmentwise maps of average  $B_1$  strength and gluCEST

Figure 5.8: Plot of relationship between average gluCEST and  $B_1$  amplitude.

Figure 5.S2 Use of high-dielectric pads to improve  $B_1$  distribution

Figure 5A.3 Dielectric pads improve  $B_1$  maps (top) and therefore gluCEST images

Figure 5A.4. Orthogonal views corresponding to 3D CEST acquisitions

Figures 5.5A, B. Example 3D gluCEST images

## **Chapter 6. Integrating $^1\text{H}$ MRS and deuterium labeled glucose for mapping the dynamics of neural metabolism in humans**

Figure 6.1 : Spectroscopic underpinnings of qCSI

Figure 6.2:: Example timecourse, CSI maps

Figure 6.3: [NAA] and ratios of glutamate varieties derived from CSI data in a single subject.

Figure 6.4: Ratios of glutamate/NAA derived from CSI data in all subjects

Figures 6.S1. Simulation of basis set glutamate metabolites

Figure 6.S2: Additional qCSI data sets

Figure 6.S3: Additional barplots of qCSI-quantified metabolites

Figure 6.S4: Blood glucose time courses after equivalent glucose ingestion

Figure 6.S5: SVS-quantified metabolites upon ingestion of unlabeled glucose.

## Preface

The centrality of glutamate cannot be overstated. It is the molecule which, perhaps more than any other, forms the link between our core metabolism inherited from the Paleozoic and the complex thoughts, feelings, and ideas which make us human beings. Stupendous achievements of the 20<sup>th</sup> century gave rise to the observation of nuclear magnetic resonance and its application to medical imaging. The work in this thesis builds directly on that of my predecessors and mentors at the Center for Magnetic Resonance and Optical Imaging at the University of Pennsylvania, as we attempt to further the capabilities of magnetic resonance based technology to detect and visualize the presence of glutamate in the human brain. This endeavor, like any other which seeks to wrench territory from the impossible and annex it to the possible, is dynamic, tenuous, and replete with opportunity for error in procedure or interpretation. However, it is my understanding that there are only three kinds of contributions that a scientist can make at any given time in history: 1) measure what you can with the tools of the day; 2) do what you can to improve the tools themselves; 3) think very hard about the problem. To this end:

Chapter 1 provides a tri-partite introduction to the field of research: 1a focuses on the history and physics of the magnetic resonance phenomenon and its application to medical imaging; 1b, on the Chemical Exchange Saturation Transfer (or CEST) experiment specifically; 1c, on the molecule glutamate itself and existing applications of the corresponding, specialized imaging technique known as gluCEST.

Chapter 2 presents a recently proposed and applied method for correcting gluCEST images for inhomogeneity of the  $B_1$  field, a set-back which has plagued this type of measurement and inhibited its expansion.

Chapter 3 explores the specific challenges of imaging glutamate in the brains of aging adults, and presents preliminary results of some of the observed trends in such experiments.

Chapter 4 applies gluCEST in an experiment which images the brains of volunteers before and after they undergo a type of non-invasive brain stimulation called TMS, which is an active area of research at Penn and around the world.

Chapter 5 communicates the first results of using a volumetric (3D) gluCEST sequence to make previously impossible measurements of very small structures of the medial temporal lobe, the locus of learning, navigation, pattern recognition and memory formation in the human brain.

Chapter 6, lastly, describes the first human application of a newly developed technique for measuring metabolic dynamics – that is, the actual conversion of one chemical to another – using only the magnetic resonance of the proton, while existing technologies required the more involved detection of other isotopes.

Thus what follows is an attempt to, to some degree, translate (3) into successful instances of (2) and then (1), the success of which may be judged by the reader-- and of course, in the end, will be fatefully judged only by the infamous and protean pantheon: Reviewers 1, 2 and 3.

*A.T.J.C.*  
*Philadelphia, 2021*

# Chapter 1: Introduction

## 1a) Magnetic Resonance Imaging and Spectroscopy: Overview of Physical

### Underpinnings

#### 1a.1 Magnetic resonance and the intrinsic property 'spin'

The history – and indeed, “prehistory” – of nuclear magnetic resonance is nothing short of an epic tale of investigative valiance. After years of adversity-laden attempts by Evgeny Zavoisky in Kazan, USSR and even published negative results by Dutch physicist Cornelius J. Gorter<sup>1,2</sup>, a nuclear magnetic moment of condensed-phase matter was finally detected for the first time by Bloch, Hansen and Packard in liquid water and Purcell, Torrey and Pound in a sample of paraffin – which, due to misestimation of relaxation times by the venerable I.I. Rabi, had already spent the night in the magnet<sup>3-5</sup>. These scientists, understanding that nuclei possessed an intrinsic angular momentum which should interact with a magnetic field, foresaw that in principle, oscillating external fields could be used to manipulate the motion of this ‘magnetization’ and that this experiment, in analogy to existing forms of spectroscopy, could be used to access information about a physical system. Pursuing this hypothesis, Isidor Isaac Rabi had won the 1944 Nobel Prize in Physics for his work on “determination of the nuclear magnetic moment through resonance with radio waves”<sup>1</sup>, which he accomplished using a sophisticated set-up in which the molecules of interest comprised a so-called ‘molecular beam’. Eight years later, in 1952, the experiments of Bloch and Purcell also earned them the Nobel Prize. The achievement

---

<sup>1</sup> This description of Rabi’s work is also from Prof. Hulthen’s presentation speech of the award to Bloch and Purcell.

for which they were recognized-- the extension of this type of measurement to condensed phase matter –came to include today’s widespread and indispensable application of NMR to analytical chemistry, biomedical imaging and other fields.

The intrinsic angular momentum of all particles, affectionately named for its familiar macroscopic counterpart, is called ‘spin’. It is a fundamental property of all matter, but manifests itself differently in the two major ‘categories’ of physical entities, fermions (protons, neutrons and electrons)<sup>2</sup> and bosons (e.g., photons). Because of their respective composition on the even smaller scale of quarks, fermions have so-called ‘spin = ½’, while bosons have ‘spin = 1’. Fascinatingly, modern theoretical physics has yet to account completely for these values; the so-called ‘spin crisis’ remains amongst the nebula of unreconciled problems which next generation particle accelerators are built to solve<sup>6</sup>.

Spin is a ‘quantum number’: an expression of a discrete properties of quantized systems (i.e., those on the time, space and energy scale such as to be described by the laws of quantum mechanics). A nucleus is composed of two types of particles: protons and neutrons. Since the nucleus is a composite particle having a certain number of protons and neutrons, its total spin is determined by the sum of these quantum numbers. This means that, depending on how many nucleons are in a particular nucleus, it may have different total spin than its neighbor on the periodic table. The existence of a non-zero total spin of the nucleus itself is the first physical requirement for observing nuclear magnetic resonance. Consider as examples a few important

---

<sup>2</sup> I think it’s actually more correct to say that the particles which *compose* protons and neutrons themselves are the fermions.

nuclei in organic matter:  $^1\text{H}$  and  $^{12}\text{C}$ , and their isotopes  $^2\text{H}$  and  $^{13}\text{C}$ . The composition of these nuclei is as follows:

Nucleus	No. of protons	No. of neutrons	Total spin	Gyrom. Ratio ( $\gamma$ ), rad.MHzT <sup>-1</sup>
$^1\text{H}$ (hydrogen)	1	0	1/2	267.5
$^2\text{H}$ (deuterium)	1	1	1	41.1
$^{12}\text{C}$ (carbon)	6	6	0	N/A
$^{13}\text{C}$	6	7	1/2	67.3

**Table 1a.1 Properties of selected nuclei**

Note that  $^{12}\text{C}$  has zero spin not because of the even number of *total* nucleons, but because of the even number of *each type*. Similar to electrons, nucleons of each type must fill their “energy shell” as pairs where each “partner” in the pair has opposite angular momentum: thus, every *pair* of protons or *pair* of neutrons contributes zero spin to the total, and only an unpaired nucleon of either type gives rise to total spin. In the case where there is one of each, the ground state interaction of the single proton and single neutron is for their spin components to be ‘parallel’, hence giving a nucleus like deuterium spin of 1, rather than 0.

Out of the nuclei enumerated above,  $^1\text{H}$ ,  $^2\text{H}$  and  $^{13}\text{C}$  – but not  $^{12}\text{C}$  – are observable by magnetic resonance. This is a key consideration in the design of experiments using NMR in biological contexts, as direct detection of carbon metabolism requires introduction of the heavy isotope.

### **1a.2 The external field $B_0$ breaks the degeneracy of spin eigenstates and induces precession**

Quantum mechanics describes that a particle with spin quantum number  $I$  (e.g.  $\frac{1}{2}$ ) has associated substates  $m_I$  described by the set  $\{-I, -I+1, \dots, I\}$ . Hence for  $I = \frac{1}{2}$ , this set is  $m_I = \{-\frac{1}{2}, \frac{1}{2}\}$ . This means that, if one solves the Schrodinger equation for a Hamiltonian which describes this physical situation, there are two possible solutions, or eigenstates.

In the absence of an external field, these eigenstates are isoenergetic – or ‘degenerate’.

According to the laws of thermodynamics, degenerate states will, on average at any given ‘instant’, be populated equally. They also have no inherent orientation with respect to physical 3-space: despite the non-zero magnetic moment of a nucleus like hydrogen, a bulk body with very many hydrogens (e.g. a person, or a bottle of water) will itself have no net magnetic moment, because these spins from the nuclei are randomly oriented, and taking their vector sum will result in a quantity which is rapidly time-averaged to zero. The absence of any difference in population or orientation means that, at zero field, these states are indistinguishable and inaccessible to experiment.

The presence of an external field does two important and related things: it breaks the degeneracy of the spin eigenstates, and couples their orientation to an external reference. It also induces a motion known as ‘precession’.

Mathematically, we can write some of these relationships as:

$$E = -\mu \cdot \mathbf{B} \quad [1.1]$$

$$\text{where } \mathbf{B} = B_0 * \mathbf{z}, \quad [1.2]$$

$$\mu = \gamma * I_z \quad [1.3]$$

where ‘E’ is the energy imparted to the system by the presence of the field,  $\mu$  is the magnetic moment of the particle, and by convention,  $\mathbf{z}$  is the direction of the magnetic field,  $\mathbf{B}$ , which has magnitude  $B_0$ <sup>3</sup>. Note that  $\mu$ , which relates the strength of the field to the energy of each state, is a function of the scalar quantity  $\gamma$ . Known as the **gyromagnetic ratio**, it relates the spin quantum

---

<sup>3</sup> For references sourcing the material in this introductory section, please see the ‘General Bibliography’ at the end of this chapter.

number of the nucleus to the magnitude of the magnetic moment that it will generate. It is related to the mass, charge, and nuclear shell geometric properties of the nucleus and can vary widely even amongst nuclei with identical total spin  $I$ . This also has important practical consequences for NMR and MRI experiment design.

$$I_x = \frac{1}{2} \begin{pmatrix} 0 & 1 \\ 1 & 0 \end{pmatrix} \quad I_y = \frac{1}{2i} \begin{pmatrix} 0 & 1 \\ -1 & 0 \end{pmatrix} \quad I_z = \frac{1}{2} \begin{pmatrix} 1 & 0 \\ 0 & -1 \end{pmatrix} \quad [1.4]$$

are the **angular momentum operators**<sup>7</sup> for spin  $\frac{1}{2}$  nucleus in the Zeeman (i.e. taking the effect of  $B_0$  into account) eigenbasis. These operators have a very important property, which is **cyclic commutation**:

$$[I_i, I_j] = i \varepsilon_{ijk} I_k \quad [1.5]$$

( $\varepsilon$  is a symbol that specifies the symmetry properties of this relation, and does not have a 'value' in and of itself.)

$I_z$  in the equation for  $\mu$  above is the value of the observable corresponding to the 'Z' angular momentum operator, which can be physically interpreted as a projection of the angular momentum onto the z-axis of the external field. It has the eigenfunctions traditionally denoted  $\{|\alpha\rangle, |\beta\rangle\}$  and the associated eigenvalues  $\pm \frac{1}{2} \hbar$ .

$$I_z |\alpha\rangle = \frac{1}{2} \hbar |\alpha\rangle \quad [1.6a]$$

$$I_z |\beta\rangle = -\frac{1}{2} \hbar |\beta\rangle \quad [1.6b]$$

The Hamiltonian of the spin- $\frac{1}{2}$  system that has been introduced into an external field now has a term corresponding to the presence of this field, and the 'energy'  $E$  as described above. Since this term arises from the presence of  $B_0$ , we'll call it  $H_0$ :



$$H_0 = -\gamma B_0 I_z \quad [1.7]$$

This operator  $H_0$  is related to the operator  $I_z$  only by the constant factors  $\gamma$  and  $B_0$ , which means that it commutes with  $I_z$ , and will have the same eigenstates – its introduction only changes the *distribution* of the system between these eigenstates, and the way that they evolve in time.

At any given moment, the state of a spin- $\frac{1}{2}$  particle can be described by the wavefunction:

$$|\psi\rangle = c_\alpha |\alpha\rangle + c_\beta |\beta\rangle \quad [1.8]$$

This equation simply expresses that the particle is described by a linear combination of its two eigenstates. The coefficients  $c$  quantify the degree to which each eigenstate is ‘inhabited’, and depend on their relative energies. In the absence of an external field or other source of ‘energy’ to perturb them, these coefficients  $c$  are equal, and the system inhabits the states equally. In the presence of  $B_0$ , one state becomes preferentially populated.

The evolution in time for this system is given by:

$$|\psi(t)\rangle = \exp(-i \mathbf{H} t) |\psi(0)\rangle \quad [1.9]$$

Where  $|\psi(t)\rangle$  for any  $t$  (including 0) is of the form indicated above.  $H$  is the Hamiltonian in question. At present, in the presence of  $B_0$  our  $H$  is  $H_0$ .

This means that, as soon as we put a spin  $-1/2$  system into an external field, its dynamics are described by the following equation:

$$|\psi(t)\rangle = \exp(-i\gamma B_0 I_z t) |\alpha\rangle + \exp(-i\gamma B_0 I_z t) |\beta\rangle \quad [1.10]$$

Expression of these exponential terms as sinusoidal functions allows us to see that this represents a system of two states, each of which are subject to **rotation about the Z axis**. The

frequency of this rotation, which is a function of  $\gamma$  and  $B_0$ , is known as the **Larmor frequency**<sup>4</sup>, and generally denoted as  $\omega_0$ .

The two states have energies  $+\frac{1}{2} \hbar \gamma B_0$  and  $-\frac{1}{2} \hbar \gamma B_0$ , making the energy difference between them

$$\Delta E = \hbar \gamma B_0 \quad [1.11]$$

Thermodynamics relates the population distribution of an ensemble between states to the difference in energy between those states and the temperature of the system. The probability,  $P$ , of a spin or other physical entity populating a state with an associated energy  $E$  at temperature  $T$  is dictated by these quantities and a distribution parameterized by the Boltzmann constant,  $k_B$  (or just  $k$  in small font):

$$P(E) \propto e^{\frac{-E}{kT}} \quad [1.12]$$

Given that  $E = \pm \frac{1}{2} \hbar \gamma B_0$ , we can calculate the **equilibrium net magnetization** – a sum of all spin vectors that are distributed according to the Boltzmann distribution-- of a sample in a field of strength  $B_0$ :

$$M_0 = \frac{N\gamma^2 \hbar^2 B_0}{16 \pi^2 k_B T} \quad [1.13]$$

where  $N$  is simply the number of spins in the sample. While **Equation 1.13** gives the theoretically exact value of the magnetization, in practice the sensitivity of the NMR experiment (i.e. the experimental value for  $M_0$ ) depends on factors including coil loading and tuning and other

---

<sup>4</sup> Named in honor of Joseph Larmor, whose theorem predicted the general existence of precession.

physical aspects of the set-up. Thus, **Equation 1.13** is frequently written expressing a proportionality rather than an exact equality.

### 1a.3 Physical and chemical factors mediating net magnetization $M_0$ and Larmor frequency $\omega_0$

Before adding more terms, we consider how the variables presented so far affect these two aspects of the spin system-- population splitting between eigenstates, and the precession of these eigenstates around the Z-axis-- as these parameters translate to key considerations in the NMR experiment. Given that we are concerned here with biomedical (i.e. mostly water) imaging and spectroscopy at ultrahigh field, we can compare the values of  $M_0$  of pure water (55 M) at 3 T and 7 T:

$$M_0 = \frac{N\gamma^2 h^2 B_0}{16 \pi^2 k_B T} = \frac{(110 \times 6.022 \times 10^{23})(2.675 \times 10^8)^2 (2.626 \times 10^{-34})^2 * B_0}{16 \pi^2 (1.381 \times 10^{-23}) * 293} = 0.195 * 10^{-18} * B_0$$

$$= 0.585 * 10^{-18} \text{ J/T at } B_0 = 3 \text{ T and } 1.365 * 10^{-18} \text{ J/T at } B_0 = 7 \text{ T.}$$

In addition to the linear dependence on field strength, the magnitude of  $M_0$  has a quadratic dependence on gyromagnetic ratio. Let's consider the same calculations using the deuterium gyromagnetic ratio  $\gamma^2 = 0.41 * 10^8 \text{ rad/s}^2$  instead of  $2.675 * 10^8$  for the proton:

$$M_{0,2H,3T} = 0.0137 * 10^{-18} \text{ J/T} \quad M_{0,2H,7T} = .0321 * 10^{-18} \text{ J/T}$$

From this calculation we can understand that detecting the signal from one NMR-active nucleus to another can be very different experiments: deuterium NMR at 3T is about 100 times less sensitive than proton NMR at 7T. Lastly, we should note the inverse dependence on temperature. This is a variable that we can't modify *in vivo*, but the increased sensitivity

achieved with lower temperatures is an extremely important aspect of NMR experiments outside of medical contexts.

In addition to the polarization or sensitivity, a difference in gyromagnetic ratio or field strength will change the Larmor frequency of the spin system. At a given field strength, this has the important practical consequence that different physical coils (or 'dual tuning' of a single coil) will be required for generating and receiving the MR signal from different nuclei. Also, the absolute frequencies (in Hz) involved in an MR experiment at 7T will be 7/3 times higher than those at 3T. This is of great pertinence when considering the interactions of these RF fields (now at frequencies approaching microwaves) with the human body. First of all, now that they are higher frequency, there is a potential for inducing rotational transitions in molecules<sup>8,9</sup> which subsequently cause heating, and we must be careful not to input too much of such energy into the human subject. Also, the shorter wavelength means that standing wave patterns resulting from the interaction with anatomical structure become more troublesome<sup>10,11</sup>. This is largely the origin of the inhomogeneity of  $B_1$  in brain imaging at 7T which will be discussed extensively in Chapter 2.

One extremely useful fact of nature is that the electron cloud of the molecule itself causes very small changes in the  $B_0$  'experienced' 'locally' by individual atoms within a compound. In other words, two protons that are not in the same position relative to the rest of the atoms in the molecule are experiencing a slightly different  $B_0$  from each other due to the 'shielding' they experience as a result of the presence of the electrons, which, as moving charges, generate some small field in and of themselves. The degree of this effect can be predicted from theory by calculating the **chemical shift tensor**,  $\sigma$  and manifests itself in the NMR spectrum as separate resonances. (See **Figure 1b.3** which shows the electrostatic potential of glutamate. The

chemical shift tensor of a molecule is closely related to the electrostatic potential, as both depend on the density of the electron cloud in space.) This ‘shielding’ quantified by  $\sigma$  scales  $B_0$ , external to a  $B_{0, \text{effective}}$  felt by a particular nucleus.

$$B_{0,eff} = (1 - \sigma)B_0 \quad [1.14]$$

Although rigorously  $\sigma$  is a tensor with respect to space and the internal molecular coordinates, in solution state (which generally includes biological tissues), the ‘tumbling’ motion of the molecule with respect to the field averages  $\sigma$  to a scalar quantity. There are, however, certain biological contexts (i.e. highly ordered tissues) in which the directional dependence of  $\sigma$ , or chemical shift anisotropy, is still relevant and can even be exploited to gain certain information.

An ensemble of spins within a sample which occupy an identical chemical environment and share a single Larmor frequency are called an ‘isochromat’, from the Greek meaning ‘same color’. The variability in chemical environment and therefore chemical shift gives rise to multiple isochromats –“spins of different color”-- in a single molecule.

In accordance with Equations 1.10 and 1.14, the absolute difference between the Larmor frequencies  $\omega$  resulting from variable  $\sigma$  -- known as **chemical shift dispersion**-- is greater at larger field. This means that our ability to detect individual nuclei in a molecule-- or those in different molecules in the same solution -- whose Larmor frequencies are similar also improves at higher field strength.

#### **1a.4 Expressing $H_0$ (and subsequent calculations) in the rotating frame of reference**

Everything that happens further in an NMR experiment is going to take place amidst the ‘background’ motion of this precession caused by  $B_0$ , the dominant ‘force’, (similar to all of the motions on earth take place against the ‘background’ of our motion around the sun). It’s

therefore convenient to proceed in mathematical treatment of the NMR experiment by considering a ‘rotating frame of reference’<sup>12</sup>. In the mathematics of quantum mechanics which we have been using, shifting our calculations over to this rotating frame means that we must apply a rotation operator, expressed in terms of the new ‘reference frequency’ at which the frame itself is rotating,  $\omega_{ref}$ , to the Hamiltonian and the wavefunction, respectively:

$$\mathbf{H}^r = \exp(i\omega_{ref} tI_z) \mathbf{H} \exp(-i\omega_{ref} tI_z) - \omega_{ref}I_z \quad [1.15]$$

$$|\psi^r\rangle = \exp(i\omega_{ref} tI_z) |\psi\rangle \quad [1.16]$$

This expression for the Hamiltonian still needs whatever the original (before the rotating frame transformation) Hamiltonian,  $\mathbf{H}$ , to be inserted to be evaluated fully. We’ll start with  $H_0$  and then move to  $H_1$  for inclusion of the RF field.

Corresponding to the notation of the main magnetic field as  $B_0$ , we can call the Hamiltonian term arising from it  $H_0$ , and the frequency of the induced precession,  $\omega_0$ . Using this notation and referring to Equations 1.1-1.3, the Hamiltonian term arising from  $B_0$  is given by:

$$\mathbf{H}_0 = -\gamma B_0 I_z \text{ or } \mathbf{H}_0 = \omega_0 I_z \quad [1.17a, 1.17b]$$

That gives us:

$$\mathbf{H}_0^r = \exp(i\omega_{ref} tI_z) \omega_0 I_z \exp(-i\omega_{ref} tI_z) - \omega_{ref} I_z \quad [1.18]$$

$\omega_0$  is a constant, so we can move it outside the operator expression:

$$\mathbf{H}_0^r = \omega_0 \exp(i\omega_{ref} tI_z) I_z \exp(-i\omega_{ref} tI_z) - \omega_{ref} I_z \quad [1.19]$$

This first term is a succession of three operators, but the rotation operator which we just introduced commutes with  $I_z$ , which allows us to permute the order of the terms:

$$\mathbf{H}_0^r = \omega_0 I_z \exp(i\omega_{ref} t I_z) \exp(-i\omega_{ref} t I_z) - \omega_{ref} I_z \quad [1.20]$$

At which point the rotation operator and its complex conjugate multiply to give 1, and we are left with the simple expression

$$\mathbf{H}_0^r = \omega_0 I_z - \omega_{ref} I_z = (\omega_0 - \omega_{ref}) I_z = \Omega I_z \quad [1.21]$$

the physical interpretation of which is that the motion of the system (according to our new way of looking at it) will be defined by the difference in frequency between the motion of the frame of reference and the Larmor frequency induced by  $B_0$ . At this point, the only reason we would have done this transformation is in order to purposely set  $\omega_{ref} = \omega_0$ , such that this Hamiltonian now equals zero, and-- at least as a result of  $B_0$ -- the net magnetization is "not moving at all". In accordance with the earlier analogy, this is akin to stating that someone is "not moving" while they are standing still on Earth.

Fascinatingly, the physical implementation of the NMR experiment mirrors this mathematical treatment of transformation to the rotating frame. The NMR signal induced in the receive coil is combined with the transmit signal carrier frequency -- which will be  $\omega_0$ -- and only the resulting difference signal is detected.

Returning to the wavefunction itself:

$$|\psi(t)\rangle = \exp(-i\gamma B_0 I_z t) |\alpha\rangle + \exp(-i\gamma B_0 I_z t) |\beta\rangle \quad [1.22]$$

$$|\psi^r\rangle = \exp(i\omega_{ref} t I_z) |\psi\rangle \quad [1.23]$$

where  $\omega_{ref} = \omega_0 = -\gamma B_0$

After we applied the rotation operator, we're back to having

$$|\psi^r\rangle = |\alpha\rangle + |\beta\rangle \quad [1.24]$$

which is what we expect: the eigenstates of the system subjected to  $B_0$ , once we assume rotation, can go back to being treated as the same eigenstates we had in the first place.

### 1a.5 The applied radio frequency (RF) field: $B_1$

Now we consider the effect of introducing another field: radiofrequency field  $B_1$ . From a practical standpoint,  $B_1$  has an extremely important role in the NMR experiment: it rotates, or ‘nutates’ the net magnetization into a position where it can be detected by the receive coils. Upon prolonged application, it also has an additional effect, which is negligibly small in most ‘regular’ NMR experiments but is the lynchpin of the CEST experiment: ‘saturating’ the magnetization, or decreasing the signal from the net magnetization that we would otherwise detect in the presence of  $B_0$ . This effect will be discussed separately in Chapter 1b.

$B_1$  differs in physical properties from  $B_0$  in three important ways:

- a) it is much, much smaller (weaker) and largely applied for a brief period (few ms)
- b) it oscillates in time and space (in the same frequency range as radio waves), rather than being static like  $B_0$ .
- c) the directions of both of its components are perpendicular to  $B_0$ : we can describe them as being along the x and y unit vectors, instead of z

**Nutation** can be understood by looking at the Hamiltonian term arising from  $B_1$  analogously to the one arising from  $B_0$ .

Mathematically, we can describe  $B_1$  as:

$$B_1(t) = x B_1(t) \cos(\omega_{rf}t) - y B_1(t) \sin(\omega_{rf}t) \quad [1.25]$$



where  $\mathbf{x}$  and  $\mathbf{y}$  are the respective unit vectors.  $B_1$ , like  $B_0$ , is a magnetic field with a certain directionality; so, like  $B_0$ , it will also induce precession to some degree, although in this context we give this physical

Note:  $\omega_{rf}$  in which 'rf' is an abbreviation for 'radio frequency' is not to be confused with  $\omega_{ref}$ , in which 'ref' stands for 'reference', to describe our rotating frame.

phenomenon a different name: "nutation". The  $B_1$  Hamiltonian corresponds to this, although it now contains the time dependence and directionality of  $B_1$ : instead of some static ' $B = B_0$ ', we have  $B = \cos(\omega_{rf}t) + \sin(\omega_{rf}t)$ . The constant used to express the magnitude of the 'nutation' (analogous to precession, but along this axis instead) is denoted  $\omega_1$ , and is a function of the magnitude of this applied, oscillating field and, as with  $\omega_0$ , the gyromagnetic ratio.

We can then write down the Hamiltonian term arising from  $B_1$ :

$$\mathbf{H}_1(t) = \omega_1 [\cos(\omega_{rf}t + \varphi) I_x + \sin(\omega_{rf}t + \varphi) I_y] \quad [1.26]$$

Doing some algebra which begins with application of the cyclically commuting operator identity, we can again show that if we've chosen  $\omega_{ref} = \omega_{rf}$ , then the Hamiltonian (now including the terms arising from both  $B_0$  and  $B_1$ ) is

$$\mathbf{H}_{0,1}^r = \omega_1 [\cos(\varphi) I_x + \sin(\varphi) I_y] + \Omega I_z \quad [1.27]$$

$\phi$  is the phase of the pulse, which would be exactly 0 for a pulse along the x axis and,  $\pi/2$  for one along y. If  $\omega_{ref} = \omega_{rf} = \omega_0$ , then the final term is zero, and this equation describes only constant rotation (the one called 'nutation') around a transverse axis. This corresponds to a) choosing a reference rotation that corresponds to the Larmor frequency, and then delivering an RF pulse that also corresponds to the Larmor frequency (i.e. is 'on resonance'). If one of the above have to be false (that is, you need to perform a calculation for off-resonant RF), it is

probably easiest to set  $\omega_{\text{ref}} = \omega_{\text{rf}}$  and have non-zero  $\Omega$ . In this case, the magnetization will nutate around an oblique axis, with an angle from the Z-axis given by

$$\theta = \arctan(\omega_1 / \Omega) \quad [1.28]$$

And the flip angle, which is the integral of the action of  $B_1$  over the duration of the pulse, is given by

$$\alpha = \sqrt{\omega_1^2 + \Omega^2} * t \quad [1.29]$$

Note that this quantity actually becomes *larger* with increased offset. However, what we detect the projection of the magnetization onto the transverse axis, and this quantity does not increase as much with nutation if the axis of that nutation is ‘less perpendicular’ to the z axis.

### 1a.6 Additional useful formalisms

The **density operator** is a mathematical way of representing very large ensembles of identical (in the sense that they are subject to the same Hamiltonian or other operators and can be expressed in the same basis set) quantum mechanical entities. Of course, such very large ensembles of quantum mechanical objects are exactly what we’re concerned with in the NMR or MRI experiment. The density matrix is a probability-weighted sum over individual state densities, where the diagonal elements represent the populations of the eigenstates  $|\alpha\rangle$  and  $|\beta\rangle$ , and the off-diagonal elements are the coherences (linear combinations or superpositions) which we detect as ‘transverse’ magnetization<sup>5</sup>.

---

<sup>5</sup> There are other, more complex ‘things’ that these off-diagonal elements can represent, but discussion of these coherences will be omitted here. The reader is referred to a more authoritative text, e.g. Dr. Brown’s book listed in the bibliography.

For our two-state system, the structure of the density matrix, usually denoted  $\rho$ , is as follows:

$$\rho = |\psi\rangle \langle\psi| = \begin{pmatrix} \rho_{\alpha\alpha} & \rho_{\alpha\beta} \\ \rho_{\beta\alpha} & \rho_{\beta\beta} \end{pmatrix} \quad [1.30]$$

Thus, in a situation where we have no transverse magnetization whatsoever, the value of this density matrix is:

$$\rho_0 = \begin{pmatrix} \rho_{\alpha\alpha,0} & 0 \\ 0 & \rho_{\beta\beta,0} \end{pmatrix} \quad [1.31]$$

where the  $|\alpha\rangle$  component of all spins are contributing to the value  $\rho_{\alpha\alpha}$  and the  $|\beta\rangle$  component of all spins, to the value  $\rho_{\beta\beta}$ . Our net magnetization is  $M_0 = \rho_{\beta\beta,0} - \rho_{\alpha\alpha,0}$ .

It should be pointed out that the density operator does not uniquely specify the ensemble: we have no idea from this representation what the individual spins are doing which contribute to the sum. This is an important point when we consider the action of relaxation (see next section). There are two ways for a sum of something to be equal to zero: either it does not exist (i.e., all individual elements are equal to zero and therefore the sum is zero, too), or the 'things' exist in and of themselves, but they have arbitrary sign and the sum of them is zero. After we create the coherences using the RF pulse, we have nonzero elements in the  $\rho_{\alpha\beta}$  and  $\rho_{\beta\alpha}$  positions. The population of these states has drained population from the  $\rho_{\alpha\alpha}$  and  $\rho_{\beta\beta}$  states, so our Z magnetization has decreased. In order for us to continue to have nonzero elements of  $\rho_{\alpha\beta}$  and  $\rho_{\beta\alpha}$ , the individual components contributing to these sums must stay in phase with each other. But quite soon after we turn off the RF pulse, this situation deteriorates, which we call  $T_2$  relaxation. If  $T_2$  relaxation is complete, we return to a situation where the density matrix has the structure  $\begin{pmatrix} \rho_{\alpha\alpha} & 0 \\ 0 & \rho_{\beta\beta} \end{pmatrix}$ -- however, these are not the  $\rho_{\alpha\alpha,0}$  and  $\rho_{\beta\beta,0}$  that we had before the

pulse. While their *sum* may vanish quickly, only after a while (as so-called  $T_1$  relaxation occurs), do the  $\rho_{\alpha\beta}$  and  $\rho_{\beta\alpha}$  components *individually* drain to zero and repopulate the  $\rho_{\alpha\alpha}$  and  $\rho_{\beta\beta}$  states.  $T_1$  and  $T_2$  relaxation will be discussed further in the next section.

The version of the Schrodinger equation which deals with density matrices instead of individual wavefunctions is called the Liouville-von Neumann equation, and has an equivalent structure:

$$\frac{d}{dt} \rho = -i [\mathbf{H}, \rho] \quad [1.32]$$

When using this equation to calculate the trajectory of an ensemble of spins (for example, under the manipulation of an RF pulse), it's useful to organize our calculation in terms of what are called **product operators**. Product operators are to the density operator as a basis set is to a wave function: they are an orthonormal set which spans the space of the entity of interest. The number of operators needed to fully describe a particular system is determined by the number of independent spins: each type of spin that needs to be considered independently introduces four degrees of freedom, so the number of basis operators will be  $4^N$ . If we're concerned with a single isochromat ( $N = 1$ ), the basis operators will be the angular momentum operators  $I_x$ ,  $I_y$  and  $I_z$  defined above along with the identity matrix,  $I$ .

For systems with more spins, we have to perform a matrix operation called the Kronecker product (hence the name) on these single-spin operators to generate the bigger operators (that is, matrices with more rows and columns) that we need for treating such systems. These mathematics are vital to understanding the NMR experiments done for deducing macromolecular structure, whose usefulness lies in detecting the coupling between many spin systems. They are also useful even in simpler systems to model the effect of a specific RF pulse. Namely, in addition to decreasing the dimensionality of the problem, they frame all calculations

in a context where identities specific to cyclically commuting operators can be applied. This reduces complex mathematical operations to simple ones analogous to rotation about an axis. In addition to the basic commutation definition supplied above, the identity

$$e^{-i\theta A} \mathbf{B} = \mathbf{B} \cos \theta + i[\mathbf{A}, \mathbf{B}] \sin \theta \quad [1.33]$$

is frequently made use of when calculating the effect of various Hamiltonian terms (the RF pulse, J-coupling, etc.) on the spin system.

### 1a.7 Relaxation (as per Bloch)

Suppose that after some duration of the RF pulse, it turns off and no relaxation occurs – and for a while, we simply have a net magnetization vector with X, Y and Z components which is precessing around the Z axis at a particular frequency. If a receiving coil is present, this magnetization will induce an electromotive force in the coil whose amplitude varies in a sinusoidal fashion, in accordance with the instantaneous angle between that magnetization and the detector. A Fourier transform of this detected signal --- which is a function over time-- will give a delta function with the peak located at the frequency of the rotation. This is the most basic possible version of an NMR measurement: we have ‘detected’ the Larmor frequency of the magnetization.

In physical reality, there are no delta functions in frequency, because nothing is of infinite duration in time: systems ‘relax’ from the state which they are in. The effect of applying the  $B_1$  pulse was to take polarization that existed with respect to the Z direction, and temporarily transfer it to the XY plane. We know that the equilibrium state of the spin ensemble with respect to the Z axis is to have a slight polarization, because of  $B_0$ . However, the equilibrium state of the spin ensemble with respect to the X or Y axes is to be evenly populated. Once the

magnetization has XY components (or ‘coherences’ in the density matrix treatment to follow), this polarization will diminish. Also, now that the  $B_1$  field is turned off, the XY components themselves are subject to decay.

To some degree, the physical origins of these relaxation mechanisms can be understood and examined from the point of view of quantum mechanics. However, a simple phenomenological model was put forward in 1946 by Felix Bloch<sup>12</sup> in which he treated the NMR phenomenon as classical electromagnetic induction arising from dampened oscillations. His approach was that decay or relaxation of mostly unspecified origin can nonetheless be captured by rate constants and used in this form to model the signal which arises in experiment. What follows is a summary and paraphrasing of the contents of the first parts of Sections 3 and 4 of Bloch’s seminal paper, the text which effectively launched the modern era of theory and experiment in nuclear magnetic resonance. Please note that where Bloch made use of the letter ‘H’ to refer to the external field, I have substituted this with ‘B’ to maintain consistency with earlier notation.

Bloch begins his treatment of ‘Nuclear Induction’ with the observation that “the quantum-mechanical expectation value of any quantity follows in its time dependence exactly the classical equations of motion”, and writes down the following equation for the net magnetic polarization vector  $\mathbf{M}$  for a nucleus with gyromagnetic ratio  $\gamma$  experiencing an external field  $\mathbf{B}$ , according to a classical picture of torque:

$$\frac{d\mathbf{M}}{dt} = \gamma [\mathbf{M} \times \mathbf{B}] \quad [1.34]$$

where the symbol ‘x’ here represents a cross product between these two vector quantities. He goes on to elaborate the case where  $B_1$ , the oscillating field, is on-resonance with the Larmor frequency of precession around  $B_0$ , arriving at “a solution for which the polarization rotates

around the z-direction, i.e., around the strong field  $[B_0]$  and in such a way that it lies at any instant in the common plane of this field and the effective rotating field.” This is the origin of the common visualization of the magnetization vector “spiraling down” upon application of the RF pulse. Just as in our quantum mechanical treatment above, Bloch arrives using this classical picture at the result that, in the presence of  $B_0$  and  $B_1$  only, the solution to the equations of motion is a net magnetization that exhibits precession about  $B_0$  and nutation about  $B_1$ .

Before even writing down equation 1.34, Bloch notes that this solution assumes the following:

1) No forces are acting on the nuclei except for the external fields  $B_0$  and  $B_1$ . Here he enumerates the following ‘sub-assumptions’:

1a) The electrons associated with these nuclei are not having any appreciable effect.

1b) The interaction between neighboring nuclei can be neglected.

1c) Thermal effects (i.e. losing energy to the surroundings because of random motion, so called by analogy to an object giving off heat) are negligible; the system retains the energy that it has as a result of the  $B_0$  and  $B_1$  terms and does not ‘relax’.

2)  $B_0$  and  $B_1$  are macroscopically homogeneous over the field of view.

In summary, assumption 1a) is usually reasonable; to address the real-life failure of assumptions 1b) and 1c), he introduced two additional terms to equation 1.34 (Bloch’s equation 11), giving us the form of the ‘Bloch equations’ as they are most usually applied today, which make use of the two relaxation parameters  $T_1$  and  $T_2$ , to be discussed in detail shortly:

$$\frac{d\mathbf{M}}{dt} = \gamma [\mathbf{M} \times \mathbf{B}] - \frac{(M_z - M_0)}{T_1} \hat{z} - \frac{M_x + M_y}{T_2} (\hat{x} + \hat{y}) \quad [1.35]$$

More specifically: Assumption 1a, regarding the independence of nuclear and electronic spins, is reasonable in most molecules, but not in the case of radicals or other circumstances where an unpaired electron spin is present. Bloch cites the pioneering work of Rabi on this interaction between nuclear and electronic spin, which is known as hyperfine coupling. It is of interest to note that today, this interaction is exploited amongst the strategies for generating dynamic nuclear polarization, as it is possible to transfer the very strong polarization of an electron spin system to a coupled nuclear one<sup>13</sup>.

Neglecting the hyperfine interaction, we are left with two important effects to deal with: in Bloch's terminology, "Thermal agitation" and "Internuclear action". While they both involve some kind of random perturbation of the spin system, they differ essentially in that a "thermal agitation" can actually change (decrease) the total energy of the spin system, while "internuclear action" describes a shuffling of energy to different degrees of freedom, rather than a change in the total amount.

Bloch points out that the 'source' of energy in the spin system in the first place is the presence of the  $B_0$  field, and thus interactions of the first type, which have to do with the total energy of the system, are necessarily those which cause some change in the z-component of the magnetization ( $M_z$ ). Wherever  $M_z$  happens to be at the moment, in the presence of any such "thermal agitations", it will follow a course from its current value back to  $M_0$ , the equilibrium polarization defined by field strength and gyromagnetic ratio. **The rate of this process is captured by the constant he called  $T_1$ .**

All effects of the second kind – "internuclear actions" – can be understood as some kind of "effective irregularity" (Bloch's words) in the field. While not 'changing the energy of the



system' – because they have no effect on the relationship of the spin system to the field, which is along the z-direction – these “irregularities” cause “smearing” of the exact orientation of the transverse components with respect to space, leading their vector sum to eventually approach zero. Explaining his treatment in quantum mechanical terms, Bloch indicates these are interactions which ‘destroy the phase relation’ of the ‘coherent mixture of states’. **These processes were likewise captured by the constant  $T_2$ .**

Presumably, Bloch settled on a regular monoexponential function to describe these dynamics based on experimental observation. He in fact does not give direct justification for this choice of function, other than to write that, “we shall now introduce these terms....chosen so as to complicate the analysis as little as possible. For this purpose we shall assume that...the change in  $M_x$  and  $M_y$  will likewise be of an exponential character.” All subsequent evidence suggests that this was a successful approach.

Nowadays, the respective types of relaxation captured by  $T_1$  and  $T_2$  are frequently referred to as ‘spin-lattice’ and ‘spin-spin’ coupling. Beyond this, mechanistic specification of their origins is nebulous, and they are generally used as phenomenological quantities which –in a fortuitous application completely unforeseen by their ‘inventor’—turned out to have diagnostic use in medical magnetic resonance imaging.

### **1a.8 Exploiting variations in $B_{0, local}$ to perform imaging and spectroscopy**

We can now understand that, rather than a delta function, the linewidth of the peak in our ‘spectrum’ is going to reflect the fastest rate of decay of this magnetization. In our binary

categorization of relaxation phenomena following Bloch, this will be  $T_2$ .<sup>6</sup> This basic NMR signal, which will be a sinusoidal signal dampened by an exponential described by  $T_2$ , is called the '**Free Induction Decay**', or **FID**. We now turn to the question of how to acquire two types of information beyond detecting a single resonance: namely, either a 'spectrum' of resonances, or an actual picture.

### *1a.8.1 NMR Spectroscopy*

Earlier, we introduced the small, "parts per million" differences in the  $B_0$  "felt" by each nucleus as a result of its chemical environment – that is, the electron shell of the other nuclei in the molecule. These small differences, or chemical shift, in the effective local field cause corresponding differences in Larmor frequency, which can be used to differentiate between nuclei in different chemical positions.

We can expand our picture of the free induction decay measurement of the single spin to include several spins in a molecule with varying frequencies (multiple isochromats). It is important to note that, in order to be able to detect all of the spins present in the sample, we must begin with an excitation pulse that is sufficiently broad (along the frequency axis) to excite all of them. A detailed discussion of excitation pulse shape in spectroscopy is beyond the scope of this report; the reader is referred to Chapter 5 of de Graaf<sup>14</sup>.

---

<sup>6</sup> In practice, the decay of the signal generally occurs more quickly even than would be predicted by theory examining the dynamics and coupling of the molecule(s) in question. This 'observed' rate of relaxation is referred to as  $T_2^*$ , and arises from what are essentially imperfections in the experiment: namely, small deviations in  $B_0$  that are caused by the magnet itself, or introduced or exacerbated by the magnetic susceptibility properties of the sample. For example, interfaces between two tissue types present a sharp change in magnetic susceptibility which perturbs  $B_{0, local}$  and decreases the observed  $T_2^*$  in that region.

Once a transverse component has been introduced to the net magnetization vector of each isochromat, these components will precess about the Z axis at different frequencies. Our receive coil now detects not a single frequency of damped oscillation, but a sum of every frequency which has been excited, in amplitude proportional to the population (or concentration, in chemical terms) of each. This signal, upon Fourier transform, then results in a spectrum with multiple peaks. In a pure sample, this NMR spectrum provides a “fingerprint” so unique that it has become the standard method in the chemistry laboratory for identifying products of chemical reactions. Sophisticated experiments exploiting extensive magnetic coupling – known as “multidimensional NMR”-- expand NMR spectroscopy from identification of small molecules to solving the structures of macromolecules like proteins and RNA, as in refs <sup>15,16</sup>.

A number of considerations make this experiment – measurement of the NMR spectrum – less straightforward *in vivo* than it is in an analytical chemistry setting. The first and overwhelmingly important of these is the presence of a dominant water signal. In analytical NMR, deuterated solvents are used to avoid detection of anything but the molecule of interest. In a living organism, the solvent is regular, proton-based water, and its concentration is orders of magnitude higher than any other contribution. In order to detect other resonances, this water resonance must be suppressed. Generally, this is accomplished by various strategies of saturation or excitation and dephasing. Suppression of water in *in vivo* spectroscopy is not a trivial problem, as it is difficult to design pulse sequences which affect the water resonance exclusively. For this reason, techniques like metabolite cycling which avoid water suppression remain an active area of research<sup>17</sup>.

Secondly, living tissue is a semi-solid matrix, rather than a true solution state. This means that all types of coupling and relaxation will occur more extensively. Furthermore, inhomogeneity of the

main field ( $B_0$ ) as well as of the transmit field ( $B_1$ ) may be non-negligible in an irregularly shaped sample. Modern pulse sequences for imaging and spectroscopy strive to be robust to the consequent variability in excitation, but achieve this only for inhomogeneities of a limited degree. Finally, in most cases the desired data is a *localized* spectrum: that is, one in which the signal is derived only from the sample volume in a prescribed region of space. This can be accomplished by spatially selective excitation schemes as in the PRESS<sup>18</sup>, STEAM<sup>19</sup> and LASER<sup>20</sup> sequences, which will be discussed briefly in the next section.

### *1a.8.2 MR Imaging: Gradients, Encoding and Pulse Sequences*

$B_{0, \text{local}}$  can also be manipulated in a controlled fashion and on a much larger scale by gradient coils, which create macroscopic gradients  $dB_0/dx$ ,  $dB_0/dy$ ,  $dB_0/dz$ . In this way, the relationship between  $B_0$  and Larmor frequency is exploited to achieve localized measurements, and thereby images – in this case, derived from the dominant signals of water and fat. This strategy is called ‘spatial encoding’. In practice, **frequency encoding** *per se* is only used to ‘encode’ a single dimension, while **slice-selective excitation** and **phase-encoding** are generally used for the other two.

Spatial encoding by field gradients was first proposed by Paul Lauterbur in 1973<sup>21</sup>. Slice selective excitation was introduced by Garroway, Grannell and Mansfield<sup>22</sup>, while phase and frequency encoding, inspired by work in the multi-dimensional NMR by Ernst and others, was introduced subsequently<sup>23</sup>. Credit is also due to Mansfield for the introduction of the popular echo-planar imaging (EPI) technique<sup>24</sup>, the most extensive application of which is probably functional magnetic resonance (fMRI) imaging of the brain. Another landmark event in the development of modern clinical radiology was the realization by R. Damadian that the relaxation times first described by Bloch can be used to discriminate healthy from cancerous tissues<sup>25</sup>.

### 1a.8.3 Magnetic Field Gradients and Spatial Encoding

The following equation describes how the Larmor frequency  $\omega$  is modified by the presence of the gradient field  $G$  at position  $r$  of the axis along which the gradient is applied.

$$\omega(r) = \gamma B_0 + \gamma \mathbf{r} \cdot \mathbf{G} \quad [1.36]$$

The spatial encoding of a three-dimensional object can be reduced to a two-dimensional problem by selecting one dimension specifying a plane (or a 'slice' – MR lingo for a plane of finite thickness) with the excitation pulse in the presence of a gradient. In other words, from an information standpoint, we're 'filtering' the excitation to magnetization defined by two dimensions, and then 'filtering' the detection of that magnetization to differentiate between the remaining two. The key to doing this is to have the gradient turned on (i.e. create a spatially-dependent distribution of frequencies) *both* during the excitation by RF pulse, *and* during the acquisition of the FID.

One might imagine that by application of additional, perpendicular gradients through the slice, perhaps a complete 3D spatial determination could be achieved. However, the spatial location of each particular frequency cannot be uniquely determined in this manner, because of symmetry. This can be understood by analogy with a multiplication table: if one wants to identify one of the squares by saying that it contains the number 27, it is ambiguous as to whether we are describing square (9,3) or (3,9). To overcome this, an iterative technique (termed 'back-projection', by inheritance from its origins in X-ray tomography, in beams actually traverse an object) was used as per the insight of Lauterbur to solve this image reconstruction problem in the early days of MRI. Nowadays, the more efficient strategy of combining frequency with phase encoding is generally preferred.

Suppose that upon frequency encoding we will have 'stripes' of the excited slice with frequencies A, B and so on. Conceptually, we now want to define a system of perpendicular stripes such that each spot in this excited grid can be identified uniquely. **Phase encoding** uses the same strategy as the above-described frequency encoding – the application of an additional linear gradient – but to a slightly different effect. Instead of applying the linear gradient (and thereby modifying the Larmor frequency) during the acquisition itself, the phase encoding gradient is applied for a short time prior to the acquisition. While this gradient is applied, the spins experience precession around a slightly different Larmor frequency *for a short time only*. The effect of this is that, although they have returned to their "original" frequency by the time of the acquisition (in this case, whatever frequency is dictated according to their location by the frequency encoding gradient), their phase  $\phi$  in this sinusoid will be different. Repeated application of a variable-strength phase encode gradient and acquisition of the resulting signals results in a collection of signals representing the algebraic problem  $\phi_i A + \phi_j B$ , where  $i$  represents the iteration over phase gradients and A, B are two (of many) signals of variable frequency whose contributions need identification in the last dimension. The contribution of each signal can be determined uniquely by doing mathematics analogous to solving a pair of equations  $\{\phi_i A + \phi_j B = 1, \phi_i A + \phi_j B = 2\}$  for the unknowns.

Conceptually, all of the magnetic resonance information present in an MRI volume can thus be thought of as having some location in the space (phase, frequency) as defined by the signal gathered when these two gradients were applied. This 'space' (in the mathematical sense) is called '**k-space**', and is useful to describe the order in which we collect the information in the image. It happens to be the Fourier Transform (FT) of intensities of the image in real space, in the same way that a diffraction pattern is the transform of a crystal structure or the information

needed to create a hologram is FT of the optical image. Depending on the pulse sequence, the informational content in k-space may be filled in in a different order.

The imaging pulse sequence can be designed such that the contrast in the resulting image predominantly reflects different physical properties of the spins in each voxel: we can ‘weight’ the amplitude of the signal in the image for  $T_1$ ,  $T_2$ , or just the number of protons present in the voxel (known as a “proton density weighted” image). A detailed discussion of imaging pulse sequences and acquisition strategies will not be included here, except for a brief explanation of the basic **gradient-echo** and related fast low-angle shot or FLASH sequence upon which our gluCEST sequences are based and a few key sequences for localized spectroscopy. Specialized acquisitions required for the CEST experiment will be discussed in Chapter 1b, in the section *The CEST Experiment in Practice*.

**Gradient echo.** It might seem that, armed with the strategies of spatial encoding described

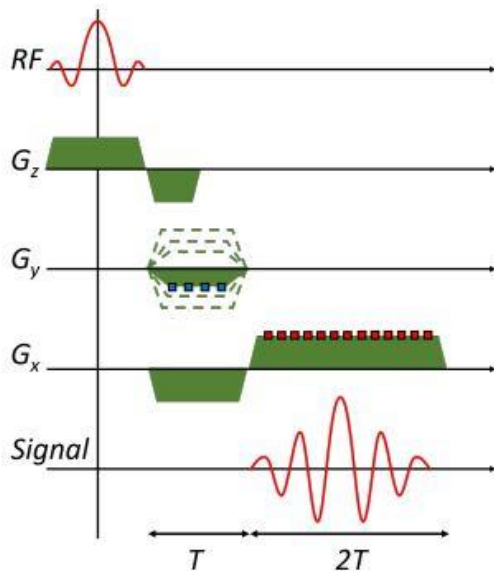


**Figure 1a.1.** Basic (unspoiled) gradient-echo pulse sequence, from S. Shah (see General Bibliography )

above, one could perform magnetic resonance imaging using the FID signal itself. This is possible, but can be disadvantageous for reasons having to do with the decay of the signal as defined by the  $T_2$  or  $T_2^*$  envelope. Namely, optimal signal-to-noise ratio will be achieved if the peak signal amplitude coincides with the acquisition of the ‘center’ of k-space, the {frequency, phase} space which defines our localization scheme. However, depending on the

acquisition scheme, the center of k-space is often not collected first with respect to time after the RF pulse. In order to cause the peak signal amplitude to recur when the center of k-space is being measured, gradients or RF pulses can be used to induce an 'echo' of the FID.

The physical explanation of this phenomenon is that any dephasing that is caused by events that are non-random, defined functions of time (e.g. interactions caused by static electronic structure of the molecule or substance) can be reversed. A popular analogy is that of runners or racecars at a starting line that move at various defined speeds: when the race begins, they will spread out over space relative to each other. However, if one had some way to make everyone suddenly stop and go backwards at the same velocity, one would expect all participants to be 'in phase' at the start line again after an equal amount of time.

There are two ways to do this to the spins in an MR experiment: 'flip' the system with another RF pulse to generate a mirror image of the current phase picture (this is called '**spin echo**'), or use gradients. The latter method, called '**gradient echo**', works by first applying a gradient to purposely dephase the spins – that is, much faster than they would be dephased 'naturally' by  $T_2$  decay – and then applying the same gradient in reverse to generate the echo. This allows for acquisition of the echo faster than in the case of using a  $180^\circ$  RF pulse. Together with the use of spoiler gradients and sometimes in combination with spin echo techniques, gradient echo is among the strategies used for accelerating acquisition, as in the popular fast low-angle shot (FLASH) sequence described below.

### **Spoiled gradient echo, including FLASH**

The faster one accelerates image acquisition, the more strategies must be employed to keep the signals from different points in k-space separate from each other. Using a low flip angle (so that



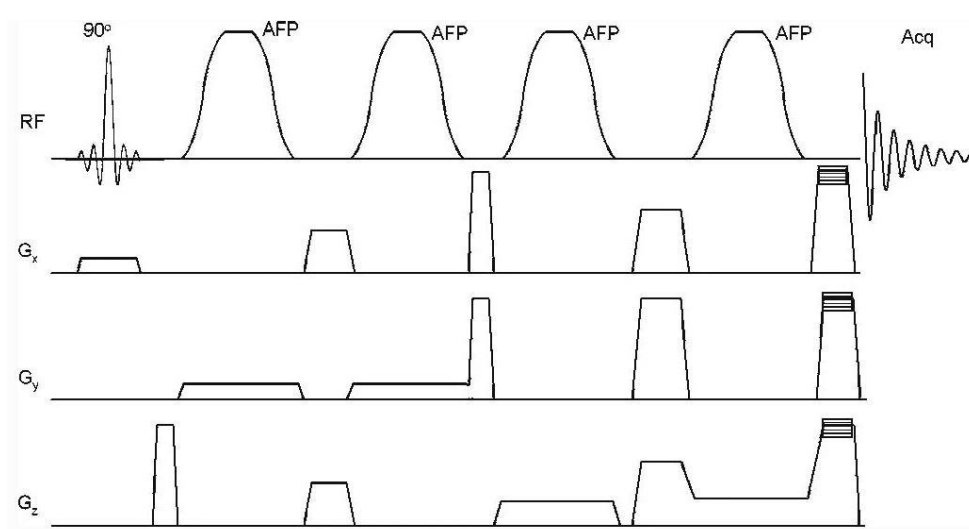
the magnetization has less “distance to travel” back to full recovery) is one strategy to avoid contribution from residual magnetization between k-space points. Furthermore, fast, repeated excitation and signal acquisition can be kept ‘clean’ from residual signal from the last iteration by a strategy called ‘spoiling’, defined as the ‘disruption of transverse coherences that may persist from cycle to cycle in a GRE sequence’<sup>26</sup>. The CEST sequences used in this thesis are based off of the Siemens product version of FLASH<sup>27</sup>, which is a spoiled gradient-echo sequence where the spoiling is primarily accomplished by spoiler gradients, with additional spoiling achieved by modulating the phase of the RF carrier frequency. It is likely that the strategy for the latter implemented in FLASH is based off of the work of Zur et al, who offered a formula for RF phase-cycling to eliminate unsolicited coherences arising from ‘resonance’ of various harmonics<sup>28</sup>.

### **PRESS, and LASER for localized spectroscopy**

As in imaging, the basic strategy of generating a localized NMR spectrum is to manipulate the spins so that excitation, phasing, or both are selective for a particular frequency and therefore a particular volume.

One popular sequence for single-voxel spectroscopy is Point Resolved Spectroscopy or **PRESS**, introduced by P. Bottomley<sup>18</sup>. It is a double spin-echo sequence: slice selective excitation is followed by two (also slice selective, for orthogonal slices) refocusing pulses. This generates two echoes, the second of which contains the desired signal which is localized in all three dimensions. The correct localization of the full spectrum relies on a sufficiently broadband refocusing pulse; otherwise, so-called chemical shift displacement errors will occur, in which the

**Figure 1a. 2.** semi-LASER pulse sequence diagram, from ref [21], which introduced this technique. A 90° slice selective pulse is followed by four adiabatic full passage (AFP) pulse which refocus the magnetization with respect to the other two dimensions.



signal from  
different  
resonances  
are arising  
from  
different  
adjacent  
volumes.  
The major  
limiting  
factor of

PRESS is that the refocusing pulses must be of limited bandwidth to accommodate limitations on total RF power. At higher field strength, the necessarily narrow bandwidth of these refocusing pulse causes a chemical shift displacement error that could be interpreted as unacceptably large.

An alternative pulse sequence is Localization by Adiabatic Selective Refocusing, or **LASER**. The basic concept of the LASER sequence is that excitation and spatial selection are separated into

two different steps. After exciting the entire sample with a  $90^\circ$  pulse, slice-selective refocusing is achieved by six (one pair per dimension)  $180^\circ$  adiabatic full passage (AFP) pulses. Use of these very broadband AFP pulses mitigates the issue of chemical shift displacement error. However, like PRESS, the performance of LASER is also limited by the allowable magnitude of RF power. A 'compromise' on this front manifested in the development of the semi-LASER sequence, in which a 'regular' slice selective excitation pulse is followed by only four, instead of six, AFP refocusing pulses<sup>20</sup>. A chemical shift imaging implementation of the semi-LASER sequence is employed in the experiments described in Chapter 6.

## References

1. Gorter CJ. Negative result of an attempt to detect nuclear magnetic spins. *Physica*. 1936;3(9):995-998. doi:10.1016/s0031-8914(36)80324-3
2. Trabesinger A. Scientific literature: Less room for failure. *Nat Phys*. 2011;7(10):745. doi:10.1038/nphys2119
3. Кессених АВ. Открытие, исследования, и применения магнитного резонанса. *Успехи Физических Наук*. 2009;179(7).
4. Purcell EM, Torrey HC, Pound R V. Resonance absorption by nuclear magnetic moments in a solid [7]. *Phys Rev*. 1946;69(1-2):37-38. doi:10.1103/PhysRev.69.37
5. Bloch F, Hansen WV, Packard M. The Nuclear Induction Experiment. *Phys Rev*. 1946;70(7-8).
6. Cartlidge E. The Spin of a Proton. *Phys World*. Published online June 2015. <https://physicsworld.com/a/the-spin-of-a-proton/>
7. Pauli W. Zur Quantenmechanik des magnetischen Elektrons. *Zeitschrift für Phys*. 1927;43(9-10):601-623.
8. Engel T. *Quantum Chemistry and Spectroscopy*. 2nd Editio. Pearson; 2009.
9. Kelley AM. *Condensed Phase Molecular Spectroscopy and Photophysics*. Wiley; 2012.
10. Van De Moortele PF, Akgun C, Adriany G, et al. B1 destructive interferences and spatial phase patterns at 7 T with a head transceiver array coil. *Magn Reson Med*. 2005;54(6):1503-1518. doi:10.1002/mrm.20708
11. Sled JG, Bruce Pike G. Standing-Wave and RF Penetration Artifacts Caused by Elliptic Geometry: An Electrodynamics Analysis of MRI. *IEEE Trans Med Imaging*. 1998;17(4):653-662. doi:10.1109/42.730409
12. Bloch F. Nuclear induction. *Phys Rev*. 1946;70(7-8):460-474. doi:10.1103/PhysRev.70.460
13. Hu KN, Yu HH, Swager TM, Griffin RG. Dynamic nuclear polarization with biradicals. *J Am Chem Soc*. 2004;126(35):10844-10845. doi:10.1021/ja039749a
14. Graaf RA de. *In Vivo NMR Spectroscopy: Principles and Techniques*. Third Edii. Wiley; 2019.
15. Ceccon A, Tugarinov V, Boughton AJ, Fushman D, Clore GM. Probing the Binding Modes of a Multidomain Protein to Lipid-based Nanoparticles by Relaxation-based NMR. *J Phys Chem Lett*. 2017;8(11):2535-2540. doi:10.1021/acs.jpcclett.7b01019
16. Becette OB, Zong G, Chen B, Taiwo KM, Case DA, Dayie TK. Solution NMR readily reveals distinct structural folds and interactions in doubly <sup>13</sup>C- And <sup>19</sup>F-labeled RNAs. *Sci Adv*. 2020;6(41):eabc6572. doi:10.1126/sciadv.abc6572
17. Giapitzakis IA, Shao T, Avdievich N, Mekle R, Kreis R, Henning A. Metabolite-cycled STEAM and semi-LASER localization for MR spectroscopy of the human brain at 9.4T. *Magn Reson Med*. 2018;79(4):1841-1850. doi:10.1002/mrm.26873
18. Bottomley PA. Spatial localization in NMR spectroscopy in vivo. *Ann N Y Acad Sci*.

1987;(508):333-348.

19. Frahm J, Merboldt KD, Hänicke W. Localized proton spectroscopy using stimulated echoes. *J Magn Reson.* 1987;72(3):502-508. doi:10.1016/0022-2364(87)90154-5
20. Scheenen TWJ, Heerschap A, Dennis , et al. Towards 1 H-MRSI of the human brain at 7T with slice-selective adiabatic refocusing pulses. *Magn Reson Mater Phy.* 2008;21:95-101. doi:10.1007/s10334-007-0094-y
21. Lauterbur PC. Image formation by induced local interactions: Examples employing nuclear magnetic resonance. *Nature.* 1973;242(5394):190-191. doi:10.1038/242190a0
22. Garroway AN, Grannell PK, Mansfield P. Image formation in NMR by a selective irradiative process. *J Phys C Solid State Phys.* 1974;7(24):L457. doi:10.1088/0022-3719/7/24/006
23. Kumar A, Welti D, Ernst RR. NMR Fourier zeugmatography. *J Magn Reson.* 1975;18(1):69-83. doi:10.1016/0022-2364(75)90224-3
24. Mansfield P, Maudsley AA. Planar spin imaging by NMR. *J Magn Reson.* 1977;27(1):101-119. doi:10.1016/0022-2364(77)90197-4
25. Damadian R. Tumor detection by nuclear magnetic resonance. *Science (80- ).* 1971;171(3976):1151-1153. doi:10.1126/science.171.3976.1151
26. Elster AD. MRI questions.com. <http://mriquestions.com/mp-rage-v-mr2rage.html>
27. Haase A, Frahm J, Matthaei D, Hanicke W, Merboldt KD. FLASH imaging. Rapid NMR imaging using low flip-angle pulses. *J Magn Reson.* 1986;67(2):258-266. doi:10.1016/0022-2364(86)90433-6
28. Zur Y, Wood ML, Neuringer LJ. Spoiling of transverse magnetization in steady-state sequences. *Magn Reson Med.* 1991;21(2):251-263. doi:10.1002/mrm.1910210210

### General Bibliography

Abraham A. Principles of Nuclear Magnetism. Clarendon Press; 1961.

Brown KC. Essential Mathematics for NMR and MRI Spectroscopists. Royal Society of Chemistry; 2017.

Dirac, P.A M. The Principles of Quantum Mechanics. Oxford University Press; 1958.

Kreis FK. Development of Magnetic Resonance Spectroscopic Imaging Methods to Assess Tumor Metabolism. Published online 2019.

Shah SM. Magnetisation Transfer Effects at Ultra High Field MRI. Published online 2016.

Wilson NE. Nonuniform and Non-Cartesian Sampling in Multidimensional Magnetic Resonance Spectroscopic Imaging. Published online 2015.

*English version of ref. 3: Kessenikh A V. Magnetic resonance: discovery, investigations, and applications. Physics-Uspekhi. 2009;52(7):695-722. doi:10.3367/ufne.0179.200907c.0737*

## 1b: The Chemical Exchange Saturation Transfer Experiment

### 1b.1 Overview and strategy of the experiment

*These next sections will provide a conceptual overview of the physics relevant to CEST. The reader is encouraged to return to this narrative explanation when reviewing the mathematical expressions in the subsequent section, 'Phenomenological Modeling of the CEST experiment'.*

Overwhelmingly, standard forms of Magnetic Resonance Imaging (MRI) detect the NMR signal from water, which forms a huge fraction (~70%) of the human body. Chemical Exchange Saturation Transfer (CEST) is a specialized MRI modality which seeks to indirectly detect the presence of specific molecules or metabolites which may exist only at millimolar concentrations *in vivo* by exploiting their interaction with the surrounding bulk water - -specifically, their propensity to undergo a process called chemical exchange. Briefly, chemical exchange is the process of nearby molecules 'trading' labile protons, where labile describes the chemical properties determining whether this proton is likely to 'come off'. (See discussion below.)

In the previous section, we introduced the notion that extended application of the RF pulse (or  $B_1$  field) could induce a temporary 'saturation', or decrease, of the NMR signal in the spin pool. It turns out that this saturation and consequent signal depression is transferable from one pool of spins in a sample to another. Nuclear spins interact with the  $B_1$  field in a frequency-specific manner, and thus any RF pulse applied for the purposes of inducing the MR-saturated state can be made specific to a particular spin system, to whatever degree that a) the Larmor frequency of that isochromat is unique (i.e. it is the only thing contributing to the resonance in that part of the spectrum) and b) it is possible to narrow the frequency bandwidth of the RF pulse itself.

In CEST, such a frequency-selective pulse is delivered to a resonance of the molecule of interest. When this pool of protons with a now non-equilibrium distribution of spin states exchanges from its original molecule to the water surrounding it, the water signal itself is now harboring this non-equilibrium state, and upon measurement exhibits a decreased net magnetization and NMR signal. The **magnitude of this CEST effect** on the water signal **will depend on:**

- a) the concentration of the saturated target metabolite
- b) the efficiency or degree of saturation
- c) the rate of exchange between that molecule and water
- d) the relaxation properties of the water

Note that the relaxation properties of the target molecule itself contribute to (b), the efficiency of saturation. Since exchange is effectively a form of relaxation, (b) and (c) are not independent. This point will be discussed further in the next section.

In this way, an experiment can be designed which consists of two basic steps: saturating the molecule of interest, and then detecting the water signal. Pulse sequences for any type of CEST experiment reflect this: they contain a 'magnetization preparation' module in which the saturation is performed, and an acquisition or 'read out' module in which the water signal is used to generate an image. In some cases, these modules may be interleaved to varying degrees. It is important to note that the acquisition module must be of a form which produces a proton density weighted image, as the CEST effect essentially manifests as a decrease in the 'concentration' of protons in that voxel of the image.

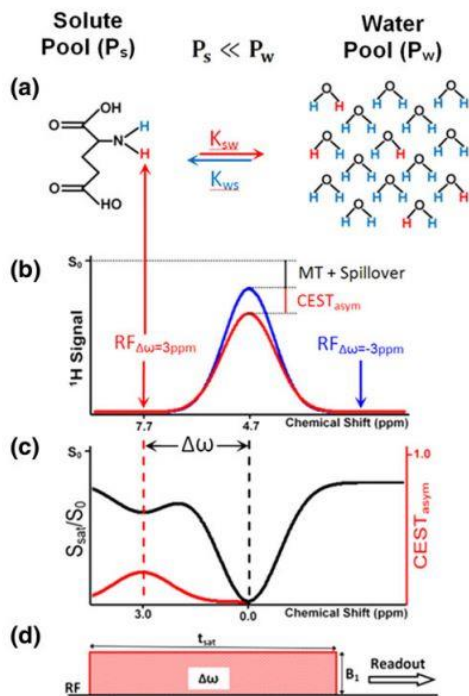


**Figure 1b.1. Illustration of CEST phenomenon and its measurement, from Kogan, Hariharan and Reddy, 2013** **a)** RF at the Larmor frequency of the labile proton induces saturation in this population. Exchange with water transfers this saturation to the water pool. **b)** The proton NMR spectra of the sample, exhibiting a decrease in the water signal when the saturation pulse is applied. **c)** The Z-spectrum, plotting the change upon saturation at a particular frequency (black) and the ‘asymmetry’ spectrum, which subtracts one side of the Z-spectrum from the other to eliminate the symmetric direct saturation peak, leaving only the peak of interest reflecting the contribution of exchange (red). **d)** Pulse sequence schematic of the CEST experiment: saturation followed by readout.

We can walk through the mechanism of the CEST experiment as follows (see Figure 1b.1)<sup>1</sup>. First of all, a measurement of the  $^1\text{H}$  NMR signal of water might give a spectrum similar to those shown in red or blue in 1b.1b. Exchangeable protons exist on some molecule dissolved in this water – in this case, attached to the nitrogen in glutamate -- and resonate at some Larmor frequency,  $\omega$ . An RF pulse is applied at frequency  $\omega$  (here, 3ppm relative to water) which saturates the NMR signal of this population of protons. These protons exchange with the bulk water which they’re dissolved in. This transfers the saturation of this portion of the signal to the water resonance (panel a). When the water NMR signal is detected again, it gives a smaller peak (panel b, red line) than it did without the saturation, or with saturation that is off-resonance from the metabolite of interest, as is indicated by the blue line. (The significance of performing this second saturation at precisely -3ppm will be discussed in the next section.) We can make a plot that shows the magnitude of this signal decrease as a function of the frequency of the



saturation pulse, called the Z-spectrum<sup>7</sup> (panel c, black line). To quantify the effect of the saturation due to exchange, we frequently report the subtraction of one side of the Z-spectrum from the other (panel c, red line), to eliminate the contribution of effects that are not of interest, such as the direct saturation of water itself at 0ppm.

While it is difficult to think of a better pictorial representation of the CEST phenomenon, illustrations such as that in Figure 1b.1a can be a bit misleading in that they suggest a ‘labeling’ of *individual* hydrogen atoms, as in the case of experiments which substitute hydrogen for deuterium. However, it is important to keep in mind that the NMR signal that is temporarily lost upon saturation is a result of changing the *sum* of all of the magnetic moments. Thus one could not, unlike in case of the isotope labeling, actually point to one proton or another in a chemical structure and state that “this proton is saturated while this one isn’t”, although this might be the idea gleaned from such a graphic.

### 1b.2 Generation and analysis of the Z-spectrum

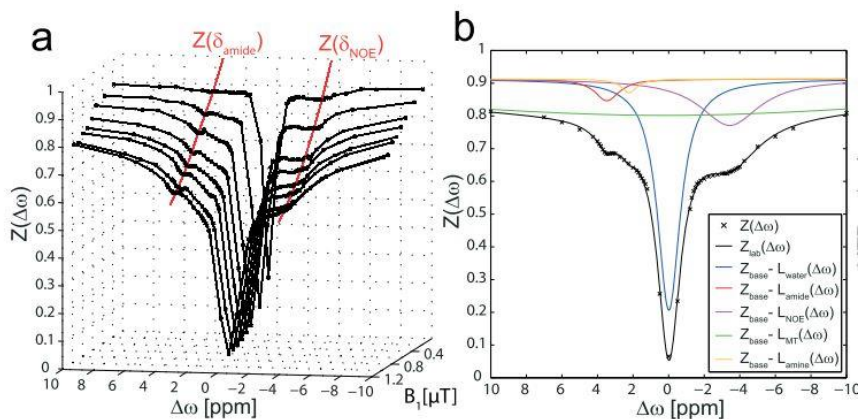


**Figure 1b.2 The Z-spectrum:  $B_1$  dependence and Lorentzian fitting.**  
From Windschuh et al 2015 [ref. 2].

As illustrated in Figure 1b.1b and 1b.1c, a so-called Z-spectrum can be generated by sweeping over frequencies of

<sup>7</sup> It appears that the term ‘Z-spectrum’ originated from the work of R.G. Bryant, in the context of cross-relaxation spectra, as in *Hinton DP, Bryant RG. Magn Reson Med. 1996;35(4):497-505*. The term was then adapted, presumably by Wolff, Balaban and others, to describe the magnetization transfer arising from chemical exchange.

the applied saturation pulse (the x-axis of the Z-spectrum) and measuring the magnitude of the post-saturation water signal (the y-axis). While the Z-spectrum illustrated in Figure 1b.1 is schematic, Z-spectra gathered from a human brain are illustrated by Figure 1b.2a, from Windschuh et al 2015<sup>2</sup>.

Other than the frequency of the saturation pulse, the second important parameter which characterizes it is amplitude; this amplitude is generally referred to as ‘saturation  $B_1$ ’ -- or just ‘ $B_1$ ’ when the context is clear. **Figure 1b.2a** nicely illustrates how the Z-spectrum evolves with varying  $B_1$  power, although the range of saturation  $B_1$  amplitudes shown here is that relevant for the APT CEST experiment. In Chapter 2, we will discuss the dependence of the CEST signal on  $B_1$  as relevant to the gluCEST experiment, which requires a  $B_1$  amplitude more than double the maximum indicated on the plot in Figure 1b.2a.

Note that in a CEST image, since the water signal has a magnitude in every pixel, every single pixel has its own Z-spectrum. (In practice, there may be some cases where averaging over several pixels is performed.) Once the series of images comprising the Z-spectrum is acquired, there are two main approaches to quantifying the CEST signal at the frequency offset of interest, which are respectively illustrated by Figures 1b.1 and 1b.2. Panel C of Figure 1b.1 illustrates the approach of “magnetization transfer asymmetry”: one side of the black ‘spectrum’ is subtracting from the other, resulting in the red line. In this approach, which is the one used in the work presented here, it is not assumed that we can assign *all* contributions to the Z-spectrum, but rather only that the contribution at a *particular* frequency offset is dominated by the signal of interest. The asymmetry approach is based on simple subtraction of directly measured signals and does not require fitting; thus it does not necessitate collecting the entire Z-spectrum beyond the frequency ranges of interest on each side of water, although some additional

bandwidth is needed to allow for  $B_0$  inhomogeneity correction. (See *The CEST Experiment in Practice.* )

Alternatively, another popular approach is to collect the entire Z-spectrum and fit the respective contributions with Lorentzian functions, not unlike the standard approach for spectroscopy data. This is the favored method of several practitioners, as in the work of M. Zaiss<sup>3</sup> and A. Singh<sup>4</sup>. Some works making use of Lorentzian fitting claim that in this way, they have overcome the challenges of specificity inherent in the CEST experiment. However, this assumes that all contributions to the Z-spectrum are known (i.e., that the basis set used for fitting is complete), which is difficult to demonstrate.

### **1b.3 The challenge of specificity in the CEST experiment**

Indeed, a major shortcoming of CEST is the ambiguity arising from the combined (and often inseparable) effects of the above-listed factors (a-d) along with the limited degree of truly frequency-selective excitation. The major categories of specificity-related challenges to CEST and strategies for their mitigation are as follows:

#### *--Excitation of species other than the target metabolite*

Two subcategories of this problem are: a) other metabolites (which exchange or cross-relax) resonating in the same region of the spectrum as the target metabolite can also be excited; b) water itself can become directly excited because of the very large magnitude (and therefore width) of its resonance peak. *Mitigation:* a) It is best practice to perform phantom experiments in which one attempts to adjust the power, shape and frequency of the saturation pulse to optimize conditions such that the dynamic range of the signal predominantly depends on the concentration of only one of the overlapping metabolites. . However, separation of those

molecules which have both similar chemical shifts and proton exchange rates can still remain quite challenging, and assumptions about relative contributions are often made on the basis of concentration. b) Use of higher field strength increases the chemical shift dispersion between water and the target metabolite, and shimming minimizes the width of the water peak, decreasing the degree of direct saturation

*--Inhomogeneity or insufficiency of the saturation-inducing radiation*

At 7T, the RF used has comparable wavelength to human anatomical dimensions. Because of this, standard transmit/receive head coils produce a high degree of inhomogeneity in  $B_1$  amplitude, arising from standing waves. Furthermore, absolute saturation power is limited by safety considerations. *Mitigation:* Addressing this problem with respect to gluCEST is the subject of Chapter 2, the introduction of which covers the challenge more generally. Also relevant is section 2.1, in which use of high dielectric pads is explored.

*--Relaxation properties ( $T_1$ ) can be confounded with the CEST effect*

This is an entirely intrinsic property of the CEST phenomenon, which is clearly expressed mathematically in Equation 1.38 of the next section. *Mitigation:* This is also perhaps the most resolvable amongst these issues, as it can be understood theoretically and corrected for. This is the basis of the commonly used AREX approach developed by Zaiss et al.<sup>5,6</sup>

*--Variability in exchange rate is difficult to separate from concentration*

The main issue here is exchange rate dependence on pH. Theoretically, this is very difficult to deconvolute, as these two terms – exchange rate and concentration -- always appear as the product [rate\*concentration].

*Mitigation:* Deciding whether variability in the CEST contrast is due to variability in

concentration or pH is generally a question of reasonable interpretation of the physiological context; e.g., if pH is known to be variable in a tumor, this may be the appropriate interpretation of the CEST maps in that case, as in ref <sup>7</sup> . Unfortunately, such pathology may also be the context of our interest in the target metabolite. This relationship between pH and exchange rate presents a very real challenge for certain CEST applications, although in other contexts, it is exploited as the main contrast of interest <sup>8-11</sup> . <sup>8-11</sup> .

#### **1b.4 The saturation pulse**

The physics of the CEST saturation pulse is an excellent example by which to illustrate the equivalency of the quantum mechanical and classical pictures of NMR. In optical forms of spectroscopy-- in which there is no option of a “classical” model—‘saturation’ of a transition explicitly implies that the two state populations have been equilibrated and thus the dominance of absorption over relaxation which forms the basis of our interaction with the system no longer holds.

Translation of this quantum mechanical notion directly to the CEST experiment does at first glance appear to explain the phenomenon: we have applied an excitation pulse sufficiently long such that it decreases our ability to interact with the system (i.e. observe or detect the magnetization). However, there is a layer of complication in the NMR experiment that has no analog in most forms of optical spectroscopy, which is the presence of transverse magnetization. In an optical experiment, we may create some coherent superposition states, but the only thing we ever detect is either the absorption or emission of a photon resulting from a transition between two eigenstates of the system. In contrast, in NMR, what we are detecting

is the *presence of the superposition coherence itself*<sup>8</sup> by way of what Bloch first dubbed ‘nuclear induction’. Thus, if we perform saturation which decreases the signal, it follows that we are in fact perturbing our ability to detect *this particular state*.

In his 1946 paper, Bloch explains that, *“it is essential, from this point of view, that we are dealing with a “coherent mixture” of states, i.e. that the relative phases of the wave functions, corresponding to the different states, do not undergo any changes. It can be expected, and will be shown later, that any cause which tends to destroy the phase relation, such as the interaction between neighboring nuclei, will diminish the actual observable value of the rotating component.”*

This concept of “phased” and “dephased” magnetization is the key bridge between quantum mechanical and classical models that allows us to understand and model the CEST experiment using only classical equations *à la* Bloch, in which the individual states  $|\alpha\rangle$  and  $|\beta\rangle$  do not appear at all. (See *Phenomenological modeling of the CEST experiment: Bloch-McConnell equations*.)

However, we can ‘translate’ between them by understanding the relationship between the transverse magnetization and the elements of the density matrix: when we perform saturation using an RF pulse, what we’re essentially doing is temporarily ‘storing’ spin angular momentum as unphased transverse magnetization  $-\rho_{\alpha\beta}$  or  $\rho_{\beta\alpha}$  which sum to zero -- giving us an  $M_Z$  where both  $\rho_{\alpha\alpha}$  and  $\rho_{\beta\beta}$  are less than  $\rho_{\alpha\alpha,0}$  and  $\rho_{\beta\beta,0}$ .<sup>9</sup> When we rotate this net  $M_Z$  into the

---

<sup>8</sup> This is a very key difference between these two experimental fields that for some reason is rarely pointed out explicitly, although I think doing so would help enhance the general understanding of the relationship between NMR “spectroscopy” and its half-siblings in other areas of chemical physics.

<sup>9</sup> However, using RF radiation in this way, we are not able to actually manipulate the ratio  $\frac{\rho_{\alpha\alpha}}{\rho_{\beta\beta}}$  itself. This is in contrast to experiments involving dynamic nuclear polarization via coupling to electron spin, in which single quantum transitions affecting the distribution between eigenstates are effected by irradiation of the electronic resonance.

transverse plane to detect it in the acquisition or readout module, we detect a lower signal than we would detect in the presence of the original  $\rho_{\alpha\alpha}$  and  $\rho_{\beta\beta}$ , which will be restored only after  $T_1$  relaxation has occurred.

Conceptually, we can trace through the process of saturation as follows: Before the saturation pulse begins, the net magnetization of both species – metabolite and water—is longitudinal and of equilibrium magnitude. We now turn on a frequency selective saturation pulse that uniquely affects the metabolite. The RF pulse begins to rotate (nutate) the metabolite magnetization, giving it a transverse component in addition to a longitudinal component. As time goes on, this component is increasing according to some function  $\cos(\theta)^{10}$ , where  $\theta$  itself represents the nutation and is a function of time defined by the pulse properties. Let's pause and think about what is happening during every instant of this process: namely, in terms of  $T_1$  and  $T_2$  relaxation.

The RF pulse acts on longitudinal magnetization, converting it to transverse, while  $T_1$  relaxation causes this transverse magnetization to decay and repopulate the longitudinal component. In the presence of an RF pulse, the system will eventually reach a steady state when the product [ $T_1$ \*amount of transverse magnetization] is equal to the product [effect of RF pulse \* amount of longitudinal magnetization]. Meanwhile,  $T_2$  relaxation – anything that dephases transverse magnetization and causes its signal to decay – is constantly occurring, and generally at a faster rate than  $T_1$ . If the action of  $T_1$  relaxation that returns transverse magnetization to the longitudinal component is equalized by the action of the saturation pulse which does the opposite, then as the saturation pulse progresses, more and more of the magnetization undergoes the dephasing known as  $T_2$  relaxation and is 'accumulating' in this unphased

---

<sup>10</sup> It should be clarified that the saturation pulse induces many multiples of  $360^\circ$  rotations of the net magnetization. This visualization is appropriate for any given period of this rotation.

transverse pool. Only when the RF pulse is turned off and  $T_1$  relaxation dominates will the signal begin to increase to its original magnitude. If there were no exchange, then if we were to measure  $M_z$  of the metabolite before  $T_1$  relaxation is complete, we would find that  $M_z$  of the metabolite would be less than its original value.

Consider now that during this process, metabolite protons are being exchanged with water protons. While a proton is resident on the metabolite and subject to the local  $B_0$  arising from its electronic configuration, it resonates at  $\omega_0$  and is subject to the action of the saturation pulse. After being exchange to water, the proton is subject to a different  $B_{0, \text{effective}}$ , has a different Larmor frequency, and is not subject to the action of the pulse. Suppose the saturation pulse lasts for 1 second, and the rate of exchange between the metabolite and water is 1000Hz, or 1k exchanges per second. This means that during the saturation pulse, each molecule of metabolite on average will have harbored 1k individual protons at the site of interest which, at the instant of residence on the metabolite, were subjected to the nutation of the pulse. These 1k protons subjected to the saturation pulse (with zero net longitudinal magnetization) are stored on water pool thereby reduce the water signal amplitude. Eventually, it's the water protons we're going to measure to "see" how they were affected by this saturation process.

### **1b.5 Effect of exchange rate**

Now we can consider what the effect would be of this exchange rate being faster or slower. On the one hand, we can understand how CEST can give rise to amplification of the signal per molecule over spectroscopy: when we do spectroscopy, we get one unit of 'signal' per proton of interest – in other words, our signal depends on (a) –although relaxation and exchange affect the lineshape, the time evolution, and ultimately the signal magnitude. But in CEST, our 'signal'



is derived from a product of factors a, b, c and d enumerated above. If (c) is very large, this can amplify the signal generated by the presence of the molecule. However, this also means that each proton is subject to the effect of the saturation pulse for less time. If the total nutation induced on a single proton is less, then the corresponding saturation of the population's signal is also less. In other words, a fast rate of exchange, while in principle amplifying the signal-per-concentration, also decreases the efficiency of the saturation. In a hypothetical limiting case, exchange would be happening so fast that no nutation occurs at all during that time, and the CEST effect doesn't manifest. In order to avoid approaching this situation, a fast-exchanging metabolite requires a higher power RF pulse with a higher nutation frequency.

Another way to think about this is that in the fast-exchange case, the linewidth of the resonance targeted by the saturation itself is very broad. It is common to all forms of spectroscopy that the lineshape of a resonance - -that is, the intensity of that 'absorption' over the frequency axis —is related to the lifetime of the states involved<sup>12</sup>. Because of the Fourier relationship between time and frequency, longer lifetimes correspond to narrower lineshapes (the limiting cases being that an infinitely long lifetime yields a delta function, and an infinitely short one, a flat line). In NMR, the lineshape of a resonance is generally defined by the  $T_2$  of that resonance: the longer the  $T_2$ , the narrower the linewidth. Effectively,  $T_2$  of any species is shortened by the presence of exchange, as expressed by Equations 1.38 and 1.39 in the section to follow.

At some point, if two resonances are sufficiently close and exchange is sufficiently fast – leading to broad lineshapes-- they coalesce, and we lose the ability to detect them separately at all. This also means that we lose the ability to excite them separately with an RF pulse. So far in our discussion, we have been assuming that there is frequency-selective excitation of the metabolite only, leaving the water protons unperturbed. However, if the lineshape of the metabolite

resonance is sufficiently broad, its separation from water in the spectrum begins to deteriorate, which means that an RF pulse targeting this metabolite will affect water, too. The practical consequence of this is that the faster the exchange of the metabolite of interest, the further the resonance has to be from water in the NMR spectrum, or otherwise the ability to perform frequency-selective excitation and thus CEST is lost.

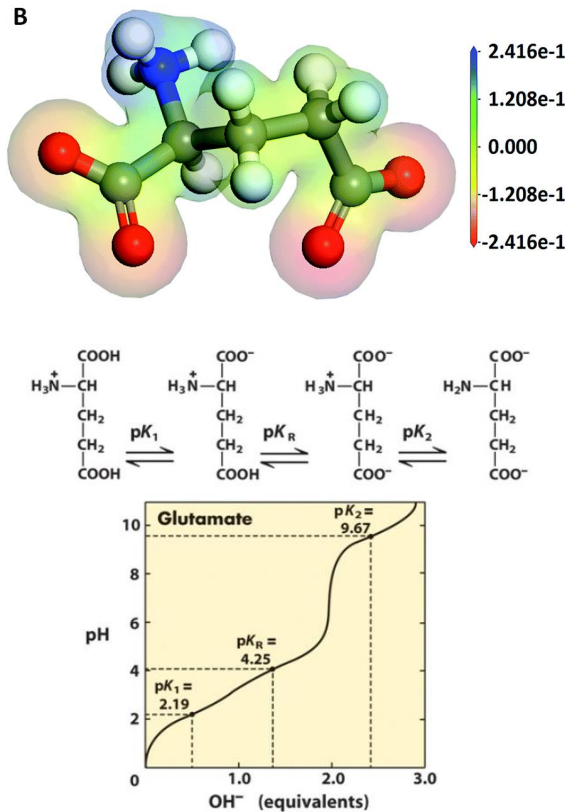
With regards to the focus of this thesis, it should be emphasized that at clinically standard field strengths (1.5 or 3 T), the exchange of the glutamate amine proton with bulk water is too fast relative to the chemical shift dispersion of frequencies and gluCEST is not possible.

On the other side of the exchange rate continuum from glutamate and gluCEST are amide protons, forming the target of interest in APT CEST. They have been estimated to exchange at a rate of  $\sim 30 \text{ Hz}^{13}$ , which is about 50-fold more slowly than the glutamate amine protons. While this sharply decreases the saturation efficiency in time, it also means that a sufficiently long pulse at low power can generate the desired signal from amide-based exchange. This has the practical consequence that APT CEST, unlike gluCEST, is possible at the more widely available 3 T field strength.

## 1b.6 Transfer of saturation from one species to another

The general thinking public may imagine molecular structures to be static, but in fact they are not. **Chemical exchange** is the phenomenon of protons becoming liberated from their structural position in one molecule and winding up involved in another. The likelihood of this process occurring with respect to any given proton on any given molecule is governed by the **pKa**, which

**Figure 1b.3. Electronic structures give rise to chemical exchange phenomena** . Top: Electrostatic potential of glutamate. Bottom: Schematic of glutamate's labile protons and their corresponding pKa.



depends on the local and overall electronic structure of the molecule. pKa quantifies the propensity of a proton to 'leave' its attachment to another atom, in units related to the pH of the solution required to cause the transition. A proton detaching from a molecule it participates in leaves that molecule in an anionic state; an additional proton attaching to a molecule in which it does not structurally participate creates a cation. The likelihood of either of these events happening is therefore determined by the stability (absolute energy) of the resulting electronic configuration.

Because carbon makes for an extremely unstable ion, protons attached to carbons are rarely perturbed in biochemical contexts, with the exception of reactions that are heavily stabilized by enzymatic environments. The spontaneous

'exchange' of protons in solution occurs only amongst protons attached to heteroatoms oxygen and nitrogen, such as in the zwitterionic forms of the amino acids.

In glutamate, there are two carboxylic acid groups and one amine group which proffer such protons. We can see from the chart in **Figure 1b.3** that the two -OH protons have low pKa, while the removal of the third proton (to the -NH<sub>2</sub> group) has a high pKa<sup>11</sup>. These electrostatic potentials and pKas translate to the fact that, at biological pH, the most likely state of the glutamate/glutamic acid molecule at any instant is to have the carboxyl groups deprotonated and the amine group protonated. Although the amine group is likely to have three protons resident at any given instant, the protons of this group are likely to be in constant flux between this position on the amine group and one of the surrounding water molecules. As explained above, we can take advantage of this phenomenon in glutamate or another exchanging molecule to 'transfer' the saturation that we incurred from the glutamate amine resonance to the bulk water resonance, 'carried' by these protons.

### **1b.7 Other forms of CEST**

While glutamate-weighted CEST "gluCEST" is the focus of this thesis<sup>14</sup>, it behooves us to briefly summarize other forms of CEST modalities demonstrated to date. At the highest level of classification is the distinction between paramagnetic and diamagnetic CEST contrast<sup>15,16</sup>. With the exception of deoxymyoglobin<sup>17</sup>, 'paraCEST' contrast agents are all exogenous. While the drastic chemical shifts afforded by coupling to a paramagnetic ion greatly enhance the specificity of this experiment, concerns about toxicity have limited the translation of paraCEST

---

<sup>11</sup> References for Figure 1b.3: (top)

[https://pubs.rsc.org/en/content/articlehtml/2017/nj/c6nj03939a?casa\\_token=oyR8Kr7JNLYAAAAA:-yV9oOdET972S1G1w\\_mljOqN\\_5qUnhGoVkv5Typo0TWi1s0Hqd3tYFF3j5rucswEBZeolTh3613tWQ](https://pubs.rsc.org/en/content/articlehtml/2017/nj/c6nj03939a?casa_token=oyR8Kr7JNLYAAAAA:-yV9oOdET972S1G1w_mljOqN_5qUnhGoVkv5Typo0TWi1s0Hqd3tYFF3j5rucswEBZeolTh3613tWQ)

(bottom) <https://slideplayer.com/slide/5675684/>

to use in human beings. Diamagnetic CEST, which follows the mechanism so far described, can be performed targeting either exogenous or endogenous molecules. Examples of exogenously introduced but highly biocompatible CEST agents are glucose<sup>18,19</sup> and artificial sweetener, as demonstrated by Bagga *et al.*<sup>20</sup>

Endogenous CEST – and most diamagnetic CEST approaches in general – fall into three main categories, corresponding to three commonly found types of exchangeable protons in biochemistry: **amine (-NH<sub>2</sub>), amide (-NH), and hydroxyl (-OH) groups**<sup>15</sup>. There are also exogenously introduced molecules which can function as CEST contrast agents, behaving in accordance to similar physics but without the complications of mechanisms arising from involvement in macromolecular structures<sup>16</sup>.

Other than glutamate, the major amine-based CEST is that of creatine<sup>21</sup>, with a signal centered at 1.8ppm. Importantly, the amine protons of creatine exchange much faster than the equivalent ones on phosphocreatine, allowing for specificity of this signal. Creatine is present in the brain in non-negligible amounts and is included in our simulations of brain gluCEST; however, the primary application of CrCEST as an independent modality has been in skeletal muscle<sup>22,23</sup> and heart<sup>24</sup>.

Amide protons are quite ubiquitous in biochemistry, with perhaps the most notorious instance being the amide bond in the backbone of the protein structure. CEST which probes the signal centered at 3.5 ppm is known as APT CEST, and is the most broadly applied CEST modality in current practice. While the origin of its signal is difficult to pinpoint, it has been demonstrated to have import in clinical radiology of brain tumors and other pathology<sup>25–28</sup> and has recently been

translated to commercial sequence implementations. Given its much slower exchange rate, APT CEST is possible at the 3 T field strength, which has facilitated its proliferation to date.

Lastly, hydroxyl groups are exploited as CEST agents in glucose and derivative biomolecules including lactate, glycogen, glycosaminoglycans and myoinositol<sup>20,29–33</sup>. Glycogen and glycosaminoglycans exist as polymers, which can complicate interpretation of the concentration:signal relationship. This ‘yield’ depends not just on concentration, but on accessibility of exchangeable protons to bulk water, and the architecture of these molecules would be challenging to replicate in phantoms.

### **1b.8 Other effects which appear in the Z- spectrum**

In addition to this chemical exchange of protons from identifiable molecules, there are some additional, less precisely assigned phenomena by which magnetization in neighboring molecules can be ‘passed around’. They strongly affect the CEST experiment and also have importance as imaging contrast mechanisms in and of themselves. These are the so-called semi-solid **Magnetization Transfer (MT)** and the **Nuclear Overhauser Effect (NOE)**. Exactly what mechanism(s) arising from what resonance(s) these effects are detecting is usually unclear, but the appearance of multiple distinct signals-- including from non-exchangeable protons-- in the Z- spectrum has been reported extensively<sup>13,16,34</sup>. Briefly, these phenomena can be described as follows:

**Semi-solid magnetization transfer:** This effect, commonly known as ‘MT’, arises from the fact that ‘bound’ water molecules in the solvation shell of large macromolecules – forming a ‘semi-solid’ matrix, as perhaps in the cytoplasm— may have a different resonant frequency from those in the bulk solvent, as a result of their extensive hydrogen bonding. Also due to hydrogen

bonding and electronic interaction with the solvated macromolecule, these bound waters undergo slow exchange, and are saturated in the vicinity of -2.4ppm relative to water at low  $B_1$  powers. However, due to the fact that MT arises from bound water molecules in a variety of physico-chemical contexts, the effect is very broad both in terms of the frequency and saturation power dimension.

**NOE:** While sweeping through the frequency spectrum, certain resonances are saturated which arise from non-exchangeable protons. These resonances, however, have still been observed to give rise to a decrease in the water signal, presumably through cross-relaxation, the mechanism of single quantum transition described by the NOE. These non-exchangeable protons, including  $\text{CH}_2$  or  $\text{CH}_3$  groups – are probably located on protein sidechains or in lipids. When attempting to interpret these signals specifically, one should keep in mind that, as with chemical exchange, a cross-relaxation interaction requires that this proton be accessible to the bulk water. This cross-relaxation, which is not affected by pH, can be distinguished by appropriate experiments from true CEST effects, as chemical exchange is highly pH-dependent, as discussed above.

In modeling the CEST experiment, we incorporate all such interactions into the Bloch-McConnell equations (see next section), in which they are treated as simple first-order exchange using rate constants reported in the literature.

### **1b.9 Phenomenological modeling of the CEST experiment: Bloch-McConnell equations**

In 1958, Harden McConnell had the insight that rather than getting entangled with spectroscopist-style derivations of lineshapes<sup>12</sup>, anyone interested in modeling the effect of

---

<sup>12</sup> This is not my comment from the peanut gallery, but is stated rather explicitly by McConnell himself in the first paragraph of his paper: “This reduces the previous rather involved derivations of (line-shape reaction-rate) formulas [several works cited] to almost trivial algebraic operations...”. If the reader is

chemical exchange in an NMR experiment could simply add some terms to the Bloch equations (introduced in Chapter 1a)<sup>35</sup>. These terms capture the “passing” back and forth of magnetization between pool A and pool B, which may each have their own intrinsic relaxation rates  $T_1$  and  $T_2$ . While McConnell’s seminal paper was not intended to treat the specific experiment of saturation transfer, his equations have been put to this purpose extensively by the CEST theory community.

The so-called Bloch-McConnell equations solved numerically to simulate the CEST experiment in this work are based on the treatment of D.E. Woessner<sup>36</sup>, whose notation of these equations is as follows:

[Equations 1.37, A-E]

$$\frac{dM_x^a}{dt} = -(\omega_a - \omega)M_y^a - k_{2a}M_x^a + C_bM_x^b$$

$$\frac{dM_x^b}{dt} = -(\omega_b - \omega)M_y^b - k_{2b}M_x^b + C_aM_x^a$$

$$\frac{dM_y^a}{dt} = (\omega_a - \omega)M_x^a - k_{2a}M_y^a + C_bM_y^b - \omega_1M_z^a$$

$$\frac{dM_y^b}{dt} = (\omega_b - \omega)M_x^b - k_{2b}M_y^b + C_aM_y^a - \omega_1M_z^b$$

$$\frac{dM_z^a}{dt} = \frac{M_0^a}{T_{1a}} - k_{1a}M_z^a + C_bM_z^b + \omega_1M_y^a$$

$$\frac{dM_z^b}{dt} = \frac{M_0^b}{T_{1b}} - k_{1b}M_z^b + C_aM_z^a + \omega_1M_y^b$$

---

unfamiliar with the arduous exercise of lineshape description in spectroscopy, they are cordially invited to peruse the textbook of Reference 9.



where

$$k_{1a} = \frac{1}{T_{1a}} + C_a \quad [1.38]$$

$$k_{2a} = \frac{1}{T_{2a}} + C_a \quad [1.39]$$

$T_{1a}$  and  $T_{2a}$  are the longitudinal and transverse relaxation times of pool A in the absence of exchange,  $\omega_a$  is the Larmor frequency of pool A,  $\omega$  is the frequency of the RF radiation comprising the saturation pulse (which may or may not be equal to either  $\omega_a$  or  $\omega_b$ ),  $\omega_1$  is the nutation rate induced by the RF of the saturation pulse, and  $C_a$  is the rate of spins leaving pool A by chemical exchange (likewise for all terms relating to pool B).

In the case of perfect saturation of pool B and no direct saturation of Pool A, the net rate of change of the Z magnetization of pool A in this two-pool system is the difference between the rate of exchange (which drains magnetization) and the rate of  $T_1$  recovery. The steady state is described by the situation when these two rates are equal:

$$C_a M_Z^a = \frac{(M_0^a - M_Z^a)}{T_{1a}} \quad [1.40]$$

At this time, the 'Z value', or  $M_Z/M_0$ , is given by:

$$Z = \frac{M_Z^a}{M_0^a} = \frac{\tau_a}{T_{1a} + \tau_a} \quad [1.41]$$

where  $\tau_a$  is the reciprocal of  $C_a$ , and represents the lifetime of a proton in Pool A (i.e., how long it's there before getting exchanged to pool B. )

The effect of direct saturation on Pool A can be described directly by Bloch's original equations, considering that  $\Delta\omega$  in this case represents the difference between the Larmor frequency of Pool A and the applied radiation (which will be at the Larmor frequency of Pool B):

$$\frac{M_{Za}}{M_{0a}} = \frac{1}{1 + \frac{\omega_1^2 T_1 T_2}{1 + \Delta\omega^2 T_2^2}} \quad [1.42]$$

For Pool B, this expression simplifies to

$$\frac{M_{Zb}}{M_{0b}} = \frac{1}{1 + \omega_1^2 T_1 T_2} \quad [1.43]$$

Now from the mathematical perspective, we can again appreciate why faster exchanging molecules must be further from water. The difference between  $M_z/M_0$  for Pool B (our real effect of interest) and  $M_z/M_0$  for Pool A (direct saturation) is determined entirely by the term  $\Delta\omega^2 T_2^2$ , where this  $T_2$  is that of Pool A. The bigger this term, the smaller the denominator on the RHS of equation W25, and the closer this  $M_{Za}/M_{0A}$  is to 1. This represents the  $M_z$  of Pool A *not changing as a result of direct saturation*, which is the desirable outcome. Fast exchange with the solute Pool B leads to lower effective  $T_2$ , which would cause this term to be smaller if  $\Delta\omega$  were the same. As exchange rate increases, the frequency dispersion  $\Delta\omega$  has to increase proportionally to the decrease in  $T_2$  in order for this term, and thus the relative contribution of direct saturation, to remain the same.

Given the form of these functions, we can see that the maximum CEST effect will be detected when the system is at steady state. However, in practice this is not always feasible, as it may require deposition of more RF power than is considered safe in human imaging. It has recently been shown that measurements at varying points in the rise to steady state (i.e. varying

durations of the saturation pulse) can be calibrated in post-processing to derive the maximum steady state value<sup>37</sup>.

Our implementation of these equations to model the gluCEST measurement in brain has six rather than two pools, representing bulk water (a), so-called ‘bound water’ in the solvation shell of macromolecules (bw), amide protons on protein backbones (b), aliphatic and similar protons (which may participate in cross-relaxation (c), rather than true chemical exchange) the amine protons on creatine (d), and those of primary interest on glutamate (e). These pools (bw, b, c, d, e) are all treated as pool B is in Woessner’s notation: that is, their only interaction with the rest of the system is by exchange of magnetization with bulk water, and not with each other. The matrices representing the ‘pulse on’ and ‘pulse off’ (relaxation) operations in this system of differential equations are shown in **Figure 1b.4** with the vector representing net magnetizations of all species specified as B. Our numerical solution solves this system using the matrix exponential, as in Woessner 2005; however, we implement the mathematical operation in C rather than in Matlab for accelerated calculation. For more discussion of simulation parameters,

**Figure 1b.4. Matrix representations of the Bloch-McConnell differential equations** describing the dynamics of a six-pool spin system where solute pools are coupled by chemical exchange to a ‘bulk’ solvent pool. The first and overwhelmingly largest of the five ‘solute pools’ is labeled ‘bw’ for ‘bound water’. The two operators represent the physical situations of the RF pulse being on (pulse) or not (relaxation).

$$\begin{array}{c}
 \mathbf{A}_{\text{pulse}} = \\
 \left[ \begin{array}{cccccccccccccccc}
 -k_{1a} & W_{1x} & W_{1y} & C_{bw} & 0 & 0 & C_b & 0 & 0 & C_c & 0 & 0 & C_d & 0 & 0 & C_e & 0 & 0 \\
 -W_{1x} & -k_{2a} & W_2 & 0 & C_{bw} & 0 & 0 & C_b & 0 & 0 & C_c & 0 & 0 & C_d & 0 & 0 & C_e & 0 \\
 W_{1y} & -W_2 & -k_{2a} & 0 & 0 & C_{bw} & 0 & 0 & C_b & 0 & 0 & C_c & 0 & 0 & C_d & 0 & 0 & C_e \\
 C_{abw} & 0 & 0 & -k_{1bw} & W_{1x} & W_{1y} & 0 & 0 & 0 & 0 & 0 & 0 & 0 & 0 & 0 & 0 & 0 & 0 \\
 0 & C_{abw} & 0 & -W_{1x} & -k_{2bw} & W_{bw} & W & \dots & \dots & \dots & \dots & \dots & \dots & \dots & \dots & \dots & \dots & \dots \\
 0 & 0 & C_{abw} & W_{1y} & -W_{bw} & -k_{2bw} & 0 & \dots & \dots & \dots & \dots & \dots & \dots & \dots & \dots & \dots & \dots & \dots \\
 C_{ab} & 0 & 0 & 0 & 0 & 0 & -k_{1b} & W_{1x} & W_{1y} & \dots & \dots & \dots & \dots & \dots & \dots & \dots & \dots & \dots \\
 0 & C_{ab} & 0 & 0 & 0 & 0 & -W_{1x} & -k_{2b} & W_2 & \dots & \dots & \dots & \dots & \dots & \dots & \dots & \dots & \dots \\
 \dots & \dots & \dots & \dots & \dots & \dots & \dots & \dots & \dots & \dots & \dots & \dots & \dots & \dots & \dots & \dots & \dots & \dots \\
 0 & 0 & C_{ab} & 0 & 0 & 0 & 0 & W_{1y} & W-W_b & -k_{2b} & 0 & \dots & \dots & \dots & \dots & \dots & \dots & \dots \\
 C_{ac} & 0 & 0 & 0 & 0 & 0 & 0 & 0 & 0 & -k_{1c} & W_{1x} & W_{1y} & \dots & \dots & \dots & \dots & \dots & \dots \\
 0 & C_{ac} & 0 & 0 & 0 & 0 & 0 & 0 & 0 & -W_{1x} & -k_{2c} & W_2 & \dots & \dots & \dots & \dots & \dots & \dots \\
 0 & 0 & C_{ac} & 0 & 0 & 0 & 0 & 0 & 0 & W_{1y} & W-W_c & -k_{2c} & 0 & \dots & \dots & \dots & \dots & \dots \\
 \dots & \dots & \dots & \dots & \dots & \dots & \dots & \dots & \dots & \dots & \dots & \dots & \dots & \dots & \dots & \dots & \dots & \dots \\
 C_{ad} & 0 & 0 & 0 & 0 & 0 & 0 & 0 & 0 & 0 & 0 & -k_{1d} & W_{1x} & W_{1y} & \dots & \dots & \dots & \dots \\
 0 & C_{ad} & 0 & 0 & 0 & 0 & 0 & 0 & 0 & 0 & 0 & -W_{1x} & -k_{2d} & W_2 & \dots & \dots & \dots & \dots \\
 0 & 0 & C_{ad} & 0 & 0 & 0 & 0 & 0 & 0 & 0 & 0 & W_{1y} & W-W_d & -k_{2d} & 0 & \dots & \dots & \dots \\
 C_{ae} & 0 & 0 & 0 & 0 & 0 & 0 & 0 & 0 & 0 & 0 & 0 & -k_{1e} & W_{1x} & W_{1y} & \dots & \dots & \dots \\
 0 & C_{ae} & 0 & 0 & 0 & 0 & 0 & 0 & 0 & 0 & 0 & -W_{1x} & -k_{2e} & W_2 & \dots & \dots & \dots & \dots \\
 0 & 0 & C_{ae} & 0 & 0 & 0 & 0 & 0 & 0 & 0 & 0 & W_{1y} & W-W_e & -k_{2e} & 0 & \dots & \dots & \dots
 \end{array} \right]
 \end{array}$$

$$\begin{array}{c}
 \mathbf{A}_{\text{relaxation}} = \\
 \left[ \begin{array}{cccccccccccccccc}
 -k_{1a} & 0 & 0 & C_{bw} & 0 & 0 & C_b & 0 & 0 & C_c & 0 & 0 & C_d & 0 & 0 & C_e & 0 & 0 \\
 0 & -k_{2a} & W_2 & 0 & C_{bw} & 0 & 0 & C_b & 0 & 0 & C_c & 0 & 0 & C_d & 0 & 0 & C_e & 0 \\
 0 & -W_2 & -k_{2a} & 0 & 0 & C_{bw} & 0 & 0 & C_b & 0 & 0 & C_c & 0 & 0 & C_d & 0 & 0 & C_e \\
 C_{abw} & 0 & 0 & -k_{1bw} & 0 & 0 & \dots & \dots & \dots & \dots & \dots & \dots & \dots & \dots & \dots & \dots & \dots & \dots \\
 0 & C_{abw} & 0 & 0 & -k_{2bw} & W_{bw} & W & \dots & \dots & \dots & \dots & \dots & \dots & \dots & \dots & \dots & \dots & \dots \\
 0 & 0 & C_{abw} & 0 & -W_{bw} & -k_{2bw} & 0 & \dots & \dots & \dots & \dots & \dots & \dots & \dots & \dots & \dots & \dots & \dots \\
 C_{ab} & 0 & 0 & 0 & 0 & 0 & -k_{1b} & 0 & \dots & \dots & \dots & \dots & \dots & \dots & \dots & \dots & \dots & \dots \\
 0 & C_{ab} & 0 & 0 & 0 & 0 & -k_{2b} & W_b & \dots & \dots & \dots & \dots & \dots & \dots & \dots & \dots & \dots & \dots \\
 0 & 0 & C_{ab} & 0 & 0 & 0 & -W_b & -k_{2b} & 0 & \dots & \dots & \dots & \dots & \dots & \dots & \dots & \dots & \dots \\
 C_{ac} & 0 & 0 & 0 & 0 & 0 & 0 & 0 & 0 & -k_{1c} & 0 & \dots & \dots & \dots & \dots & \dots & \dots & \dots \\
 0 & C_{ac} & 0 & 0 & 0 & 0 & 0 & 0 & 0 & -W_c & -k_{2c} & W_c & \dots & \dots & \dots & \dots & \dots & \dots \\
 0 & 0 & C_{ac} & 0 & 0 & 0 & 0 & 0 & 0 & -W_c & -k_{2c} & 0 & \dots & \dots & \dots & \dots & \dots & \dots \\
 C_{ad} & 0 & 0 & 0 & 0 & 0 & 0 & 0 & 0 & 0 & 0 & -k_{1d} & 0 & \dots & \dots & \dots & \dots & \dots \\
 0 & C_{ad} & 0 & 0 & 0 & 0 & 0 & 0 & 0 & 0 & 0 & -k_{2d} & W_d & \dots & \dots & \dots & \dots & \dots \\
 0 & 0 & C_{ad} & 0 & 0 & 0 & 0 & 0 & 0 & 0 & 0 & -W_d & -k_{2d} & 0 & \dots & \dots & \dots & \dots \\
 C_{ae} & 0 & 0 & 0 & 0 & 0 & 0 & 0 & 0 & 0 & 0 & 0 & 0 & -k_{1e} & 0 & \dots & \dots & \dots \\
 0 & C_{ae} & 0 & 0 & 0 & 0 & 0 & 0 & 0 & 0 & 0 & 0 & 0 & -k_{2e} & W_e & \dots & \dots & \dots \\
 0 & 0 & C_{ae} & 0 & 0 & 0 & 0 & 0 & 0 & 0 & 0 & 0 & 0 & -W_e & -k_{2e} & \dots & \dots & \dots
 \end{array} \right]
 \end{array}$$

$$\mathbf{B} = [M_{2a} \ M_{1a} \ M_{xa} \ M_{2bw} \ M_{ybw} \ M_{xbw} \ M_{2b} \ M_{yb} \ M_{xb} \ M_{2c} \ M_{yc} \ M_{xc} \ M_{2d} \ M_{yd} \ M_{xd} \ M_{2e} \ M_{ye} \ M_{xe}]$$

results, and application to development of  $B_1$  inhomogeneity correction in gluCEST, please see Chapter 2. For complete documentation of these Bloch-McConnell simulations, please see Appendix A.

### **1b.10 The CEST experiment in practice**

From the above discussion, one might suppose that the CEST experiment consists of a single sequence: saturation at the frequency of interest, followed by read-out of the proton density weighted image. However, in practice the following considerations extend the CEST acquisition to a multipartite affair. The first of these (a) was illustrated by Figure 1b.1 in the previous section.

- a) The need to eliminate the effect of direct saturation (and arguably other broad, mostly symmetric contributions) requires at least two acquisitions, on either side of the water peak.
- b) Even if the analysis of choice is asymmetry, rather than Z-spectrum fitting, additional frequency offsets must be acquired to make the measurement robust to inhomogeneities in  $B_0$ .
- c) A  $B_0$  map must be acquired to report on those inhomogeneities.
- d) A  $B_1$  map must be acquired if we are going to attempt correction for this inhomogeneity, too.
- e) Any maps which are auxiliary to the  $B_1$  correction implemented are also needed: in the present approach, the  $T_1$  map from MP2RAGE. In our group's previous approaches, this was an

MT sequence. The following flowchart, reproduced from Chapter 2, illustrates the various steps in acquisition and processing of a gluCEST experiment as is done in all chapters of this thesis:

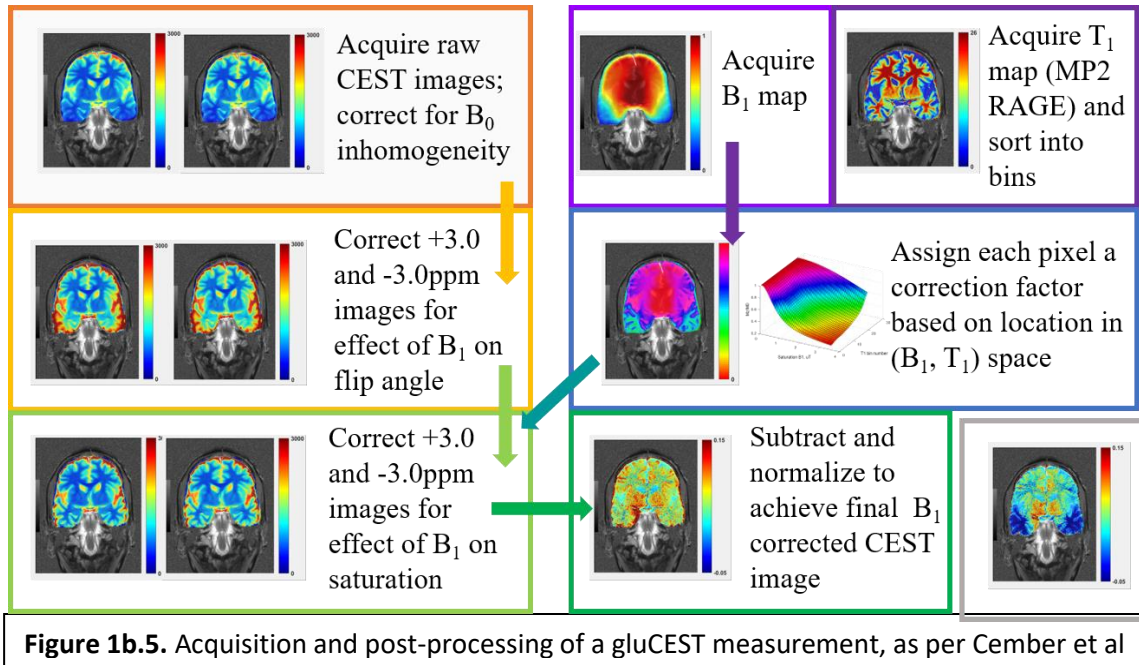


**Figure 1b.5.** Acquisition and post-processing of a gluCEST measurement, as per Cember et al

The steps referred to in the top row (orange and purple boxes) will be explained in more detail below. The remaining steps, introduced by the author, are the subject of Chapter 2.

### 1b.10.1 The raw CEST acquisition

The CEST acquisition itself will include several repetitions of the basic saturate-read sequence, varying the frequency of the saturation pulse to create a ‘spectrum’ (the Z-spectrum) of images which essentially contain the information  $M_z/M_0(\Delta\omega)$ . There are two basic options for analyzing this data further: if enough offsets were collected, the Z-spectrum through each voxel can be fit to a Lorentzian function, which is the approach of many groups in the CEST community.

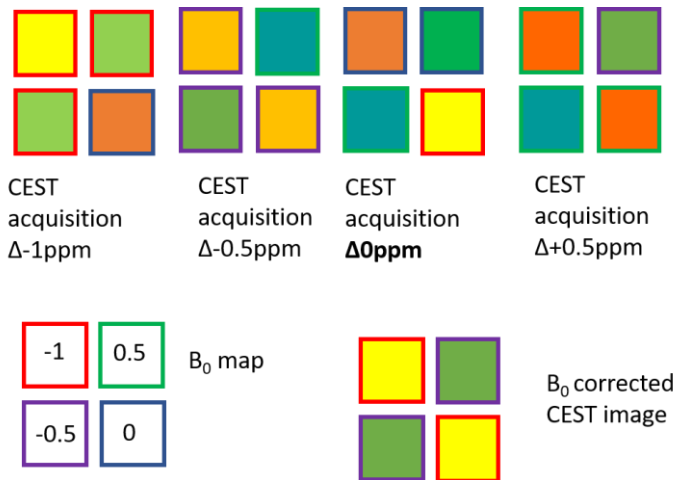
Alternatively, as in the approach presented here, only a subset of these Z-spectrum points can be collected, sufficient to correct each ‘side’ of the spectrum for  $B_0$  inhomogeneity. In **Figure 1b.6**, these multiple offsets are symbolized by the top row of ‘images’ of varying ‘contrast’. The

final 'B<sub>0</sub> corrected CEST images' for each side of the Z-spectrum (bottom right in **Figure 1b.6**) are symbolized in the orange box in **Figure 1b.5**.

### 1b.10.2 B<sub>0</sub> map: WASSR

Accurate asymmetry-based quantification of CEST depends very strongly on correction of the acquired Z-spectrum (or sub-spectrum of points) for inhomogeneity in B<sub>0</sub>. As in most other MRI applications, the dominant signal in the Z-spectrum is water: in this case, it is the strong decrease in that signal as the RF pulse gets closer to the resonant frequency of water itself-- considered in CEST as '0 ppm'—causing the signal to become more and more saturated. Since this so-called direct saturation peak is so salient, its center can be used as the reference to determine the exact resonant frequency of water in a particular voxel in the presence of small voxel-to-voxel inhomogeneities in B<sub>0</sub> which cause the Larmor frequencies of every component of the spectrum to shift. The strategy of using a separate, specialized CEST-type acquisition

**Figure 1b.6.** Schematic of 'image synthesis' approach to B<sub>0</sub> correction. In this illustration, each square represents a 'pixel' in the 2x2 image.



specifically for this purpose was first introduced in *Kim et al 2009*, who coined the term Water Saturation Shift Referencing, or WASSR<sup>38</sup>. Like the CEST acquisition, the WASSR acquisition sweeps over several frequency offsets, applying a saturation pulse followed by a proton-density-

weighted imaging module. Generally, the saturation pulse used in the WASSR scan is of

significantly lower power and shorter duration (as the target molecule is bulk water itself, not an exchanging solute or metabolite), and the frequency offsets or Z-spectrum points are sampled more finely, e.g. in the range of  $\pm 1.0$  ppm.

### *1b.10.3 Correcting CEST data for $B_0$ inhomogeneity*

The exact location of the water center frequency as determined by interpolating the points of the WASSR acquisition is used to generate a map of  $B_0$  inhomogeneity over the field of view, where the value of each pixel represents the relative shift of the water center frequency from its nominal location of 0 ppm. The partial Z-spectrum itself is also interpolated for each pixel from the CEST acquisition images. The correct value for each pixel is then determined by “shifting” along this interpolation curve from the nominal offset frequency by the amount indicated by the  $B_0$  map. In this way, the final corrected images are ‘synthesized’ by the  $B_0$  correction algorithm from the array of images acquired in that neighborhood of offset frequencies. In the schematic of **Figure 1b.6**, this process is symbolized by the correct color square being chosen for each ‘pixel’ of the  $B_0$  map; if there were no  $B_0$  inhomogeneity, the correct image would simply be the one labeled ‘CEST acquisition,  $\Delta 0$ ppm’.

**Figure 1b.7** illustrates the concept using example Z-spectra (blue) and the resulting calculation of asymmetry (green, red). Suppose our resonance of interest is at -1ppm. From the left plot, which illustrates the spectrum measured in a voxel with no  $B_0$  shift, we can read off a value of 0.3 for the asymmetry at -1ppm, calculated by subtracting the value at -1ppm (0.6) from the value at 1ppm (0.9). The plot on the right represents a voxel in which there is a 0.5ppm shift in  $B_0$  which we do not account for. In other words, we believe 0.5ppm to be “0 ppm”, and perform the subtraction as if this were the case. We now get an erroneous 0.6 as the asymmetry at

1ppm – because instead of the correct calculation, we subtracted what is actually the value at -0.5ppm from that at 1.5ppm.

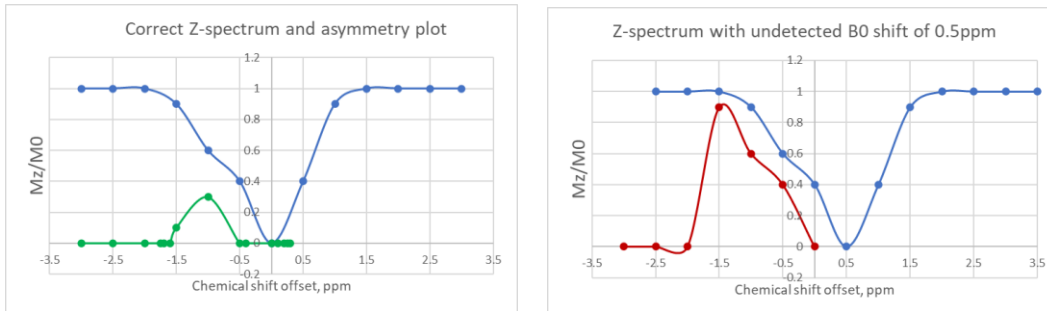


**Figure. 1b.7.** Illustration of inaccurate CEST asymmetry calculation due to uncorrected  $B_0$  shift. The green line is the correct CEST asymmetry calculation for this Z-spectrum. The red line is the resulting value from performing the calculation without  $B_0$  correction on the shifted data.

#### 1b.10.4 $B_1$ mapping

Our approach to generating  $B_1$  maps is based on the paper by Volz *et al*, 2010<sup>39</sup>. At the time of that work, a number of  $B_1$  mapping techniques existed, but faced a general problem of lengthiness. As applied to CEST or MT imaging, this is especially problematic, as the main sequence itself is also time-consuming. The basic strategy is to acquire two images, each with a magnetization preparation pulse which induce flip angles  $\alpha_0$  and  $\alpha_1$ , respectively. The imaging module which directly follows it should yield an image that is proportional to the ‘prepared’ longitudinal magnetization. In the simplest case if  $\alpha_0 = 0$  (which has cosine of 1), then dividing one image by the other results in the quantity  $\cos(\alpha_1)$ . If  $\alpha_{ref}$  is the nominal flip angle defined on the scanner interface, then the relative  $B_1 = \alpha_1 / \alpha_{ref}$ .

#### 1b.10.5 MP2RAGE for $T_1$ mapping

It was recognized early on that gluCEST would require correction for  $B_1$  inhomogeneity and that this correction may need to be tissue-specific<sup>14,40</sup>. A new and improved method for this



correction, the focus of Chapter 2 of this thesis, makes use of  $T_1$  mapping to characterize voxels. The sequence used for this purpose is the Siemens product sequence MP2RAGE. This sequence uses two turbo-FLASH GRE readouts between two  $180^\circ$  inversion pulses. The first readout produces an image which is mostly  $T_1$ -weighted; the second, mostly proton density weighted<sup>41</sup>. Reconstruction and analysis using both of these images can produce a quantitative  $T_1$  map, which is the image of interest in our acquisition.

A final note on the acquisition of CEST data is that achieving as good a shim as possible - -that is, a narrow lineshape of the water resonance – over the field of view is an extremely important factor in the sensitivity of the CEST experiment. From our earlier considerations, we saw that lineshape as a result of exchange plays a large role our ability to detect CEST differentially from direct saturation of water, with the theoretical underpinning that exchange effectively shortens  $T_2$ . By the same token, local inhomogeneities in the  $B_0$  field also shorten  $T_2$ , and will pose the same problem.

One may suppose that our  $B_0$  correction somehow deals *post facto* with this effect, but in fact it does not: one can correct for the water *center frequency* being shifted in any particular pixel, but not for the broadening of the lineshape that occurs due to the  $T_2$  shortening caused by this  $B_0$  inhomogeneity. Because this effects the magnitude of the measured CEST effect and can confound results, it is best practice for the experimenter to record the linewidth of the water resonance upon acquisition.

## References

1. Kogan F, Hariharan H, Reddy R. Chemical Exchange Saturation Transfer (CEST) Imaging: Description of Technique and Potential Clinical Applications. *Innov Clin MRI*. doi:10.1007/s40134-013-0010-3
2. Windschuh J, Zaiss M, Meissner JE, et al. Correction of B1-inhomogeneities for relaxation-compensated CEST imaging at 7T. *NMR Biomed*. 2015;28(5):529-537. doi:10.1002/nbm.3283
3. Zaiß M, Schmitt B, Bachert P. Quantitative separation of CEST effect from magnetization transfer and spillover effects by Lorentzian-line-fit analysis of z-spectra. *J Magn Reson*. 2011;211(2):149-155. doi:10.1016/j.jmr.2011.05.001
4. Cai K, Singh A, Poptani H, et al. CEST signal at 2 ppm (CEST@2ppm) from Z -spectral fitting correlates with creatine distribution in brain tumor. *NMR Biomed*. 2014;28(1):n/a-n/a. doi:10.1002/nbm.3216
5. Zaiss M, Windschuh J, Paech D, et al. Relaxation-compensated CEST-MRI of the human brain at 7T: Unbiased insight into NOE and amide signal changes in human glioblastoma. *Neuroimage*. 2015;112:180-188. doi:10.1016/j.neuroimage.2015.02.040
6. Zaiss M, Zu Z, Xu J, et al. A combined analytical solution for chemical exchange saturation transfer and semi-solid magnetization transfer. *NMR Biomed*. 2015;28(2):217-230. doi:10.1002/nbm.3237
7. Zhou J, Hong X, Zhao X, Gao JH, Yuan J. APT-weighted and NOE-weighted image contrasts in glioma with different RF saturation powers based on magnetization transfer ratio asymmetry analyses. *Magn Reson Med*. 2013;70(2):320-327. doi:10.1002/mrm.24784
8. Rerich E, Zaiss M, Korzowski A, Ladd ME, Bachert P. Relaxation-compensated CEST-MRI at 7T for mapping of creatine content and pH - preliminary application in human muscle tissue in vivo. *NMR Biomed*. 2015;28(11):1402-1412. doi:10.1002/nbm.3367
9. Khlebnikov V, Siero JCW, Bhogal AA, Luijten PR, Klomp DWJ, Hoogduin H. Establishing upper limits on neuronal activity-evoked pH changes with APT-CEST MRI at 7 T. *Magn Reson Med*. 2018;80(1):126-136. doi:10.1002/mrm.27013
10. Sun PZ, Farrar CT, Sorensen AG. Correction for artifacts induced by B0 and B1 field inhomogeneities in pH-sensitive chemical exchange saturation transfer (CEST) imaging. *Magn Reson Med*. 2007;58(6):1207-1215. doi:10.1002/mrm.21398
11. Ward KM, Balaban RS. Determination of pH using water protons and Chemical Exchange Dependent Saturation Transfer (CEST). *Magn Reson Med*. 2000;44(5):799-802. doi:10.1002/1522-2594(200011)44:5<799::AID-MRM18>3.0.CO;2-S
12. Kelley AM. *Condensed Phase Molecular Spectroscopy and Photophysics*. Wiley; 2012.
13. Zhou J, Wilson DA, Sun PZ, Klaus JA, Van Zijl PCM. Quantitative Description of Proton Exchange Processes between Water and Endogenous and Exogenous Agents for WEX, CEST, and APT Experiments. *Magn Reson Med*. 2004;51(5):945-952.

doi:10.1002/mrm.20048

14. Cai K, Haris M, Singh A, et al. Magnetic resonance imaging of glutamate. *Nat Med*. 2012;18(2):302-306. doi:10.1038/nm.2615
15. Kogan F, Hariharan H, Reddy R. Chemical Exchange Saturation Transfer (CEST) Imaging: Description of Technique and Potential Clinical Applications. *Curr Radiol Rep*. 2013;1(2):102-114. doi:10.1007/s40134-013-0010-3
16. Van Zijl PCM, Yadav NN. Chemical exchange saturation transfer (CEST): What is in a name and what isn't? *Magn Reson Med*. 2011;65(4):927-948. doi:10.1002/mrm.22761
17. Wang Z, Wang D-J, Noyszewski EA, et al. Sensitivity of in vivo mrs of the  $\alpha$ -proton in proximal histidine of deoxymyoglobin. *Magn Reson Med*. 1992;27(2):362-367. doi:10.1002/mrm.1910270217
18. Chan K W Y, McMahon MT, Kato Y, et al. Natural D -glucose as a biodegradable MRI contrast agent for detecting cancer. *Magn Reson Med*. 2012;68(6):1764-1773. doi:10.1002/mrm.24520
19. Xu X, Sehgal AA, Yadav NN, et al.  $\alpha$ -glucose weighted chemical exchange saturation transfer (glucoCEST)-based dynamic glucose enhanced (DGE) MRI at 3T: early experience in healthy volunteers and brain tumor patients. *Magn Reson Med*. 2020;84(1):247-262. doi:10.1002/mrm.28124
20. Bagga P, Wilson N, Rich L, et al. Sugar alcohol provides imaging contrast in cancer detection. *Sci Rep*. 2019;9(1):11092. doi:10.1038/s41598-019-47275-5
21. Haris M, Nanga RPR, Singh A, et al. Exchange rates of creatine kinase metabolites: feasibility of imaging creatine by chemical exchange saturation transfer MRI. *NMR Biomed*. 2012;25(11):1305-1309. doi:10.1002/nbm.2792
22. Kogan F, Haris M, Singh A, et al. Method for high-resolution imaging of creatine in vivo using chemical exchange saturation transfer. *Magn Reson Med*. 2014;71(1):164-172. doi:10.1002/mrm.24641
23. Kumar D, Nanga RPR, Thakuri D, et al. Recovery kinetics of creatine in mild plantar flexion exercise using 3D creatine CEST imaging at 7 Tesla. *Magn Reson Med*. 2021;85(2):802-817. doi:10.1002/mrm.28463
24. Haris M, Singh A, Cai K, et al. A technique for in vivo mapping of myocardial creatine kinase metabolism. *Nat Med*. 2014;20(2):209-214. doi:10.1038/nm.3436
25. Heo HY, Jones CK, Hua J, et al. Whole-brain amide proton transfer (APT) and nuclear overhauser enhancement (NOE) imaging in glioma patients using low-power steady-state pulsed chemical exchange saturation transfer (CEST) imaging at 7T. *J Magn Reson Imaging*. 2016;44(1):41-50. doi:10.1002/jmri.25108
26. Togao O, Hiwatashi A, Keupp J, et al. Scan-rescan reproducibility of parallel transmission based amide proton transfer imaging of brain tumors. *J Magn Reson Imaging*. 2015;42(5):1346-1353. doi:10.1002/jmri.24895

27. Vinogradov E, Sherry AD, Lenkinski RE. CEST: From basic principles to applications, challenges and opportunities. *J Magn Reson*. 2013;229:155-172. doi:10.1016/j.jmr.2012.11.024
28. Zhou J, Lal B, Wilson DA, Larterra J, Van Zijl PCM. Amide Proton Transfer (APT) Contrast for Imaging of Brain Tumors. *Magn Reson Med*. 2003;50(6):1120-1126. doi:10.1002/mrm.10651
29. Van Zijl PCM, Jones CK, Ren J, Malloy CR, Sherry AD. MRI detection of glycogen in vivo by using chemical exchange saturation transfer imaging (glycoCEST). *Proc Natl Acad Sci U S A*. 2007;104(11):4359-4364. doi:10.1073/pnas.0700281104
30. Krishnamoorthy G, Nanga RPR, Bagga P, Hariharan H, Reddy R. High quality three-dimensional gagCEST imaging of in vivo human knee cartilage at 7 Tesla. *Magn Reson Med*. 2017;77(5):1866-1873. doi:10.1002/mrm.26265
31. Haris M, Singh A, Cai K, et al. MICEST: A potential tool for non-invasive detection of molecular changes in Alzheimer's disease. *J Neurosci Methods*. 2013;212(1):87-93. doi:10.1016/j.jneumeth.2012.09.025
32. Haris M, Cai K, Singh A, Hariharan H, Reddy R. In vivo mapping of brain myo-inositol. *Neuroimage*. 2011;54(3):2079-2085. doi:10.1016/j.neuroimage.2010.10.017
33. DeBrosse C, Nanga RPR, Bagga P, et al. Lactate Chemical Exchange Saturation Transfer (LATEST) Imaging in vivo A Biomarker for LDH Activity. *Sci Rep*. 2016;6. doi:10.1038/srep19517
34. Liu D, Zhou J, Xue R, Zuo Z, An J, Wang DJJ. Quantitative characterization of nuclear overhauser enhancement and amide proton transfer effects in the human brain at 7 Tesla. *Magn Reson Med*. 2013;70(4):1070-1081. doi:10.1002/mrm.24560
35. McConnell HM. Reaction rates by nuclear magnetic resonance. *J Chem Phys*. 1958;28(3):430-431. doi:10.1063/1.1744152
36. Woessner DE, Zhang S, Merritt ME, Sherry AD. Numerical solution of the Bloch equations provides insights into the optimum design of PARACEST agents for MRI. *Magn Reson Med*. 2005;53(4):790-799. doi:10.1002/mrm.20408
37. Sun PZ. Quasi-steady state chemical exchange saturation transfer (QUASS CEST) analysis—correction of the finite relaxation delay and saturation time for robust CEST measurement. *Magn Reson Med*. 2021;(November 2020):1-9. doi:10.1002/mrm.28653
38. Kim M, Gillen J, Landman BA, Zhou J, Van Zijl PCM. Water saturation shift referencing (WASSR) for chemical exchange saturation transfer (CEST) experiments. *Magn Reson Med*. 2009;61(6):1441-1450. doi:10.1002/mrm.21873
39. Volz S, Nöth U, Rotarska-Jagiela A, Deichmann R. A fast B1-mapping method for the correction and normalization of magnetization transfer ratio maps at 3 T. *Neuroimage*. 2010;49(4):3015-3026. doi:10.1016/j.neuroimage.2009.11.054
40. Singh A, Cai K, Haris M, Hariharan H, Reddy R. On B 1 inhomogeneity correction of in vivo

human brain glutamate chemical exchange saturation transfer contrast at 7T. *Magn Reson Med*. 2013;69(3):818-824. doi:10.1002/mrm.24290

41. Elster AD. MRI questions.com. <http://mriquestions.com/mp-rage-v-mr2rage.html>

# 1c: *In vivo* glutamate measurement: biochemical significance and current state of the art

## 1c.1 Neurobiological context of glutamate

Glutamate is one of the twenty standard proteinogenic amino acids in eukaryotes<sup>1</sup>. In vertebrates, it also functions as a neurotransmitter. Likewise in some invertebrates, although with greater variability.<sup>2,3</sup>) In the current context, our interest is in the role of glutamate as the primary excitatory neurotransmitter in the mammalian, and particularly human, brain.

Glutamate is synthesized during the TCA cycle of core oxidative metabolism, from which it can be syphoned off for use in protein construction or neurotransmission. Importantly, it serves as the chemical precursor for gamma-aminobutyric acid (GABA), which is the main inhibitory neurotransmitter – the molecule that “does the opposite” of glutamate. Thus on both a

chemical and functional level, these two metabolites and their relative concentrations and effects in the nervous system are closely linked.

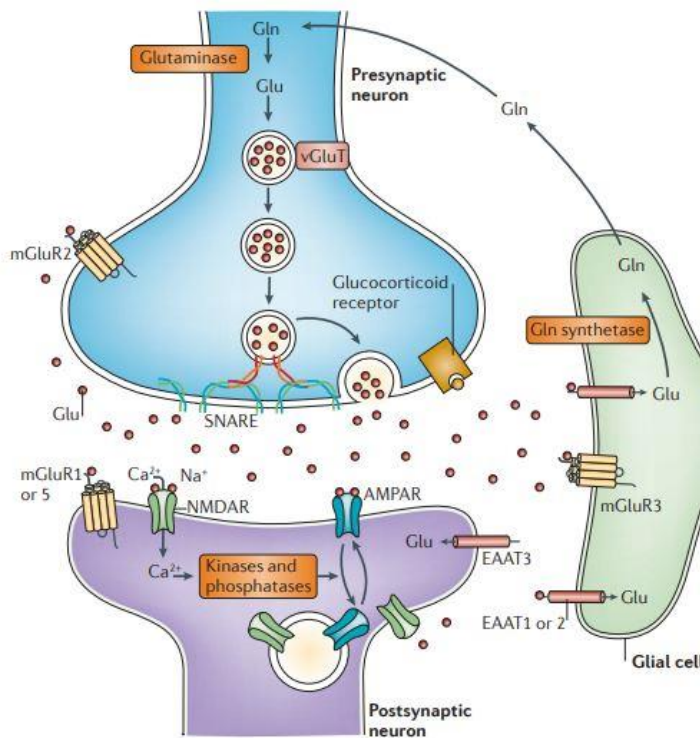


**Figure 1c.1** The glutamatergic synapse. The cycling of glutamate (Glu) and glutamine (Gln) between the glial cell and the presynaptic neuron is illustrated with the arrow. From Popoli M, Yan Z, McEwen BS, Sanacora G. *Nat Rev Neurosci.* 2012;13(1):22-37. doi:10.1038/nrn3138.

As it participates in such a central metabolic process, glutamate is present in all cell types, but its auxiliary processes are quite specialized in different types of neurons. One useful way to organize and understand the dynamics of glutamate in the nervous system is the 'four compartment model': blood and plasma, glutamatergic neurons, GABAergic neurons, and astroglia<sup>4,5</sup>. The role of blood in this narrative is to supply glucose as input to glycolysis and the TCA cycle, and then to receive glutamine which is effluxed from the astroglia to maintain nitrogen homeostasis in the brain.

**Glutamatergic neurons** are the locus of glutamate's action as an excitatory neurotransmitter. Inside this type of neuron, glutamate is concentrated in so-called pre-synaptic vesicles near the membrane, in preparation to be released into the excitatory synapse. The depolarizing stimulus-- or action potential-- causes an influx of calcium. This triggers calcium-dependent vesicle fusion to the membrane, releasing glutamate into the synapse.

Once glutamate has bound to the receptors on the post-synaptic neuron, its job is done, and it must be cleared from the synapse for 'recycling'. There are three key protein types involved in this mechanism:

- a) the glutamate receptors on the post-synaptic neuron which bind the glutamate
- b) the glutamate transporters, which exist both on the post-synaptic neuron and the astroglia in the vicinity of the synapse
- c) the enzyme glutamine synthetase, located in astroglia, which converts glutamate to glutamine.

Thus, **astroglia** play a key role in the conversion of glutamate to glutamine, which they transport back to the glutamatergic neuron, which again converts it to glutamate. This process is known as the **glutamate-glutamine cycle**.

In **GABAergic neurons**, GABA is synthesized from glutamate by the enzyme glutamate decarboxylase. In symmetry to the glutamate/glutamine cycle, there is a GABA/glutamine cycle in which astroglia take up the GABA released into the synapse, converted it to glutamine, and restore this glutamine to the GABAergic neuron. The concentrations of glutamate, glutamine and GABA in the brain are approximately 10mM, 3mM and 1mM, respectively<sup>5</sup>.

Glutamate as a neurotransmitter is at the center of neural function in health and disease. In a healthy brain, glutamate signaling is particularly central to the function of the hippocampus and its neighboring structures in the medial temporal lobe, the locus of learning and memory formation<sup>4,6-8</sup>. Changes in the glutamate/GABA balance may underlie the larger-scale electrophysiologic effects known as “potentiation” and “depression”, which have both physiological and pathological relevance<sup>9</sup>. Dysregulation of glutamate is thought to underlie neurophysiological conditions like epilepsy<sup>10</sup> and neuropsychological conditions such as schizophrenia<sup>4</sup>.

One important model that has come to light in the recent era of research on neurodegeneration is the **excitotoxicity hypothesis**<sup>11-14</sup>. This model maintains that an excess of glutamate in the synapse, which can arise due to dysfunction in any of the above steps, is toxic to neurons, and that this glutamic accumulation induces the neuronal death manifesting in several diseases<sup>15</sup>. Lastly, any metabolic pathology or genetic variation which affects core oxidative metabolism may be coupled to neurological function if flux through the glutamate-related pathways are



perturbed. This includes everything from rare conditions such as hyperinsulinemism/hyperammonemia<sup>16</sup> to the universal considerations of how diversity in baseline metabolism may influence an individual's susceptibility to cognitive decline with age.

The ability to image glutamate *in vivo* advances our understanding of normal brain physiology and function, sheds light on the etiology of disease, reports on the efficacy of treatment approaches, and in some cases, can even inform surgical decisions. Unfortunately, until now, detecting glutamate in a specific and non-invasive fashion is a largely underdeveloped technology. For decades, the only option was to perform single-voxel spectroscopy, which detects glutamate only weakly in comparison to other metabolites and has limited spatial resolution. Recently, spectroscopic imaging and molecular imaging techniques like CEST – largely made possible by advances in scanner magnetic field strength-- have begun to open technical doors to imaging this important molecule.

## 1c.2 MR-based detection of glutamate

*In vivo* magnetic resonance spectroscopy (MRS) has been practiced in the field of medical imaging since the early days of MRI. In the brain, the largest peaks visible in the NMR spectrum

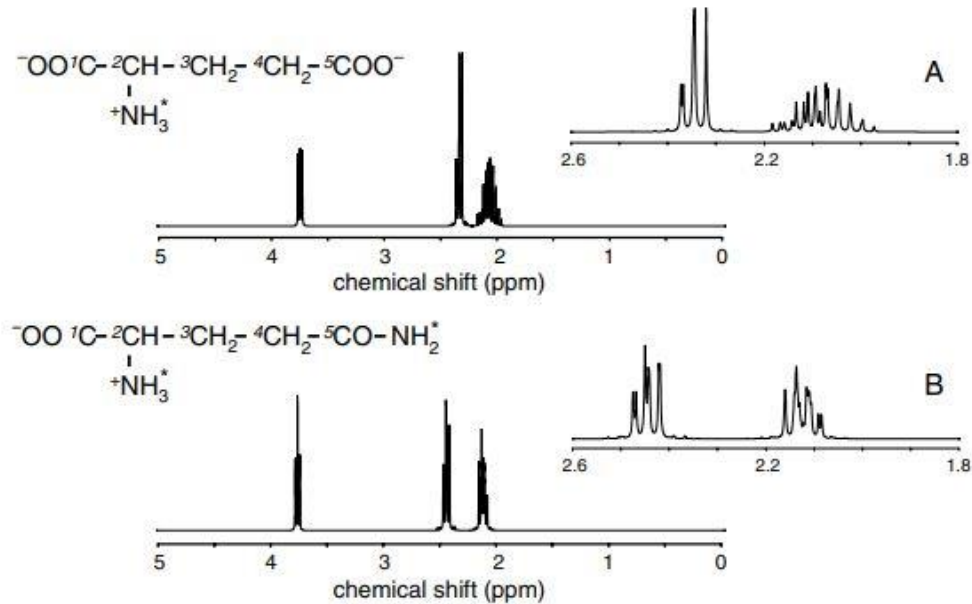


**Figure 1c.2:** NMR spectra of glutamate (A) and glutamine (B) [ref]. From de Graaf (ref. 5)

are N-acetyl-aspartate, choline and creatine. The ability to detect glutamate reliably for many years remained elusive. Other than being of relatively low concentration compared to the “big three”, a major challenge on this front is the high degree of spectral similarity between glutamate and glutamine. As we can see in Figure 1c.2, the spectra of glutamate and glutamine both contain three main resonances, each with complex splitting patterns. These correspond to the hydrogens indexed as H2, H4 and H3, in order from ‘downfield’ to ‘upfield’. Glutamate and glutamine differ structurally from each other only after carbon no. 4, attached to which is a carboxylic acid moiety in glutamate and an amide in glutamine. Therefore, it is this H4 resonance which begins to differentiate glutamate from glutamine – but only at field strengths where chemical shift dispersion is sufficiently high. According to de Graaf, these resonances are

“visually separated” only 7T field strength or higher; in the absence of this clear separation, individual quantification of glutamate and glutamine depends on mathematical fitting to the amorphous lineshape known as ‘Glx’ in the lower-field spectrum. The protons of the amine group on these molecules exchange too quickly to appear in the NMR spectrum, however, the amide protons on glutamine exchange more slowly and can be detected with sufficient spectral bandwidth.

These three adjacent carbons and their affiliated protons H2, H3 and H4 are strongly coupled, responsible for the extensive splitting of the spectrum. In addition to defining the lineshape, the strong scalar coupling affects the relaxation properties of these spins:  $T_2$  relaxation arises precisely from such interactions. The presence of this strong coupling dictates the choice of optimal sequences for spectroscopic detection of such molecules. Specifically, the tendency of J-evolution to quickly destroy phased magnetization and detectable resonances makes long echo-time sequences prone to signal loss. de Graaf’s book recommends that localization by adiabatic selective refocusing, or LASER, is an ideal sequence for spectroscopy of glutamine and glutamate, as opposed to the more canonical spectroscopy sequences PRESS or STEAM, in which the measurement may be plagued by the deleterious effects of spin-spin relaxation. For more about the LASER sequence, please see Chapter 1a.

In the best case scenario, a well shimmed, high-SNR (meaning either large volume or many averages) single voxel spectrum at 7T may provide a measurement in which one has confidence in the fit and resulting quantification of glutamate and glutamine separately. Arguably, such results can even be expanded to spectroscopic imaging, as in recent work by Hingerl et al<sup>17</sup>, to introduce spatial resolution to the measurement. In this thesis, the work presented in Chapter 5 makes use of spectroscopic imaging, but does not claim to distinguish the various components

of the Glx resonance. Under any conditions, the sensitivity and specificity of spectroscopic approaches to detecting glutamate *in vivo*, particularly with any degree of spatial resolution, remain somewhat dismal.

The detection of glutamate by CEST is not wholly straightforward, either (see Chapter 1b). However, as explained in Chapter 1b, the very mechanism of CEST provides it with the advantage of amplification due to exchange, and some degree of specificity resulting from the variable exchange-rate dependent contributions. The overwhelming advantage of using gluCEST as opposed to spectroscopy lies in the incomparable spatial resolution. Because the presence of glutamate is being detected by proxy through the water resonance, the resolution of the gluCEST image approaches the resolution possible in a 'regular' structural image. In practice, the in-plane resolution used is somewhat lower than a structural image, in order to achieve adequate SNR. Furthermore, the limitations of time and ability to correct for inhomogeneities have so far constrained gluCEST in humans to less than full-brain acquisitions. However, exciting findings to date provide a strong impetus for continued development of this technology, and indicate its potential to provide truly unique pictures of neurometabolism.

### **1c.3 Summary of human and animal gluCEST applications to date**

Since its introduction in 2012<sup>18</sup>, gluCEST has led to a number of intriguing preclinical and clinical imaging studies. It has been applied extensively in rodents and humans, to a limited degree in primates, and interest has even been expressed in using gluCEST to probe the mysteries of aquatic invertebrate neurophysiology<sup>3</sup>. Preclinical applications in rodents include the study of Parkinson's Disease<sup>19,20</sup>, Huntington's Disease<sup>21-23</sup>, the general etiology of tau pathology<sup>24</sup>,

Friedrich's Ataxia<sup>25</sup>, inflammation, encephalitis and traumatic brain injury<sup>26–28</sup>, and cancer metabolism<sup>29</sup>. Alzheimer's Disease has been studied using gluCEST in primates<sup>30</sup> and humans<sup>31</sup>.

Further human clinical applications have demonstrated that gluCEST can serve as a powerful biomarker in the monitoring of neurological and psychiatric conditions where other forms of non-invasive physiological information are very sparse. These include epilepsy<sup>10</sup>, schizophrenia and related psychoses<sup>32–34</sup>, glioma<sup>35</sup>, hyperinsulinemism/hyperammonemia (HIHA)<sup>16</sup> and multiple sclerosis<sup>36</sup>.

One gluCEST application that has yet to be translated to clinical studies is spinal cord imaging of neuropathologies –such as Friedrich's Ataxia, as in Pépin's murine study<sup>25</sup>. However, spinal cord gluCEST imaging has already been successfully demonstrated in healthy human volunteers<sup>37</sup>, suggesting that the possibility is open for expansion of gluCEST clinical applications to all of the central nervous system. Only a few published studies have tried to truly capitalize on the spatial resolution of gluCEST to push the envelope of fine-grained regional analysis. In the preclinical realm, this includes the work of Pépin<sup>38</sup> and Crescenzi<sup>39</sup>, who augment their investigations with corresponding histology. In human beings, perhaps the leading example of this to date is Cai *et al* 2013, who used a single-slice sagittal gluCEST acquisition to capture and analyze gluCEST signal in a number of subcortical regions<sup>40</sup>. However, with this limited-volume acquisition, analysis of very small structures like hippocampal subfields was not possible.

#### **1c.4 Summary of advances presented in this thesis**

The results herein represent technical improvement of the gluCEST measurement (Chapters 2, 5A), and findings in the realms of aging (Chapter 3), potential therapeutic mechanisms (Chapter 4), and neurochemistry of the healthy brain (Chapter 5). The final chapter diverges from CEST to

present an additional modality for studying the *dynamics* of glutamate metabolism, in which the conversion of glucose to glutamate can be indirectly observed (Chapter 6). More specifically:

It was emphasized in Chapter 1b that fast-exchanging metabolites require high  $B_1$  power for successful and valid CEST measurements. Unfortunately, the 7T head coil provides very inhomogeneous  $B_1$  field, which means both that a) there are regions in which sufficient saturation power for gluCEST may not be achieved, and b) even where in principle the threshold for sufficient saturation has been crossed, it is not homogeneous over the field of view, and this needs to be corrected for so that different regions of the image can be compared properly. The work in **Chapter 2** provides an improved strategy for (b) and also demonstrates that actually (a) generally occurs only rarely, and the apparent total loss of signal in some regions of the image arises from flip angle loss in the acquisition module.

**Chapter 3** focuses on the gluCEST measurement in the aging brain. Upon application to gluCEST in older subjects, it was found that more reasonable results are achieved when  $B_1$  correction ‘surfaces’ are used which are very roughly age-matched ( $\pm 10$  years) to the subject. We hypothesize that this may reflect decreased lipid content in the brains of older people relative to younger, and therefore a different contribution to the NOE resonance that would arise from these molecules. These preliminary results are presented in **Chapter 3A**. The gluCEST results to date from a study on older adults with and without Mild Cognitive Impairment (MCI), which thus far are inconclusive, form the content of **Chapter 3B**. This investigation, while ongoing, provides an excellent case study of the challenges of the gluCEST measurement, and an illustration of why it would be preferable to use a 3D, rather than 2D acquisition.

In **Chapter 4**, we use 2D gluCEST to examine the brains of healthy volunteers before and after they have received continuous theta burst stimulation (cTBS), a type of non-invasive transcranial magnetic stimulation (TMS), to the left motor cortex. We find small but strongly statistically significant decreases ( $p < 1e-4$ ) in gluCEST on the order of 0.1-0.3% CEST contrast (where the baseline average is around 7-8%-- thus this represents a 1-3% change) in most of the left hemisphere of stimulated subjects. Some less statistically significant changes ( $p < 1e-2$ ) were detected sporadically in the right hemisphere and in subjects who received a placebo stimulation, but these appear to be spurious. To the best of our knowledge, this work is the first of its kind to use molecular imaging to study the effects of TMS in a spatially resolved fashion.

In **Chapter 5**, the 3D gluCEST measurement is acquired in the medial temporal lobe of healthy volunteers. Upon segmentation and regional analysis, we find that the dentate gyrus has an extremely statistically significant elevation of gluCEST compared to other subfields of the hippocampus and remaining medial temporal lobe. (The highest p-value in this comparison was  $6e-4$  for the difference between CA2/DG, with the next highest being  $9e-12$  for CA3/DG). This finding makes sense in light of current understanding of neurophysiology, which hypothesizes that the DG is the most prominent locus of neurogenesis, and was preceded by an analogous finding in the work of Crescenzi *et al* in murine experiments. However, we believe this to be the first time that this neurometabolic phenomenon has ever been detected in human beings. **The supplementary information to Chapter 5** contains additional material relevant to our progress from 2D to 3D gluCEST.

**Chapter 6** explores the application of a newly developed spectroscopy and spectroscopic imaging technique<sup>41</sup> in human beings. Here, instead of gluCEST, we use proton spectroscopy to detect the metabolism of glucose into glutamate and glutamine in a dynamic fashion. The

lynchpin of this experiment is that subjects have ingested a large amount of glucose in which one proton is replaced with deuterium, which is invisible to the proton NMR measurement. In this way, we are able to detect the “missing” proton and thus the conversion of their ingested glucose into neurotransmitters in the brain. This technique, dubbed qMRS, can serve an excellent complement to gluCEST, as it provides dynamic, albeit lower-resolution information about neural glutamate.

In addition to these research chapters, two Appendices provide full, user-friendly documentation for the Bloch-McConnell simulations and gluCEST post-processing code used in this thesis, much of the original version of which was developed by Dr. Anup Singh and Dr. Hari Hariharan, but with minimal documentation or comment. These appendices are fully auxiliary to the research results themselves, but included here as a strategic effort to avoid their loss to posterity.



## References

1. Lehninger AL, Nelson DL, Cox MM. *Principles of Biochemistry*. Fourth. W.H. Freeman and Company
2. Coles JA. Glial cells: Invertebrate. In: *Encyclopedia of Neuroscience*. Elsevier Ltd; 2009:749-759. doi:10.1016/B978-008045046-9.01011-1
3. Wermter FC, Bock C, Dreher W. Investigating GluCEST and its specificity for pH mapping at low temperatures. *NMR Biomed*. 2015;28(11):1507-1517. doi:10.1002/nbm.3416
4. Tamminga CA, Southcott S, Sacco C, Wagner AD, Ghose S. Glutamate Dysfunction in Hippocampus: Relevance of Dentate Gyrus and CA3 Signaling. *Schizophr Bull*. 2012;38(5):927-935. doi:10.1093/schbul/sbs062
5. Graaf RA de. *In Vivo NMR Spectroscopy: Principles and Techniques*. Third Edii. Wiley; 2019.
6. Berron D, Schütze H, Maass A, et al. Strong evidence for pattern separation in human dentate gyrus. *J Neurosci*. 2016;36(29):7569-7579. doi:10.1523/JNEUROSCI.0518-16.2016
7. Anacker C, Hen R. Adult hippocampal neurogenesis and cognitive flexibility-linking memory and mood. *Nat Rev Neurosci*. 2017;18(6):335-346. doi:10.1038/nrn.2017.45
8. Lee E, Son H. Adult hippocampal neurogenesis and related neurotrophic factors. *BMB Rep*. 2009;42(5):239-244. doi:10.5483/BMBRep.2009.42.5.239
9. Cuypers K, Marsman A. Transcranial magnetic stimulation and magnetic resonance spectroscopy: Opportunities for a bimodal approach in human neuroscience. *Neuroimage*. 2021;224:117394. doi:10.1016/j.neuroimage.2020.117394
10. Davis KA, Nanga RPR, Das S, et al. Glutamate imaging (GluCEST) lateralizes epileptic foci in nonlesional temporal lobe epilepsy. *Sci Transl Med*. 2015;7(309):309ra161-309ra161. doi:10.1126/scitranslmed.aaa7095
11. Rudy CC, Hunsberger HC, Weitzner DS, Reed MN. The role of the tripartite glutamatergic synapse in the pathophysiology of Alzheimer's disease. *Aging Dis*. 2015;6(2):131-148. doi:10.14336/AD.2014.0423
12. Gardoni F, Di Luca M. New targets for pharmacological intervention in the glutamatergic synapse. *Eur J Pharmacol*. 2006;545(1):2-10. doi:10.1016/j.ejphar.2006.06.022
13. Hawkins RA. The blood-brain barrier and glutamate. *Am J Clin Nutr*. 2009;90(3). doi:10.3945/ajcn.2009.27462BB
14. Minkeviciene R, Ihalainen J, Malm T, et al. Age-related decrease in stimulated glutamate release and vesicular glutamate transporters in APP/PS1 transgenic and wild-type mice. *J Neurochem*. 2008;105(3):584-594. doi:10.1111/j.1471-4159.2007.05147.x
15. Velasco M, Quintero JR, Castillo MC, et al. Excitotoxicity: An Organized Crime at The Cellular Level. *J Neurol Neurosci*. 2017;08(03):193. doi:10.21767/2171-6625.1000193
16. Rosenfeld E, Nanga RPR, Reddy R, et al. MON-110 Utilization of GluCEST, a Novel Neuroimaging Technique, to Characterize the Brain Phenotype in

- Hyperinsulinism/Hyperammonemia Syndrome. *J Endocr Soc.* 2020;4(Supplement\_1). doi:10.1210/jendso/bvaa046.594
17. Hingerl L, Strasser B, Moser P, et al. Clinical High-Resolution 3D-MR Spectroscopic Imaging of the Human Brain at 7 T. *Invest Radiol.* 2020;55(4):239-248. doi:10.1097/RLI.0000000000000626
  18. Cai K, Haris M, Singh A, et al. Magnetic resonance imaging of glutamate. *Nat Med.* 2012;18(2):302-306. doi:10.1038/nm.2615
  19. Bagga P, Crescenzi R, Krishnamoorthy G, et al. Mapping the alterations in glutamate with GluCEST MRI in a mouse model of dopamine deficiency. *J Neurochem.* 2016;139(3):432-439. doi:10.1111/jnc.13771
  20. Bagga P, Pickup S, Crescenzi R, et al. In vivo GluCEST MRI: Reproducibility, background contribution and source of glutamate changes in the MPTP model of Parkinson's disease. *Sci Rep.* 2018;8(1):1-9. doi:10.1038/s41598-018-21035-3
  21. Pépin J, Longprez L, Trovero F, Brouillet E, Valette J, Flament J. Complementarity of gluCEST and <sup>1</sup>H-MRS for the study of mouse models of Huntington's disease. *NMR Biomed.* 2020;33(7):e4301. doi:10.1002/nbm.4301
  22. Pépin J, Francelle L, Carrillo-de Sauvage MA, et al. In vivo imaging of brain glutamate defects in a knock-in mouse model of Huntington's disease. *Neuroimage.* 2016;139:53-64. doi:10.1016/j.neuroimage.2016.06.023
  23. Flament J, Pépin J, Francelle L, et al. B40 In vivo imaging of brain glutamate defects in a knock-in mouse model of huntington's disease. *J Neurol Neurosurg Psychiatry.* 2016;87(Suppl 1):A23.2-A23. doi:10.1136/jnnp-2016-314597.71
  24. Crescenzi R, DeBrosse C, Nanga RPR, et al. In vivo measurement of glutamate loss is associated with synapse loss in a mouse model of tauopathy. *Neuroimage.* 2014;101:185-192. doi:10.1016/j.neuroimage.2014.06.067
  25. Pepin J, Pigué F, Puccio H, Flament J. *GluCEST Imaging of Spinal Cord in a Mouse Model of Friedreich Ataxia.*; 2020. [https://www.researchgate.net/profile/Julien-Flament/publication/303549841\\_GluCEST\\_imaging\\_of\\_spinal\\_cord\\_in\\_a\\_mouse\\_model\\_of\\_Friedreich\\_ataxia/links/5748090f08ae2301b0b83faa/GluCEST-imaging-of-spinal-cord-in-a-mouse-model-of-Friedreich-ataxia.pdf](https://www.researchgate.net/profile/Julien-Flament/publication/303549841_GluCEST_imaging_of_spinal_cord_in_a_mouse_model_of_Friedreich_ataxia/links/5748090f08ae2301b0b83faa/GluCEST-imaging-of-spinal-cord-in-a-mouse-model-of-Friedreich-ataxia.pdf)
  26. Zhuang Z, Shen Z, Chen Y, et al. Mapping the Changes of Glutamate Using Glutamate Chemical Exchange Saturation Transfer (GluCEST) Technique in a Traumatic Brain Injury Model: A Longitudinal Pilot Study. *ACS Chem Neurosci.* 2019;10(1):649-657. doi:10.1021/acscchemneuro.8b00482
  27. Jia Y, Chen Y, Geng K, et al. Glutamate Chemical Exchange Saturation Transfer (GluCEST) Magnetic Resonance Imaging in Pre-clinical and Clinical Applications for Encephalitis. *Front Neurosci.* 2020;14. doi:10.3389/fnins.2020.00750
  28. Chen Y, Dai Z, Shen Z, et al. Imaging of glutamate in brain abscess using GLUCEST at 7T. *Radiol Infect Dis.* 2018;5(4):148-153. doi:10.1016/j.jrid.2018.11.001
  29. Zhou R, Bagga P, Nath K, Hariharan H, Mankoff DA, Reddy R. Glutamate-weighted chemical

- exchange saturation transfer magnetic resonance imaging detects glutaminase inhibition in a mouse model of triple-negative breast cancer. *Cancer Res.* 2018;78(19):5521-5526. doi:10.1158/0008-5472.CAN-17-3988
30. Flament J, Gary C, Koch J, et al. *GluCEST Imaging in a Primate Model of Alzheimer's Disease* .; 2015. Accessed March 14, 2021. <https://www.researchgate.net/publication/278030632>
  31. Haris M, Nath K, Cai K, et al. Imaging of glutamate neurotransmitter alterations in Alzheimer's disease. *NMR Biomed.* 2013;26(4):386-391. doi:10.1002/nbm.2875
  32. Nanga RPR, Roalf DR, Hariharan H, Prabhakaran K, Reddy R. *GluCEST in the Olfactory Cortex as a Marker of Heightened Clinical Risk for Schizophrenia.*; 2015. Accessed March 14, 2021. <https://www.researchgate.net/publication/293223610>
  33. Sydnor VJ, Larsen B, Kohler C, et al. Diminished reward responsiveness is associated with lower reward network GluCEST: an ultra-high field glutamate imaging study. *Mol Psychiatry.* Published online January 21, 2021:1-11. doi:10.1038/s41380-020-00986-y
  34. Roalf DR, Nanga RPR, Rupert PE, et al. Glutamate imaging (GluCEST) reveals lower brain GluCEST contrast in patients on the psychosis spectrum. *Mol Psychiatry.* 2017;22(9):1298-1305. doi:10.1038/mp.2016.258
  35. Neal A, Moffat BA, Stein JM, et al. Glutamate weighted imaging contrast in gliomas with 7 Tesla magnetic resonance imaging. *NeuroImage Clin.* 2019;22:101694. doi:10.1016/j.nicl.2019.101694
  36. O'Grady KP, Dula AN, Lyttle BD, et al. Glutamate-sensitive imaging and evaluation of cognitive impairment in multiple sclerosis. *Mult Scler J.* 2019;25(12):1580-1592. doi:10.1177/1352458518799583
  37. Kogan F, Singh A, Debrosse C, et al. Imaging of glutamate in the spinal cord using GluCEST. *Neuroimage.* 2013;77:262-267. doi:10.1016/j.neuroimage.2013.03.072
  38. Pepin J, Jégo P, Valette J, Bonvento G, Flament J. *Imaging of Neuronal Compartment Using GluCEST Method.*; 2018. [https://www.researchgate.net/profile/Jeremy-Pepin/publication/317014174\\_Imaging\\_of\\_neuronal\\_compartment\\_using\\_gluCEST\\_method/links/591ef1daa6fdcc233fd4d374/Imaging-of-neuronal-compartment-using-gluCEST-method.pdf](https://www.researchgate.net/profile/Jeremy-Pepin/publication/317014174_Imaging_of_neuronal_compartment_using_gluCEST_method/links/591ef1daa6fdcc233fd4d374/Imaging-of-neuronal-compartment-using-gluCEST-method.pdf)
  39. Crescenzi R, DeBrosse C, Nanga RPR, et al. Longitudinal imaging reveals subhippocampal dynamics in glutamate levels associated with histopathologic events in a mouse model of tauopathy and healthy mice. *Hippocampus.* 2017;27(3):285-302. doi:10.1002/hipo.22693
  40. Cai K, Singh A, Roalf DR, et al. Mapping glutamate in subcortical brain structures using high-resolution GluCEST MRI. *NMR Biomed.* 2013;26(10):1278-1284. doi:10.1002/nbm.2949
  41. Rich LJ, Bagga P, Wilson NE, et al. 1H magnetic resonance spectroscopy of 2H-to-1H exchange quantifies the dynamics of cellular metabolism in vivo. *Nat Biomed Eng.* 2020;4(3):335-342. doi:10.1038/s41551-019-0499-8

# **Chapter 2: An improved method for post-processing correction of $B_1$ inhomogeneity in gluCEST images of the human brain**

## **2.1 Introduction**

CEST is a suite of magnetic resonance imaging techniques which generate contrast weighted by the presence of endogenous or exogenous metabolites, mediated by hydrogen exchange with bulk water<sup>1-4</sup>. Like many MRI applications, CEST has been greatly advanced by the adoption of ultra-high field strength ( $> 7T$ ) magnets. However, with higher field strength, radio frequency (RF)  $B_1$  field inhomogeneity becomes an increasingly salient phenomenon, as the RF wavelength becomes comparable to the dimensions of the human body and head<sup>5-8</sup>. This inhomogeneity in the  $B_1$  field is problematic for the accuracy of CEST measurements and particularly, as discussed below, for glutamate-weighted imaging (gluCEST)<sup>9</sup>. Unlike in the acquisition of a traditional  $T_1$  or  $T_2$ -weighted image -- in which the role of  $B_1$  is simply to rotate the net magnetization to measure the inherently variable recovery-- the contrast in a CEST experiment is actually created by so-called 'saturation  $B_1$ ' in a 'magnetization preparation' module prior to acquisition. Thus, in a CEST experiment, the variable amplitude of  $B_1$  results in inhomogeneous saturation and resulting contrast in addition to different flip angles during the acquisition module.

$B_1$  inhomogeneity can in some cases be mitigated by the use of paddings with high-dielectric or ferroelectric gels, and recently, the primary hardware-based approach

to mitigating  $B_1$  inhomogeneity has been the introduction of parallel transmit (PTX). The literature includes many implementations of PTX, including with some application to CEST imaging<sup>10-12</sup>. However, it appears that while PTX has had success at “ $B_1$  shimming” or alleviating inhomogeneity, it has not been demonstrated to maintain high ( $B_{1, rms} > 3\mu T$ ) absolute  $B_1$  power over the field of view. While it could be argued that PTX has reached a state which obviates the need for post-processing correction in low-power modalities like amide proton transfer (APT) CEST (see Figure 2.S2), our data suggests that in the case of gluCEST, parallel transmit, dielectric padding and post-processing correction will all be required to produce high-quality volumetric images.

Our previous post-processing correction of gluCEST data for  $B_1$  inhomogeneity relied on segmenting all non-CSF brain tissue into one of two categories – gray and white matter – for each of which it was assumed that a single calibration curve to the gluCEST maps could be applied<sup>13,14</sup>. These calibration curves were generated by collecting calibration data (repeated CEST experiments) at varying nominal  $B_1$  strengths, e.g. {1.5, 2.0, 1.5, 3  $\mu T$ }, doing a binary segmentation for gray and white matter based on MTR asymmetry maps, and then fitting many ROIs of “gray matter” and many ROIs of “white matter” *en masse* to a third-order polynomial. However, using this method we felt it necessary to collect calibration data for each new experimental protocol focusing on a particular brain region, having noticed that the  $B_1$  calibration curves calculated for each slice tended to vary. Upon closer inspection, it was clear that this was arising from heterogeneity amongst tissues in the slice that would be grouped together by this

binary segmentation (see **Figure 2.S1**). The calibration data from individual pixels, or even ROIs, could rarely be satisfactorily fit to a polynomial function; apparent “goodness of fit” was arising from the spread of pixel values. In areas of low  $B_1$ , these functions were particularly inadequate.

A recent article has emphasized the dependence of CEST contrast on  $T_1$ <sup>15</sup>. While the work in [15] focuses on amide proton CEST at 3.5 ppm, the authors’ conclusions are equally valid for gluCEST at 3.0 ppm, although the dependence of contrast on  $T_1$  values diminishes as  $B_1$  power increases. Our investigations of CEST at 3.0 ppm corroborated the observation that the Z-spectrum is a steep function of  $T_1$  at low saturation power, thus leading to our decision to bin pixels for correction according to  $T_1$  values. When a binary segmentation and  $B_1$  correction are applied, as in earlier works, that assume all pixels to be either “gray” or “white” matter regardless of  $T_1$  heterogeneity, inaccuracies are introduced which can either falsely increase or decrease the apparent gluCEST contrast.

In this paper, we provide an improved method for correcting gluCEST images in the brain for  $B_1$  inhomogeneity. Three key advantages of this new method are a) a more accurate description of the functional form  $CEST_{3.0\text{ppm}}(B_1, \text{saturation})$  informed by Bloch-McConnell simulations and confirmed by experimental data; b) retention of the original signal-to-noise ratio (SNR) achieved in the positive and negative offset images by correcting these points in the Z-spectrum separately rather than correcting their

subtraction; c) fine categorization of brain tissue based on  $T_1$  maps, rather than binary classification into gray and white matter.

## **2.2 Methods**

### ***2.2.1 Bloch-McConnell Simulations***

Our simulations model the effect of the saturation pulse by finding numerical solutions to a six-pool Bloch-McConnell equation (Bloch equations modified to include chemical exchange)<sup>16</sup>. The six pools represented include: bulk water, bound water (water associated with or in the solvation shell of macromolecules), NOE-active protons (likely aliphatic protons from lipids and proteins), amide protons which exchange from protein backbones (APT), creatine and glutamate. Chemical exchange and cross-relaxation are both treated as coupling (off-diagonal) elements between the relevant metabolite and bulk water magnetization. No off-diagonal elements representing any type of interaction that may couple magnetization directly between the five “solute” pools solute are included. Other matrix elements include saturation  $B_1$ , relaxation rates, and offset frequency relative to the water resonance. The calculation includes two sets of coupled differential equations -- “pulse on” and “pulse off”—which are identical except for the inclusion of  $\omega_1$ . A Hamming-windowed pulse shape is used as in <sup>9</sup>. Simulation parameters are enumerated in Table S1 and example simulations shown in Figure 2.S2.

### ***2.2.2 Image Acquisition and Standard Post-Processing Procedures***

All images were obtained on a Siemens 7.0T MAGNETOM Terra scanner (Siemens Healthcare, Erlangen, Germany) outfitted with a single volume transmit/32 channel

receive phased array head coil (Nova Medical, Wilmington, MA, USA). All volunteers used in gathering  $B_1$  calibration data were healthy subjects ages 24-69, scanned with informed consent under an approved institutional regulatory board protocol. The general structure of a CEST-weighted acquisition is as follows: ‘magnetization preparation’ followed by ‘readout’.  $B_1$  calibration data was collected with a single-slice CEST sequence with the ‘readout’ module based on gradient-recalled echo with the following parameters: TR/TE = 4.7/2.3 ms,  $10^\circ$  flip angle, 5 mm slice thickness, with  $0.75 \times 0.75$  mm<sup>2</sup> in plane resolution over a  $156 \times 192$  mm<sup>2</sup> field of view. Magnetization preparation was achieved using eight  $3.1\mu\text{T}$  RMS amplitude, 95 ms Hamming-window shaped pulses with 5 ms inter-pulse delay applied at offset frequencies  $\{\pm 1.8, 2.1, 2.4, 2.7, 3.0, 3.3, 3.6, 3.9, 4.2\}$  ppm relative to water. CEST-weighted images were corrected for the  $B_0$  field distribution using a water saturation acquisition (WASSR)<sup>17</sup> and  $B_1$  field maps were generated as in <sup>18</sup>.  $T_1$  maps used are from the Siemens product sequence MP2RAGE. These auxiliary images had identical resolution and field of view as the CEST acquisition, although the  $B_1$  map was smoothed before application of the  $B_1$ -dependent correction to avoid numerical inconsistencies. A flowchart of the full CEST acquisition and post-processing procedure, including the  $B_1$  correction as described in this paper, is given in **Figure 2.2**.

### **2.3 Theory: Simple Parameterization of the Functional Form of $M_z/M_0 (B_{1, \text{sat}})$**

Simulations allowed us to examine the form of the function  $M_z/M_0 (B_{1, \text{saturation}})$  and the resulting function  $\text{CEST}_{3.0\text{ppm}} (B_{1, \text{saturation}})$ , including its dependence on many other



parameters. We were interested in identifying a simple, low-parameter mathematical expression that could describe the function  $M_z/M_0$  ( $B_{1, \text{saturation}}$ ) generated by virtually any simulation conditions. Assuming that our simulations accurately recapitulate the CEST experiment, we should then be able to fit our experimental calibration data to this function.

The general form of this equation was inspired by the theoretical treatment of the CEST and MT effects given in Zaiss et al, 2015<sup>19</sup>. Equation 5 in this work is an expression for the water Z-magnetization (denoted  $M_z$  in the present paper) after the saturation pulse:

$$z(\Delta\omega) = \frac{\cos^2 \theta * R_{1a}}{R_{1\rho}(\Delta\omega)} \quad [2.i]$$

Where  $\Delta\omega$  is the offset frequency of the saturation,  $R_{1a}$  is the longitudinal relaxation rate of bulk water, and  $R_{1\rho}$  is the longitudinal relaxation rate in the rotating frame, to which CEST and other effects may contribute. This work continues by providing expressions for MT and CEST contributions to  $R_{1\rho}$ :

$$R_{ex}^{CEST} = f_b k_{ba} \frac{\omega_1^2}{\omega_1^2 + k_{ba}(k_{ba} + R_{2b})} \quad R_{ex}^{MT} = \dots + \omega_1^2 (r_{2a} + k_{ca} + r_{1c}) \quad [2.ii, 2.iii]$$

where the first term of equation 2.iii is quite complex but also includes a quadratic term of  $\omega_1$ , which represents the magnitude of the RF pulse used for the saturation or ‘magnetization preparation’ module. Regardless of the values of any constants ( $k$ ,  $r$ ), or the relative weights of these contributions ( $MT$ ,  $CEST$ ), according to this treatment the

function  $Z(\Delta\omega, \omega_1)$  – that is, net magnetization as a function of the frequency and amplitude of the saturation pulse – will be an even function of  $\omega_1$ . Thus, needing only the simplest possible phenomenological functional form for our purposes, we investigated the possibility of using only a few even terms of  $\omega_1$  to describe  $M_Z(\omega_1)$ . To determine an appropriate form, we performed many iterations of six-pool Bloch-McConnell simulations with various parameters and tested whether a given minimal-parameter functional form was able to robustly fit these very high dimensionality simulations.

We attempted such fitting with the following simple equations:

$$\frac{M_Z}{M_0}(B_1) = 1 + \frac{1}{\beta * B_1^2 + 1} \quad [2.1a]$$

$$\frac{M_Z}{M_0}(B_1) = 1 + \frac{\alpha * B_1^2}{\beta * B_1^2 + 1} \quad [2.1b]$$

$$\frac{M_Z}{M_0}(B_1) = 1 + \frac{1}{\beta * B_1^2 + 1} - \gamma * B_1^2 \quad [2.1c]$$

$$\frac{M_Z}{M_0}(B_1) = 1 + \frac{\alpha * B_1^2}{\beta * B_1^2 + 1} - \gamma * B_1^2 \quad [2.1]$$

We found that while equation [2.1b] is able to fit  $M_Z/M_0(B_{1, \text{saturation}})$  quite closely in most situations, Equation [2.1] outperforms it to a slight degree. When fitting real calibration data from human brains, we found that parameter  $\gamma$  could even be held constant after a first iteration of fitting to determine its value, but still improves the fit.

Our results suggest that this parameter is largely capturing the contribution of direct saturation to the decrease in  $M_z/M_0$ . Note that the value of parameter  $\alpha$  is always negative, giving these functions a maximum of 1, corresponding to the physical situation of being subject to no saturation.

For clarity, we would like to emphasize that we are not ‘fitting the Z-spectra’. (This is done during the  $B_0$  correction, but that is independent of the  $B_1$  correction at hand.) The ‘Z-spectrum’ refers to the function  $M_z(\omega, B_1 = \text{constant})$ , but the function addressed here and fit by Equation [2.1] is  $M_z(B_1, \omega = \pm 3.0)$ . This can be thought of as a cross-section of the Z-spectrum at a particular frequency offset (in this case, either  $\pm 3.0$  ppm relative to water).

## 2.4 Acquisition and Use of Calibration Data

*Overview.* (See **Figure 2.S3** for schematic). For each set of calibration data (collected on a single subject), CEST images at 4-6 nominal saturation  $B_1$  values were acquired, as well as WASSR images,  $B_1$  maps,  $T_1$  maps, and reference (no saturation) images. Each pixel within the brain ROI was sorted into one of 26 bins based on its  $T_1$  value. After  $B_0$  correction, pixels in a particular mask were then fit to Equation [2.1] for both the positive and negative offset data. This results in two separate "Correction Surfaces", one for positive and one for negative saturation offset, for  $M_z$  as a function of  $B_1$  strength and  $T_1$  value, parameterized by three parameters--  $\alpha$ ,  $\beta$ ,  $\gamma$  -- for each  $T_1$  bin. After parameter values with the two-free-parameter fit were obtained for all three calibration

data sets, a weighted average of these parameter values was calculated ( $\alpha$  and  $\beta$  for each  $T_1$  bin, with  $\gamma$  at a static value, and  $M_0$  set to 1 ). The weighting was done according to the reciprocal of the residual norm, such that the parameter values from fits with lower residual norms (better fits) contributed more to the final value. (See Figure 2.S4 for examining fits and residuals.) Before this, the residual norm itself (as returned by Matlab's *lsqcurvefit*) was normalized for the value of  $M_0$  (corresponding to the magnitude of the data) used in the second fit and the number of points in the vectors. Evaluating Equation [2.1] with each of these parameter values gives positive and negative offset correction surfaces. Finally, these surfaces were smoothed along the  $T_1$  axis with a Gaussian filter with a kernel size of 2, and the resulting surface was refit to Equation [2.1], giving the final "smoothed" correction surfaces. The positive-offset one is shown visually in Figure 2.1B, and a complete list of parameters for both surfaces are displayed in **Table 2.S2E**. The final correction surface used in the results presented was generated from calibration data gathered on three healthy male subjects ages 25, 38 and 68.

**2.4.1 Fitting of calibration data with four free parameters.** Calibration data was acquired and handled according to the process shown in **Figure 2.S3**, including being fit to Equation [2.1] with four free parameters  $\{\alpha, \beta, \gamma, M_0\}$  using Matlab's *lsqcurvefit* (see **Tables 2.S2A-D** for parameters of the *lsqcurvefit* function). The data was sorted such that only points with relative  $B_1 > \sim 0.2$  were included in the fit, in order to avoid noise and variability caused by  $B_1$  of the acquisition module being very low. (In correction of

actual experimental data, this effect is mitigated by applying a linear correction for flip angle in acquisition  $B_1$  --See **Figure 2.2.**)

*Fitting of calibration data with two free parameters.* It was then observed that over all  $T_1$  bins variability in parameter  $\gamma$  was low, and it was frozen to a static value in order to stabilize the other fitting parameters.  $M_0$  was also given a fixed value over certain bins for each data set, to account for the initial signal magnitude differences between tissue types. Constraining parameters  $\gamma$  and  $M_0$  in this way resulted in the three data sets having similar values of the remaining two free parameters,  $\alpha$  and  $\beta$ , as a function of  $T_1$  value.

#### **2.4.2 Generation of final correction surface by residuals-weighted average**

$$[2.1^*] \quad \frac{M_{z,PN,b}}{M_0}(B_1) = \left[ 1 + \frac{\alpha_{PN,b} * B_1^2}{\beta_{PN,b} * B_1^2 + 1} - \gamma * B_1^2 \right]$$

Equation [2.1\*] is the functional form found to describe the value of  $M_z$  after a saturation pulse of amplitude  $B_1$  at a particular frequency offset, now expressed with subscripts indicating ‘positive’ 3.0ppm (P) and ‘negative’ -3.0ppm (N) frequency offsets for the saturation pulse. In the gluCEST experiment, the saturation frequencies are measured in pairs symmetric around the water resonance, referred to as “positive” (P) or “negative” (N) offset. We describe this as a family of functions depending on  $T_1$  value, which we discretize into bins  $b$ . Therefore, each  $T_1$  bin  $b$  has two particular functions  $M_z/M_0(B_{1, \text{saturation}})$  – one for saturation applied at = +3.0 ppm,  $P$ , and one for saturation

applied at -3.0ppm,  $N_{--}$  described in our approach by two free parameters,  $\alpha_{P,b}$  and  $\beta_{P,b}$  or  $\alpha_{N,b}$  and  $\beta_{N,b}$ , respectively.

In this paper, three different calibration data sets were fit to Equation [2.1] to determine this family of functions, or the “correction surface”. Because  $M_0$  (the net magnetization of water, measured in arbitrary units by the signal intensity of a proton density weighted image) can vary between experiments, pixels acquired on different subjects at different times were not combined before fitting; rather, three different correction surfaces were determined, and their parameter values were combined using a weighted average to produce the final surface. Because of the varying number of pixels in each bin, differing  $B_1$  distributions, and other experimental factors between subjects, the quality of the data and resulting fit for any given  $T_1$  bin was somewhat variable between data sets. This average was therefore weighted such that binwise fits with lower residuals were given more weight than those with higher residuals:

$$R_{U,PN,b} = \frac{Res_{U,PN,b}}{M_{0,U,b}^2 * n_{T,b}}$$

Where U indicates a particular data set out of three, hereon denoted as {U,V,W}. This quantity R is the residual norm (quantifying the quality of the fit) normalized by the value of  $M_0$  used for this bin and the number of points it includes. The following algebra was done to convert this quantity into a coefficient to weight the contribution of that parameter value for that bin in its contribution to the weighted average:

$$S_{PN,b} = \frac{1}{R_{U,PN,b}} + \frac{1}{R_{V,PN,b}} + \frac{1}{R_{W,PN,b}}$$

$$T_{U,PN,b} = \frac{1}{R_{U,PN,b}} * \frac{1}{S_{U,PN,b}}$$

Thus:

$$\alpha_{P,b} = T_U * \alpha_{U,P,b} + T_V * \alpha_{V,P,b} + T_W * \alpha_{W,P,b}$$

$$\beta_{P,b} = T_U * \beta_{U,P,b} + T_V * \beta_{V,P,b} + T_W * \beta_{W,P,b}$$

$$\alpha_{N,b} = T_U * \alpha_{U,N,b} + T_V * \alpha_{V,N,b} + T_W * \alpha_{W,N,b}$$

$$\beta_{N,b} = T_U * \beta_{U,N,b} + T_V * \beta_{V,N,b} + T_W * \beta_{W,N,b}$$

## 2.5 Results

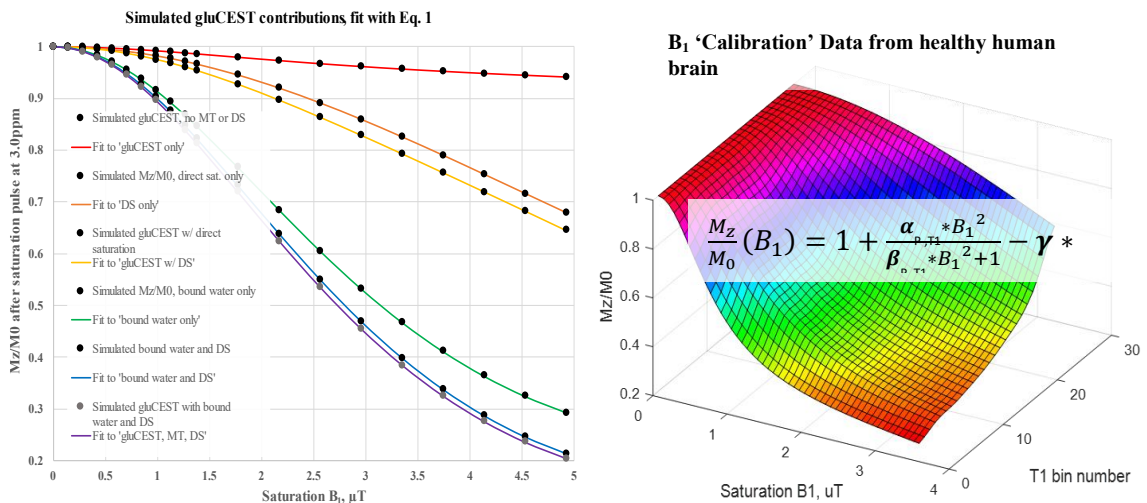
Bloch McConnell simulations allowed us to understand why sufficient B<sub>1</sub> power is necessary for gluCEST imaging, given the proton exchange rate of the metabolite of interest. In contrast to the more widespread technique of APT imaging, accurate gluCEST imaging requires a high and constant B<sub>1</sub> power. B<sub>1</sub> strengths below approximately 1.25μT are insensitive to glutamate; they almost exclusively reflect differences in water and lipid properties (See **Figures 2.5** and 2.S2).

Another key advantage of simulations in this case is the ability to isolate individual terms from each other, which would be challenging, if not impossible, to do in phantom experiments. Our simulations contain six contributing “populations” or terms: bulk water, which is subject to direct saturation (DS); “bound” water, which has a very

short  $T_2$  and undergoes proton exchange with the bulk water (magnetization transfer, or MT); exchangeable protons on protein amides, creatine, and glutamate; and aliphatic protons from lipids and proteins, which exhibit NOE-type cross-relaxation with the bulk water protons (See **Table 2.S1** for simulation parameters.) Mathematically, our treatment of the supposed cross-relaxation is identical to the other terms representing true chemical proton exchange.

**Figure 2.1** provides an illustration of how each of these terms contributes to  $M_z/M_0 (B_1, \text{saturation})$  and how this function manifests itself in actual brain data. In **Figure 2.1A**, simulated values of  $M_z/M_0$  are shown as solid markers, in series according to the terms included in the simulation. The simulations – which themselves have ~40 potentially free parameters-- were then fit with **Equation [2.1]**. Specifically, the plot

**Figure 2.1. Origin and application of Equation 2.1:** Fitting Bloch-McConnell simulations and  $T_1$ -binned brain data with a simple parameterization of the function  $M_z/M_0 (B_1, \text{sat})$ . **A.** Simulated data (six pools, see Table S1 for list of parameters) fit with Equation 2.1. **B.** Data from human brain gathered by repeated acquisition of CEST at 3.0ppm at varying nominal  $B_1$ , binned by  $T_1$  value and fit with Equation 2.1.



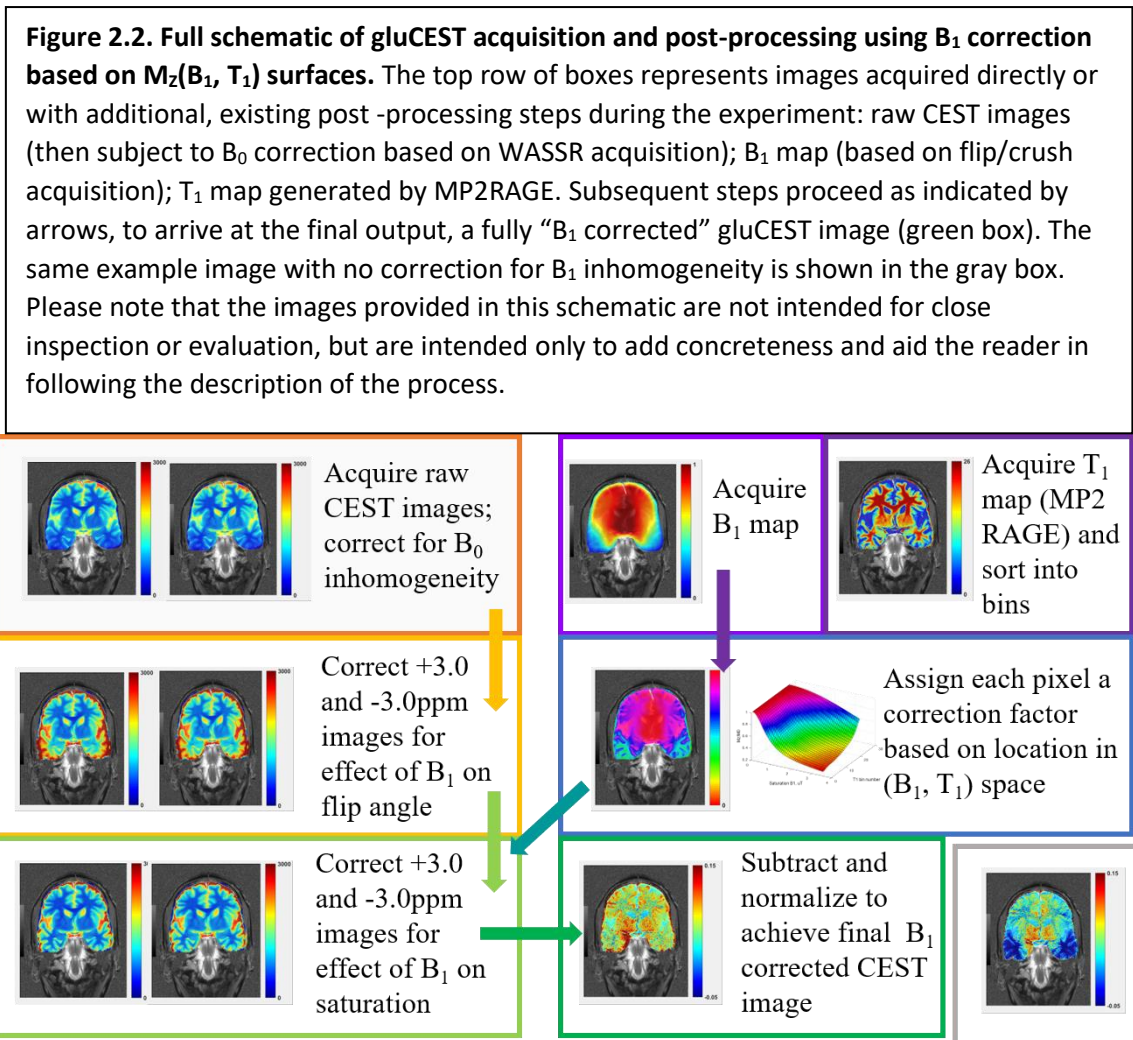


illustrates the relative shapes of bulk water direct saturation (DS) and bound water magnetization transfer (MT), as well as illustrating the effect of introducing the exchanging glutamate pool (gluCEST) in each case. We found that the three variables used to parameterize this surface vary smoothly with simulation parameters as well as with  $T_1$  bins (see Figure 2.S5), indicating that the  $T_1$  value does in fact reflect the physical parameters – bound water content, lipid content, etc. – determining the shape of this function.

Having identified this simple and robust expression for  $M_z/M_0(B_1, \text{saturation})$  using simulations, we proceeded to use this function to fit real ‘calibration’ data collected from human subjects. As explained above, this calibration data was used to generate surfaces (as in **Figure 2.1B**) over the dimensions  $\{B_1, T_1\}$  parameterized by  $\{\alpha, \beta\}$  of Equation 1 for both sides of the Z-spectrum which are relevant to the gluCEST measurement :  $\pm 3.0\text{ppm}$  relative to water. The shape of the individual functions  $M_z/M_0(B_1, T_1)$  comprising the surface shown in Figure 2.1B reflect the expected form based on simulation. Namely, very high  $T_1$  bins are those which contain a large partial volume of CSF, and the curve in this part of the surface resembles the simulation dominated by direct saturation (orange and yellow lines in Figure 2.1A). As  $T_1$  decreases, we move into the realms of gray and then white matter, which become increasingly dominated by contributions from bound water magnetization transfer (MT: green, blue, and purple lines in Figure 2.1A), and NOE. NOE is not included in the simulations shown in Figure 2.1A, and is not a major contributor to the data shown in Figure 2.1B, as this is the

positive offset (+3.0ppm) surface, while the center of the NOE contribution is on the other side of the water peak. GluCEST imaging data was then corrected for  $B_1$  inhomogeneity using these surfaces, as described above (see Methods) and outlined in **Figure 2.2**.

We evaluated the success of this approach by comparing its results with our previous method, identifying the limits of our ability to correct gluCEST images for low  $B_1$  amplitude, and comparing this performance with what might be expected from theory and simulation. **Figure 2.3** shows three examples of gluCEST images, comparing



the  $B_1$  post-processing correction described in this paper (final column, 4) with the previous method (second column, 2). The first row (A) shows a deep, oblique transverse slice which we often use for investigations of the hippocampus and neighboring areas in the medial temporal lobe. In this slice,  $B_1$  is high in the center of the brain but falls off

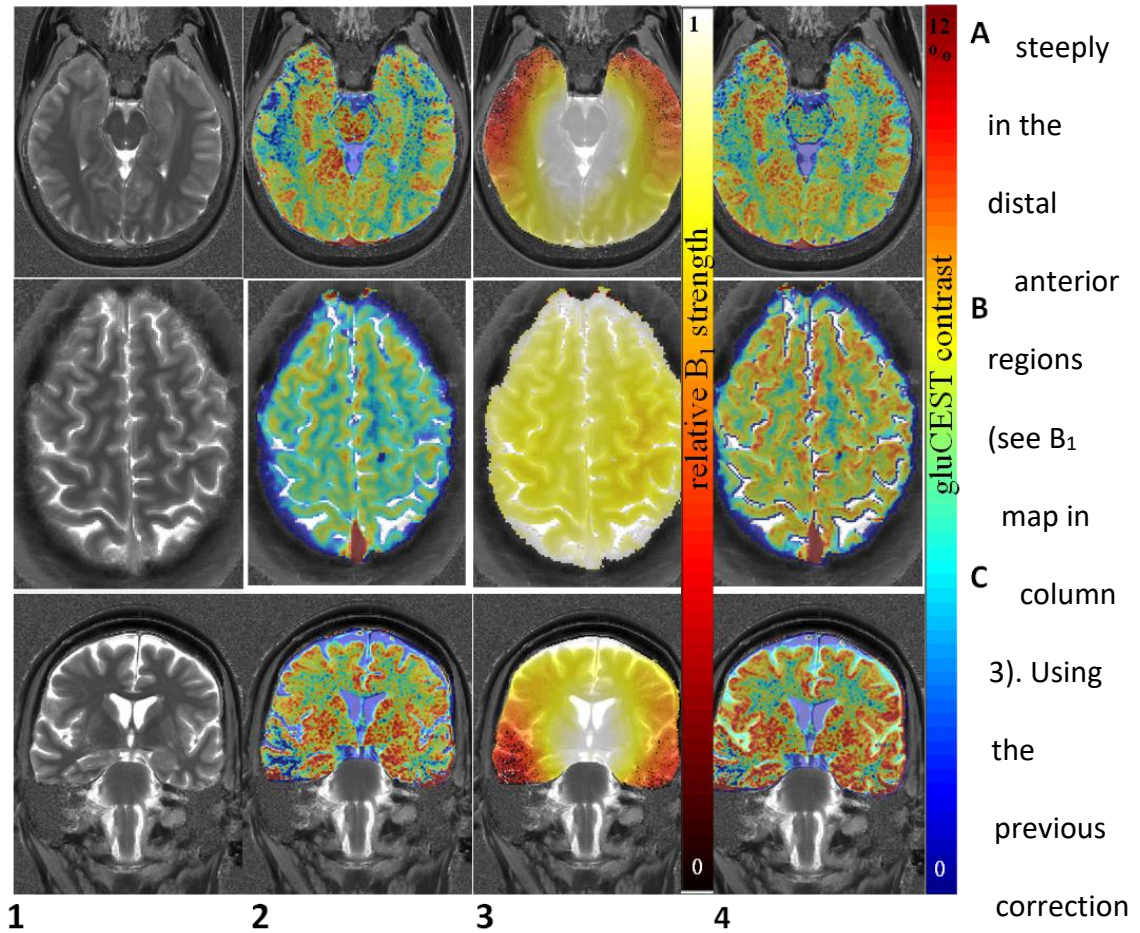


**Figure 2.3: Image comparison with previous correction method.** Each row of this figure corresponds to an image taken from a healthy control subject in various experiments. Top: lower axial slice from a 53-year old female (Example A). Middle: upper axial slice from 32-year-old male (Example B). Bottom: coronal slice from 74-year-old female (Example C). The first column from the left shows the T1 map (MP2RAGE), over which the other images are displayed with partial transparency in the subsequent columns. The second column shows the gluCEST map (filtered with a Gaussian filter of kernel size 2), as produced with the previously published  $B_1$  correction. The last column shows the gluCEST map as produced with the surface-based correction presented in this paper, while the third shows the relative  $B_1$  map. The scale for the gluCEST images (in 'jet') is 0-12%, negative-normalized asymmetry; for the  $B_1$  maps (in 'hot'), 0-100% of the nominal  $B_1$  RMS, 3.1uT.

method, signal loss is apparent in these regions, particularly on the left side. A similar problem is encountered when imaging this region of the brain in the coronal view (bottom row, C). Use of the new correction method yields similar results to the previous method for high  $B_1$  portions of the image, but “rescues” more of the low- $B_1$  portion

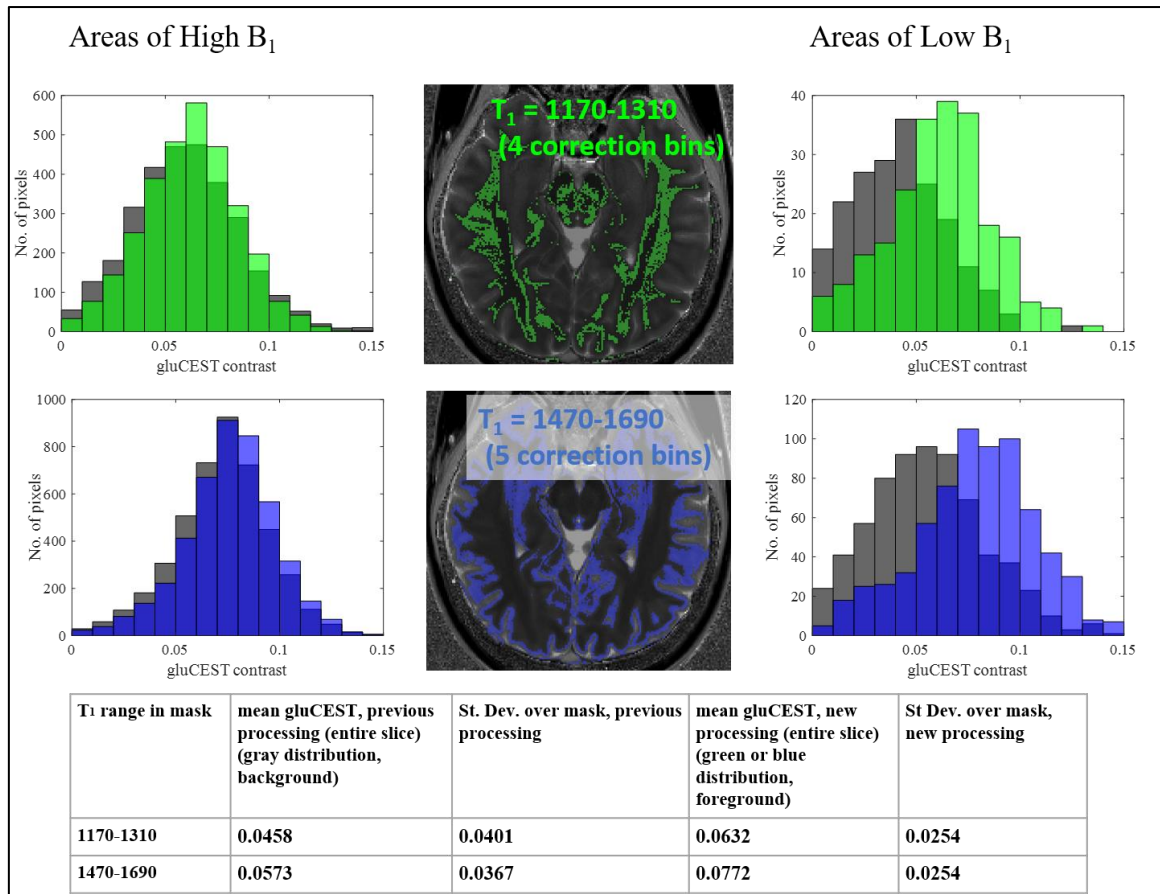


**Figure 2.4. Example histogram-based comparison of performance of ‘Old’ and ‘New’  $B_1$  correction methods in areas of high and low  $B_1$ .** Histograms show the distribution of gluCEST values for two different “zones” of the featured slice, as color coded in the center images. The  $T_1$  values corresponding to these zones are listed in the table, along with the mean and standard deviation of gluCEST values when calculated with the two different  $B_1$  corrections. The left half of the figure presents results from pixels where relative  $B_1 > 0.5$  (“High  $B_1$ ”), while the right half of the figure shows data where relative  $B_1 < 0.5$  (“Low  $B_1$ ”). Gray histogram bars in the background correspond to the distribution computed with the “old” processing method, colors, to “new”.

from extremely low CEST contrast. This result is demonstrated quantitatively in **Figure 2.4**.

The middle row (B) of **Figure 2.3**, featuring an upper axial slice, illustrates a somewhat different situation. Here, relative to the “old” image, the newly corrected image has higher gluCEST overall, and better contrast between different tissues. Inspection of the  $B_1$  map will show that in this slice,  $B_1$  tends to be uniform but somewhat low (70-80% of the nominal value). In this case, improvement in image quality can be mostly attributed to the finer binning of  $T_1$  masks. Pixels in the very center of white matter tracts do not have identical  $T_1$  values to pixels closer to gray matter, and gray matter pixels likewise have a gradient of intensity towards the periphery of the cortical tissue where partial voluming begins to occur with CSF. Ignoring this subtle but important gradient results in “smearing” of tissue contrast when correcting in the region of relative  $B_1 = 75-100\%$ , where the contrast ( $B_1$ ) function approaches linearity.

**Figure 2.4** provides histograms comparing the distribution of gluCEST values in selected tissue layers in the brain slice shown, illustrating that with the new correction, the low- $B_1$  and high- $B_1$  gluCEST distributions are much better reconciled. We attribute this improvement in very low- $B_1$  areas primarily to the fact that we are now correcting positive and negative sides of the Z-spectrum separately. The +3.0ppm and -3.0ppm images each have SNR sufficient to clearly distinguish brain structure in these regions; however, a subtraction of the two often does not. By correcting the images acquired on each side separately, we are retaining a greater portion of the CEST contrast that arises

from non-glutamate sources, which is needed to make these areas comparable to the rest of the image. **Figures 2.S7, A-C** provide additional histograms comparing the results of these two correction approaches.

The plot that forms the background of **Figure 2.5** illustrates simulated CEST contrast upon saturation at 3.0ppm for conditions emulating human brain tissue. Varying glutamate concentration gives rise to increasing variation in measured contrast as  $B_1$  power increases within the plotted range, which reflects the allowable  $B_1$  power in the 7T headcoil. These simulations suggest that  $B_1$  strengths below approximately 1.25 $\mu$ T are insensitive to glutamate, and almost exclusively reflect differences in water and lipid properties. Thus, one should expect that below a certain  $B_1$  power, no post-processing correction is able to restore contrast to a gluCEST image, as the contrast simply has not been adequately created by the saturation pulse.



Our results upon acquiring and correcting a series of gluCEST images at varying nominal saturation  $B_1$  power indeed reflect this (**Figure 2.5**, inlaid images and histograms). In the images shown in Figure 2.5, gluCEST at 3.0ppm was purposely collected at lower nominal  $B_1$ , similar to the procedure for acquiring calibration data. In each case, we performed correction of the image as if it had been acquired with the optimal  $B_1$  of 3.1 $\mu$ T, in order to understand the limits of the correction strategy. Above

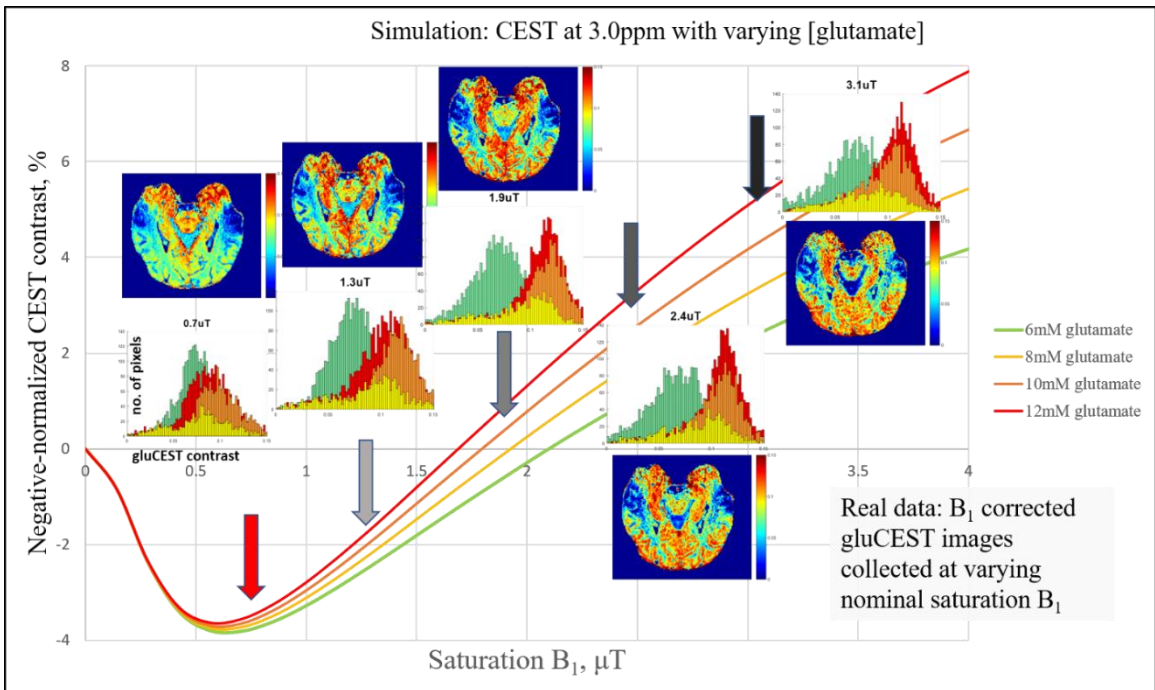


**Figure 2.5. Evaluation of  $M_2(B_1, T_1)$  surface-based correction for varying  $B_1$  strength; comparison with simulation.** Background: simulation of CEST contrast at 3.0ppm in white-matter-like physical conditions, with varying glutamate concentration. Foreground: GluCEST images collected at purposefully varying nominal saturation  $B_1$  {0.7, 1.3, 1.9, 2.4 and 3.1  $\mu$ T}, with attempted correction for  $B_1$  inhomogeneity. Colored distribution in histograms correspond to four different tissue layers (combinations of 4-5 of the  $T_1$  bins used for correction). It is clear that contrast between these layers is insufficient when nominal  $B_1$  is only 0.7 $\mu$ T, despite attempted correction. Simulations indicate that this is the expected result, as dynamic contrast resulting from variable [glutamate] is vanishing at this  $B_1$  power. The correction performs reasonably well for areas where absolute  $B_1 > \sim 1.25\mu$ T, provided that the flip angle in this region is sufficient for the acquisition module

the red arrow are shown an image and corresponding histogram of gluCEST values

collected at a nominal saturation  $B_1$  of  $0.7\mu\text{T}$ . It is clear both from visual inspection of this image as well as the corresponding histogram that contrast which might otherwise exist in this image has been irrecoverably forfeited by lack of saturation power. This result corresponds to the simulated situation indicated by the red arrow, in which varying concentrations of glutamate do not yet give rise to variations in CEST contrast at  $3.0\text{ppm}$ . Note that in this plot, the varying glutamate concentrations have been simulated in "tissue" that has otherwise identical properties. If these properties -- such as bound water or lipid content -- are changed, the location of the local minimum of this CEST ( $B_1$ ) curve changes. This corresponds to the residual tissue contrast visible in this low- $B_1$  image. As might further be expected from simulation, images and corresponding histograms collected at saturation  $B_1$  powers of  $1.3$ ,  $1.9$ ,  $2.4$  and  $3\mu\text{T}$  -- show good agreement upon  $B_1$  correction, with the  $1.3\mu\text{T}$  image still lacking some of the contrast which arises at higher powers.

One will note that, with the current approach, large "blue" patches of very low CEST signal remain in parts of these images despite apparently successful correction for saturation  $B_1$ . This signal loss actually originates from low flip angle during the acquisition module, rather than insufficient saturation (see Figure 2.S6 for further explanation). No matter what the nominal saturation  $B_1$ , the head coil used produces a non-trivial flip angle deficit in these regions, which our current correction approach does not adequately handle. We are exploring hardware, pulse sequence and post-processing methods to address this issue, which is beyond the scope of this report.



## 2.6 Discussion

In this paper, we've presented a new way to correct for  $B_1$  inhomogeneity in gluCEST measurements in the brain based on categorization of pixels by  $T_1$  value and a simple function describing the response of their saturated signal,  $M_z$ , to variation in  $B_1$  strength. Our description of this function is based on the results of Bloch-McConnell simulations and fitting to calibration data gathered in three volunteers, with additional subject scans used for evaluation of the new approach.

Perhaps the most direct precedent in the literature for this type of correction is that of Windschuh et al, 2015<sup>20</sup> who used various functional forms to fit the  $B_1$ -dependence of Z-spectrum components at  $\pm 3.5$  ppm in order to correct the APT CEST signal for  $B_1$  inhomogeneity. By using only three CEST acquisitions per subject at various  $B_1$ , they were able to achieve high quality images in the upper axial slice shown in their figures. We acknowledge that a pixel-by-pixel fitting for each subject is, time permitting, an optimal solution. However, for gluCEST imaging, the nominal  $B_1$  power is about three-fold higher than for APT CEST, and thus the absolute spread of  $B_1$  power over the field of view is commensurably enlarged. The pixel-wise fitting we performed to generate the calibration data presented here did not work well with fewer than five input points, suggesting that a method for gluCEST analogous to that used for APT CEST in [20] would require five, rather than 2-3,  $B_1$  acquisitions in order to achieve acceptable results. In most experimental cases, due to scan time constraints on patients,

circumstances strongly favor acquiring as few CEST acquisitions as possible. Thus, our approach retains the possibility of acquiring only one.

While our group has not yet attempted to use parallel transmit in CEST measurements, the capacities of PTX have been explored and documented by others (see refs. [10-12]). As mentioned above, the ‘problem that was solved’ by PTX – and what is indeed relevant for many imaging applications, including lower-power CEST modalities – is homogeneity of  $B_1$  over the field of view. But homogeneity *per se* is not the main challenge with respect to gluCEST; rather, the challenge is to have sufficiently high  $B_1$  in absolute terms. In a gluCEST experiment, one would rather have a higher degree of inhomogeneity – which can be corrected for-- with as much of the image as possible at a higher saturation power. The limiting factor with regard to  $B_1$  is SAR, and implementation of PTX does not overcome this.

We have, on the other hand, explored the use of high-dielectric padding to mitigate the  $B_1$  drop-off. The effects of these pads is certainly beneficial, but by no means obviates the need for post-processing correction; rather, the effect is simply to move a greater fraction of the image into the regime for which we believe that this correction is valid. At the time of this study, institutional approval for use of this padding was limited, but they will be incorporated in future studies.

The authors of [20] also point out correctly that a calibration-based approach cannot be assumed applicable in a disease state, where the composition of brain tissue is unknown. For these cases, we are currently taking an intermediate approach: gluCEST

is acquired at 2-3  $B_1$  points, and these data are mapped to existing correction surface "libraries" using a quantitative similarity metric. Further work in this direction is in progress.

To this end, another tactic we are exploring for accurate gluCEST imaging, particularly in pathological cases, is multi-dimensional pixel classification: instead of binning only by  $T_1$  values as in the present paper, pixels can be sorted using additional information gathered from scans which are already included in the clinical protocol, such as the several types of contrast returned by a multi-echo MP2RAGE sequence<sup>21</sup>. This information can serve as a "prior" from which, like in the present case with  $T_1$  bins, certain assumptions about lipid and bound water contributions can be made more safely. It is worth noting that in the present strategy the choice of any precise number of  $T_1$  bins is somewhat arbitrary; however, the general approach of using a number of  $T_1$  bins in this neighborhood ( 20+ ) is based on quantitative evaluation of fit performance. **Figure 2.S4B** explores the dependence of the goodness of fit of Equation 1 to experimental data as an increasing number of  $T_1$  bins are used.

While the proposed method improved results upon the previous method in almost all cases, we also came to notice that gluCEST images give more reasonable results when the correction surface applied was generated by fitting data from subjects of roughly the same age group ( $\pm 10$  years) as the experimental subject. This

observation was presented recently<sup>22</sup> and will be elaborated in more detail in future work.

Despite these advances, it is important to note the inherent limitations of correcting any CEST measurements – and particularly measurements of fast exchangers like glutamate-- for areas of low saturation  $B_1$ . With proper calibration factors in hand, it is always possible to correct the signal back towards a value that appears reasonable for a particular tissue type. However, theory tells, and simulations demonstrate, that at very low saturation  $B_1$  values ( $< \sim 1\mu\text{T}$ ) CEST contrast at 3.0 ppm is only weakly dependent on glutamate concentration. Therefore, for any particular experimental and tissue parameters, there will be a saturation  $B_1$  limit below which calculated CEST contrast between two pixels is predominantly due to tissue structural properties (lipids, bound water). We emphasize that for gluCEST measurements it is advisable to use as high of a nominal  $B_1$  as possible to ensure that all parts of the CEST images are acquired in a regime in which post-processing  $B_1$  correction is capable of yielding a valid quantification.

## **Conclusions**

Using a phenomenological equation, Bloch-McConnell simulations, and experiments on healthy subjects at 7T, we demonstrated an improved  $B_1$  correction approach for gluCEST imaging of the human brain. This method improves contrast and quantitative accuracy upon our previous  $B_1$  correction, making a larger difference in lower  $B_1$  areas.

This method takes into account the subtle  $T_1$  differences between pixels and retains more of the SNR of the original, pre-correction measurement, decreasing the noise in the resulting image. While this method is demonstrated in the context of gluCEST, the same general strategy for determining accurate phenomenological correction functions is expected to apply to CEST imaging of other metabolites in the brain such as creatine<sup>23</sup>, myo-inositol<sup>24</sup>, lactate<sup>25</sup> and sugars<sup>26</sup>.

## 2.7 Supplementary Information

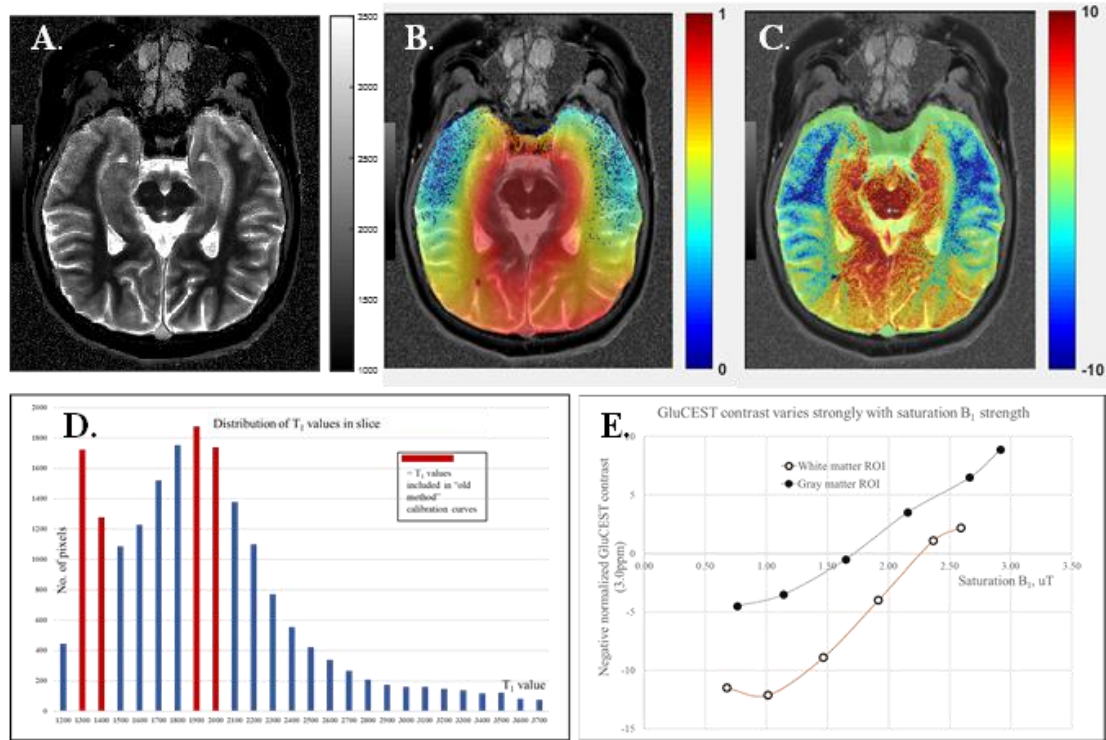


**Figure 2.S1. Introduction to the problem of correcting GluCEST for B<sub>1</sub> inhomogeneity.** **A.** T<sub>1</sub> map (MP2RAGE) of an oblique axial slice of interest in several research protocols. **B.** Map of typical B<sub>1</sub> strength over this slice, relative to a nominal B<sub>1</sub> of 3.1 μT. Color bar shows B<sub>1</sub> strength relative to the nominal value. **C.** GluCEST map over the slice, uncorrected for B<sub>1</sub> inhomogeneity. Color bar scale is -10-10% asymmetry. **D.** Histogram of T<sub>1</sub> values over this slice. Red bars indicate the only T<sub>1</sub> ranges taken into account in the former correction method. **E.** Example of CEST contrast as a function of saturation B<sub>1</sub> in ROIs visually identified as “gray matter” or “white matter”. Such hand-drawn ROIs were previously fitted with third-order polynomials which were then used to correct all pixels that fell within a range defined by a binary (gray/white) segmentation. The line segment connecting the points in this plot is a visual aid only, and not does represent any form of fit.

**Table 2.S1. Simulation parameters, unless otherwise noted**

Parameter description	Value (s)
<b>General parameters</b>	
Pulse shape	Hamming window
Pulse duration	800ms
B <sub>1</sub> strength	
Pulse offset, w/reference to water resonance	3.0ppm
Pulse duty cycle	99.8%
Total water concentration	70 - 90 M
<b>Pool 1: Bulk water</b>	
Concentration [2 * H <sub>2</sub> O, bulk]	50 – 80 M
T <sub>1</sub>	1.7s
T <sub>2</sub>	80 – 90 ms
Chemical shift offset	0ppm
<b>Pool 2: Bound water</b>	
Concentration [2 * H <sub>2</sub> O, bound]	10 - 20 M
T <sub>1</sub>	1s
T <sub>2</sub>	2e-5s (20us)
Chemical shift offset	-2.4ppm
Exchange rate with bulk water	20Hz
<b>Pool 3: Protein amides</b>	
Concentration [ <sup>1</sup> H, APT]	70mM
T <sub>1</sub>	1s
T <sub>2</sub>	1ms
Chemical shift offset	3.5ppm
Exchange rate with bulk water	30Hz
<b>Pool 4: NOE-active protons (lipids, etc.)</b>	
Concentration [ <sup>1</sup> H, NOE]	1 - 5 M
T <sub>1</sub>	1s
T <sub>2</sub>	0.5 – 1ms
Chemical shift offset	-3.4ppm
Cross-relaxation rate with bulk water	1 – 5 Hz
<b>Pool 5: Creatine</b>	
Concentration [ <sup>1</sup> H, Cr]	32mM
T <sub>1</sub>	1

T <sub>2</sub>	10ms
Chemical shift offset	1.8ppm
Exchange rate with bulk water	800Hz
<b>Pool 6: Glutamate</b>	
Concentration [ <sup>1</sup> H, Glu]	15-36mM
T <sub>1</sub>	1s
T <sub>2</sub>	10ms
Chemical shift offset	3.0ppm
Exchange rate with bulk water	1800Hz

### **Bibliography, Simulation Parameters:**

1. Zhou J, Payen JF, Wilson DA, Traystman RJ, Van Zijl PCM. Using the amide proton signals of intracellular proteins and peptides to detect pH effects in MRI. *Nature Medicine*. August 2003;9(8):1085-1090.
2. Zhou J, Wilson DA, Sun PZ, Klaus JA, Van Zijl PCM. Quantitative Description of Proton Exchange Processes between Water and Endogenous and Exogenous Agents for WEX, CEST, and APT Experiments. *Magnetic Resonance in Medicine*. May 2004;51(5):945-952.
3. Van Zijl PCM, Yadav NN. Chemical exchange saturation transfer (CEST): What is in a name and what isn't? *Magnetic Resonance in Medicine*. April 2011;65(4):927-948.
4. Sled JG, Pike GB. *Quantitative Imaging of Magnetization Transfer Exchange and Relaxation Properties In Vivo Using MRI* 2001.
5. Mougin OE, Coxon RC, Pitiot A, Gowland PA. Magnetization transfer phenomenon in the human brain at 7 T. *NeuroImage*. January 2010;49(1):272-281.
6. Hua J, Jones CK, Blakeley J, Smith SA, Van Zijl PCM, Zhou J. Quantitative description of the asymmetry in magnetization transfer effects around the water resonance in the human brain. *Magnetic Resonance in Medicine*. October 2007;58(4):786-793.



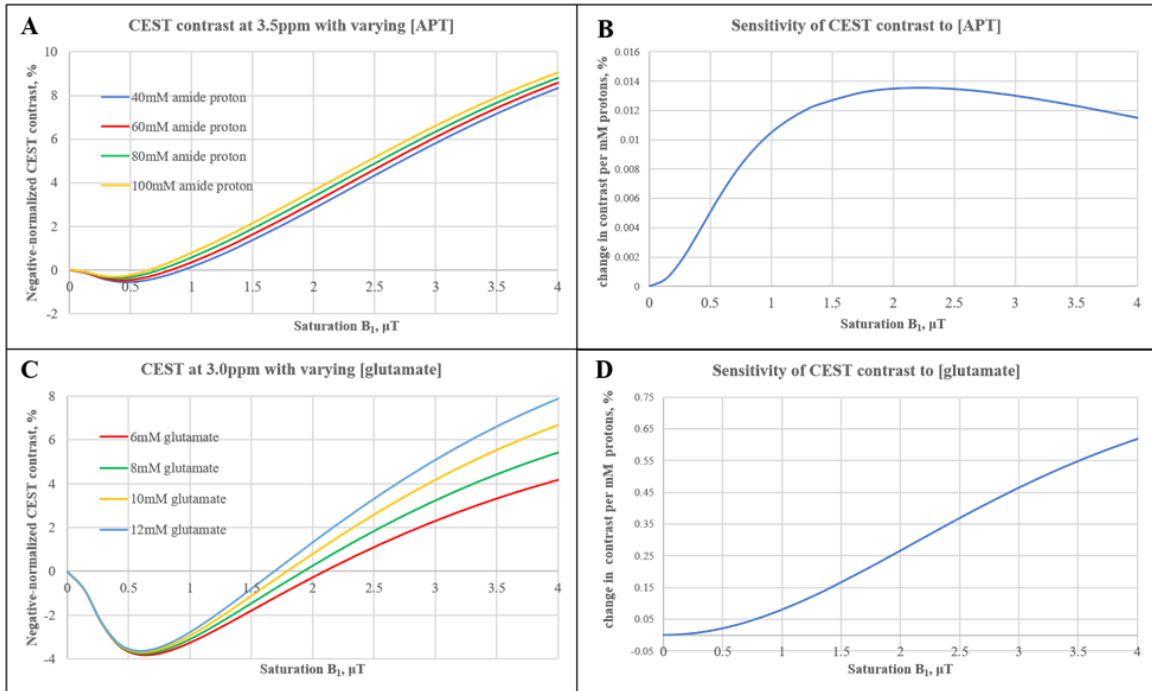


**Figure 2.S2. Simulations of contrast as a function of saturation  $B_1$ , comparing gluCEST and APT CEST.** Simulations illustrate that, in contrast to the more widespread technique of APT imaging, accurate gluCEST imaging requires a high and constant  $B_1$  power. Figure A shows the simulated CEST contrast from saturation at 3.5ppm as a function of  $B_1$  strength for different concentrations of amide protons. The plot illustrates that CEST at 3.5ppm will comparably detect differences in [APT] for a broad range of  $B_1$  power, starting at around 0.7 $\mu\text{T}$ . This sensitivity is quantified in Figure B, where the slope of the difference in CEST signal from two concentrations is plotted against the  $B_1$  power used. The slope is relatively stable from 1-4  $\mu\text{T}$ , meaning that experiments done anywhere within this range and corrected linearly (or even not at all) for  $B_1$  inhomogeneity can be expected to generate consistent results. Figure C shows the CEST contrast at 3.0ppm (gluCEST) and illustrates its ability to detect differences in the concentration of glutamate. In sharp contrast to APT CEST measurements,  $B_1$  strengths below approximately 1.5 $\mu\text{T}$  are insensitive to glutamate; they almost exclusively reflect differences in water and lipid properties. Figure D illustrates that optimal gluCEST contrast is actually achieved with the highest possible  $B_1$ . (We have been unable to use  $B_1$  stronger than  $\sim 3.5\mu\text{T}$  in human experiments, due to SAR limitations.)

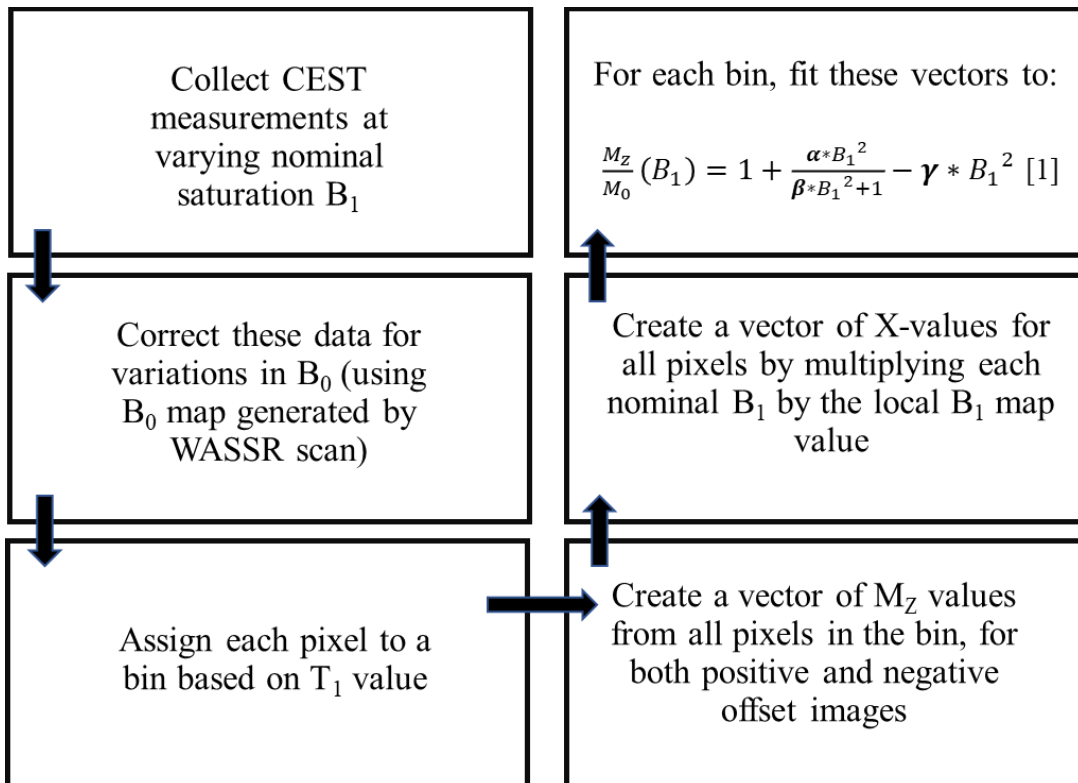


**Figure 2.S3. Schematic: generating  $M_z(B_1, T_1)$  correction surfaces from calibration data.**

For each set of calibration data, CEST images at 4-6 nominal saturation  $B_1$  values were acquired, as well as WASSR images,  $B_1$  maps,  $T_1$  maps, and reference (no saturation) images. Each pixel within the brain ROI was sorted into one of 26 bins based on its  $T_1$  value. After  $B_0$  correction, pixels in a particular mask were then fit to Equation 1 for both the positive and negative offset data. This results in two separate "Correction Surfaces", one for positive and one for negative saturation offset, for  $M_z$  as a function of  $B_1$  strength and  $T_1$  value, parameterized by three parameters--  $\alpha$ ,  $\beta$ ,  $\gamma$  -- for each  $T_1$  bin.

**Tables 2.S2, A-E. Tables relating to fitting and generation of correction surfaces**

**A.** Initial values and parameter bounds used for fitting simulated data:

Parameter	Initial value	Lower Bound	Upper Bound
$\alpha$	1	-1000	1000
$\beta$	1	0	1000
$\gamma$	0	-1000	1000
$M_0$	1	-1000	10,000

**B.** For fitting experimental data, first iteration (all parameters free):

Parameter	Initial value	Lower Bound	Upper Bound
$\alpha$	-2.25e-5	-1e-3	1
$\beta$	1.85e-5	1e-7	1
$\gamma$	8e-7	-1	1e-5
$M_0$	2000 (Based on experimental $M_0$ image intensity)	-100	10,000

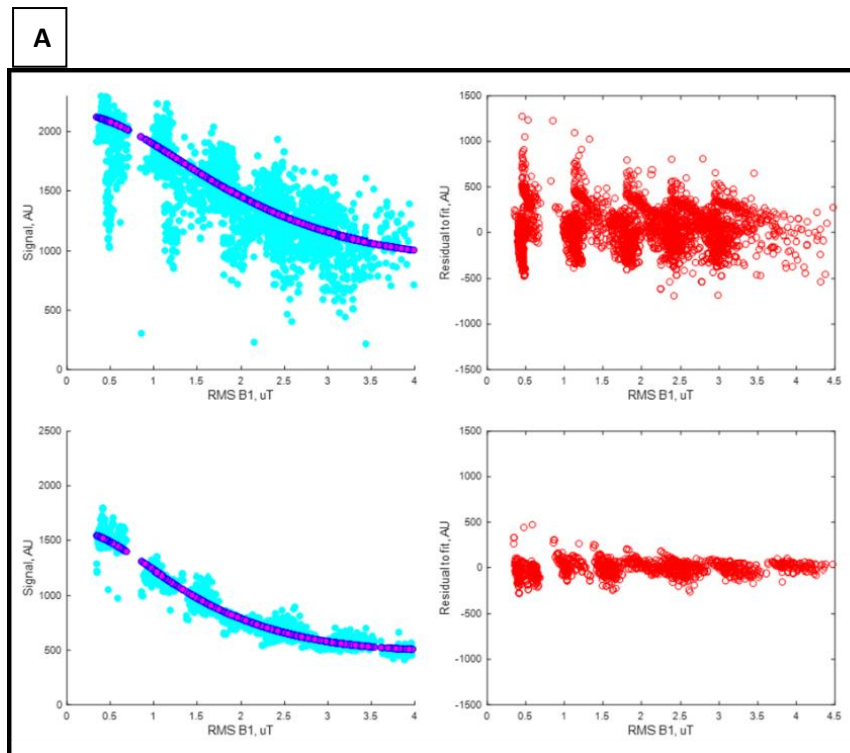
**C.** For fitting experimental data, second iteration (parameter D and E fixed):

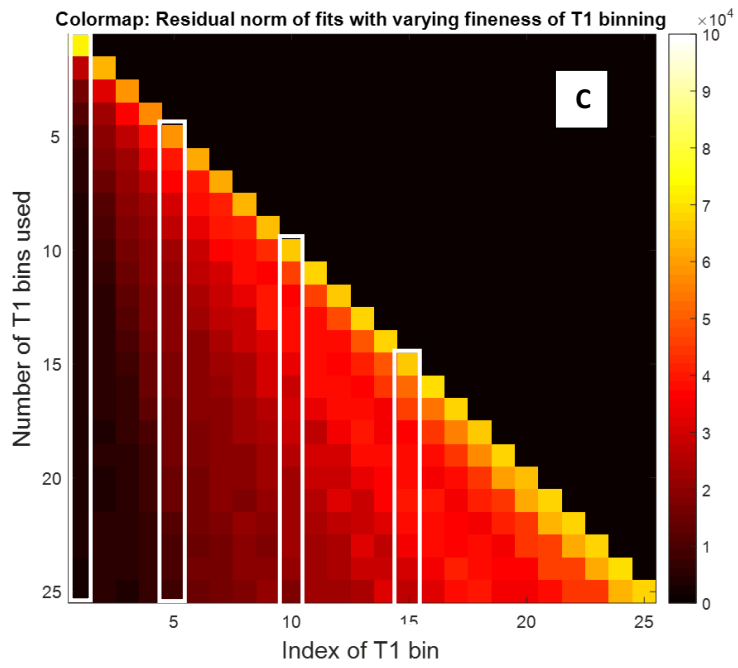
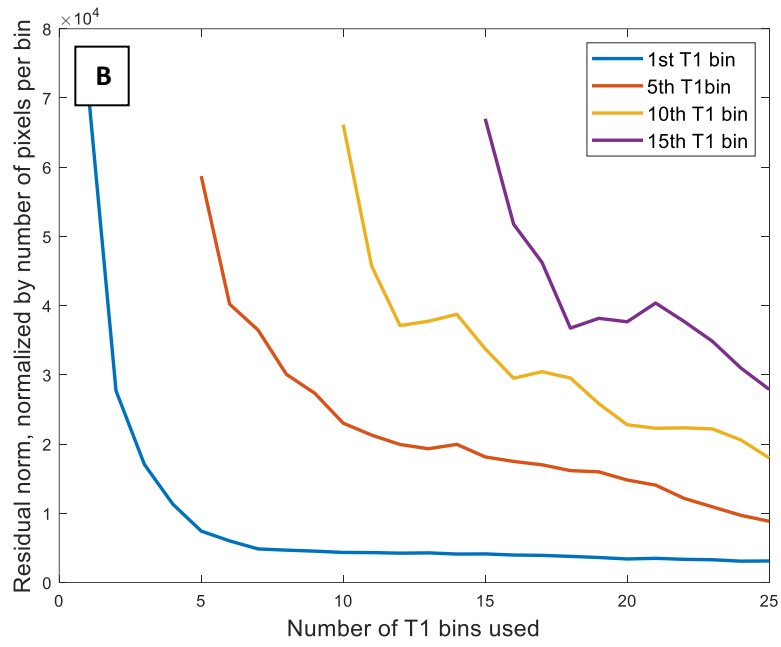
Parameter	Initial value	Lower Bound	Upper Bound
$\alpha$	-2.25e-5	-1e-3	1
$\beta$	1.85e-5	1e-7	1
$\gamma$	6e-7	<i>same as initial value</i>	<i>same as initial value</i>
$M_0$	<i>variable</i>	<i>same as initial value</i>	<i>same as initial value</i>

**D.** Data was fit using the Matlab function *lsqcurvefit()* with the trust-region-reflective algorithm. The following options were changed from the default:

Option	Value for fitting simulations	Value for fitting experiment
Function tolerance	1e-18	1e-12
Step tolerance	1e-12	1e-12
Max. function evaluations	10,000	1,000
Max. iterations	10,000	10,000

**Figure 2.S4:** Fitting performance of Equation 1 and dependence on number of  $T_1$  bins **A**. Example fits with residuals from two  $T_1$  bins. **B, C.** Dependence of fitting performance on number of  $T_1$  bins. To generate these plots, the following was done in an iterative fashion, for  $N = 1-25$ : calibration data was sorted into  $N$  number of  $T_1$  bins, and fit to Equation 1 (analogous to examples in Figure A). The residual norms were divided by the number of pixels in the resulting bins, so that this function is not convolved with  $y = 1/x$ . It can be seen that in fact, Equation 1 works best for tissue with low  $T_1$  (white matter), intermediately well for gray matter, and least for tissue with very high  $T_1$  (always included in the highest  $T_1$  bin per iteration), indicating high partial voluming of CSF. The white outlines in the colormap indicate the traces which are plotted in B.

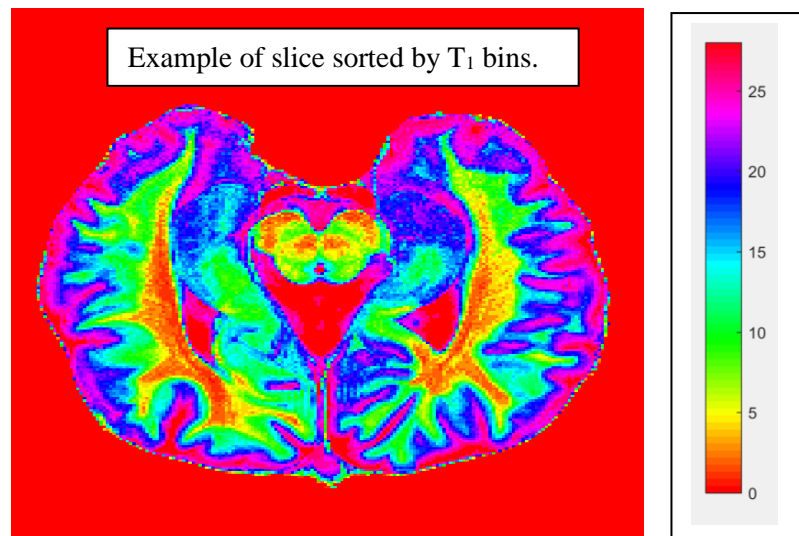




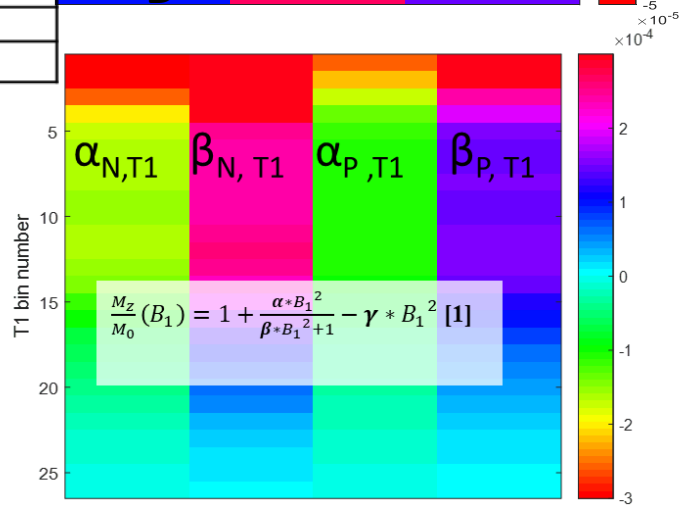
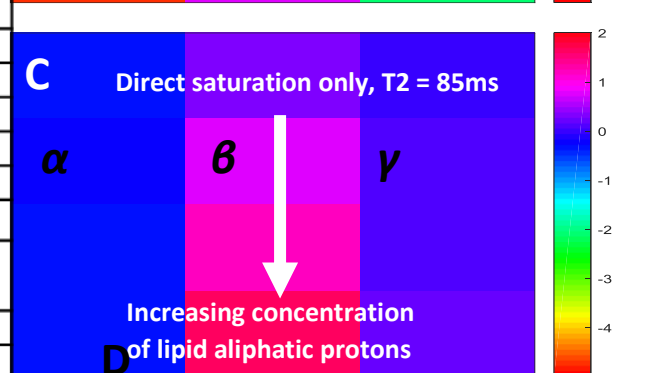
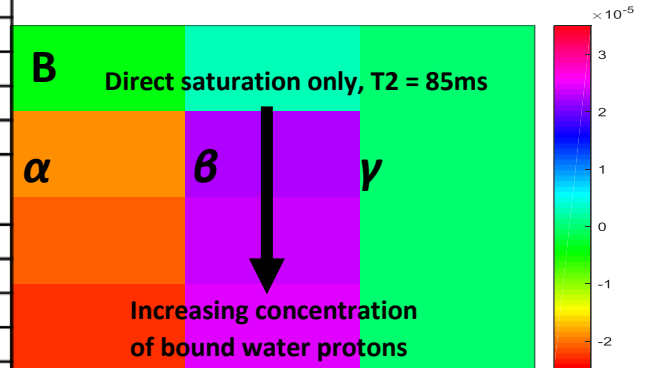
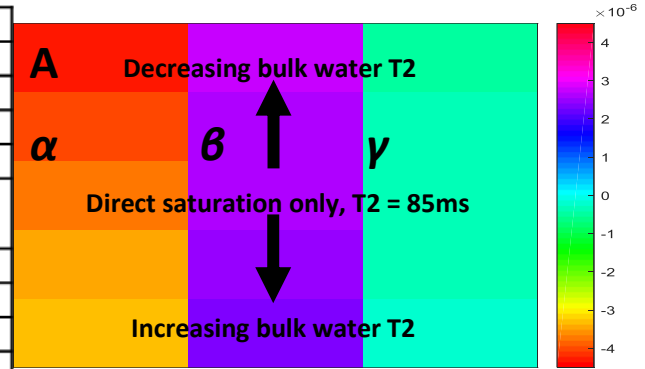
E. Fitting parameters for weighted-average-derived correction surface, smoothed

	$T_1$		$\alpha_N$	$\alpha_P$	$\beta_N$	$\beta_P$	$\gamma_N$	$\gamma_P$	$M_0$
Bin no.	LB	UB	1e-3*	1e-3*	1e-3*	1e-3*	1e-4*	1e-4*	
1	1001	1062	-0.3846	-0.2791	0.5407	0.3736	0.006	0.006	1
2	1062	1104	-0.3137	-0.2214	0.4487	0.2991	0.006	0.006	1
3	1104	1138	-0.2557	-0.1763	0.371	0.2389	0.006	0.006	1
4	1138	1171	-0.2052	-0.1389	0.301	0.1877	0.006	0.006	1
5	1171	1204	-0.1619	-0.1092	0.2408	0.147	0.006	0.006	1
6	1204	1238	-0.1462	-0.1007	0.2165	0.1341	0.006	0.006	1
7	1238	1274	-0.1346	-0.0943	0.2001	0.1254	0.006	0.006	1
8	1274	1311	-0.1173	-0.0838	0.1755	0.1111	0.006	0.006	1
9	1311	1350	-0.1001	-0.0732	0.1506	0.0964	0.006	0.006	1
10	1350	1391	-0.0851	-0.0636	0.1286	0.0833	0.006	0.006	1
11	1391	1433	-0.0738	-0.0571	0.112	0.0744	0.006	0.006	1
12	1433	1473	-0.0639	-0.0508	0.0972	0.0659	0.006	0.006	1
13	1473	1517	-0.0569	-0.0467	0.0871	0.0605	0.006	0.006	1
14	1517	1561	-0.0515	-0.043	0.0792	0.0558	0.006	0.006	1
15	1561	1605	-0.0475	-0.0403	0.0738	0.0526	0.006	0.006	1
16	1605	1648	-0.0437	-0.0376	0.0685	0.0492	0.006	0.006	1
17	1648	1694	-0.0391	-0.0342	0.0612	0.0443	0.006	0.006	1
18	1694	1742	-0.0346	-0.0306	0.0539	0.0391	0.006	0.006	1
19	1742	1796	-0.0306	-0.0275	0.0477	0.0348	0.006	0.006	1
20	1796	1852	-0.0259	-0.0239	0.04	0.0296	0.006	0.006	1
21	1852	1914	-0.0218	-0.0206	0.0331	0.0246	0.006	0.006	1
22	1914	1987	-0.0179	-0.0174	0.027	0.0204	0.006	0.006	1
23	1987	2078	-0.0136	-0.0138	0.0202	0.0154	0.006	0.006	1
24	2078	2200	-0.0095	-0.0102	0.0143	0.0111	0.006	0.006	1
25	2200	2408	-0.0067	-0.0076	0.0101	0.0079	0.006	0.006	1
26	2408	2999	-0.0043	-0.0053	0.005	0.0042	0.006	0.006	1

**Figure 2.S5. (next page) Fitting parameters vary smoothly with both simulated (A-C) physical parameters and with real  $T_1$  values (D).** **A** represents the value of the three fitting parameters  $\{\alpha, \beta, \gamma\}$  in five series of simulations as a colormap. In these simulations, only the direct saturation of water is simulated, and the  $T_2$  of this bulk water is varied. This variation is clearly captured in parameters  $\alpha$  and  $\beta$  of Equation [1]. **B** shows an analogous series of simulations, but rather than altering the  $T_2$  of bulk water, the changing variable is the presence of bound water (responsible for the 'MT' effect), which is being introduced increasingly from top to bottom rows. Again, we see that this change is captured by the values of parameters  $\alpha$  and  $\beta$ . **C** again begins with the 'direct saturation only' case and introduces the pool of slow "exchanging" protons which we attributed to cross-relaxation from lipids or similar aliphatic protons. Interestingly, this effect is captured overwhelmingly by parameter  $\beta$ . **D** represents the parameters values displayed in Table 2E visually as an analogous colormap ( $\alpha_N, \beta_N$  parameterize the negative offset surface;  $\alpha_p, \beta_p$ , the positive offset surface).



Parameter description
<b>General parameters</b>
Pulse shape
Pulse duration
B <sub>1</sub> strength
Pulse offset, w/reference to water resonance
Pulse duty cycle
Total water concentration
<b>Pool 1: Bulk water</b>
Concentration [2 * H <sub>2</sub> O, bulk]
T <sub>1</sub>
<b>T<sub>2</sub> (varying in Figure A)</b>
Chemical shift offset
<b>Pool 2: Bound water</b>
Concentration [2 * H <sub>2</sub> O, bound] (varying in Figure B)
T <sub>1</sub>
T <sub>2</sub>
Chemical shift offset
Exchange rate with bulk water
<b>Pool 3: Protein amides</b>
Concentration [ <sup>1</sup> H, APT]
T <sub>1</sub>
T <sub>2</sub>
Chemical shift offset
Exchange rate with bulk water
<b>Pool 4: NOE-active protons (lipids, etc.)</b>
Concentration [ <sup>1</sup> H, NOE] (varying in Figure C)
T <sub>1</sub>
T <sub>2</sub>
Chemical shift offset
Cross-relaxation rate with bulk water





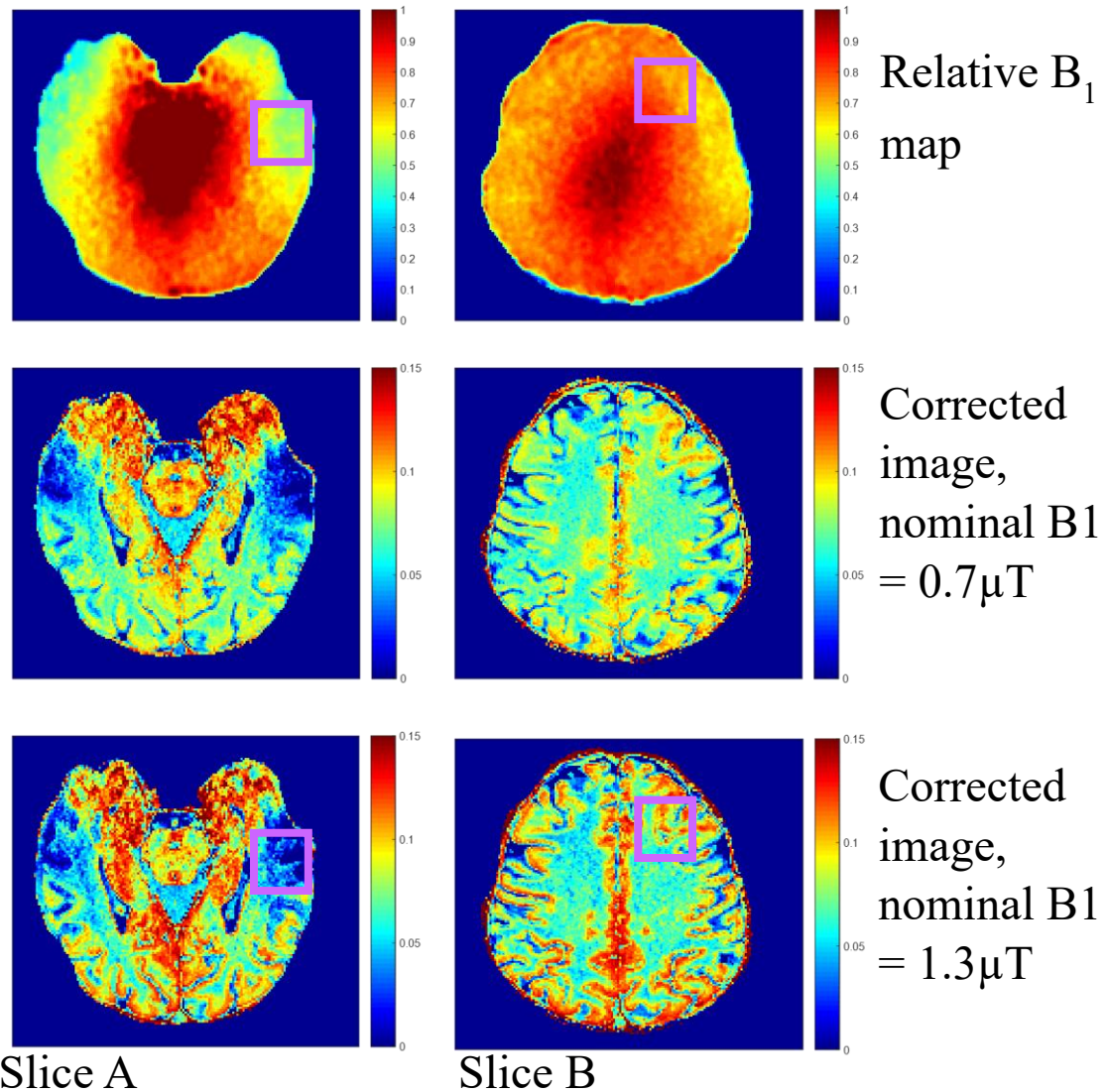


**Figure 2.S6: Comparison of surface-based  $B_1$  correction on different slices indicates that limiting factor is flip angle  $B_1$ , rather than saturation  $B_1$  power.**

One will note that from Figure 5 of the main text that large "blue" patches of very low CEST signal remain in slice A despite apparently successful correction for saturation  $B_1$  in terms of reconciling images generated by lower  $B_1$  and higher  $B_1$  acquisitions. This signal loss actually originates from low flip angle during the acquisition module, rather than insufficient saturation. This is clear upon more careful consideration of the presented results: At  $3\mu\text{T}$ , even areas where relative  $B_1$  is, for example, 0.5, have an absolute  $B_1$  amplitude of  $1.5\mu\text{T}$ . This approximately corresponds to areas of the  $1.9\mu\text{T}$  image where relative  $B_1$  is 0.8. We see that in these regions, gluCEST contrast can be well restored with our correction for saturation  $B_1$ . Thus, it is not a saturation  $B_1$  amplitude of  $1.5\mu\text{T}$  which is causing the lack of signal in the "blue" regions of the  $3\mu\text{T}$  image, but rather the fact that no matter what the nominal saturation  $B_1$ , the head coil used produces a non-trivial flip angle deficit in these regions, which our current correction approach does not adequately handle. We are exploring hardware, pulse sequence and post-processing methods to address this issue, which is beyond the scope of this report. This can also be observed by comparing the success of correcting Slices A and B, which have very different relative  $B_1$  distributions.

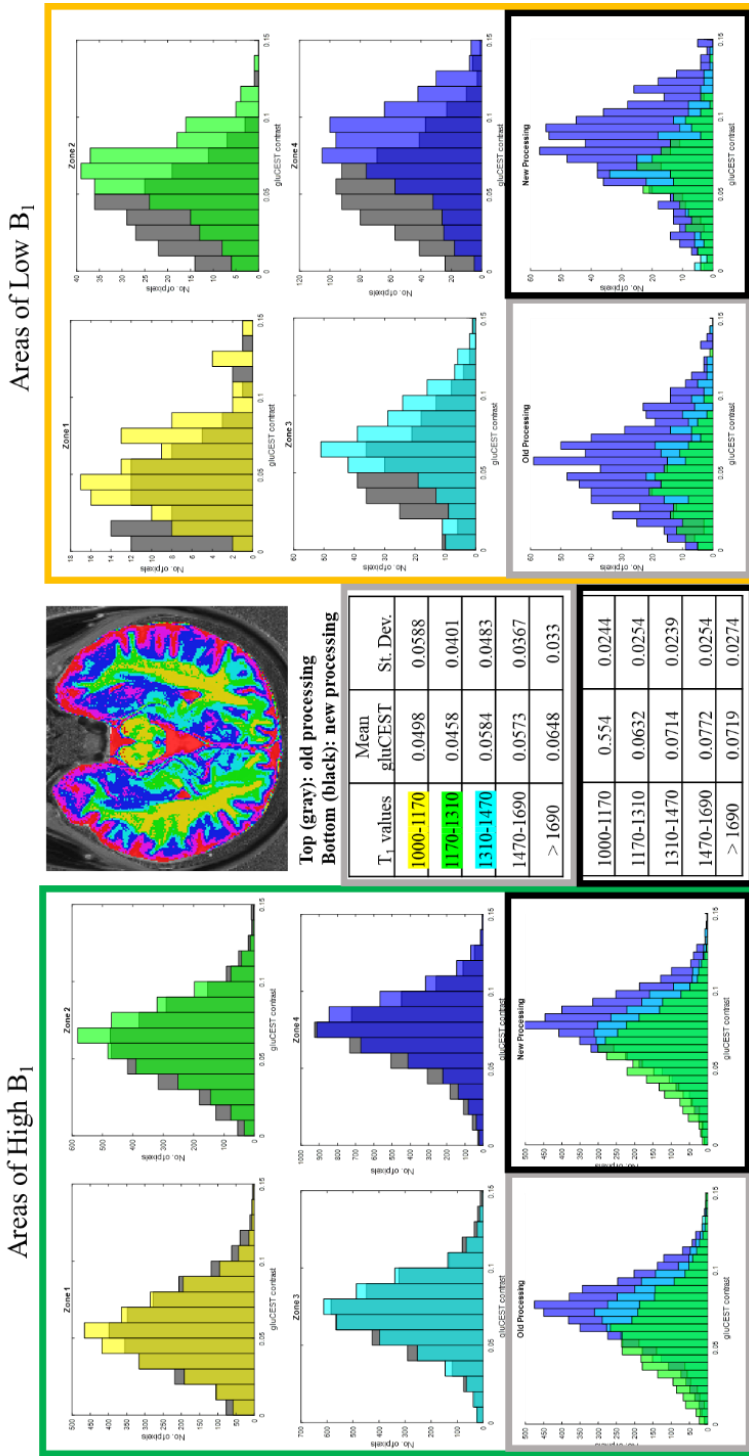
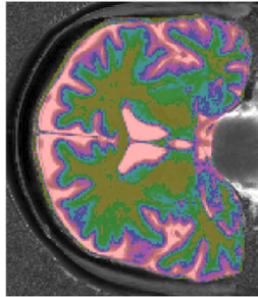
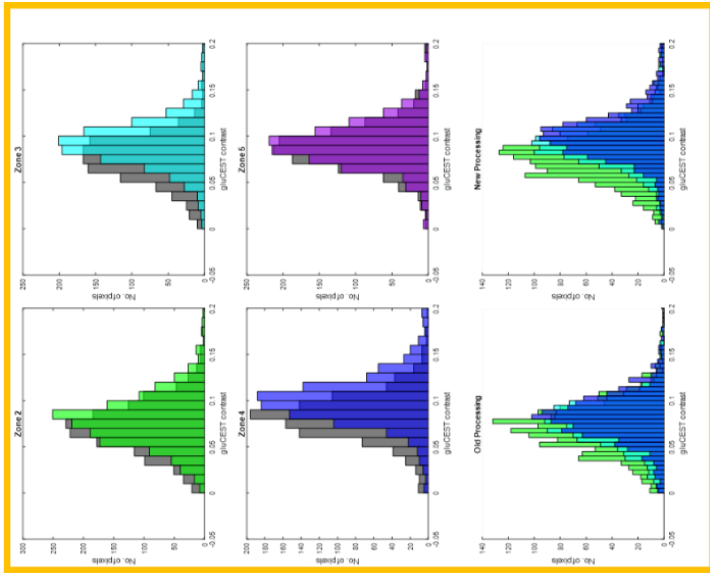


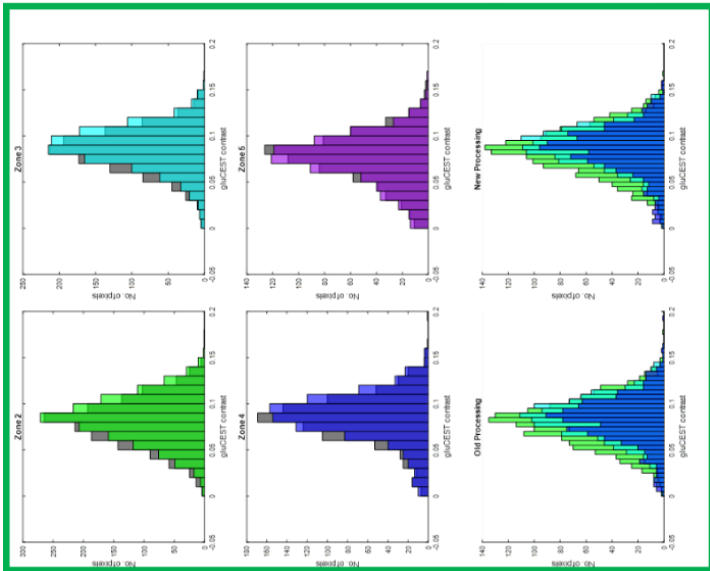
**Figure 2.57, A-C : Expanded histogram-based analysis of correction performance in example slices:** comparison of high and low  $B_1$  areas, tissue types, old and new methods. Histograms show the distribution of gluCEST values for different "zones" of the slices shown in Figure 3 of the main text, as color coded in the image. The  $T_1$  values corresponding to these zones are listed in the table, along with the mean and standard deviation of gluCEST values when calculated with the two different  $B_1$  corrections. The colors of the histogram bars correspond with the colors of the pixels in the color-coded image: roughly, the yellow mask is pure white matter; green, gray matter on the border with white matter; blue, outer layer of gray matter; violet, gray matter on the border of CSF. In the top two rows, gray histogram bars in the background correspond to the distribution computed with the "old" processing method, colors, to "new". In the bottom row, the same information is rearranged for comparison: the distributions from the green, cyan and blue masks are plotted together, but results from old and new processing are separated. The left half of the figure presents results from pixels where relative  $B_1 > 0.5$  ("High  $B_1$ "), while the right half of the figure shows data where relative  $B_1 < 0.5$  ("Low  $B_1$ "). In the center table of values, the top half of the table holds results from 'old' processing, and the bottom from 'new', as indicated by the gray and black borders matching the corresponding histograms.

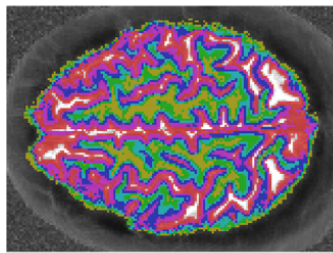
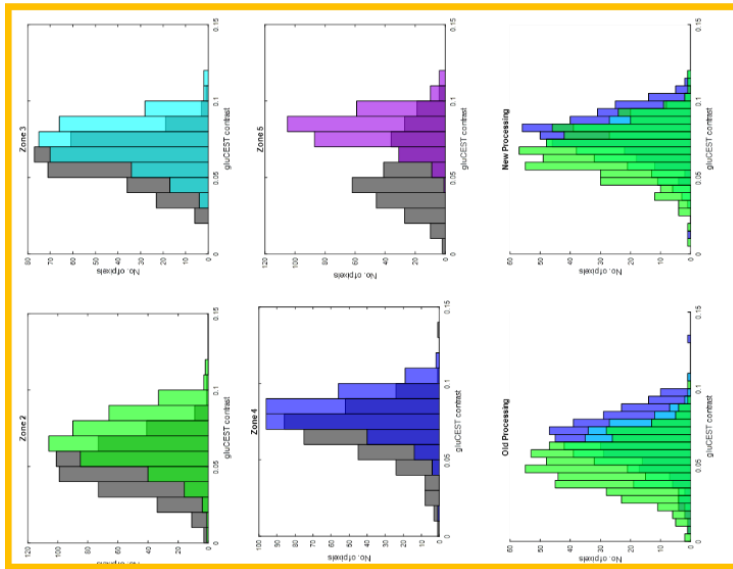


T <sub>1</sub> values	Mean gtuCEST	St. Dev.
1000-1170	0.09	0.1094
<b>1170-1310</b>	<b>0.085</b>	<b>0.0561</b>
<b>1310-1470</b>	<b>0.1005</b>	<b>0.0711</b>
<b>1470-1690</b>	<b>0.1088</b>	<b>0.064</b>
<b>&gt; 1690</b>	<b>0.096</b>	<b>0.0469</b>

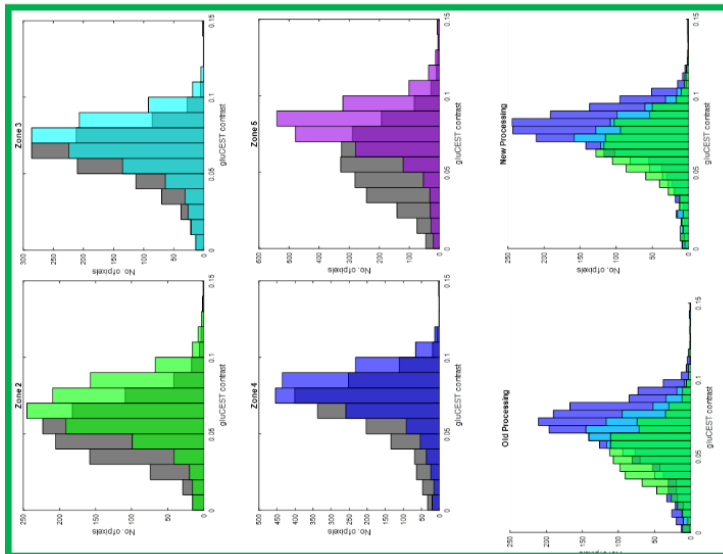
  

1000-1170	0.0694	0.0664
<b>1170-1310</b>	<b>0.0736</b>	<b>0.0415</b>
<b>1310-1470</b>	<b>0.0834</b>	<b>0.0757</b>
<b>1470-1690</b>	<b>0.0904</b>	<b>0.0686</b>
<b>&gt; 1690</b>	<b>0.0917</b>	<b>0.0469</b>





T <sub>1</sub> values	Mean gluCEST	St. Dev.
1000-1170	0.0483	0.0255
1170-1310	0.0509	0.0187
1310-1470	0.0609	0.0142
1470-1690	0.0683	0.013
> 1690	0.055	0.0115
1000-1170	0.0595	0.0264
1170-1310	0.0678	0.0201
1310-1470	0.0725	0.0145
1470-1690	0.0807	0.0172
> 1690	0.0822	0.0223



## References

1. Wolff SD, Balaban RS. NMR imaging of labile proton exchange. *J Magn Reson.* 1990;86(1):164-169. doi:10.1016/0022-2364(90)90220-4
2. Forsén S, Huffman RA. Study of moderately rapid chemical exchange reactions by means of nuclear magnetic double resonance. *J Chem Phys.* 1963;39(11):2892-2901. doi:10.1063/1.1734121
3. Kogan F, Hariharan H, Reddy R. Chemical Exchange Saturation Transfer (CEST) Imaging: Description of Technique and Potential Clinical Applications. *Innov Clin MRI.* doi:10.1007/s40134-013-0010-3
4. Vinogradov E, Sherry AD, Lenkinski RE. CEST: From basic principles to applications, challenges and opportunities. *J Magn Reson.* 2013;229:155-172. doi:10.1016/j.jmr.2012.11.024
5. Bottomley PA, Andrew ER. RF magnetic field penetration, phase shift and power dissipation in biological tissue: Implications for NMR imaging. *Phys Med Biol.* 1978;23(4):630-643. doi:10.1088/0031-9155/23/4/006
6. Foo TKF, Hayes CE, Kang Y -W. Reduction of RF penetration effects in high field imaging. *Magn Reson Med.* 1992;23(2):287-301. doi:10.1002/mrm.1910230209
7. Sled JG, Bruce Pike G. Standing-Wave and RF Penetration Artifacts Caused by Elliptic Geometry: An Electrodynamics Analysis of MRI. *IEEE Trans Med Imaging.* 1998;17(4):653-662. doi:10.1109/42.730409
8. Van De Moortele PF, Akgun C, Adriany G, et al. B1 destructive interferences and spatial phase patterns at 7 T with a head transceiver array coil. *Magn Reson Med.* 2005;54(6):1503-1518. doi:10.1002/mrm.20708
9. Cai K, Haris M, Singh A, et al. Magnetic resonance imaging of glutamate. *Nat Med.* 2012;18(2):302-306. doi:10.1038/nm.2615
10. Liebert A, Zaiss M, Gumbrecht R, et al. Multiple interleaved mode saturation (MIMOSA) for B1+ inhomogeneity mitigation in chemical exchange saturation transfer. *Magn Reson Med.* 2019;82(2):693-705. doi:10.1002/mrm.27762
11. Tse DHY, da Silva NA, Poser BA, Shah NJ. B1+ inhomogeneity mitigation in CEST using parallel transmission. *Magn Reson Med.* 2017;78(6):2216-2225. doi:10.1002/mrm.26624
12. Padormo F, Beqiri A, Hajnal J V., Malik SJ. Parallel transmission for ultrahigh-field imaging. *NMR Biomed.* 2016;29(9):1145-1161. doi:10.1002/nbm.3313
13. Singh A, Cai K, Haris M, Hariharan H, Reddy R. On B1 inhomogeneity correction of in vivo human brain glutamate chemical exchange saturation transfer contrast at 7T. *Magn Reson Med.* 2013;69(3):818-824. doi:10.1002/mrm.24290
14. Nanga RPR, DeBrosse C, Kumar D, et al. Reproducibility of 2D <sup>1</sup>H <sup>13</sup>C CEST in healthy human volunteers at 7T. *Magn Reson Med.* 2018;80(5):2033-2039. doi:10.1002/mrm.27362
15. Khlebnikov V, Polders D, Hendrikse J, et al. Amide proton transfer (APT) imaging of brain

- tumors at 7 T: The role of tissue water  $T_1$ -Relaxation properties. *Magn Reson Med*. 2017;77(4):1525-1532. doi:10.1002/mrm.26232
16. McConnell HM. Reaction rates by nuclear magnetic resonance. *J Chem Phys*. 1958;28(3):430-431. doi:10.1063/1.1744152
  17. Kim M, Gillen J, Landman BA, Zhou J, Van Zijl PCM. Water saturation shift referencing (WASSR) for chemical exchange saturation transfer (CEST) experiments. *Magn Reson Med*. 2009;61(6):1441-1450. doi:10.1002/mrm.21873
  18. Volz S, Nöth U, Rotarska-Jagiela A, Deichmann R. A fast B1-mapping method for the correction and normalization of magnetization transfer ratio maps at 3 T. *Neuroimage*. 2010;49(4):3015-3026. doi:10.1016/j.neuroimage.2009.11.054
  19. Zaiss M, Zu Z, Xu J, et al. A combined analytical solution for chemical exchange saturation transfer and semi-solid magnetization transfer. *NMR Biomed*. 2015;28(2):217-230. doi:10.1002/nbm.3237
  20. Windschuh J, Zaiss M, Meissner JE, et al. Correction of B1-inhomogeneities for relaxation-compensated CEST imaging at 7T. *NMR Biomed*. 2015;28(5):529-537. doi:10.1002/nbm.3283
  21. Metere R, Kober T, Möller HE, Schäfer A. Simultaneous quantitative MRI mapping of T1, T2\* and magnetic susceptibility with Multi-Echo MP2RAGE. *PLoS One*. 2017;12(1). doi:10.1371/journal.pone.0169265
  22. Cember ATJ, Bagga P, Hariharan H, Reddy R. Age-dependent variation in CEST signal at low B1 may reflect decline of lipids in older brain tissue. In: *Proceedings of the Annual Meeting of the International Society for Magnetic Resonance in Medicine*. ; 2020.
  23. Haris M, Nanga RPR, Singh A, et al. Exchange rates of creatine kinase metabolites: feasibility of imaging creatine by chemical exchange saturation transfer MRI. *NMR Biomed*. 2012;25(11):1305-1309. doi:10.1002/nbm.2792
  24. Haris M, Cai K, Singh A, Hariharan H, Reddy R. In vivo mapping of brain myo-inositol. *Neuroimage*. 2011;54(3):2079-2085. doi:10.1016/j.neuroimage.2010.10.017
  25. DeBrosse C, Nanga RPR, Bagga P, et al. Lactate Chemical Exchange Saturation Transfer (LATEST) Imaging in vivo A Biomarker for LDH Activity. *Sci Rep*. 2016;6. doi:10.1038/srep19517
  26. Bagga P, Wilson N, Rich L, et al. Sugar alcohol provides imaging contrast in cancer detection. *Sci Rep*. 2019;9(1):11092. doi:10.1038/s41598-019-47275-5

## Chapter 3: GluCEST measurements of the aging brain

### 3A. Age-dependent variation in CEST signal at low $B_1$ may reflect contribution of lipids

The previous chapter presented our latest surface-based strategy for correction of  $B_1$  inhomogeneity in gluCEST images. Upon the development of this new technique, we undertook to investigate its application to subjects of varying age. An ongoing study of older adults, to be discussed further in the next section, provided us with gluCEST images of healthy individuals > 60 y.o.a. on which to test the updated  $B_1$  correction strategy. Fortuitously, one of the healthy volunteers on whom we had collected  $B_1$  calibration data for generation of our surfaces was also of the same range as many of the subjects in this investigation, namely, 69 years of age at the time of acquisition. Other volunteers available ranged in age from 20-45 years old. This gave us an opportunity to experiment with the use of 'age matched' correction surfaces to develop an understanding of any age dependent trends in the gluCEST measurement and, in light of these, the best practice for performing  $B_1$  correction.

Initially we encountered an unexpected finding: when using the same correction surface on all subjects, gluCEST in the white matter appeared to be higher in older subjects (see **Figure 3A.1**). This seemed like an unreasonable result, and potentially an artefact of misapplication of the correction. Pragmatically, it was determined that the correction surfaces worked best when the surface itself was derived from subjects broadly of the same age range as that of the target image.



The reason for this can be understood from the heat map style plots in **Figure 3A.2**. The top row of this figure shows example CEST contrast surfaces derived from fits to data from one younger and one older subject. Recall that at low  $B_1$ , CEST asymmetry at 3.0 ppm is actually negative, a phenomenon attributed to NOE-like cross-relaxation with lipid aliphatic chains and other

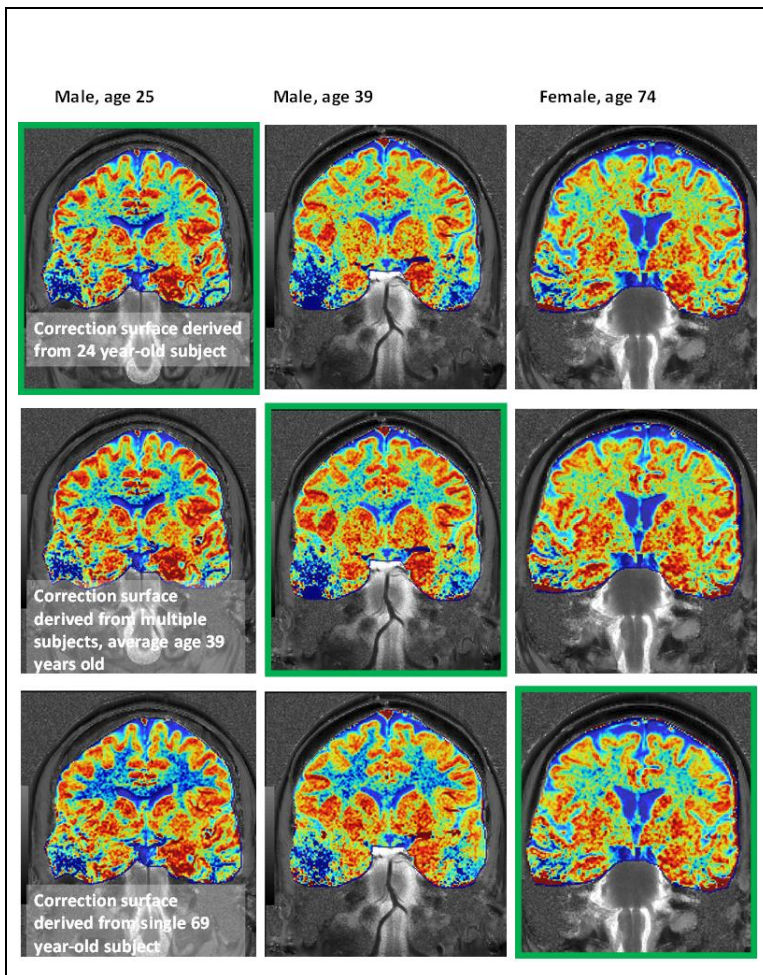


**Figure 3A.1. Coronal gluCEST images of healthy subjects of three different ages (25, 39 and 74 y.o.)** are processed with three different correction surfaces. For any given correction applied (by row), older subjects have higher apparent white matter gluCEST. It appears from our measurements that the contribution of lipids to the white matter CEST signal decreases with age, which lowers the apparent contrast due to glutamate in younger people if an identical correction scheme is applied to all ages. In this figure, we believe the most accurate of the three images shown to be that outlined in green.

moieties centered at -3.5 ppm relative to water. <sup>1</sup>

At low  $B_1$  in these heatmaps (minimum at approximately 1uT), lower-T1 masks exhibit a strong negative signal, attributed to NOE contributions from lipid aliphatic chains. This “valley” is



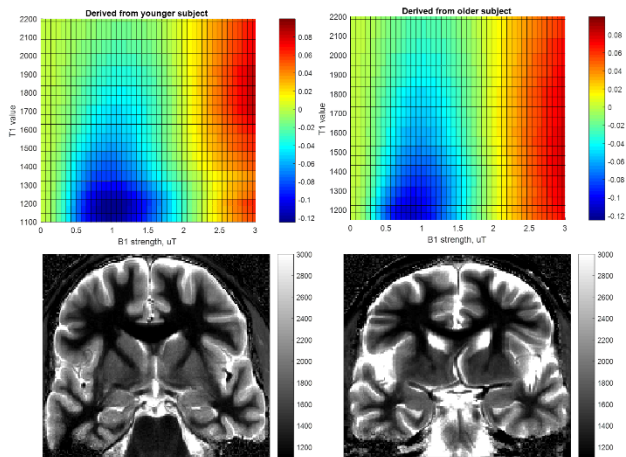


**Figure 3A.2.** Top: CEST contrast (negative-normalized) surface derived from fits to data from one younger (age 24) and older (age 69) subject. At low B1 (minimum at approximately 1uT), lower-T1 masks exhibit a strong negative signal, attributed to NOE contributions from lipid aliphatic chains. This “valley” is deeper in the white matter of younger subjects, likely reflecting the higher concentration of lipids present in their tissue. If not accounted for when performing B1 correction, white matter of older subjects will appear to have higher gluCEST. Bottom: T1 maps of the corresponding subjects.

deeper in the white matter of younger subjects, likely reflecting the higher concentration of lipids present in their tissue. If not accounted for when performing B<sub>1</sub> correction, white matter of older subjects will appear (incorrectly, we believe) to have higher gluCEST.

It will be noticed that the “T<sub>1</sub> value” axis in Figure 3A.2 begins at 1100ms for the younger subject, but at 1150ms for the older one. According to our measurements, pixels with T<sub>1</sub> value < 1150ms are almost completely absent in subjects aged 60 and above. Increase in

T1 value with aging has been documented in earlier literature<sup>2,3</sup>, but does not appear to have been quantified yet at ultra-high field strength. Our preliminary results on this front are displayed in **Figure 3A.3**.

At first, we supposed that the difference in CEST contrast at low  $B_1$  across different ages was simply a reflection of the shift in  $T_1$  values; i.e. the same family of curves could be used for all subjects for a given absolute  $T_1$ . However, inspection of Figure 3A.2 illustrates that this is not the case: even for a given  $T_1$  value, the dependence of the CEST signal on saturation  $B_1$  differs with age. This supports the notion that low- $B_1$  contrast is reflecting a physico-chemical change distinct from that manifesting in the shift of  $T_1$  values.

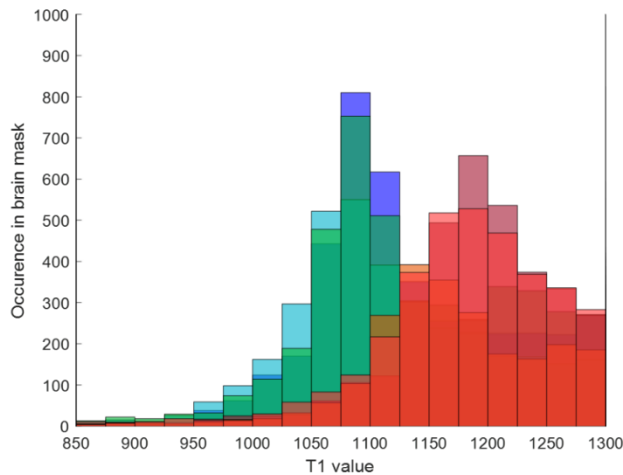


**Figure 3A.3 . Histogram of white matter  $T_1$  values** in the brains of healthy individuals, measured at 7T. Green/blue distribution: individuals 25-39. Red distribution: individuals 68-74.

As to the nature of this change, it has been reported that the human brain loses myelin, a tissue rich in lipids, with aging<sup>4,5</sup>. We therefore hypothesize that the age-dependent differences in CEST signal at low  $B_1$  arise from a decreasing presence of lipids in older adults. NOE at 7T has been used to examine glioma patients<sup>6,7</sup>, but little has been

reported about its use in other contexts. While the purpose of this data collection and analysis was not observation of the NOE effect *per se*, we believe that the age-dependent differences we observe in this function may be the first detection of brain lipid decline in aging populations by a magnetization transfer-based technique. This signal, while detected incidentally in the present results, could in the future be measured explicitly as an indicator of brain health and aging progression.

## **3B. Glutamate Weighted Imaging (GluCEST) as a Biomarker of Cognitive**

### **Function: Preliminary Findings from GluCEST MRI in Older Adults**

#### **3B.1 MCI and AD: Additional Background**

Alzheimer's disease (AD) is the sixth leading cause of death in the US<sup>8</sup>. Its characteristics include the progressive memory loss, decline in other cognitive skills, and adverse behavioral changes. The hallmark brain neuropathologies of AD include accumulations of extracellular amyloid- $\beta$  (A $\beta$ ) plaques and intracellular neurofibrillary tangles (NFTs) formed by aggregates of all 6 tau protein isoforms. These proteinopathies cause early synaptotoxicity and neurotransmitter alterations, gliosis, and ultimately loss of neurons and gross brain atrophy<sup>9-13</sup>. Mounting evidence indicates that early cognitive changes in AD may result from the dysregulation of excitatory glutamatergic neurotransmission by soluble A $\beta$  oligomers, leading to tau phosphorylation and glutamate over stimulation of extra-synaptic N-methyl-D-aspartate receptors (ENMDARs) and synaptic alterations<sup>8</sup>. It has been shown that synapse loss, rather than A $\beta$  plaques or NFTs, is the best correlate of memory deficits in AD<sup>14,15</sup>. Previous work in animals from our lab has demonstrated that decreasing gluCEST signal is correlated with synapse loss<sup>16</sup>. In this study, our goal is to extend use of this technique to image the brains of human patients experiencing cognitive decline.

Experimental protocol: We will now discuss the findings to date of the gluCEST study of MCI and healthy aging in older adults. The gluCEST images gathered in this study were corrected with the 'age matched' correction surface, as in the final row of **Figure 3A.1**. All other acquisition and post-processing is as described in **Figure 1b.5** and the Methods section of Chapter 2.

### 3B.2 Analysis

T<sub>1</sub> and T<sub>2</sub>-weighted images are used to perform segmentation of Medial Temporal Lobe structures using the Penn Memory Center (PMC) atlas available in ITK-SNAP's Distributed Segmentation Service<sup>17-19</sup>. CEST images are registered to the T<sub>2</sub> weighted images and thereby the segmentation map. Functions from the c3d library available in ITK-SNAP are then used to calculate thresholded averages over pixel assigned to a particular segment.

### 3B.3 Results and Discussion

Figure 3B.1 shows ten gluCEST maps gathered in older adults: five healthy controls (top row) and five presenting with MCI (bottom). The regional analysis in this study focuses on the fine gray matter structures of the medial temporal lobe, as this region is thought to be the main

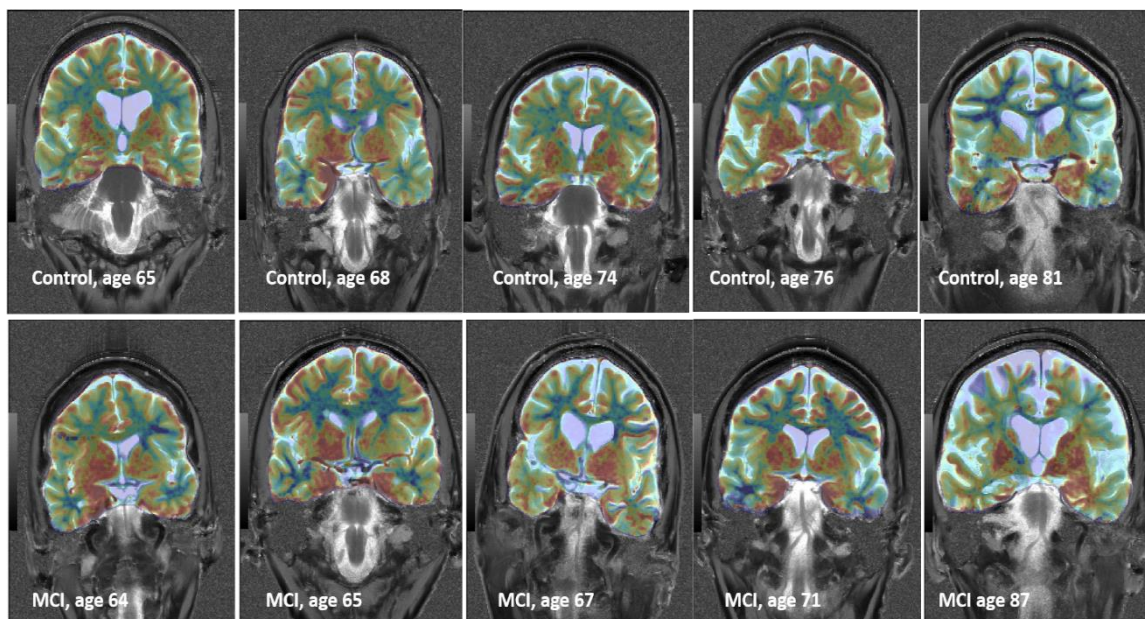
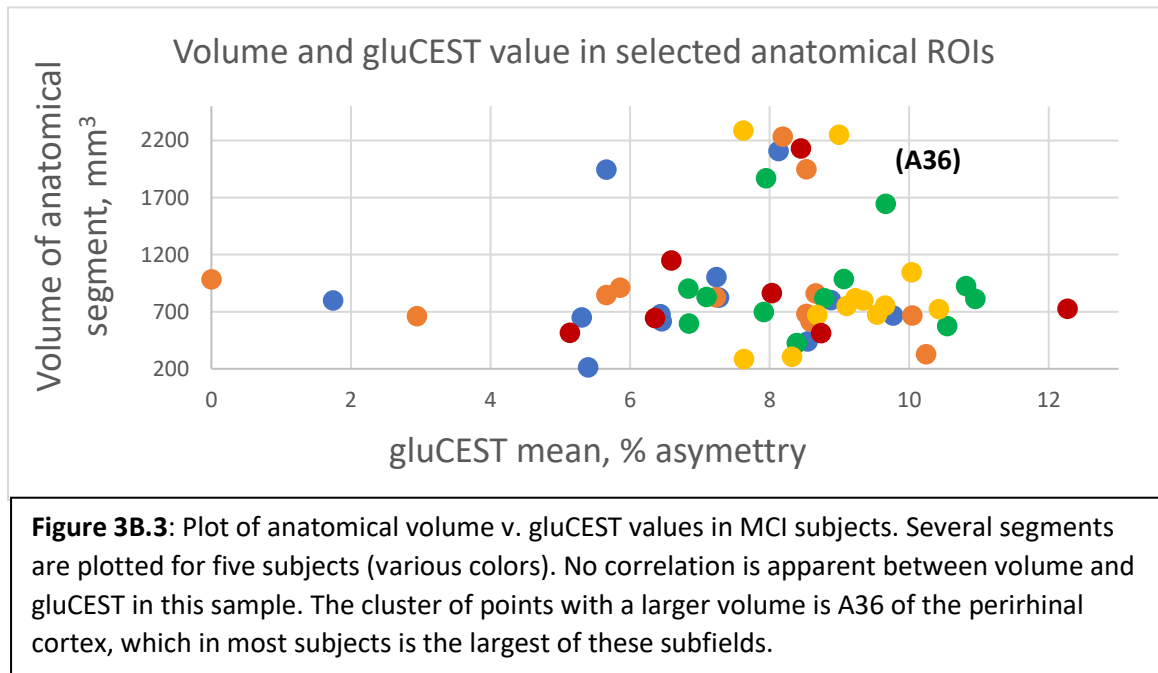


**Figure 3B.1:** GluCEST maps of selected control (top) and MCI subjects (bottom), overlaid onto T<sub>2</sub>-weighted structural image. Interestingly, the most striking feature visible on a large scale is the apparent lower gluCEST in white matter of MCI subjects (darker blue color). The only control subject with a similar value is the oldest healthy participant, at 81 years of age.

locus of cognitive and memory related function in the human brain. It is difficult to gain

information about these small regions of the brain by visual inspection. However, interestingly, the white matter gluCEST appears to show differences between control and MCI subjects that are not strongly localized and visible in these coronal CEST maps. The correct interpretation of these white matter differences is still a matter of ongoing work.

**Figure 3B.2** illustrates the method of regional analysis used to inspect the gluCEST of the medial temporal lobe structures in these subjects. On the left, the subfield segmentation is shown overlaid with the T<sub>2</sub> structural image used to generate it. On the right, the same structural image is shown overlaid with a gluCEST map set with high transparency so that the anatomy can be seen clearly underneath. Registration of the segmentation shown on the left with the gluCEST map shown on the right allows for calculating regional averages of gluCEST values over each anatomical segment. Accurate segmentation depends on the success of registering the experimental scan to an existing atlas. Unfortunately, no atlas has been developed for medial temporal lobe subfields which is specific both to aging adults (who universally have some degree



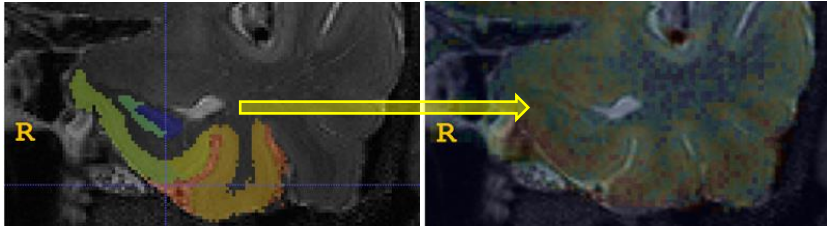


**Figure 3B.2. High-resolution structural segmentation** of medial temporal lobe structures used for regional analysis of gluCEST images: visualization of computational process. The atlas used for this investigation was specific to older adults but not for 7T images, which caused some challenges. The converse option was equally plagued with inaccurate results.

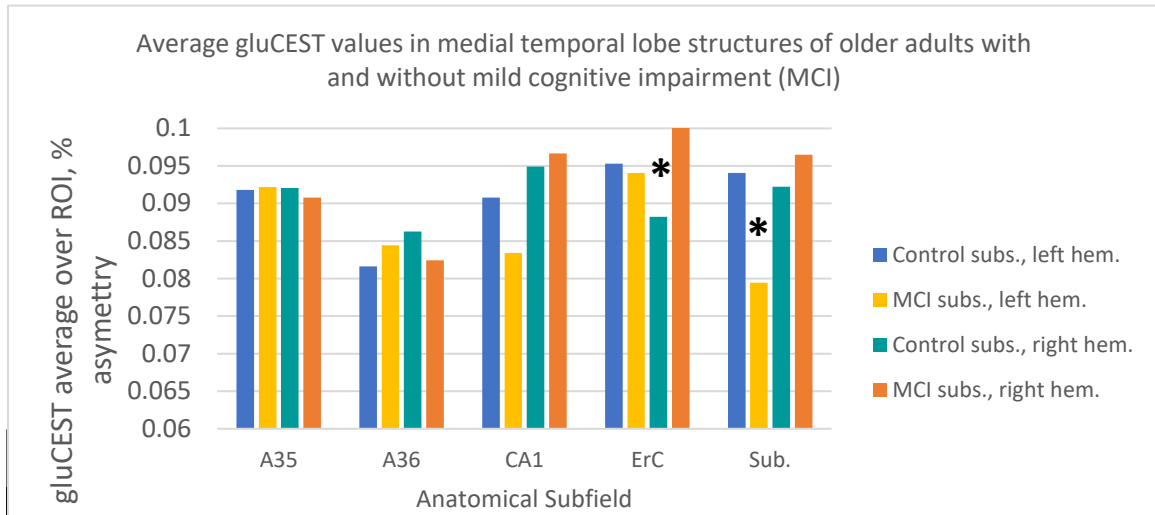
neural atrophy) and for 7T images, which have contrast slightly different from 3T images. For this study, it was determined to be optimal to use an atlas developed specifically for older

adults (Penn Memory Center Atlas) despite the fact that this algorithm was expecting contrast from 3T images. In most cases, this was a suitable solution; however, some cases of segmentation failure occurred that may have resulted in part from this discrepancy.

The structural segmentation performed also returns information about the volume of each of these segments, calculated from the full-brain structural images (not the slim cross-section captured by the gluCEST image). We investigated whether there was a correlation between the volume of the full segment, and the average gluCEST measured in the sliver of this segment captured by our acquisition slice. No such correlation was found (see plot in **Figure 3B.3**). If this lack of correlation is a true finding, it could be interpreted to mean that metabolic changes which may increase or decrease the presence of glutamate-- reflecting physiological phenomena like excitotoxicity or synapse loss-- may occur only loosely correlated in time to structural degradation of the neurons and surrounding tissue. Indeed, many investigators in the field have concluded that, "by the time you see the structural loss, it's too late", and that real disease progression precedes this step. Alternatively, it's quite possible that a subtle correlation exists

but was not detected in our current data precisely because of the fact that only a small fraction of the structure is captured in CEST slice.

**Figure 3B.4** displays the calculated mean gluCEST values in two different ways: by bar plot, in which only the most consistently captured segments are represented, and in an 'image', in which the color of the segment represents its average value in that population. Statistical tests revealed that the average gluCEST between two of the segments had a "statistically significant" difference between MCI and control subjects: namely, the right entorhinal cortex and the left subiculum. However, given the lack of consistency in direction, laterality or anatomical identity between these two results, it seems likely that this reflects abnormally high or low values in specific subjects which, while perhaps having significance in the physiology of the individual, does not reflect any consistent group trend.



young adults (blue), older adults without cognitive impairment (green), and older adults with

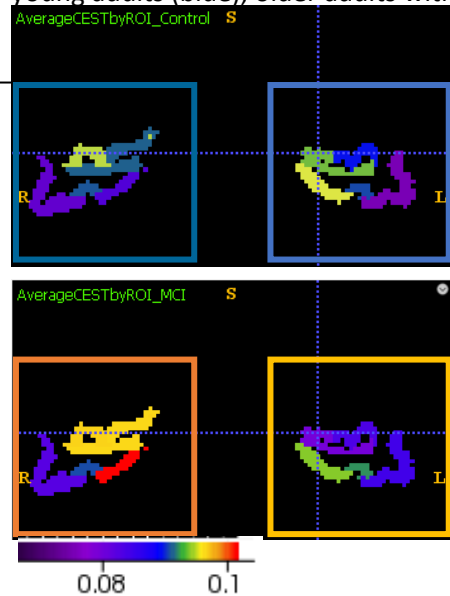


**Figure 3B.4** Representations of **average gluCEST values** of MTL subfields. **Top: Bar plot** of average gluCEST values in ROIs with sufficient coverage over all subjects. Data is separated by laterality and by MCI vs. control. The subfields shown include regions A35 and A36 of the perirhinal cortex, CA1 of the hippocampus, the entorhinal cortex (ErC) and the subiculum. The asterisk represents segments in which a statistically significant difference was calculated between MCI and control subjects. **Left: ROI averages by colormap**, projected onto the anatomy of a single subject for visualization. Control (top) and MCI (bottom). For example the elevated average gluCEST in the right ErC and subiculum of MCI subjects is seen in the red and orange colors shading this anatomy in the bottom panel.

Finally, Figure 3B.5 examines the gluCEST values in one segment, the entorhinal cortex, as a distribution. The goal of this type of analysis is to elucidate the relationship between gluCEST changes in healthy aging as opposed to in those patients presenting with MCI. On the left, the distribution of gluCEST values measured in the entorhinal cortex of younger subjects (blue) is plotted together with that from older healthy subjects (green). The apparent low-magnitude left



shift of this distribution would seem to be a reasonable result. This comparison is not entirely rigorous, however, as the data from younger subjects was gathered using the 3D gluCEST sequence, while the data from older subjects, the 2D sequence. While we believe the resulting magnitude of gluCEST to be comparable between these sequences, the bigger discrepancy which makes these data sets hard to compare lies in the number of pixels captured. It can be seen that the blue distribution comes much closer to an idealized 'normal' shape, while the green one is 'noisy'. These distributions are normalized for comparison, but in reality the distribution derived from the 3D CEST data contains an order of magnitude more pixels, although it comes from a comparable number of subjects. It can be understood readily from this plot that identification of the properties of the distribution – and thus, answers to biological questions – can be attained much more readily with the information provided by a 3D acquisition.

The plot on the right contains the 2D-derived data for MCI v. control subjects (the green distribution is identical in both plots). What would appear to be the case from these comparisons is that individuals with MCI have a greater *spread* of gluCEST values-- suggesting dysregulation of normally tightly controlled processes-- while normal aging involves a slow decline in glutamate concentration (perhaps due to hypometabolism or synapse loss), but without extreme values in either direction.

In the current data set of older adults, the entorhinal cortex was amongst the only segments which had a 'smooth' enough distribution to make any sense of such plots. This is unfortunate, as histograms may be our best tool to interpret what in reality is likely a complex and multi-modal situation: subjects with MCI may have higher gluCEST if we're capturing the 'excitotoxicity' phase, or lower, if we're capturing the 'loss-of-synapses' phase. There may even

be a bimodal distribution of gluCEST values amongst these subjects, which would need a particular large amount of data to detect cleanly. Ideally, we could even do regional analysis based on the particular sub-classification of cognitive impairment that the patient is presenting: for example, a deficit in verbal capacity as opposed to spatial navigation could be reflected in changes in different respective subregions.

### **3B.4 Limitations of the Study**

This study has imaged fewer than 20 participants to date, and employed only our 5mM, '2D' gluCEST sequence (see pulse sequence parameters in 2A.1). In a 2D acquisition aiming to capture specific, small anatomy, slice placement must be very exact, and even so, the data acquired is very limited. Moreover, the structural degradation and variability in older brains makes the challenge of repeated capturing of the same anatomy in each scan particularly steep. This limited amount of information per subject makes it difficult to identify consistent trends at the current stage of investigation; however, this ongoing work provides an excellent case study for the challenges of the gluCEST measurement and its analysis, and a quintessential illustration of the impetus for our expansion to 3D acquisition described in chapter 5.

### **3B.5 Conclusions**

In summary, the complexity of neurodegeneration and consequent cognitive decline with aging is a problem which requires the maximal amount of information to deconvolute all of the potentially relevant variables-- this is a problem with many degrees of freedom, and thus needs many points of input to gain insight into its 'ground truth'. GluCEST is an incredible tool for such a task, but it requires that we be able to image as much volume as possible. To these ends, we hope that future work in imaging these populations of older adults will employ a 3D acquisition

as will be presented in Chapter 5, in which excellent understandings of the distributions of gluCEST values in particular brain segments--their means, medians, extents, and subtle differences from each other—was achieved from the data of only ten healthy subjects. Expanding our attainable data even to this degree could have a revolutionary contribution to the goal of creating an ‘atlas’ of brain glutamate distributions in healthy and impaired aging.

## References

1. Liu D, Zhou J, Xue R, Zuo Z, An J, Wang DJJ. Quantitative characterization of nuclear overhauser enhancement and amide proton transfer effects in the human brain at 7 Tesla. *Magn Reson Med*. 2013;70(4):1070-1081. doi:10.1002/mrm.24560
2. Cho S, Jones D, Reddick WE, Ogg RJ, Grant Steen R. Establishing norms for age-related changes in proton T1 of human brain tissue in vivo. *Magn Reson Imaging*. Published online 1997. doi:10.1016/S0730-725X(97)00202-6
3. Maniega SM, Valdés Hernández MC, Clayden JD, et al. White matter hyperintensities and normal-appearing white matter integrity in the aging brain. *Neurobiol Aging*. 2015;36(2):909-918. doi:10.1016/j.neurobiolaging.2014.07.048
4. Svennerholm L, Boström K, Helander CG, Jungbjer B. Membrane Lipids in the Aging Human Brain. *J Neurochem*. 1991;56(6):2051-2059. doi:10.1111/j.1471-4159.1991.tb03466.x
5. Bartzokis G, Lu PH, Geschwind DH, Edwards N, Mintz J, Cummings JL. Apolipoprotein E genotype and age-related myelin breakdown in healthy individuals: Implications for cognitive decline and dementia. *Arch Gen Psychiatry*. 2006;63(1):63-72. doi:10.1001/archpsyc.63.1.63
6. Zaiss M, Windschuh J, Paech D, et al. Relaxation-compensated CEST-MRI of the human brain at 7T: Unbiased insight into NOE and amide signal changes in human glioblastoma. *Neuroimage*. 2015;112:180-188. doi:10.1016/j.neuroimage.2015.02.040
7. Heo HY, Jones CK, Hua J, et al. Whole-brain amide proton transfer (APT) and nuclear overhauser enhancement (NOE) imaging in glioma patients using low-power steady-state pulsed chemical exchange saturation transfer (CEST) imaging at 7T. *J Magn Reson Imaging*. 2016;44(1):41-50. doi:10.1002/jmri.25108
8. Rudy CC, Hunsberger HC, Weitzner DS, Reed MN. The role of the tripartite glutamatergic synapse in the pathophysiology of Alzheimer's disease. *Aging Dis*. 2015;6(2):131-148. doi:10.14336/AD.2014.0423
9. Yanker B. *Mechanisms of Neuronal Degeneration Review in Alzheimer's Disease*.
10. Heininger K. A unifying hypothesis of Alzheimer's disease. III. Risk factors. *Hum Psychopharmacol Clin Exp*. 2000;15(1):1-70. doi:10.1002/(SICI)1099-1077(200001)15:1<1::AID-HUP153>3.0.CO;2-1
11. Bell KFS, Claudio Cuello A. Altered synaptic function in Alzheimer's disease. *Eur J Pharmacol*. 2006;545(1):11-21. doi:10.1016/j.ejphar.2006.06.045
12. Citron M. Alzheimer's disease: Strategies for disease modification. *Nat Rev Drug Discov*. 2010;9(5):387-398. doi:10.1038/nrd2896
13. Braak H, Braak E, Bohl J. Staging of Alzheimer-Related Cortical Destruction. *Eur Neurol*. 1993;33(6):403-408. doi:10.1159/000116984

14. Terry RD, Masliah E, Salmon DP, et al. Physical basis of cognitive alterations in alzheimer's disease: Synapse loss is the major correlate of cognitive impairment. *Ann Neurol*. 1991;30(4):572-580. doi:10.1002/ana.410300410
15. Makin S. The amyloid hypothesis on trial. *Nature*. 2018;559(7715):S4-S4. Accessed March 2, 2021.  
<https://go.gale.com/ps/i.do?p=AONE&sw=w&issn=00280836&v=2.1&it=r&id=GALE%7CA572728086&sid=googleScholar&linkaccess=fulltext>
16. Crescenzi R, DeBrosse C, Nanga RPR, et al. Longitudinal imaging reveals subhippocampal dynamics in glutamate levels associated with histopathologic events in a mouse model of tauopathy and healthy mice. *Hippocampus*. 2017;27(3):285-302. doi:10.1002/hipo.22693
17. Yushkevich PA, Pluta JB, Wang H, et al. Automated volumetry and regional thickness analysis of hippocampal subfields and medial temporal cortical structures in mild cognitive impairment. *Hum Brain Mapp*. 2015;36(1):258-287. doi:10.1002/hbm.22627
18. Yushkevich PA, Piven J, Hazlett HC, et al. User-guided 3D active contour segmentation of anatomical structures: Significantly improved efficiency and reliability. *Neuroimage*. 2006;31(3):1116-1128. doi:10.1016/j.neuroimage.2006.01.015
19. Berron D, Vieweg P, Hochkepler A, et al. A protocol for manual segmentation of medial temporal lobe subregions in 7 Tesla MRI. *NeuroImage Clin*. 2017;15:466-482. doi:10.1016/j.nicl.2017.05.022

# Chapter 4: Using gluCEST to probe the mechanism of transcranial magnetic stimulation (TMS)

## 4.1 Introduction

Transcranial magnetic stimulation (TMS) is a non-invasive brain stimulation technique which has been deployed extensively by cognitive neuroscientists, physiologists, and clinicians<sup>1</sup>. TMS uses electromagnetic induction to generate electrical current in the cortex of the brain, and causes depolarization of neurons at the site of stimulation (See Figure 4.1)<sup>2,3</sup>. Specifically, TMS uses a strong and rapidly fluctuating electrical current which is transmitted through loops of conductive wires surrounded by a protective casing and held in proximity to the skull. The generated current penetrates the scalp and skull, inducing electrical and subsequent chemical changes within the cortex<sup>4,5</sup>. TMS to the motor cortex has been shown to activate cortical interneurons and pyramidal neurons, leading to corticospinal tract activation and ultimately inducing muscle twitches<sup>6</sup>. When applied to other regions of the cortex, TMS can interrupt normal cognitive function and can provide therapeutic relief of complex neurobiological disorders such as depression<sup>7,8</sup>. Given the already wide-ranging application of this technique, it is ever more imperative for scientists and clinicians to understand the mechanisms by which TMS influences the brain and subsequent behaviors.

To this end, multiple TMS protocols have been developed by researchers who seek to characterize their various effects<sup>1</sup>. The focus of our study is a particular implementation known as continuous theta burst stimulation (cTBS)<sup>9</sup>, consisting of 3–5 pulses at 100 Hz repeated at 5 Hz for 40s, a protocol considered to fall into the broader category of ‘repetitive TMS’ (rTMS). Previous studies have shown that the use of rTMS protocols such as cTBS can induce long term changes -- termed by neuroscientists as long-term potentiation (LTP) and long term depression

(LTD) -- within the motor cortex or other regions of the brain<sup>10-13</sup>. The changes induced by cTBS are typically monitored and reported by measuring motor evoked potentials (MEPs) and believed to last up to 1 hour post stimulation<sup>14</sup>. The direction and magnitude of these changes are thought to be dependent on the pattern of the administered stimulation.<sup>15</sup> While some models have been recognized which describe the electrophysiologic response as a function of stimulation pattern, the precise cellular mechanisms which are at play here are not well understood.

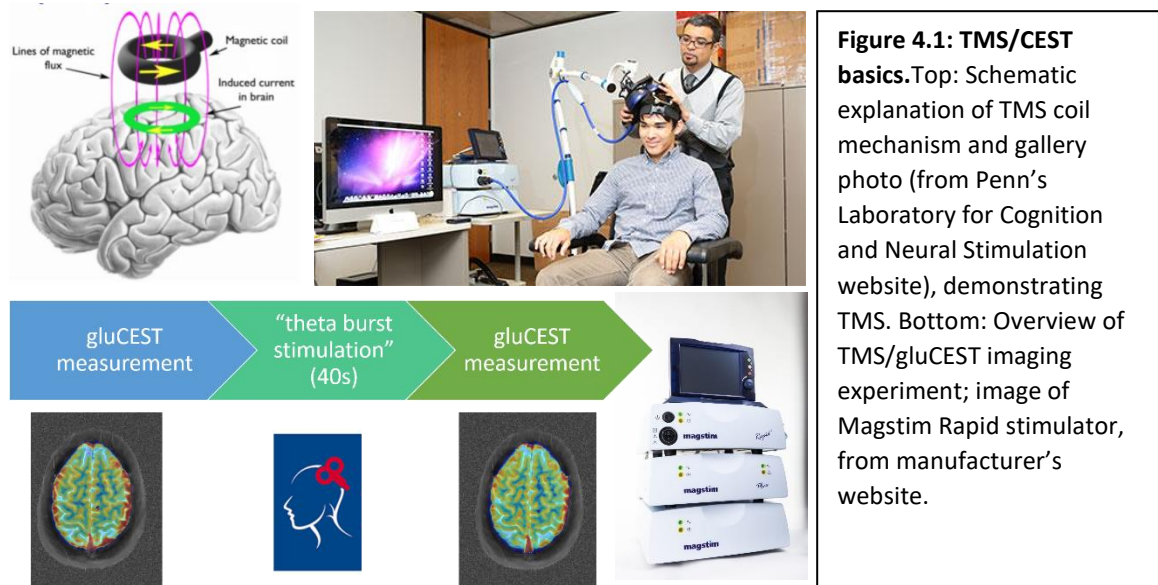
Current hypotheses include the idea that changes in MEPs occur due to the modulation in interneuron and/or pyramidal cell membrane excitability, or due to a change in the ability of neurons to effectively communicate through their synaptic processes<sup>6</sup>. More recent studies have pointed to membrane potentials being influenced mostly at the level of inhibitory/excitatory interneurons within the cortex, as stimulation protocols such as cTBS are generally not considered to be sufficiently intense to activate deeper cortical pyramidal neurons<sup>16</sup>. cTBS is believed to specifically activate inhibitory GABA<sub>A</sub> and GABA<sub>B</sub> interneurons within the motor cortex<sup>14,17,18</sup>. Strong evidence of molecular changes after rTMS and cTBS come from drug studies which have shown that the use of glutamatergic NMDA antagonists dextromethorphan and GABA receptor agonists alter the responses to rTMS protocols<sup>19-21</sup>. More specifically, the use of the partial NMDA agonist D-cycloserine, has been shown to modulate the effect of theta burst stimulation<sup>22</sup>.

Interest in understanding the neurometabolic underpinnings of TMS has given rise to a number of magnetic resonance spectroscopy (MRS) based investigations<sup>23</sup>. Multiple studies have found that cTBS and related protocols can induce changes in MRS-measured GABA concentration<sup>24-29</sup> or have linked TMS-based measures of electrophysiology to GABA content<sup>30,31</sup>. However, despite

the pharmaceutical-based evidence that the glutamatergic signaling system is also involved in TMS response, changes in glutamate have not been detected robustly in MRS studies to date of cTBS to the motor cortex. In this study, rather than single voxel spectroscopy, we used gluCEST<sup>32</sup> to assess the effects of cTBS on cortical glutamate. To the best of our knowledge, this technique has not ever been previously applied to investigate TMS.

As described in the previous chapters, gluCEST relies on a different mechanism than spectroscopy: rather than detecting the resonance of the glutamate protons directly, the gluCEST signal originates from the interaction of the glutamate with bulk water, and the signal measured – as in most other forms of MR imaging – is the water itself.

In this work, we capitalize on the ability of gluCEST to generate spatially resolved brain ‘maps’ weighted for glutamate to investigate the short-term neurometabolic effects of cTBS on healthy



humans. Our study design involves sequential collection of gluCEST imaging before and after subjects have undergone cTBS or a placebo (“sham”) stimulation. Our results suggest that we have been able to detect transient shifts in the neurochemical profile of stimulated subjects, which may underlie the electrophysiological and other more lasting effects attributed to cTBS.



This is a pilot study in which only general trends amongst a small population of healthy subjects were determined. However, we believe that this novel type of data may open doors for further understanding the molecular mechanisms of TMS, the geometric and temporal extent of its effects, the varying effect of different TMS protocols, and the origin of variability in response to TMS within the population.

## **4.2 Materials and Methods**

### ***4.2.1 Human subjects information***

15 healthy individuals (mean age = 29.5 , St.D. = 8.8 years, 5 female) were recruited for this study. Subjects provided informed, written consent and all procedures were carried out in accordance with the guidelines of the Institutional Review Board/Human Subjects Committee at University of Pennsylvania. A non-invasive type of brain stimulation, TMS, was administered to all subjects in accordance with the procedure described in <sup>14</sup>. Subjects were randomly assigned into either the active stimulation group (n = 10) or the sham group (n = 5). All subjects were right-handed participants with no prior history of neurologic or psychiatric disease.

### ***4.2.2 cTBS and sham***

The TMS coil was used to find the subject's right hand first dorsal interosseous (FDI) muscle via the neuronavigation software Brainsight (Rogue Research, Montreal, Québec, Canada). A subject's resting motor threshold was determined when the FDI muscle was activated at rest 50% of the time, as determined by measured motor evoked potentials (MEPs). A subject's active motor threshold was determined when the FDI muscle was engaged in a motor task 50% of the time (determined by MEPs). The resting and active motor threshold values (i.e. the machine output when at rest or doing the active task) were noted. Subjects then participated in two

imaging sessions ( "pre-TMS" and "post-TMS"). Between the two sessions, either active or sham TMS was administered. In the active TMS group, we administered continuous theta burst stimulation<sup>14</sup> (cTBS) as described in reference [12], at 80% active motor threshold to the identified FDI muscle target in the left motor cortex. Briefly, cTBS is a 40-second procedure of uninterrupted theta-burst stimulation, to total 600 pulses. Stimulation was delivered with the 70mM hand-held figure-eight coil of the Magstim Super Rapid Stimulator (Magstim, Inc., Whitland, Dyfed, UK.). To create the sham condition, TMS was administered to the vertex, rather to the motor target, with the coil held perpendicularly to the subject's head (90° rotation from normal position).

#### ***4.2.3 MRI acquisition procedure***

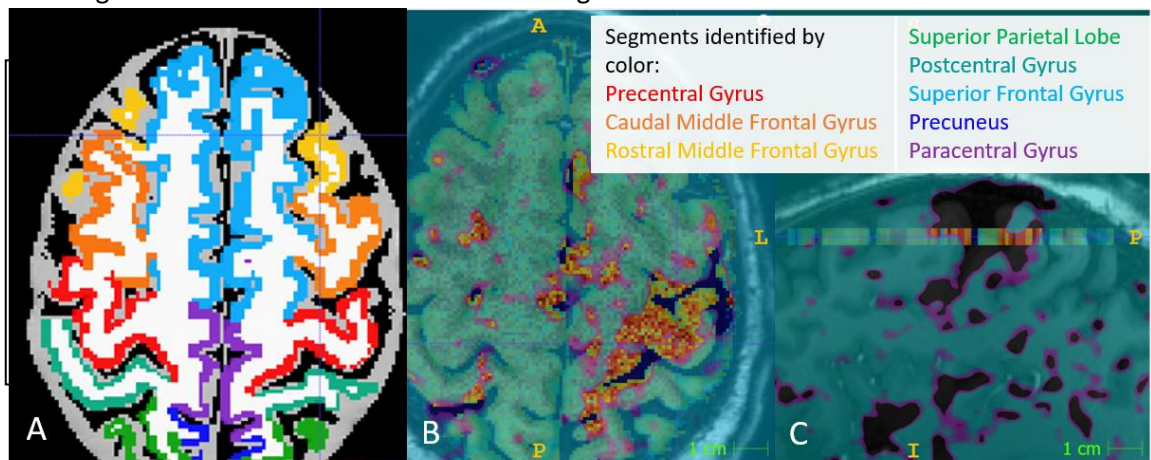
All images were obtained on a Siemens 7.0T MAGNETOM Terra scanner (Siemens Healthcare, Erlangen, Germany) outfitted with a single volume transmit/32 channel receive phased array head coil (Nova Medical, Wilmington, MA, USA). All subjects underwent two sessions of MR imaging: one prior to either cTBS or sham stimulation, and one directly following the stimulation session. Prior to beginning the initial CEST measurement, structural and BOLD scans (fMRI) were acquired and processed in order to locate the target region of stimulation for accurate placement of the CEST slice. Subjects were instructed to perform voluntary motion of the first dorsal interosseus muscle (index finger), the same motion which is induced involuntarily by the cTBS protocol when administered above motor threshold. This voluntary motion led to a localized BOLD signal that could be visualized and then registered to the structural image visible on the scanner interface where slice placement is performed by the operator. The CEST slice was then acquired in such a fashion as to maximally capture the activated region. See Figure 4.1 for illustration.

GluCEST data was collected with a single-slice CEST sequence based on gradient-recalled echo with the following parameters: TR/TE = 4.7/2.3 ms, 10° flip angle, 5 mm slice thickness, with 0.75 x 0.75 mm<sup>2</sup> in plane resolution over a 156 x 192 mm field of view. Magnetization preparation was achieved using eight 3.1μT RMS amplitude, 98 ms Hamming-window shaped pulses with 2 ms inter-pulse delay applied at offset frequencies {±1.8, 2.1, 2.4, 2.7, 3.0, 3.3, 3.6, 3.9, 4.2} ppm relative to water. Additional acquisitions over the same field of view included a water saturation acquisition (WASSR) for B<sub>0</sub> mapping<sup>33</sup>, a flip/crush sequence for B<sub>1</sub> mapping<sup>34</sup>, and the Siemens product sequence MP2RAGE for generation of T<sub>1</sub> maps. A 'reference' image consisting of only the read-out module of the CEST sequence (with no saturation) was also collected for each slice.

#### 4.2.4 Data processing and analysis

CEST-weighted images were corrected for the  $B_0$  field distribution using the  $B_0$  image generated by the WASSR scan, as described in <sup>32</sup>. CEST images were corrected for  $B_1$  inhomogeneity using a recently developed procedure (detailed in chapter 2) based on  $B_1$  and  $T_1$  mapping<sup>35</sup>.  $T_1$  and  $T_2$  weighted full-brain structural images were used for segmentation by Freesurfer's 'Recon All' function<sup>36</sup> (Freesurfer: Martinos Center for Biomedical Imaging, Charlestown, MA, USA). The output from Recon All (segmentation image) was transformed back into the original acquisition space, and resliced to correspond to the CEST acquisition for pixelwise regional analysis. Regional averages and distributions were calculated and visualized using in-house code written in Matlab (Mathworks, Natick, MA, USA); statistical analysis was done using Matlab's unpaired T-test function. Plots and visualizations were generated using Matlab and ITK-SNAP<sup>37,38</sup>.

Good agreement was found between the in-magnet localization of M1 and the atlas-based



segmentation used for data analysis. Visualizations of the CEST slice used in this experiment are provided in **Figure 4.2**. Example gluCEST data masked for M1 from two stimulated subjects with a visually apparent change in this region are shown in **Figure 4.3**, along with the corresponding histograms.

### 4.3 Results

While initial analysis focused on M1, **in fact a highly non-localized response, manifesting in a decrease in gluCEST signal throughout the left (ipsilateral) hemisphere**, was detected in subjects who received cTBS. **Figure 4.4** shows segment-wise average gluCEST data from all subjects, projected onto the anatomy of a single subject for visualization. Figure 4.4A shows the average gluCEST values by segment in the baseline scan, containing data from all 15 subjects

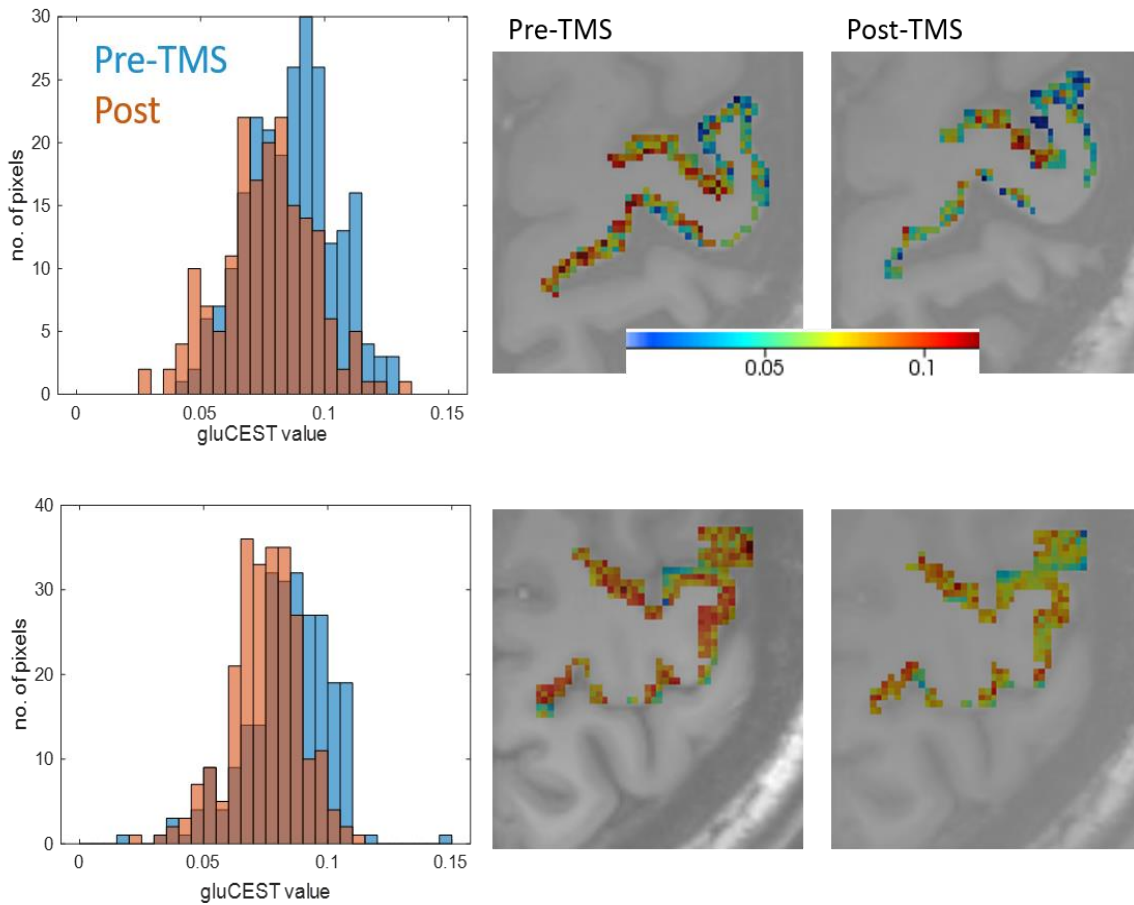


**Figure 4.3:** Sample CEST maps and histograms for gluCEST in the left precentral gyrus of stimulated subjects with apparent stronger response. Data is shown from two subjects, one in each row. Color scale in CEST maps is 0-13%, negative normalized contrast. The slight left shift in the histograms reflects the color change seen in the maps. The 99% confidence interval for the mean change in the left precentral gyrus (locus of M1) for all stimulated subjects was .13-.33% gluCEST contrast. A 0.3% decrease, for example, would correspond to a shift from .083 to .08 on this axis.

before they had received either the sham or real stimulation. Average gluCEST values range from 7-9%, typical for gray matter regions in healthy subjects using this protocol. Interestingly, there appears to be some anatomic variability in gluCEST values in this slice at baseline; however, we did not attempt to further interpret these results, given the limited number of subjects. Figure 4.4B shows the same data in the sham subjects (n = 5), 'post-sham'. While there is some noise in the data, these values generally appear to remain unchanged in comparison to the baseline values for the whole group shown in 4.4A. In contrast, Figure 4.4C, showing the post-stimulation (cTBS) gluCEST averages (n = 10), is quite different from the baseline and post-sham results. Several segments, not only M1 (stimulation target, indicated by green arrow) show a decrease in average gluCEST value compared to the baseline measurement.

**Unpaired T-tests** were performed comparing the pixelwise data of these segments between the 'pre' and 'post' scans for both groups. **Table 4.1** lists the results of these T-tests in the form of the upper and lower 99% confidence intervals of the mean change in that segment (post-pre) as well as the corresponding P-value. Very low P-values, indicating high statistical significance, are highlighted in bold. This includes many segments in the left hemisphere of the brain of stimulated subjects, and one in the right hemisphere. No very low P-values ( $P < 1e^{-4}$ ) were calculated for sham subject data. Interestingly, the left precentral gyrus – the locus of M1—is not the segment with the greatest change in mean value, and the contralateral right precentral gyrus is not amongst those segments in which a strongly statistically significant change was observed. The same data is presented in bar plots in **Figure 4.5**.

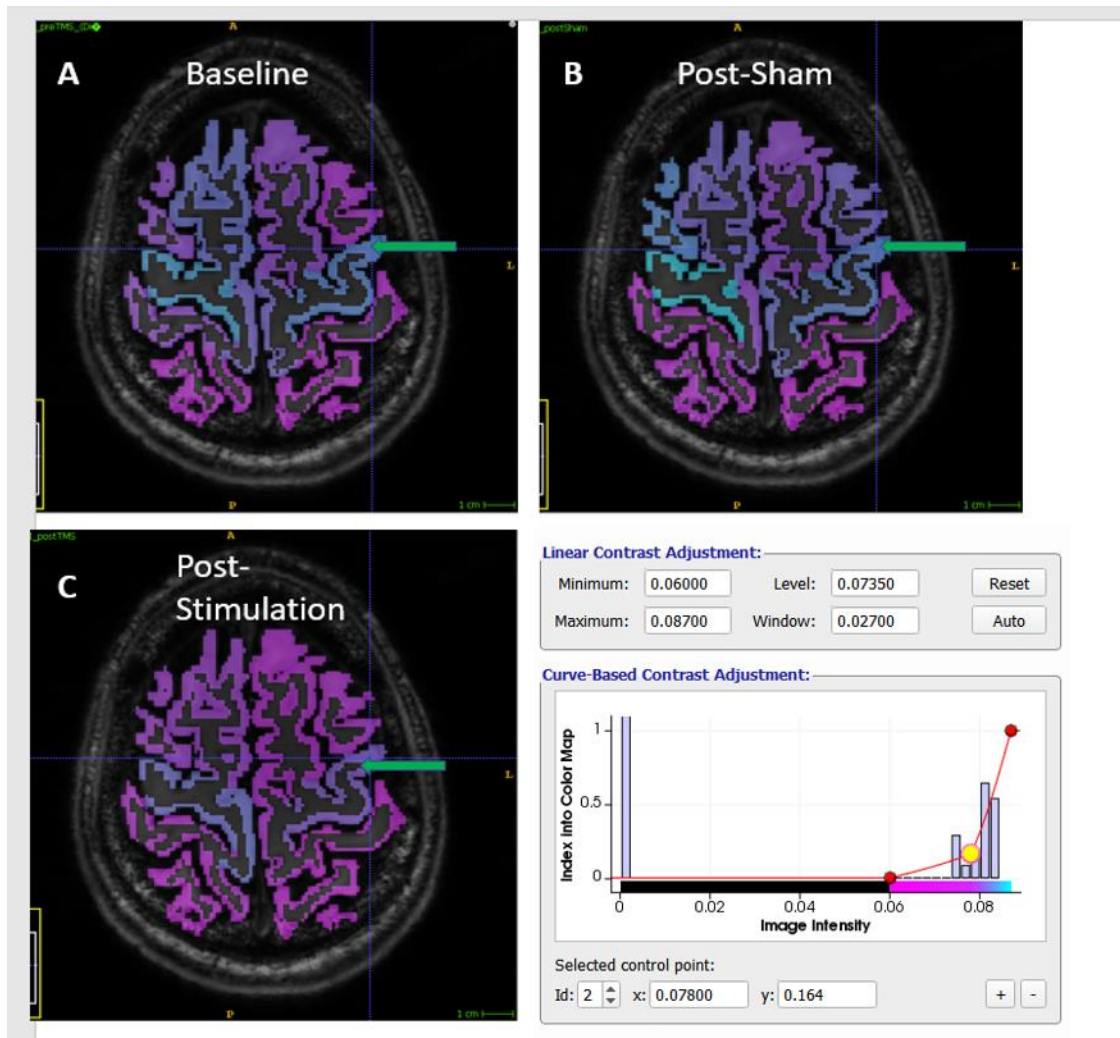


**Figure 4.4. Segmentwise gluCEST maps.** Data from all subjects projected onto the anatomy of a single subject for visual representation. A) average gluCEST by segment, baseline (pre-stimulation) -15 subjects. B) post "sham" (placebo) stimulation - 5 subjects. C) post cTBS (real) stimulation -- 10 subjects. The color scale is identical in all maps, with settings as shown in the screenshot from ITK-SNAP. Green arrow indicates the left precentral gyrus, the intended target of cTBS in stimulated subjects. Please see the color coding in **Figure 4.2** for full listing of anatomical segments treated distinctly in this analysis.

<b>Table 4.1</b>	<b>Sham subjects</b>			<b>Stimulated Subjects</b>		
<b>Left</b>	Upper bound	Lower bound	P-value	Upper bound	Lower bound	P-value
Precentral Gyrus	0.26	-0.05	7.9E-02	-0.11	-0.33	<b>3.5E-07</b>
Caudal Middle Frontal Gyrus	0.01	-0.33	1.4E-02	0.05	-0.16	1.8E-01
Rostral Middle Frontal Gyrus	0.03	-0.26	3.8E-02	0.08	-0.3	1.5E-01
Superior Frontal Gyrus	0.16	-0.04	1.3E-01	-0.1	-0.24	<b>4.2E-10</b>
Postcentral Gyrus	0.40	0	9.7E-03	-0.14	-0.44	<b>5.5E-07</b>
Superior Parietal Lobe	0.31	-0.1	1.9E-01	-0.13	-0.44	<b>3.5E-06</b>
Precuneus	0.41	-0.2	3.6E-01	-0.23	-0.82	<b>6.4E-06</b>
Paracentral Gyrus	0.58	0.1	3.0E-04	-0.12	-0.44	<b>6.6E-06</b>
<b>Right</b>						
Precentral Gyrus	0.18	-0.12	5.7E-01	0.03	-0.17	7.4E-02
Caudal Middle Frontal Gyrus	0.14	-0.19	7.1E-01	0.12	-0.1	7.9E-01
Rostral Middle Frontal Gyrus	0.01	-0.31	1.9E-02	0.47	0.05	1.8E-03
Superior Frontal Gyrus	0.05	-0.17	1.7E-01	-0.11	-0.25	<b>1.6E-11</b>
Postcentral Gyrus	-0.09	-0.49	2.0E-04	-0.06	-0.32	1.6E-04
Superior Parietal Lobe	0.29	-0.12	2.9E-01	-0.05	-0.3	4.6E-04
Precuneus	0.15	-0.43	2.1E-01	0.27	-0.33	8.0E-01

#### 4.4 Discussion

In this study, we used gluCEST, a unique form of MRI in which the image contrast is weighted for the presence of glutamate, to image the brains of healthy volunteers who have undergone continuous theta-burst stimulation (cTBS). A number of studies have performed magnetic resonance spectroscopy (MRS) upon TMS; a recent review gives a comprehensive summary of their contexts and findings<sup>23</sup>. However, it appears that this is the first time that gluCEST has been used for this purpose. Excitingly, gluCEST presents a tool that directly ameliorates some of the shortcomings of MRS for measuring glutamate: namely, sensitivity and spatial resolution.



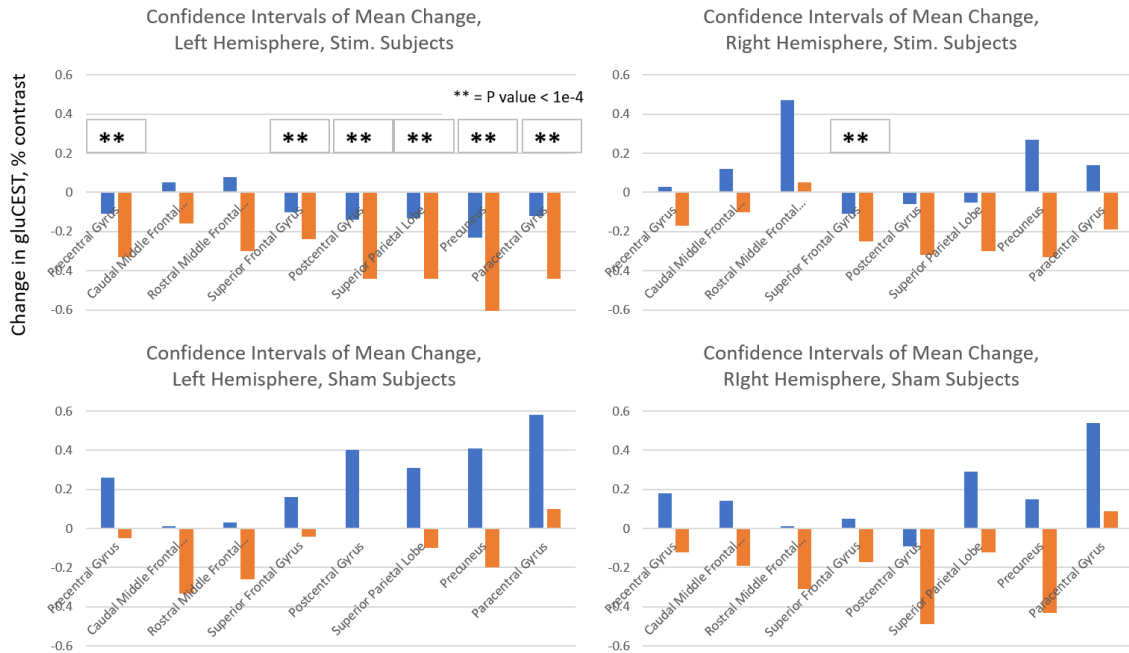


**Figure 4.5:** Barplot of gluCEST changes by segment: 99% confidence intervals (CI) of mean change, as report by unpaired T-test. A cluster of two bars, representing the upper and lower bound of the confidence interval, is shown for each segment, beginning with the Precentral Gyrus for each side. The 'true' change likely lies between the two confidence intervals, generally giving a value near zero for sham subjects and most right hemisphere segments, but a small negative value for stimulated subjects. The double asterisks indicate where p-values reflected a high statistical significance of the change.

We find that on average, small but very statistically significant changes appear in the gluCEST values from the brains of stimulated subjects; specifically, that gluCEST decreases in the left hemisphere in stimulated subjects, but not generally in the right hemisphere and not in subjects who received a 'sham' stimulation in between imaging sessions. The gluCEST decrease, which was on the order of 0-5% of the baseline value (varying between subject and area of the brain) and was not strongly localized, but appeared in several segments that are topologically contiguous with the left motor cortex (M1), which was the site of stimulation. There are perhaps two separate and interesting observations here which merit discussion and interpretation in the context of existing literature:

- a) the spatial distribution of the measured change
- b) the sign of this change –i.e. decrease of gluCEST upon administration of cTBS

The observation of the **spatial distribution** of a TMS-effected metabolic change other than BOLD is unique to this study. GluCEST is perhaps the only way to detect glutamate *in vivo* with spatial resolution comparable to other forms of magnetic resonance imaging (MRI). For MR-based detection of specific metabolites, the standard approach is to use single-voxel MR spectroscopy (MRS or SVS) , as employed in existing studies of TMS. Spectroscopy is an optimal and robust way to measure a number of chemicals in the brain; and indeed, the only way to measure some of them. Spatially resolved versions of spectroscopy are known as Magnetic Resonance Spectroscopic Imaging (MSRI) or Chemical Shift Imaging (CSI). The ability of these techniques to detect any particular molecule with high spatial resolution is limited by the SNR of that molecule's contribution to the NMR spectrum. Even for the highest-concentration neurometabolites like N-acetyl aspartate, creatine and choline, the spatial resolution of spectroscopic imaging has not been demonstrated to exceed a few millimeters in each dimension, as in recent work<sup>39</sup>. Glutamate is in fact difficult to quantify accurately even with SVS, due to its high degree of spectral overlap with glutamine<sup>40</sup>. Robust measurement and quantification of glutamate by a spectroscopy-based technique requires a large voxel with a high number of averages.

While our results measuring the spatial distribution of the TMS-induced changes are preliminary, they serve to highlight that the TMS pulse effects more than just its nominal target, which is often a motor target whose stimulation results in an observable muscle motion. The fact that the two segments of the ipsilateral hemisphere which apparently remain unperturbed by cTBS to M1 – the caudal and rostral middle frontal lobes—are proximal to, but not

topologically contiguous with, M1 suggests that the distribution of effects may have to do more with neural connectivity rather than off-target action of the pulsed field itself. Interestingly, the only contralateral effect we observed was in the superior frontal gyrus. We anticipate additional informative findings about the spatial profile of TMS-induced metabolic effects as we replace the single-slice gluCEST image with a larger, volumetric acquisition in future studies.

As for observations (b) and (c), it would appear from reviewing the literature that little conclusive understanding of the relationship between administration of particular TMS protocols and concentrations of glutamate has been gained by MRS<sup>23</sup>. According to the review by Cuypers and Marsman, a number of apparently contradictory results have been reported regarding the existence and sign of a correlation between TMS-based measures of electrophysiology and MRS-based measurements of glutamate and other metabolites. The same is true regarding measurements of the effect of TMS itself. With regard to glutamate, this is not terribly surprising, given the limitations of spectroscopy for detecting it -- particularly at 3T, at which the overwhelming number of studies were performed. Moreover, variability in the TMS protocols under investigation adds degrees of freedom that make such meta-analysis difficult. However, one particularly comprehensive study of metabolic changes upon TMS was that of Dyke *et al* 2017, one of the few studies to perform spectroscopy at 7T and compare to it several different electrophysiology based measures that are used in the field<sup>41</sup>. They find statistically significant correlations between spectroscopic measurements of glutamate and two different TMS-based measures: what they designate as "Intracortical Facilitation" and the "Input/Output plateau". Interestingly, they find that these two correlations are of opposite sign, suggesting that the relationships between metabolite concentrations and various electrophysiologic parameters may be more complex and sensitive than many of the existing analyses allow for.

Our measurement indicates that the concentration of glutamate decreases in the brains of stimulated subjects at ~30 minutes post-cTBS. It is difficult to say definitively whether, on the whole, this imaging result corroborates existing work about cTBS physiology, as no directly comparable experiment has been done before.

#### **4.5 Conclusions**

We believe that the increased sensitivity of gluCEST relative to spectroscopy has allowed us to detect subtle changes in glutamate concentration that so far have been inaccessible to the TMS research community. Furthermore, our results provide information about the spatial distribution of the TMS effect which is unprecedented in existing measurements.

Given the preliminary nature of our study, we refrain at this time from putting forth any specific mechanistic conclusions about cTBS based on our observations. Indeed, the goal of this preliminary study was simply to explore the utility of gluCEST as a method to study TMS. The presence of coherent, statistically significant findings despite the small number of participants in the study is very encouraging, and illustrates that indeed the spatially resolved molecular imaging capabilities of gluCEST have a role to play in elucidating the chemical mechanisms of therapy by non-invasive stimulation. The obvious areas for expansion in our further work include implementation of a newly developed volumetric gluCEST protocol, acquisition of additional types of MEP-related measures, and experiments which interleave in-magnet administration of TMS with real-time MR measurements.

## References

1. Valero-Cabré A, Amengual JL, Stengel C, Pascual-Leone A, Coubard OA. Transcranial magnetic stimulation in basic and clinical neuroscience: A comprehensive review of fundamental principles and novel insights. *Neurosci Biobehav Rev*. 2017;83:381-404. doi:10.1016/j.neubiorev.2017.10.006
2. transcranial-brain-stimulation-science-and-ethics-3-638.jpg (638x493). Accessed April 3, 2021. <https://image.slidesharecdn.com/stimethics-101123120122-phpapp01/95/transcranial-brain-stimulation-science-and-ethics-3-638.jpg?cb=1422521038>
3. Home | Laboratory for Cognition and Neural Stimulation | Perelman School of Medicine at the University of Pennsylvania. Accessed April 3, 2021. <https://www.med.upenn.edu/lcns/>
4. Barker AT, Jalinous R, Freeston II. Non-invasive magnetic stimulation of human motor cortex. *Lancet*. Published online May 1985. <http://www.bem.fi/library/1985-002.pdf>
5. Wagner T, Valero-Cabre A, Pascual-Leone A. Noninvasive Human Brain Stimulation. *Annu Rev Biomed Eng*. 2007;9(1):527-565. doi:10.1146/annurev.bioeng.9.061206.133100
6. Cheeran B, Koch G, Stagg CJ, Baig F, Teo J. Transcranial magnetic stimulation: From neurophysiology to pharmacology, molecular biology and genomics. *Neuroscientist*. 2010;16(3):210-221. doi:10.1177/1073858409349901
7. Coslett HB, Monsul N. Reading with the right-hemisphere: Evidence from transcranial magnetic stimulation. *Brain Lang*. 1994;46(2):198-211. doi:10.1006/brln.1994.1012
8. McNamara B, Ray JL, Arthurs OJ, Boniface S. Transcranial magnetic stimulation for depression and other psychiatric disorders. *Psychol Med*. 2001;31:1141-1146. doi:10.1017/S0033291701004378
9. Suppa A, Huang YZ, Funke K, et al. Ten Years of Theta Burst Stimulation in Humans: Established Knowledge, Unknowns and Prospects. *Brain Stimul*. 2016;9(3):323-335. doi:10.1016/j.brs.2016.01.006
10. Trippe J, Mix A, Aydin-Abidin S, Funke K, Benali A. Theta burst and conventional low-frequency rTMS differentially affect GABAergic neurotransmission in the rat cortex. *Exp Brain Res*. 2009;199(3-4):411-421. doi:10.1007/s00221-009-1961-8
11. Michael N, Gössling M, Reutemann M, et al. Metabolic changes after repetitive transcranial magnetic stimulation (rTMS) of the left prefrontal cortex: a sham-controlled proton magnetic resonance spectroscopy ( $^1\text{H}$  MRS) study of healthy brain. *Eur J Neurosci*. 2003;17(11):2462-2468. doi:10.1046/j.1460-9568.2003.02683.x
12. Di Lazzaro V, Pilato F, Dileone M, et al. The physiological basis of the effects of intermittent theta burst stimulation of the human motor cortex. *J Physiol*. 2008;586(16):3871-3879. doi:10.1113/jphysiol.2008.152736
13. Tang A, Thickbroom G, Rodger J. Repetitive Transcranial Magnetic Stimulation of the Brain: Mechanisms from Animal and Experimental Models. *Neuroscientist*. 2017;23(1):82-94. doi:10.1177/1073858415618897
14. Huang YZ, Edwards MJ, Rounis E, Bhatia KP, Rothwell JC. Theta burst stimulation of the

- human motor cortex. *Neuron*. 2005;45(2):201-206. doi:10.1016/j.neuron.2004.12.033
15. Huang YZ, Rothwell JC, Chen RS, Lu CS, Chuang WL. The theoretical model of theta burst form of repetitive transcranial magnetic stimulation. *Clin Neurophysiol*. 2011;122(5):1011-1018. doi:10.1016/j.clinph.2010.08.016
  16. Di Lazzaro V, Pilato F, Saturno E, et al. Theta-burst repetitive transcranial magnetic stimulation suppresses specific excitatory circuits in the human motor cortex. *J Physiol*. 2005;565(3):945-950. doi:10.1113/jphysiol.2005.087288
  17. Rosenkranz K, Rothwell JC. Differences between the effects of three plasticity inducing protocols on the organization of the human motor cortex. *Eur J Neurosci*. 2006;23(3):822-829. doi:10.1111/j.1460-9568.2006.04605.x
  18. Russmann H, Lamy JC, Shamim EA, Meunier S, Hallett M. Associative plasticity in intracortical inhibitory circuits in human motor cortex. *Clin Neurophysiol*. 2009;120(6):1204-1212. doi:10.1016/j.clinph.2009.04.005
  19. Ziemann U, Hallett M, Cohen LG. Mechanisms of deafferentation-induced plasticity in human motor cortex. *J Neurosci*. 1998;18(17):7000-7007. doi:10.1523/jneurosci.18-17-07000.1998
  20. Huang Y-Z, Rothwell JC, Edwards MJ, Chen R-S. Effect of Physiological Activity on an NMDA-Dependent Form of Cortical Plasticity in Human. *Cereb Cortex*. 2008;18(3):563-570. doi:10.1093/cercor/bhm087
  21. Artola A, Singer W. Long-term potentiation and NMDA receptors in rat visual cortex. *Nature*. 1987;330(6149):649-652. doi:10.1038/330649a0
  22. Teo JTH, Swayne OB, Rothwell JC. Further evidence for NMDA-dependence of the after-effects of human theta burst stimulation. *Clin Neurophysiol*. 2007;118(7):1649-1651. doi:10.1016/j.clinph.2007.04.010
  23. Cuypers K, Marsman A. Transcranial magnetic stimulation and magnetic resonance spectroscopy: Opportunities for a bimodal approach in human neuroscience. *Neuroimage*. 2021;224:117394. doi:10.1016/j.neuroimage.2020.117394
  24. Stagg CJ, Wylezinska M, Matthews PM, et al. Neurochemical effects of theta burst stimulation as assessed by magnetic resonance spectroscopy. *J Neurophysiol*. 2009;101(6):2872-2877. doi:10.1152/jn.91060.2008
  25. Patel AB, de Graaf RA, Martin DL, Battaglioli G, Behar KL. Evidence that GAD<sub>65</sub> mediates increased GABA synthesis during intense neuronal activity *in vivo*. *J Neurochem*. 2006;97(2):385-396. doi:10.1111/j.1471-4159.2006.03741.x
  26. Allen CPG, Dunkley BT, Muthukumaraswamy SD, et al. Enhanced awareness followed reversible inhibition of human visual cortex: A combined TMS, MRS and MEG study. *PLoS One*. 2014;9(6). doi:10.1371/journal.pone.0100350
  27. Vidal-Piñeiro D, Martín-Trias P, Falcón C, et al. Neurochemical modulation in posteromedial default-mode network cortex induced by transcranial magnetic stimulation. *Brain Stimul*. 2015;8(5):937-944. doi:10.1016/j.brs.2015.04.005
  28. Marjańska M, Lehericy S, Valabrègue R, et al. Brain dynamic neurochemical changes in

- dystonic patients: A magnetic resonance spectroscopy study. *Mov Disord*. 2013;28(2):201-209. doi:10.1002/mds.25279
29. Dubin MJ, Mao X, Banerjee S, et al. Elevated prefrontal cortex GABA in patients with major depressive disorder after TMS treatment measured with proton magnetic resonance spectroscopy. *J Psychiatry Neurosci*. 2016;41(3):E37-E45. doi:10.1503/jpn.150223
  30. Greenhouse I, King M, Noah S, Maddock RJ, Ivry RB. Individual differences in resting corticospinal excitability are correlated with reaction time and GABA content in motor cortex. *J Neurosci*. 2017;37(10):2686-2696. doi:10.1523/JNEUROSCI.3129-16.2017
  31. Du X, Rowland LM, Summerfelt A, et al. TMS evoked N100 reflects local GABA and glutamate balance. *Brain Stimul*. 2018;11(5):1071-1079. doi:10.1016/j.brs.2018.05.002
  32. Cai K, Haris M, Singh A, et al. Magnetic resonance imaging of glutamate. *Nat Med*. 2012;18(2):302-306. doi:10.1038/nm.2615
  33. Kim M, Gillen J, Landman BA, Zhou J, Van Zijl PCM. Water saturation shift referencing (WASSR) for chemical exchange saturation transfer (CEST) experiments. *Magn Reson Med*. 2009;61(6):1441-1450. doi:10.1002/mrm.21873
  34. Volz S, Nöth U, Rotarska-Jagiela A, Deichmann R. A fast B1-mapping method for the correction and normalization of magnetization transfer ratio maps at 3 T. *Neuroimage*. 2010;49(4):3015-3026. doi:10.1016/j.neuroimage.2009.11.054
  35. Cember ATJ, Hariharan H, Kumar D, Nanga RPR, Reddy R. Improved method for post-processing correction of B1 inhomogeneity in glutamate weighted CEST images of the human brain. *NMR Biomed*. 2021;in press.
  36. Desikan RS, Ségonne F, Fischl B, et al. An automated labeling system for subdividing the human cerebral cortex on MRI scans into gyral based regions of interest. *Neuroimage*. 2006;31(3):968-980. doi:10.1016/j.neuroimage.2006.01.021
  37. Yushkevich PA, Piven J, Hazlett HC, et al. User-guided 3D active contour segmentation of anatomical structures: Significantly improved efficiency and reliability. *Neuroimage*. 2006;31(3):1116-1128. doi:10.1016/j.neuroimage.2006.01.015
  38. Yushkevich PA, Pluta JB, Wang H, et al. Automated volumetry and regional thickness analysis of hippocampal subfields and medial temporal cortical structures in mild cognitive impairment. *Hum Brain Mapp*. 2015;36(1):258-287. doi:10.1002/hbm.22627
  39. Hingerl L, Strasser B, Moser P, et al. Clinical High-Resolution 3D-MR Spectroscopic Imaging of the Human Brain at 7 T. *Invest Radiol*. 2020;55(4):239-248. doi:10.1097/RLI.0000000000000626
  40. Graaf RA de. *In Vivo NMR Spectroscopy: Principles and Techniques*. Third Edii. Wiley; 2019.
  41. Dyke K, Pépés SE, Chen C, et al. Comparing GABA-dependent physiological measures of inhibition with proton magnetic resonance spectroscopy measurement of GABA using ultra-high-field MRI. *Neuroimage*. 2017;152:360-370.

# Chapter 5: Volumetric (3D) gluCEST enables *in vivo* detection of metabolic differences between human hippocampal subfields

## 5.1 Introduction

The medial temporal lobe (MTL) has been identified by modern neuroscience to be the locus of learning and memory formation, and many neurodegenerative conditions gradually impair cognitive ability because of their damage to these structures. The MTL is generally considered to include the hippocampus proper, the dentate gyrus (DG), entorhinal cortex (EC), and subiculum<sup>1</sup>

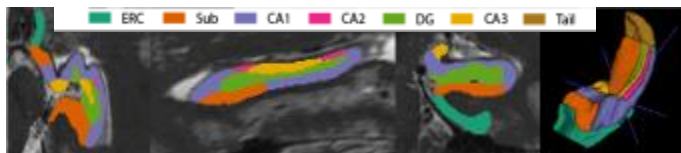
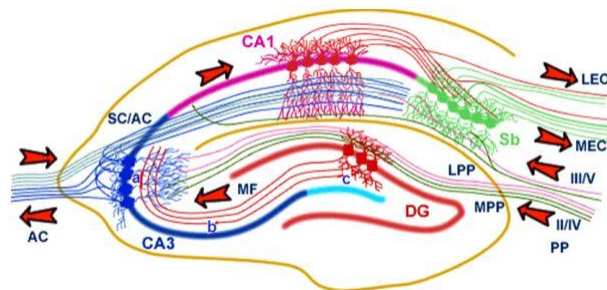


**Figure 5.1. The Human Hippocampus.** Top: Schematic of hypothesized connections and information flow during “pattern separation” activities of the hippocampus and neighboring regions [ref. 11]. Bottom: Illustration of the ever-evolving field of image analysis specialized for the MTL, including a 3D reconstruction (right).

(see **Figure 5.1**<sup>13</sup>). Together with the perirhinal and parahippocampal cortices, these structures play vital roles in cognitive function which rely on glutamate-mediated signaling<sup>2-6</sup>. Within this role, different subfields are known to have distinct functions; for example, the DG has been assigned as the locus of ‘pattern separation’<sup>7-9</sup> and spatial memory formation,

<sup>13</sup> Ref for bottom portion of Figure 5.1: Lund DR, Gade MT, Jensen T, et al. Multi-Contrast Hippocampal Subfield Segmentation for Ultra-High Field 7T MRI Data Using Deep Learning. In: Proc. of Ann. Meeting of the Intl. Soc. Mag. Res. Med..2020.



while CA3<sup>14</sup>, of ‘pattern completion’<sup>1,7,8,10–12</sup>. The distinct role of CA1, particularly as separate from the DG, remains under investigation and discussion<sup>9,10,13–18</sup>. The DG is known to be the locus of neurogenesis in both physiological and pathological contexts<sup>19,20</sup>, but it is unclear whether it shares that capacity with other nearby subfields<sup>10</sup>. Interestingly, it has been shown that certain glutamate receptors, particularly the N-methyl-D-aspartate (NMDA) receptor, are expressed in higher density in dentate gyrus cells than in those of CA1 and other subfields<sup>18,21</sup>. One could hypothesize that amongst other molecular differences, variability in and sensitivity to glutamate metabolism and signaling may underlie the very specific functionality of the MTL subfields.

As previously discussed, gluCEST<sup>22</sup> is nearly unique in its ability to provide non-invasive, spatially resolved measurements of glutamate *in vivo*. In both preclinical and clinical studies, gluCEST measurements have been shown to correlate with the presence or progression of disease in the brain<sup>23–32</sup>. One previous work from our group demonstrated that a decrease in gluCEST was correlated with synapse loss – as verified by histopathology - -in animal models of neurodegeneration<sup>23</sup>. A detail from the findings of this work was that in all animals – genetic variant and WT, and across all ages – the gluCEST measured in the dentate gyrus was higher than in other regions. However, it is both technically challenging to identify anatomy accurately in images of the mouse brain and conceptually unclear in some cases how to map findings to human neurological function, as the subfield anatomy is not identical and the functions are of obviously disparate complexity. In human beings, perhaps the leading example of gluCEST

---

<sup>14</sup> The initials ‘CA’ stand for the Latin name *cornu ammonis*, an earlier name for these regions now classified as the hippocampus. This full term is rarely found in the current scientific literature, while certain subfields retain the vestigial labels CA1, CA2, CA3 and CA4. Apparently, general opinion has favored the comparison with sea horse (*hippocampus*) rather than ram’s horn (*cornu ammonis*) to describe the morphology of this important anatomy.

regional analysis to date is Cai 2013, who used a single-slice sagittal acquisition to capture and analyze gluCEST signal in a number of subcortical regions<sup>33</sup>. However, with this limited-volume acquisition, analysis of very small structures like hippocampal subfields was not possible.

We recently developed an improved correction for  $B_1$  inhomogeneity of gluCEST images of the human brain<sup>34</sup> which enabled high resolution, truly volumetric (3D k-space) imaging, even in inferior regions where  $B_1$  inhomogeneity is problematic. In this work, we extend single slice gluCEST MRI to partial 3D gluCEST imaging at 7T to image the MTL of healthy subjects.

## **5.2 Methods**

### ***5.2.1 MRI acquisition procedure***

This protocol was approved by the Institutional Review Board at the University of Pennsylvania, with written informed consent obtained prior to participation. Ten healthy adult subjects (3 female/7 male) ages 19-45 were scanned on a 7T scanner (MAGNETOM Terra, Siemens Healthcare, Erlangen, Germany) equipped with a 1Tx/32Rx head coil (Nova Medical, Wilmington, MA, USA). Our 3D CEST sequence is a spoiled gradient-echo acquisition, modified to include two saturation modules consisting of eight 100ms Hamming-windowed pulses at  $3.1\mu\text{T}$  RMS  $B_1$ , with a duty cycle of 99%. The acquisition has  $1 \times 1 \text{ mm}^2$  in-plane resolution over a field of view of  $240 \times 180 \text{ mm}^2$ , with the third dimension comprising of 12 slices of 2mm thickness each. The sequence implements GRAPPA with an acceleration factor of 2, and elliptical k-space acquisition with centric ordering in the slice and phase-encoding directions. Additional acquisitions over the same field of view included a water saturation acquisition (WASSR)<sup>35</sup> for  $B_0$  mapping, a flip/crush sequence for  $B_1$  mapping<sup>36</sup>, and the Siemens product sequence MP2RAGE for generation of  $T_1$  maps. A 3D reference image without saturation over the same FOV is also

collected for each slice. The total acquisition time of the 3D CEST experiment with these parameters, including manual optimization of the  $B_0$  field shim, is approximately 30 min.

### 5.2.3 Data processing and analysis

Post-processing was performed using in-house code written in MATLAB and MEX (Mathworks,

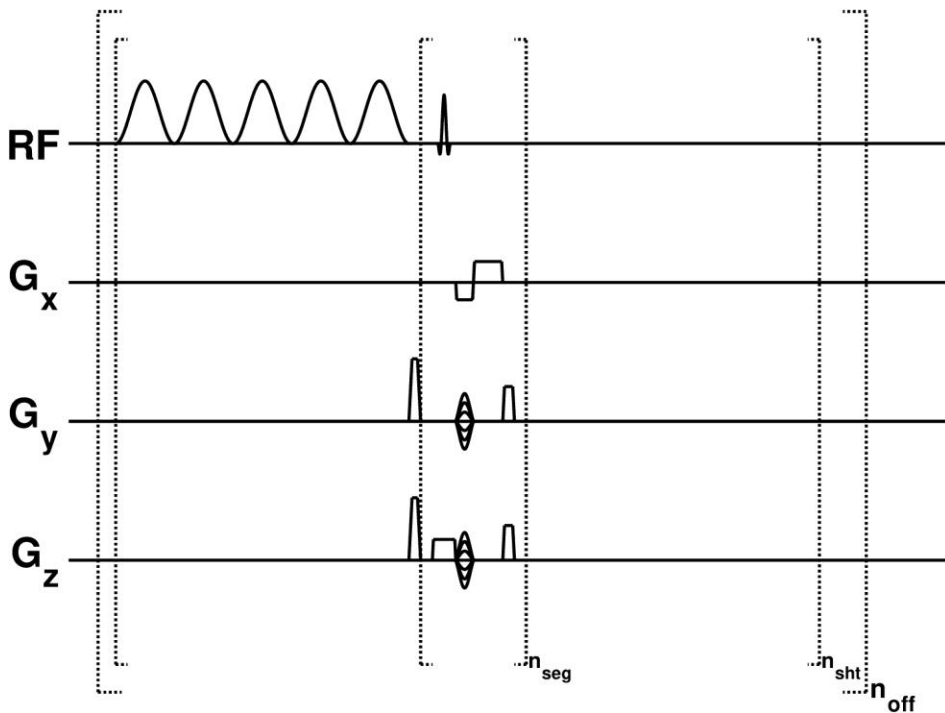


**Figure 5.2 Schematic of 3D CEST sequence.** Saturation module is depicted as the initial 5 broad-band pulses on the ‘RF’ line.  $N_{shots} = 2$ ;  $N_{shots} = 12$  or  $16$  for gluCEST, correspond to number of slices. (This pulse sequence as shown is not necessarily specific to gluCEST.) *Courtesy of N.E. Wilson.*

Natick, MA, USA), as described in<sup>33,37,38</sup> and in Chapters 1 and 2. CEST-weighted images were corrected for the  $B_0$  field distribution using WASSR. CEST images were corrected for  $B_1$  inhomogeneity using a procedure based on  $B_1$  and  $T_1$  mapping. A flowchart of the full CEST acquisition and post-processing procedure, including a summary of the  $B_1$  correction, is given as **Figure 1b.4** in this thesis.

Segmentation of the medial temporal lobe (MTL) was performed using the Magdeburg 7T Atlas available in the Distributed Segmentation Service of ITK-SNAP<sup>39-41</sup>, with T<sub>1</sub> and T<sub>2</sub>-weighted structural images as input. Regional averages and distributions were calculated and visualized using in-house code written in Matlab; statistical analysis was done using Matlab's 'T-test' function.

### 5.3 Results

**Figure 5.3 (next page): Individual slices of 3D gluCEST volume, shown with segmentation and B<sub>1</sub> maps.** First column: gluCEST image ('jet' color map, 0-15% negative-normalized asymmetry), filtered and overlaid with partial transparency on the T<sub>2</sub>-weighted structural image with color-coded segmentation. This view allows for observation of the fine differences in anatomy captured in each consecutive slice. Second column: only the unfiltered gluCEST map for the corresponding slice. Third column: relative B<sub>1</sub> maps for each slice ('hot' colormap) also overlaid with the segmented structural image. The dynamic contrast range shown in these maps is 0.4-1.0, such that the B<sub>1</sub> map is black and transparent in areas with relative B<sub>1</sub> < 0.4. This is the relative B<sub>1</sub> value below which it has been determined that measurement of gluCEST is not valid (see Chapter 2). We can observe that this B<sub>1</sub> drop-off occurs predominantly in the distal edges of the brain, and fortuitously does not strongly affect measurements of medial temporal lobe structures in most subjects, with the possible exception of area A36 of the perirhinal cortex.

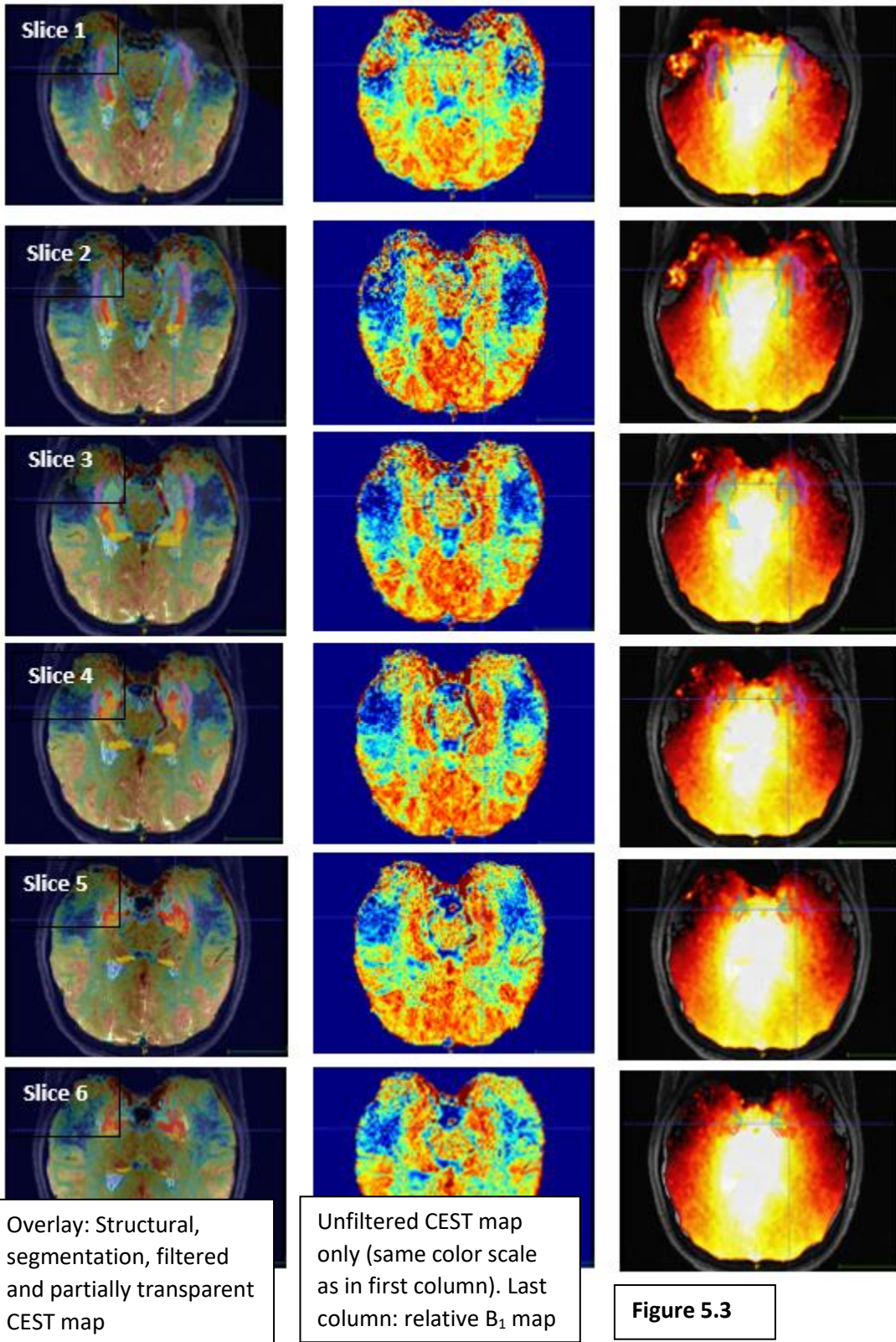


**Figure 5.3** shows six consecutive slices of our 12-slice 3D gluCEST acquisition, focusing on the medial temporal lobe (MTL) region. The slices are ordered in the direction inferior-superior, with the most inferior slice being Slice 1 and the most superior being Slice 6. (The total acquisition includes six additional slices in the superior direction, to make 12 total, but these are omitted from the figure so as to focus on the region containing the segments of interest.) The **left column** of this figure features an overlay of the CEST map ('jet' colormap, filtered) on the structural image on which a segmentation for hippocampal subfields is shown in opaque colors. This view demonstrates the value of acquiring higher resolution images along the superior-inferior axis, as the anatomy represented changes significantly from one 2mm slice to the next. In the 2D 5mm slice acquisition used previously, our field of view would have included only two of these six slices, and they would be superimposed on each other in a single image. Clearly, this is suboptimal for imaging of such fine structures such as those in the medial temporal lobe.

The **middle column** of **Figure 5.3** shows the gluCEST map, unfiltered and without the structural underlay. It is clear that there are still large portions of signal drop-out bilaterally in this inferior region of the brain, where the gluCEST signal is artificially very low (blue patches). This is a direct reflection of the  $B_1$  amplitude in these regions; the corresponding  $B_1$  maps for each slice are shown in the **right column**. These  $B_1$  maps ('hot' colormap) are scaled such that areas with relative  $B_1 < 0.4$  are without color; this is the value of relative  $B_1$  known to us to be insufficient for measurement of gluCEST. . Fortuitously for our present analysis, in most subjects this area of

low  $B_1$  does not strongly affect the MTL structures of interest, as they are located in the center of the head.

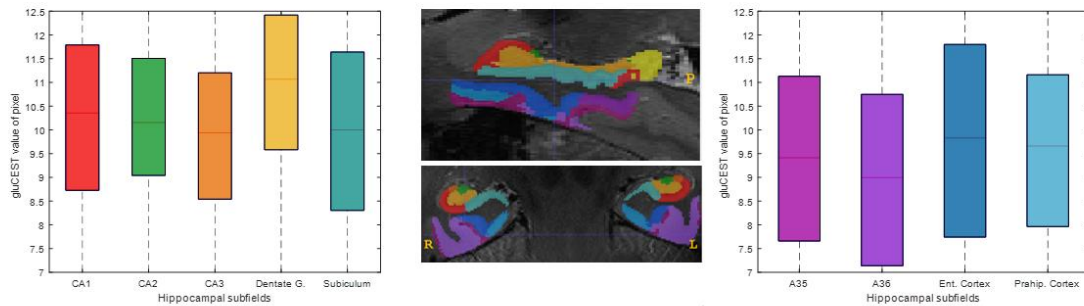


**Figure 5.4. Box plots of gluCEST values by segment.** *Center:* An example MTL segmentation is shown, with coloring of segments corresponding to the boxplots containing their gluCEST values. These include the CA1, CA2, CA3 and dentate gyrus subfields of the hippocampus, as well as the more inferior segments: the entorhinal and parahippocampal cortices and A35 and A36 of the perirhinal cortex. *Left, Right:* The gluCEST values over all pixels in the ROI and all subjects ( $n = 10$ ) are plotted as box and whisker plots, where the 25% and 75% percentiles form the boundaries of the box. The hippocampal tail, shown in yellow in the top portion of the segmented image (sagittal view), was not included in this analysis, as it was captured to

### 5.3.1 Identification of subfield-level metabolic differences: Elevated gluCEST in the dentate gyrus

Figure 5.4 shows box and whisker plots of bilateral gluCEST values (right and left sides of the brain tallied together) by MTL structures. The color of the boxes in the plot corresponds to the segmentation shown in the center, with the left plot featuring the subfields of the hippocampus, and the right plot featuring the perirhinal, entorhinal, and parahippocampal cortices. The colored portion of the box shows the middle two quartiles (25<sup>th</sup> percentile-75<sup>th</sup> percentile) of data, with the red line indicating the median. The number of pixels included in each of these vectors is tabulated in Table 1. The distribution of gluCEST values in the dentate gyrus is noticeably shifted relative to the remaining segments, with the 25<sup>th</sup> percentile, median, and 75<sup>th</sup> percentile all higher than the corresponding values in the other vectors. One will also notice that

region A36 of the perirhinal cortex has the lowest such values. However, upon inspection of the B<sub>1</sub> maps in the rightmost column of Figure 5.3, one can appreciate that in many subjects, the region of B<sub>1</sub> drop-off begins to overlap with the volume occupied by segment A36 (in purple). and, we have not been able to demonstrate that the gluCEST measurements of segment A36 are independent of B<sub>1</sub> value (see **Figures 5.7** and **5.8**).

**Figure 5.5** examines the laterality of these results. In this analysis, the five subfields of the hippocampus are treated separately between right and left hemispheres of the brain. A high degree of lateral symmetry is observed in the gluCEST values of the larger subfields – CA1, dentate gyrus (DG), and subiculum – with the measurement being less stable in the smaller subfields CA2 and CA3. We observe that the elevated gluCEST of the dentate gyrus is apparently a bilateral effect. The bottom portion of Figure 5.3 shows the distributions of the CA1 and DG

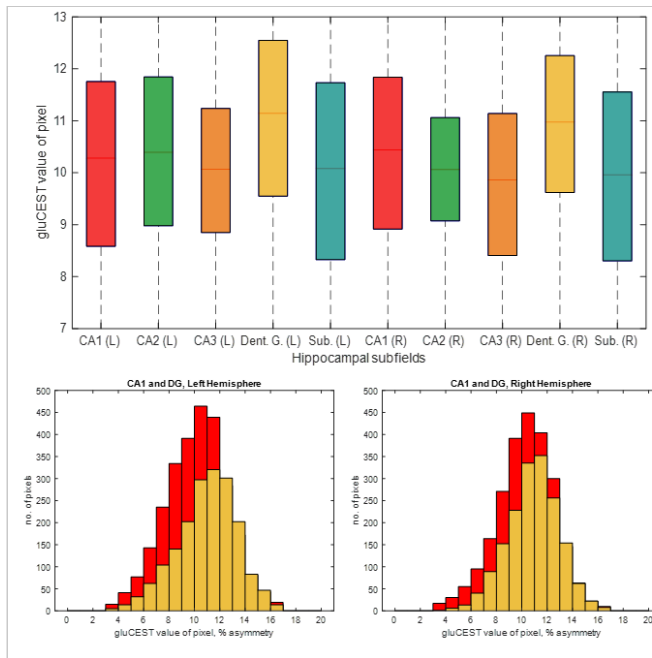


**Figure 5.5: Comparison of gluCEST values in left and right hippocampal subfields.** Top: This boxplot is analogous to those in 5.3, although rather than combining the corresponding measurements on the left and right sides of the brain, we inspect each separately. It can be seen from this plot that the gluCEST distribution in the dentate gyrus is higher than in the other subfields to a corresponding degree on both sides of the brain. Bottom: Histograms corresponding to the distribution of gluCEST values in CA1 and dentate gyrus of each laterality.

measurements – the same data shown in the box and

whisker plot-- as histograms. **Table 5.1** lists the means, standard deviations, and number of



**Table 5.1: GluCEST values measured in Medial Temporal Lobe subfields of healthy subjects (n = 10)**

Left/Right	Segment Name	No. of Pixels	Mean B <sub>1</sub>	Mean gluCEST	St. Dev, gluCEST
	A35 (Perirhinal Cortex)	1498	0.694146	8.79	2.59
	A36 (Perirhinal Cortex)	4697	0.616555	8.66	2.64
	CA1 (Hippocampus)	2738	0.741667	10.18	2.41
	CA2 (Hippocampus)	160	0.722587	10.29	2.26
	CA3 (Hippocampus)	307	0.78346	10.29	2.38
	<b>Dentate Gyrus</b>	415	0.806718	9.99	2.08
	Entorhinal Cortex	1823	0.749962	10.96	2.34
	Parahippocampal Cortex	2108	0.753862	9.69	2.94
	Subiculum	1507	0.760571	9.38	2.49
		2730	0.767093	9.85	2.56

**Table 5.1. GluCEST means and standard deviations by segment.** The first column lists the number of pixels included in the analysis vector (corresponding to the box and whisker plots in Figure 5.4; in Figure 5.5, right and left sides are combined). The next columns show the mean relative B<sub>1</sub> amplitude and gluCEST of the segment, with the standard deviation of the gluCEST measurement listed in the last column. Differences in the number of pixels included in a particular ROI largely arise from differences in slab placement relative to subject anatomy and head position.

pixels included  
in the vector  
of all  
segments as  
well as the  
corresponding  
average  
relative B<sub>1</sub>  
value over the  
segment.  
Having  
observed  
higher gluCEST  
in the dentate  
gyrus by  
examination  
of the mean  
values and  
distributions  
in all the

subfields measured, we sought to perform a statistical test that would confirm the observation more quantitatively. To this end, an unpaired T-test was performed evaluating the mean difference between all of the MTL subfields.

Figure 5.6 represents the results of this T-test in the form of colormaps showing the 99%

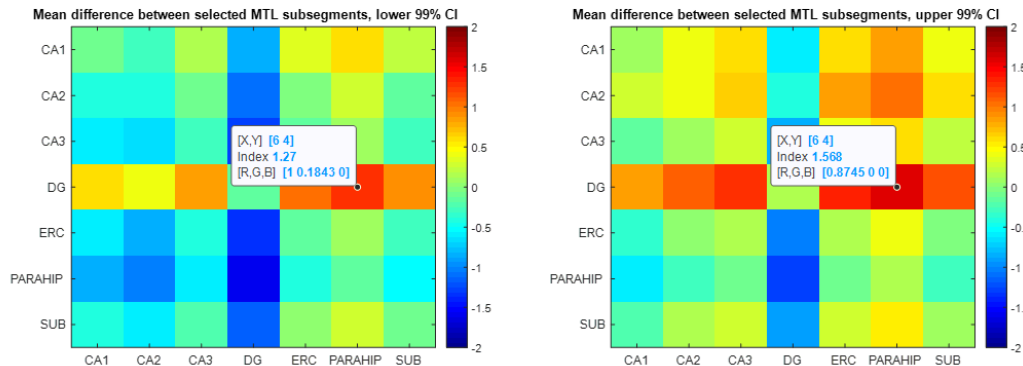


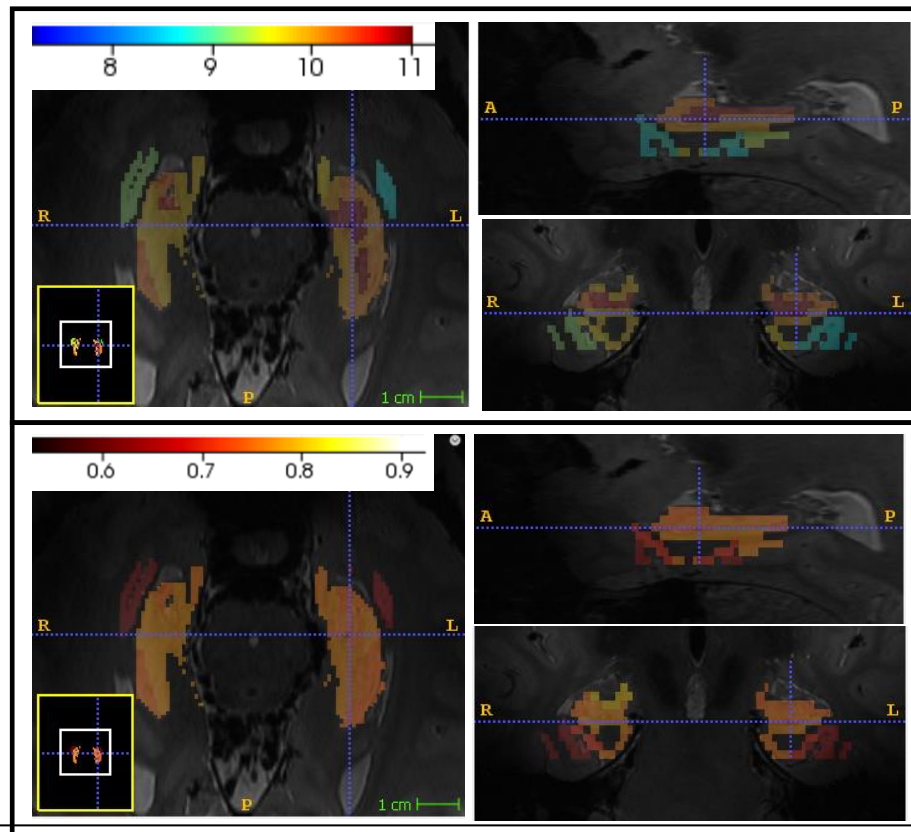
**Figure 5.6. T-test for statistically significant difference in gluCEST between segments: confidence interval colormaps.** The upper or lower 99% confidence intervals of the mean difference between two segments is shown as the corresponding matrix element. For example, the cursor is placed on the matrix element corresponding to the mean difference in gluCEST between the Dentate Gyrus (DG) and the Parahippocampal Cortex (PC). The results of this T-test indicate with 99% “confidence” that the DG has average gluCEST between 1.27 and 1.57 contrast units (% asymmetry) higher than the PC.

confidence intervals for the difference between mean values. The colormaps shown here represent these upper and lower values, C1 and C2, which estimate the difference between segment A and segment B, in a form analogous to a matrix or look-up table. The diagonal elements of each colormap are zero, as these elements represent the difference in mean between one segment and itself; corresponding elements reflected across the diagonal are additive inverses: (segment A – segment B) or (segment B- segment A). While most elements of the colormaps are filled with values close to zero (and colors close to green), the row and column representing gluCEST of the dentate gyrus exhibit a robust trend of higher mean value relative to all other segments shown. For example, the cursor in **Figure 5.6** is placed on the matrix elements representing MTL the 99% confidence interval for the quantity (mean gluCEST, dentate gyrus – mean gluCEST, parahip. cortex), giving the values 1.27 and 1.57. The estimate of

a 1.27-1.57 % contrast difference between these two segments agrees well with the differences in mean value calculated for each side (see Table 5.1):  $10.96 - 9.38 = 1.58$ ;  $10.88 - 9.66 = 1.22$ , respectively.

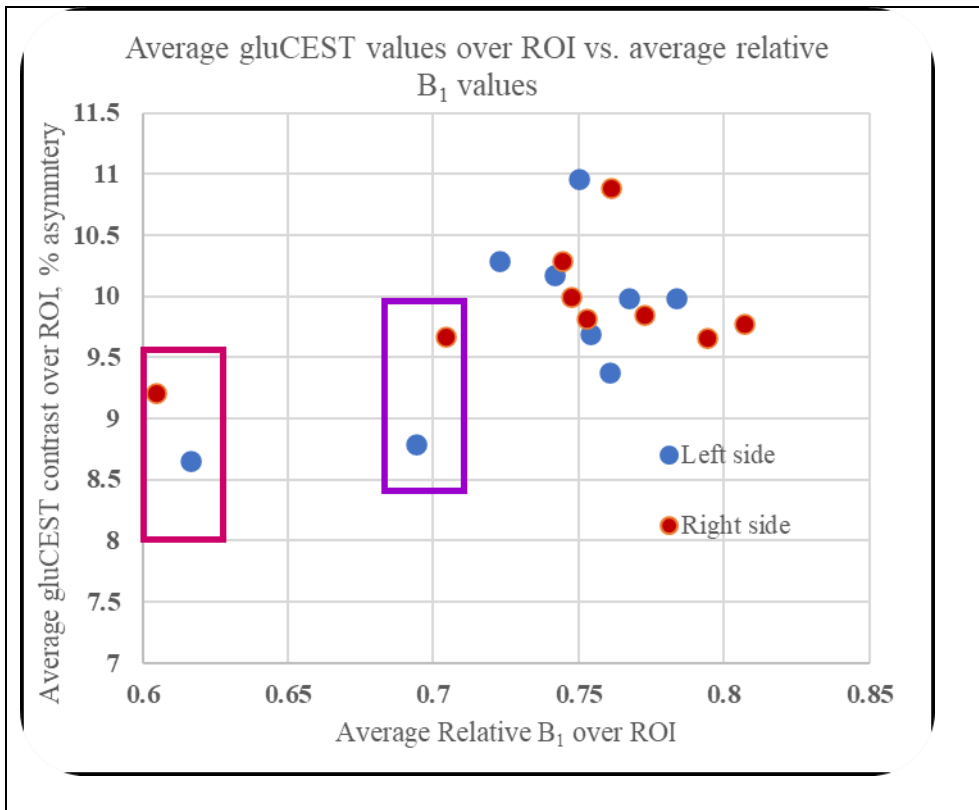
### 5.3.2 *gluCEST findings are independent of $B_1$ amplitude*

Figure 5.7 shows average values of gluCEST (top) and  $B_1$  amplitude (bottom) for all subjects, projected onto the anatomy of a single subject for visualization. The color of each segment



**Figure 5.7: Segmentwise maps of average  $B_1$  strength and gluCEST.** The color of each segment represents the average value over all pixels from this segment in all ten subjects. **Top: Average gluCEST (%) by segment.** The dentate gyrus, which has the highest average gluCEST is displayed in red, corresponding to its value. Some asymmetry is observed between the right and left sides in the perirhinal cortex (most inferior segments); this is likely due to the asymmetry of the  $B_1$  distribution in this part of the headcoil. **Bottom: Average relative  $B_1$  amplitude by segment.** It can be observed that while there is some inhomogeneity in the  $B_1$  amplitude over the MTL region, the gluCEST differences seen within the hippocampal subfields – such as the elevated gluCEST in the dentate gyrus – do not appear to reflect or originate from corresponding  $B_1$  amplitudes.

represents the average value over all pixels from this segment in all ten subjects. This visualization allows for an appreciation of the gluCEST ‘hot spot’ of the dentate gyrus, and also to illustrate the independence of the gluCEST measurement in the hippocampal subfields from the  $B_1$  distribution – which is quite uniform—in this region. In contrast, this representation does suggest, as posited above, that the lower gluCEST measured in A36 likely reflects the lower average  $B_1$  in this segment.



**Figure 5.8 : Relationship between average gluCEST and  $B_1$  amplitude.** While the ‘gluCEST as a function of  $B_1$ ’ plot appears to be flat in the range of average relative  $B_1 > 0.7$ , the data points representing segments A35 (pink rectangle) and A36 (purple rectangle) of the perirhinal cortex – the most inferior of measured subfields-- on either side are separate from the cluster of remaining segments.

**Figure 5.8**  
examines this  
relationship

between relative  $B_1$  and gluCEST. The two quantities (as listed in t **Table 5.1**) are plotted against

each other for each segment in the scatterplot. This plot appears to have no slope-- at least for the segments (all except A36) for which the average  $B_1$  is  $> 0.65$ .

## 5.4 Discussion

### *Elevated gluCEST in the dentate gyrus: literature precedents and interpretation*

Using a newly developed volumetric (3D) gluCEST protocol, we detected a statistically significantly higher glutamate signal in the dentate gyrus relative to other MTL subfields.

This is a novel finding enabled by the unique spatial resolution of gluCEST, but appears to be consistent with current knowledge of the neurochemistry in the MTL. It is generally understood that glutamate signaling is especially important in the medial temporal lobe, and that this high degree of excitatory signaling is correlated with synaptic and neural growth, plasticity, and memory formation. Moreover, the dentate gyrus is known to have roles distinct from other nearby subfields, amongst which it has been hypothesized that the DG may be the sole location of neurogenesis within the hippocampus. Our finding of slightly increased glutamate in the DG relative to other MTL subfields corroborates the paradigm that neurogenesis occurs preferentially in the dentate gyrus and is strongly dependent on glutamate signaling.

The closest precedent for this work was that of Crescenzi *et al*, who performed gluCEST imaging in murine models<sup>23</sup>. In this work, the authors detected an apparent k-means clustering of gluCEST signals from the hippocampus, corresponding to known functional subregions which have analogs in the more complex human structures. While the focus of this paper was differences between wild type mice and those with a genetic variant making them prone to neurodegeneration, the relatively elevated gluCEST signal in the dentate gyrus compared to the other regions held throughout mice of varying ages and in both populations. Along with

corroborating mechanistic understanding of the neurogenic role of the DG, the consistency of these results suggested a robust phenomenon likely conserved in the brains of other mammals.

It is worth noting explicitly the difference in regional analysis which produced the results of each of these studies: In Crescenzi et al, pixel values were clustered by k-means algorithm blind to their location in the image, and then these 'cluster masks' were visualized and found to correspond with anatomical regions. In this paper, recently developed high-resolution hippocampal subfield segmentations were registered to the CEST maps in order to classify pixels directly into their anatomical structures. The degree to which 'reslicing' the anatomical image into the grid of the CEST acquisition caused a decrease in resolution can be visualized in Figure 5.6, where some coarseness of the pixels is still apparent, particularly in the vertical (non-axial dimensions), in which the resolution of our gluCEST acquisition is only 2mm.

With continued collection of MTL gluCEST data using the present protocol or an updated iteration, we hope to document the MTL subfield gluCEST distributions on a full range of healthy subjects throughout the lifespan. Expansion of the current results will provide powerful insight into basic neurophysiology, and form a baseline reference to which results on aging, neurodegeneration, and other sources of variability can be compared.

### *3D gluCEST as a method to map neurochemistry: strengths, shortcomings and ongoing improvements*

At the moment, we believe that 3D gluCEST is the leading option for spatially resolved *in vivo* measurements of glutamate. The other <sup>1</sup>HNMR based option is spectroscopic imaging, whereby a spectrum is acquired in each voxel and fit for the components representing each metabolite.

At 7T it has been argued that spectroscopic imaging is able to produce spectra in which

glutamate and glutamine can be resolved<sup>42</sup>. Hingerl *et al*, for example, report maps of glutamate and glutamine fit separately in an MRSI map with  $3.8 \times 3.8 \times 3.8 \text{ mm}^3$  voxel size, although there are some features of these results which are difficult to interpret. Moreover, this does not match the spatial resolution of the gluCEST protocol attained here ( $1 \times 1 \times 2 \text{ mm}^3$ ). Likely, their approach could meet this resolution, but with extended scan time that would exceed the limits of human subject scanning. Their work does not attempt substructure analysis of the resulting measurements, but it would be of interest to compare results from gluCEST and such state of the art spectroscopic imaging methods, should comparable resolution be achieved.

On a practical level, for a few reasons there is a very high value of using a volumetric 3D slab as in this report –rather than a ‘single slice’ acquisition – in clinical CEST studies. Firstly, one simply captures more pixels per subject, lending greater statistical power for detecting what generally are quite subtle effects. Indeed, it is only severe pathology that could lead to a change in glutamate concentration on the order of multiple mM. For example, we would not have been able to confidently distinguish the elevated gluCEST signal from the dentate gyrus, as reported here, using a 2D imaging slice. Secondly, brain anatomy differs from person to person, and ‘single slice’ imaging studies invariably capture uneven and sometimes incomparable cross sections between subjects, despite the best practice of the experimenter. Lastly, CEST is extremely sensitive to subject motion, given that the final image is derived from multiple acquisitions fed as input into a multi-step post-processing pipeline in which there must be voxel-to-voxel correspondence. In the event of motion, unlike 2D slices, 3D volumes can be registered to each other to some degree, making the 3D experiment more motion-robust.

A weakness of gluCEST is its high sensitivity to  $B_1$  inhomogeneity<sup>37</sup>. The physics of the headcoil at 7T are such that standing waves generate large  $B_1$  variations over the brain, with a particularly

problematic drop-off of the  $B_1$  amplitude in the inferior portions. The larger the field of view of the gluCEST image, the wider range of  $B_1$  inhomogeneity present, and imaging inferior portions of the medial temporal lobe adequately previously posed a challenge. A recent update to our post-processing correction for  $B_1$  inhomogeneity improved the quality of the images we were able to generate using this 3D acquisition and increased our confidence in their accuracy. Nonetheless, in the current analysis we took several steps to ensure that the findings did not reflect residual influence of  $B_1$  inhomogeneity. While we believe the relative signals of the hippocampal subfields to be a true finding, we remain suspicious of the apparently lower signal in the A36 region of the perirhinal cortex, as this location is clearly plagued by lower  $B_1$  amplitude than the remaining anatomy. Fortunately, preliminary results (not presented here) indicate that application of high-dielectric padding may mitigate the remaining problem in this region.

Until recently, we considered this  $B_1$  inhomogeneity to be a major factor limiting our ability to expand gluCEST to a whole brain acquisition. However, in light of the demonstrated progress in  $B_1$  post-processing correction (See Chapter 2), as well as the improvement afforded by use of high-dielectric padding (see Chapter 5A),  $B_1$  inhomogeneity no longer represents the major challenge to expanding the coverage of gluCEST. Rather, meeting reasonable limitations on scan time is the major impediment to whole-brain imaging in a single session.

As with any imaging protocol, optimizations can be performed regarding the k-space sampling during the readout of the CEST sequence to allow for faster acquisition. However, a CEST acquisition presents a particular challenge on this front, as it relies on a saturation module which precedes the readout. The effect of the saturation pulse - -that is, the resulting CEST contrast – begins to decay when the saturation module is over. Thus, k-space points collected



later in the readout module contain less of the desired contrast than those collected earlier, in addition to any such considerations regarding the inherent contrast (PWD or  $T_1$ -weighted) of the readout module itself. At some point, this signal decay becomes limiting, and we must perform the imaging in multiple 'shots'; that is, more than one iteration of (saturation + readout) in order to cover all desired k-space volume. For our current 12 slice acquisition, we use two such shots. Obviously, the need for repeating the saturation pulse exacerbates the existing need for accelerating the acquisition. Computational mitigation of this decay is possible to some degree: one can correct for the decay of the saturation during the pulse train, provided one has estimated the kinetics of this process. However, like post-processing  $B_1$  correction, this is limited by the fact that, at a certain point, the signal is simply absent.

In principle, one could elect to expand our existing protocol to provide full-brain coverage with sacrifice of in-plane resolution. (The isotropic resolution of recently published full-brain APT CEST in the literature, for example, is lower than that of our gluCEST acquisition.<sup>43,44</sup>) However, we generally consider that in most cases, the scientific benefit afforded by increasing resolution more quickly exceeds that of expanding volume coverage -- although this, of course, this depends on the application. One can imagine that for a localization-type problem (e.g. finding an epileptic focus), very high resolution may be less important than covering more volume, if location is uncertain. On the other hand, an analysis of very small substructures like the one presented here could yet benefit from finer resolution.

Lastly, for gluCEST, it is imperative to have  $B_0$  and  $B_1$  maps accompanying the CEST acquisition. Thus the additional time needed for acquiring more volume is multiplied by the need for also expanding the coverage of these mapping techniques. For  $B_0$  mapping, a WASSR scan is approximately equivalent to a CEST scan in terms of temporal duration per volume. It would be

optimal to use faster phase-based field mapping techniques, provided we can ensure that the resulting  $B_0$  map is of equivalent accuracy. Replacing the field mapping step is amongst the protocol updates currently being tested.

## 5.5 Supplementary Information and Appendices to Chapter 5

### 5.5.1 Specifications of the 3D gluCEST sequence: comparison with 2D

Table 5.S1 Pulse sequence parameters	2D gluCEST: -B <sub>1</sub> calibration data -TMS -MCI	3D gluCEST
Base sequence	'prep MOCO' (gradient-recalled echo)	'prep TFL' (turbo-FLASH)
Additional sequence notes		--spoiled gradient-echo acquisition, modified to include two saturation modules --elliptical k-space acquisition with combined slice and phase-encode spiraling --GRAPPA acceleration factor: 2
TR, shot TR	4.7ms, (N/A, single shot)	3.5ms, 6s
TE	2.3ms	1.79ms
Flip angle	10°	6°
Field of view	156 x 192 x 5 mm	240 x 180 x 24 (or 32) mm
In-plane resolution	0.75 x 0.75 mm	1 x 1 mm
In-plane grid size	256 x 208	240 x 180
Saturation offset frequencies (Z-spectrum points) acquired, ppm relative to water	± {1.8, 2.1, 2.4, 2.7, 3.0, 3.3, 3.6, 3.9, 4.2}	± {1.8, 2.1, 2.4, 2.7, 3.0, 3.3, 3.6, 3.9, 4.2}
Saturation B <sub>1</sub> strength (nominal), RMS	210Hz (3.1μT)	210Hz (3.1μT)
B <sub>1</sub> pulse shape	Hamming window	Hamming window
Saturation pulse duration	800ms	800ms
Saturation pulse duty cycle	95%	99%
Saturation 'shots' per acquisition	1	2
Slices per acquisition	1	12 or 16
Slice thickness	5mm	2mm
Total thickness acquired	5mm	24 or 32 mm

Author's note: These pulse sequences were developed by Drs. Keija Cai, Mohammad Haris, Anup Singh, Hari Hariharan, Neil Wilson and others at the Center for Magnetic Resonance and Optical Imaging, U. Penn., 2012-2020. The work presented in this thesis centers on understanding the physical and chemical origin of the gluCEST signal, its dependence on saturation power, post-processing and analysis strategies for the acquired images, and resulting findings. Credit for the

programming of the sequences *per se* is due to the aforementioned individuals, whose contributions are gratefully acknowledged.

### ***5.5.2 Volumetric (3D) gluCEST facilitated by mitigation of $B_1$ inhomogeneity using dielectric padding***

#### ***5.5.2.1 Introduction***

As previously discussed,  $B_1$  inhomogeneity is an inherent problem in brain imaging at ultra-high field because of the comparable dimensions of the RF wavelength and the human head. CEST methods rely on the  $B_1$  field to create endogenous but transient contrast by applying a metabolite-selective saturation pulse. CEST is therefore significantly more vulnerable to  $B_1$  inconsistencies than most imaging sequences. Glutamate-weighted gluCEST is particularly challenging in this regard because, due to the fast exchange of its proton with water, it both requires ultra-high field (7T) and high ( $\sim 3\mu\text{T}$ )  $B_1$  strength to generate adequate contrast. In moving from single-slice (2D) imaging to volumetric slabs (3D), the absolute spread of  $B_1$  amplitude over the field of view increases and, because one now needs to collect more points in k-space per saturation pulse, the minimum  $B_1$  amplitude required to maintain glutamate-derived contrast at an acceptable level increases.

So far, we have discussed post-processing correction for  $B_1$  inhomogeneity in gluCEST. However, the fruitfulness of post-processing is of course limited by the content of the acquired signal itself. Investigators using gluCEST – and even those performing structural and functional imaging at 7T -- have struggled with the severe  $B_1$  drop-off in the inferior and anterior parts of the brain. Apart from ‘in silico’ post-processing solutions, there are two main categories ‘physical’ solutions to this problem: doing something differently with the RF hardware (as in parallel transmit), or doing something to change the physics of the RF propagation itself once it leaves

the coil. The latter concept gave rise to the approach of using high-dielectric paddings to manipulate the effective geometry of the “sample”, i.e. the human head, inside the coil. This approach is gaining popularity in the MR research community but remains investigational for reasons of safety and reproducibility.

Here we present 3D gluCEST data that has been improved by the use of dielectric pads to augment the  $B_1$  amplitude during acquisition. While dielectric pads have already been adopted in several 7T imaging studies, including NOE and APT CEST measurements<sup>7,20,21</sup>, their utility for glutamate imaging specifically has not yet been explored, despite the fact that this an application where they could make a particularly key improvement.

#### **5.5.2.2 Methods**

All images were obtained on a 7.0T scanner (MAGNETOM Terra, Siemens Healthcare, Erlangen, Germany) outfitted with a single volume transmit/32 channel receive phased array head coil (Nova Medical, Wilmington, MA, USA). Five volunteers ages 24-39 were scanned with informed consent under local regulatory supervision. Dielectric pads used were composed of  $\text{CaTiO}_3$  in  $\text{D}_2\text{O}$  (7TNS, Multiwave Imaging, Geneva, Switzerland). By positioning the three dielectric pads around the subject’s head --including, in deviation from manufacturer's instructions, some mask-like coverage of the face -- we were able to expand the portion of the image which has relative  $B_1 > 0.4$ , which we use as a threshold for useability in gluCEST measurements. (Images are still subjected to post processing correction for  $B_1$  inhomogeneity.) All gluCEST post-processing, including  $B_1$  correction, was done as previously described.

### 5.5.2.3 Results and Discussion

**Figure 5.S2** Left and middle: Dielectric (DE) pads shown by themselves and positioned relative to a subject (head coil not shown). When used with the 32-channel headcoil, the pads are held snugly curved around the subject's head, with the lateral pads partially covering the jaw, cheekbones and eyes beneath the coil visor. Right: B<sub>1</sub> map measured in deep axial slice including the hippocampus and surrounding structures. Upon use of DE pads, the B<sub>1</sub> map is significantly improved in the anterior portion of the head, which is poorly covered by the coil.

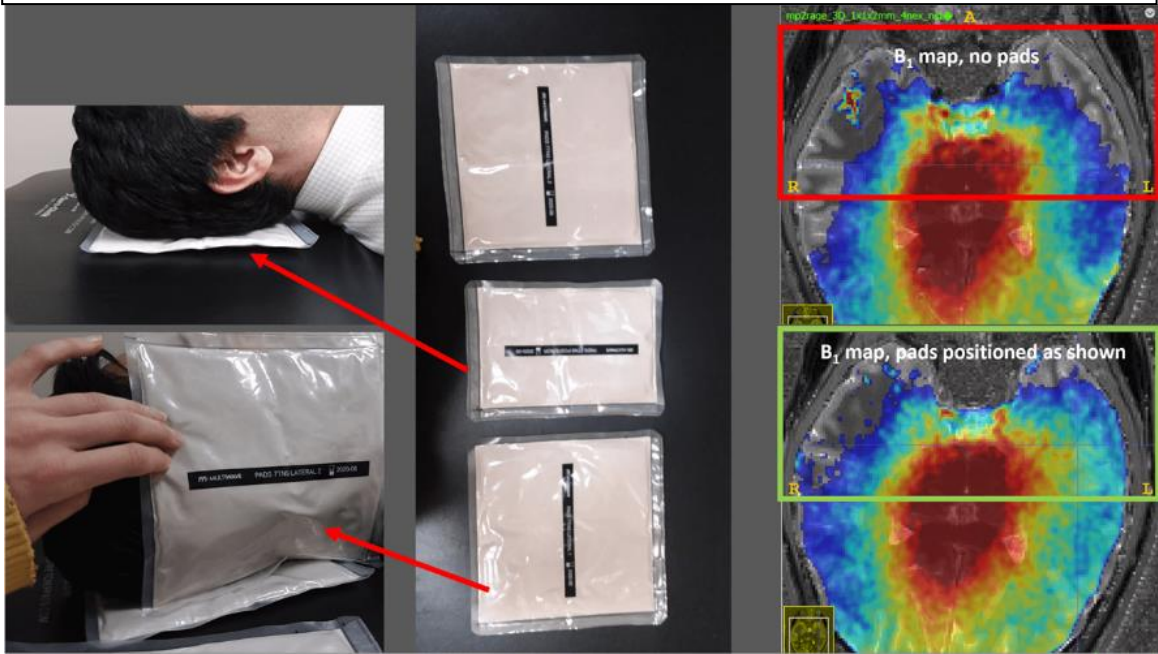


**Figure 5.S2** illustrates the pads themselves, and a deep axial slice acquired with and without their use. The maps are scaled such that areas which receive B<sub>1</sub> amplitude insufficient to generate valid gluCEST signal are colorless. It is clear from this comparison that application of the pads decreased this 'lost' portion of the image, although the asymmetry of headcoil performance between the right and left sides remains obvious. Presumably, the protocol could be optimized such that asymmetric placement of the pads themselves is able to compensate for this inherent standing wave pattern in the headcoil. Such experimentation, aided by modeling for the RF distribution, is amongst future work.

**Figure 5.S3** shows single slices of 3D gluCEST acquisitions, now in the coronal view, with and without use of the pads. The coronal images reflect that the improvement of the  $B_1$  profile afforded by the pads is not uniform over the field of view: in fact, although the inferior portion is improved as in the axial slice in Figure 5.S2, the  $B_1$  in the upper part of the head has actually decreased, arguably to a problematic degree. The images in Figures 5.S2 and 5.S3 were acquired with the same positioning of the high-DE pads relative to the subject, despite the fact that the orientation of the target slab was different. Until we reach a stage where full-brain acquisitions are standard for gluCEST, it likely makes sense to attempt optimization of pad positioning for each orientation.

Our results to date indicate that the effects of the high-DE padding is quite sensitive to their positioning, meaning that while they may be an indispensable tool for improving image quality, a great deal of optimization and protocol standardization will be required in order to achieve reproducible results. Moreover, we are optimistic that collaboration with the manufacturer will lead to designs that are more comfortable for subjects, as this has been a challenge with the

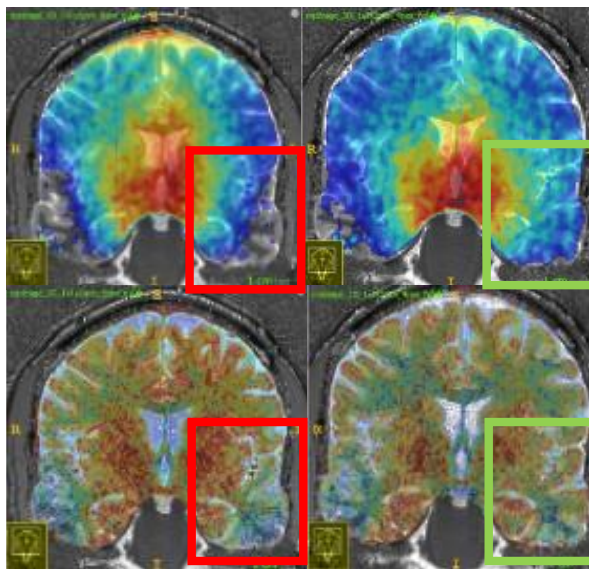


**Figure 5.S3** Dielectric pads improve  $B_1$  maps (top) and therefore gluCEST images (bottom) in problematic regions. Left:  $B_1$  map and corresponding CEST image acquired without the use of dielectric pads. Color scale in the  $B_1$  maps is from 0.5 – 1.0 relative  $B_1$  strength and transparent from 0 – 0.5, to highlight areas where nominal  $B_1$  is less than 50% and gluCEST signal is very low or absent. Despite post-processing correction, CEST remains low where  $B_1$  falls below the indicated range. Right:  $B_1$  map and corresponding CEST image acquired on the same subject, using dielectric pads positioned roughly as shown in Figure 5.S2.

current design and further aggravates

reproducibility issues. Stipulating these improvements, the primary advantage of high-DE pad use is to bring areas of the field of view which otherwise have almost no gluCEST contrast into a regime where signal emerges and can be adjusted by post-processing correction. In typical circumstances, areas affected by the presence of the pads exhibit up to a 50% increase in  $B_1$  amplitude and ~500% increase in gluCEST signal. In our view, parallel transmit (not implemented here), dielectric padding and post-processing correction are likely all necessary to produce volumetric gluCEST images of the highest possible quality, particularly in full-brain or near-full-brain acquisitions.

### ***5.5.3 Example 3D CEST images***

The following pages provide example images acquired using the 3D gluCEST pulse sequence described in 5A.1 and post-processed according to the procedure introduced in Chapter 2. In both example images, 12 slices out of a 16 slice acquisition are presented. They represent the highest quality images currently attainable with this gluCEST acquisition and post-processing protocol, with and without the use of high-dielectric padding. Snapshots from the two orthogonal views are provided below. The colormap corresponds to the snapshot shown in (A) from the ITK-SNAP contrast inspector, which also indicates the histogram of the CEST values in the image corresponding to the colorbar.

A) Oblique/axial slice, no high-DE pads. 23 year old female. Overlaid with  $T_1$ -weighted (MPRAGE) full-brain structural scan. Filtered: Gaussian filter, kernel size = 2. B) Coronal slice, high-DE pads used (complete acquisition including image featured in Figure 5A.3, bottom right) . 35 year old male. Overlaid with localizer image (low-resolution structural), as MPRAGE or other structural image was not acquired here. Unfiltered.



**Figure 5.S4.** Orthogonal views corresponding to 3D CEST acquisitions featured on the following pages. Left: Sagittal and coronal views of image series A. Right: Axial and sagittal views of image series B.

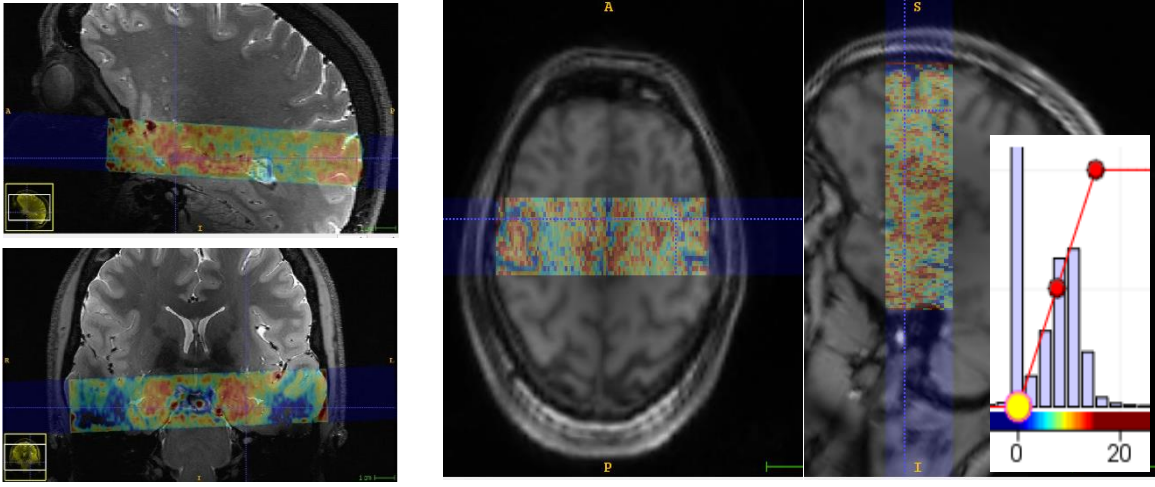


Figure 5.S5

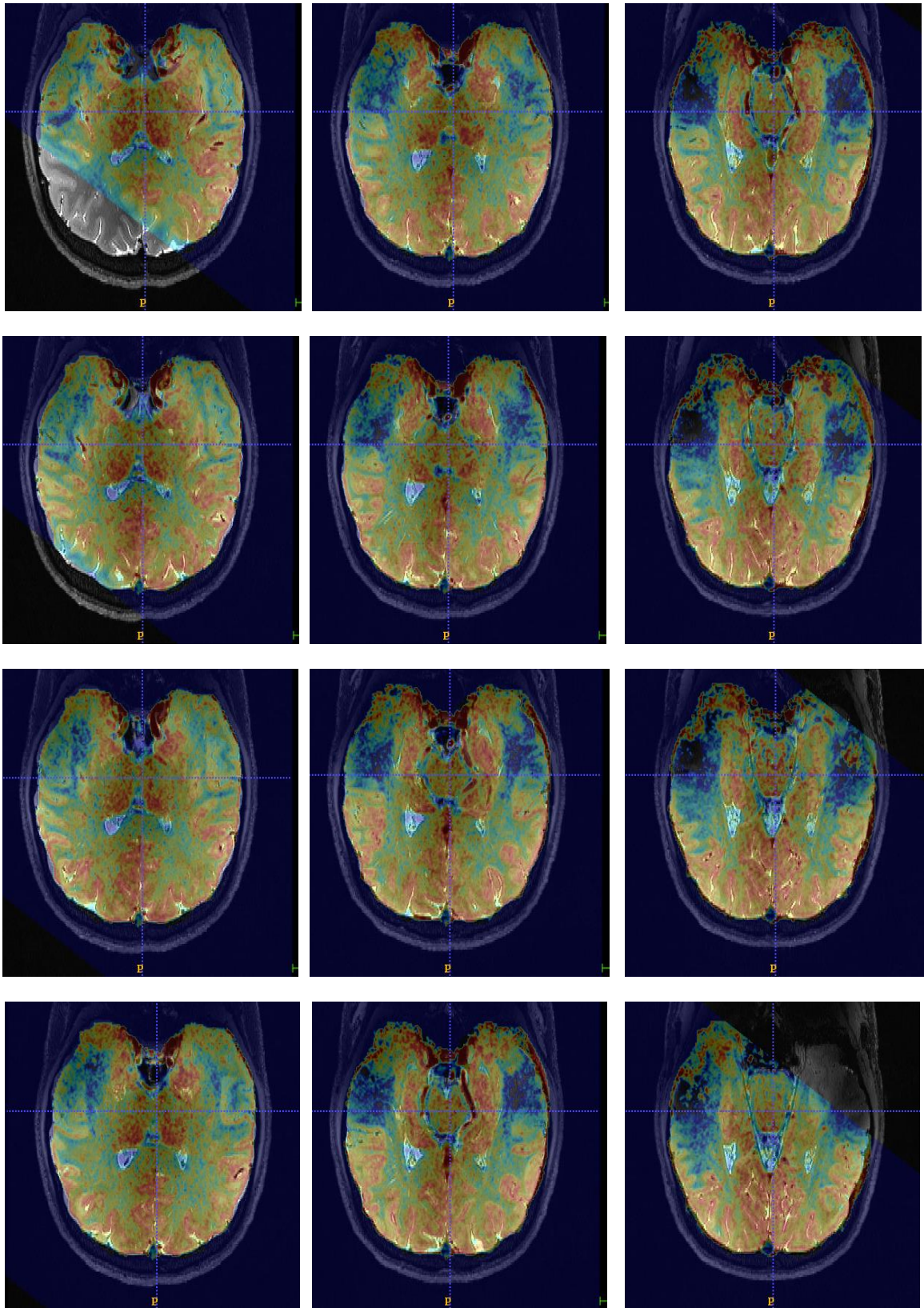
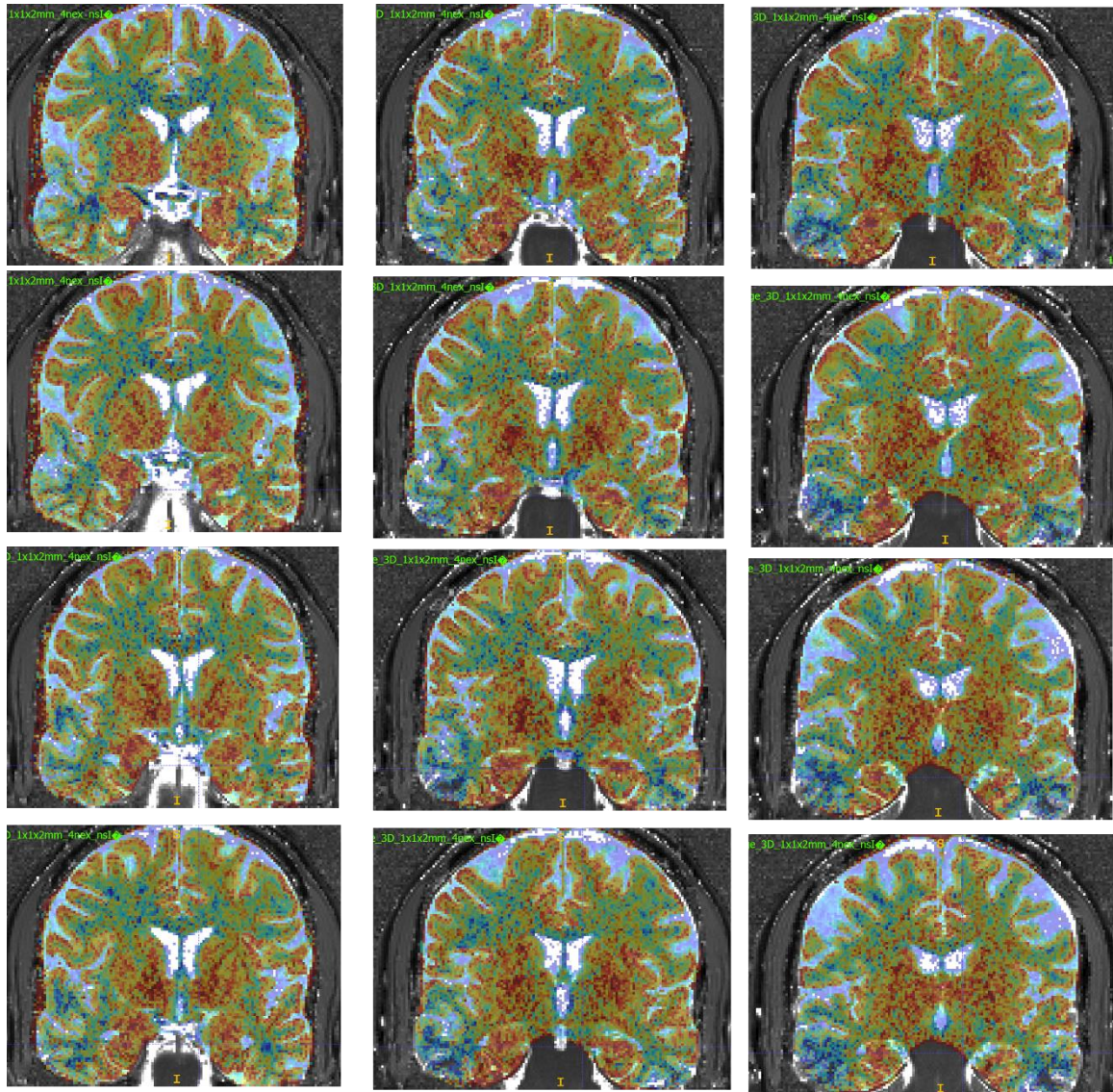




Figure 5.S5, B



## References

1. Tamminga CA, Southcott S, Sacco C, Wagner AD, Ghose S. Glutamate Dysfunction in Hippocampus: Relevance of Dentate Gyrus and CA3 Signaling. *Schizophr Bull.* 2012;38(5):927-935. doi:10.1093/schbul/sbs062
2. Amaral DG, Witter MP. The three-dimensional organization of the hippocampal formation: A review of anatomical data. *Neuroscience.* 1989;31(3):571-591. doi:10.1016/0306-4522(89)90424-7
3. Lavenex P, Amaral DG. Hippocampal-neocortical interaction: A hierarchy of associativity. *Hippocampus.* 2000;10(4):420-430. doi:10.1002/1098-1063(2000)10:4<420::AID-HIPO8>3.0.CO;2-5
4. Duvernoy H. *The Human Hippocampus.* Springer; 1998.
5. O'Reilly RC, McClelland JL. Hippocampal conjunctive encoding, storage, and recall: Avoiding a trade-off. *Hippocampus.* 1994;4(6):661-682. doi:10.1002/hipo.450040605
6. Zola-Morgan S, Squire LR. Neuroanatomy of memory. *Annu Rev Neurosci.* 1993;16:547-563. doi:10.1146/annurev.ne.16.030193.002555
7. Berron D, Schütze H, Maass A, et al. Strong evidence for pattern separation in human dentate gyrus. *J Neurosci.* 2016;36(29):7569-7579. doi:10.1523/JNEUROSCI.0518-16.2016
8. Baker S, Vieweg P, Gao F, et al. The Human Dentate Gyrus Plays a Necessary Role in Discriminating New Memories. *Curr Biol.* 2016;26(19):2629-2634. doi:10.1016/j.cub.2016.07.081
9. Gilbert PE, Kesner RP, Lee I. Dissociating hippocampal subregions: A double dissociation between dentate gyrus and CA1. *Hippocampus.* 2001;11(6):626-636. doi:10.1002/hipo.1077
10. Alkadhi KA. Cellular and Molecular Differences Between Area CA1 and the Dentate Gyrus of the Hippocampus. *Mol Neurobiol.* 2019;56(9):6566-6580. doi:10.1007/s12035-019-1541-2
11. Grande X, Berron D, Horner AJ, Bisby JA, Düzel E, Burgess N. Holistic Recollection via Pattern Completion Involves Hippocampal Subfield CA3. *J Neurosci.* 2019;39(41):8100-8111. doi:10.1523/JNEUROSCI.0722-19.2019
12. Kesner RP. Role of the hippocampus in mediating interference as measured by pattern separation processes. *Behav Processes.* 2013;93:148-154. doi:10.1016/j.beproc.2012.09.018
13. Gerges NZ, Alkadhi KA. Hypothyroidism impairs late LTP in CA1 region but not in dentate gyrus of the intact rat hippocampus: MAPK involvement. *Hippocampus.* 2004;14(1):40-45. doi:10.1002/hipo.10165
14. Parfitt KD, Van Doze A, Madison D V., Browning MD. Isoproterenol increases the phosphorylation of the synapsins and increases synaptic transmission in dentate gyrus,

but not in area CA1, of the hippocampus. *Hippocampus*. 1992;2(1):59-64.  
doi:10.1002/hipo.450020108

15. Davis S, Laroche S. Activation of metabotropic glutamate receptors induce differential effects on synaptic transmission in the dentate gyrus and CA1 of the hippocampus in the anaesthetized rat. *Neuropharmacology*. 1996;35(3):337-346. doi:10.1016/0028-3908(95)00185-9
16. Hsu JC, Zhang Y, Takagi N, et al. Decreased expression and functionality of NMDA receptor complexes persist in the CA1, but not in the dentate gyrus after transient cerebral ischemia. *J Cereb Blood Flow Metab*. 1998;18(7):768-775.  
doi:10.1097/00004647-199807000-00008
17. Matthies H, Schroeder H, Becker A, Loh H, Höllt V, Krug M. Lack of expression of long-term potentiation in the dentate gyrus but not in the CA1 region of the hippocampus of  $\mu$ -opioid receptor-deficient mice. *Neuropharmacology*. 2000;39(6):952-960.  
doi:10.1016/S0028-3908(99)00203-8
18. Song D, Xie X, Wang Z, Berger TW. Differential effect of TEA on long-term synaptic modification in hippocampal CA1 and dentate gyrus in vitro. *Neurobiol Learn Mem*. 2001;76(3):375-387. doi:10.1006/nlme.2001.4032
19. Sawada M, Sawamoto K. Mechanisms of neurogenesis in the normal and injured adult brain. *Keio J Med*. 2013;62(1):13-28. doi:10.2302/kjm.2012-0005-RE
20. Aimone JB, Wiles J, Gage FH. Potential role for adult neurogenesis in the encoding of time in new memories. *Nat Neurosci*. 2006;9(6):723-727. doi:10.1038/nn1707
21. Coultrap SJ, Nixon KM, Alvestad RM, Fernando Valenzuela C, Browning MD. Differential expression of NMDA receptor subunits and splice variants among the CA1, CA3 and dentate gyrus of the adult rat. *Mol Brain Res*. 2005;135(1-2):104-111.  
doi:10.1016/j.molbrainres.2004.12.005
22. Cai K, Haris M, Singh A, et al. Magnetic resonance imaging of glutamate. *Nat Med*. 2012;18(2):302-306. doi:10.1038/nm.2615
23. Crescenzi R, DeBrosse C, Nanga RPR, et al. Longitudinal imaging reveals subhippocampal dynamics in glutamate levels associated with histopathologic events in a mouse model of tauopathy and healthy mice. *Hippocampus*. 2017;27(3):285-302. doi:10.1002/hipo.22693
24. Crescenzi R, DeBrosse C, Nanga RPR, et al. In vivo measurement of glutamate loss is associated with synapse loss in a mouse model of tauopathy. *Neuroimage*. 2014;101:185-192. doi:10.1016/j.neuroimage.2014.06.067
25. Bagga P, Crescenzi R, Krishnamoorthy G, et al. Mapping the alterations in glutamate with GluCEST MRI in a mouse model of dopamine deficiency. *J Neurochem*. 2016;139(3):432-439. doi:10.1111/jnc.13771
26. Bagga P, Pickup S, Crescenzi R, et al. In vivo GluCEST MRI: Reproducibility, background contribution and source of glutamate changes in the MPTP model of Parkinson's disease. *Sci Rep*. 2018;8(1):1-9. doi:10.1038/s41598-018-21035-3

27. Nanga RPR, Roalf DR, Hariharan H, Prabhakaran K, Reddy R. *GluCEST in the Olfactory Cortex as a Marker of Heightened Clinical Risk for Schizophrenia.*; 2015. Accessed March 14, 2021. <https://www.researchgate.net/publication/293223610>
28. Rosenfeld E, Nanga RPR, Reddy R, et al. MON-110 Utilization of GluCEST, a Novel Neuroimaging Technique, to Characterize the Brain Phenotype in Hyperinsulinism/Hyperammonemia Syndrome. *J Endocr Soc.* 2020;4(Supplement\_1). doi:10.1210/jendso/bvaa046.594
29. Pepin J, Piguet F, Puccio H, Flament J. *GluCEST Imaging of Spinal Cord in a Mouse Model of Friedreich Ataxia.*; 2020. [https://www.researchgate.net/profile/Julien-Flament/publication/303549841\\_GluCEST\\_imaging\\_of\\_spinal\\_cord\\_in\\_a\\_mouse\\_model\\_of\\_Friedreich\\_ataxia/links/5748090f08ae2301b0b83faa/GluCEST-imaging-of-spinal-cord-in-a-mouse-model-of-Friedreich-ataxia.pdf](https://www.researchgate.net/profile/Julien-Flament/publication/303549841_GluCEST_imaging_of_spinal_cord_in_a_mouse_model_of_Friedreich_ataxia/links/5748090f08ae2301b0b83faa/GluCEST-imaging-of-spinal-cord-in-a-mouse-model-of-Friedreich-ataxia.pdf)
30. Flament J, Pépin J, Francelle L, et al. B40 In vivo imaging of brain glutamate defects in a knock-in mouse model of huntington's disease. *J Neurol Neurosurg Psychiatry.* 2016;87(Suppl 1):A23.2-A23. doi:10.1136/jnnp-2016-314597.71
31. DeBrosse C, Nanga RPR, Bagga P, et al. Lactate Chemical Exchange Saturation Transfer (LATEST) Imaging in vivo A Biomarker for LDH Activity. *Sci Rep.* 2016;6. doi:10.1038/srep19517
32. Zhou R, Bagga P, Nath K, Hariharan H, Mankoff DA, Reddy R. Glutamate-weighted chemical exchange saturation transfer magnetic resonance imaging detects glutaminase inhibition in a mouse model of triple-negative breast cancer. *Cancer Res.* 2018;78(19):5521-5526. doi:10.1158/0008-5472.CAN-17-3988
33. Cai K, Singh A, Roalf DR, et al. Mapping glutamate in subcortical brain structures using high-resolution GluCEST MRI. *NMR Biomed.* 2013;26(10):1278-1284. doi:10.1002/nbm.2949
34. Cember ATJ, Hariharan H, Kumar D, Nanga RPR, Reddy R. Improved method for post-processing correction of  $B_1$  inhomogeneity in glutamate-weighted CEST images of the human brain. *NMR Biomed.* Published online March 21, 2021:e4503. doi:10.1002/nbm.4503
35. Kim M, Gillen J, Landman BA, Zhou J, Van Zijl PCM. Water saturation shift referencing (WASSR) for chemical exchange saturation transfer (CEST) experiments. *Magn Reson Med.* 2009;61(6):1441-1450. doi:10.1002/mrm.21873
36. Volz S, Nöth U, Rotarska-Jagiela A, Deichmann R. A fast B1-mapping method for the correction and normalization of magnetization transfer ratio maps at 3 T. *Neuroimage.* 2010;49(4):3015-3026. doi:10.1016/j.neuroimage.2009.11.054
37. Cember ATJ, Hariharan H, Kumar D, Nanga RPR, Reddy R. Improved method for post-processing correction of B1 inhomogeneity in glutamate weighted CEST images of the human brain. *NMR Biomed.* 2021;in press.
38. Cai K, Haris M, Singh A, et al. Magnetic resonance imaging of glutamate. *Nat Med.*

2012;18(2):302-306. doi:10.1038/nm.2615

39. Berron D, Vieweg P, Hochkepler A, et al. A protocol for manual segmentation of medial temporal lobe subregions in 7 Tesla MRI. *NeuroImage Clin.* 2017;15:466-482. doi:10.1016/j.nicl.2017.05.022
40. Yushkevich PA, Pluta JB, Wang H, et al. Automated volumetry and regional thickness analysis of hippocampal subfields and medial temporal cortical structures in mild cognitive impairment. *Hum Brain Mapp.* 2015;36(1):258-287. doi:10.1002/hbm.22627
41. Yushkevich PA, Piven J, Hazlett HC, et al. User-guided 3D active contour segmentation of anatomical structures: Significantly improved efficiency and reliability. *Neuroimage.* 2006;31(3):1116-1128. doi:10.1016/j.neuroimage.2006.01.015
42. Hingerl L, Strasser B, Moser P, et al. Clinical High-Resolution 3D-MR Spectroscopic Imaging of the Human Brain at 7 T. *Invest Radiol.* 2020;55(4):239-248. doi:10.1097/RLI.0000000000000626
43. Liebert A, Tkotz K, Herrler J, et al. Whole-brain quantitative CEST MRI at 7T using parallel transmission methods and correction. *Magn Reson Med.* 2021;00:mrm.28745. doi:10.1002/mrm.28745
44. Akbey S, Ehses P, Stirnberg R, Zaiss M, Stöcker T. Whole-brain snapshot CEST imaging at 7 T using 3D-EPI. *Magn Reson Med.* 2019;82(5):1741-1752. doi:10.1002/mrm.27866

# Chapter 6: Integrating $^1\text{H}$ MRS and deuterium labeled glucose for mapping the dynamics of neural metabolism in humans

## *Preface*

*So far, this thesis has focused on gluCEST, a proton-density weighted imaging technique with underpinnings in chemical exchange. Despite offering many interesting new possibilities for molecular imaging, gluCEST and other exchange-based modalities still fail to address a major challenge in medical imaging: how to capture dynamic information. As will be explained in the Introduction to Chapter 6, proton-based in vivo magnetic resonance spectroscopy, the other major option for MR-detection of specific chemicals, also failed to address this challenge for many years. The work presented in this chapter deviates from the realm of CEST imaging to expand our quest for imaging glutamate and related metabolism into the dynamic, temporal dimension. While the presented technique, qCSI, is currently quite incomparable to gluCEST in terms of spatial resolution, it has several advantages over non-proton MRSI methods for measuring dynamics of metabolism. The ability of qCSI to detect and visualize the dynamic metabolism of glucose to glutamate provides a deeply complimentary source of information to gluCEST. In the future, qCSI and gluCEST could be used in tandem to provide next-generation precision diagnostics for patients suffering from neurological maladies with metabolic etiology.*

## **6.1 Introduction**

For the past century, the study of cellular metabolism has revolutionized our understanding of biological energy production, phenotypic variation, and disease etiology. With the advent of non-invasive medical imaging technologies, continued efforts have focused on expanding the



capabilities of such technology to provide information beyond structural and mechanistic aspects and into the realm of molecular biochemical and physiological insights<sup>1</sup>.

Despite the obvious appeal of such goals, the only metabolic imaging technique used routinely in the clinic is positron emission tomography (PET), which provides information reflecting tissue glucose uptake after infusion of the radioactive glucose analog 2-<sup>18</sup>F-fluoro-2-deoxy-D-glucose (<sup>18</sup>FDG)<sup>1,2</sup>. PET is most commonly applied in clinical oncology, where elevated glycolytic metabolism in cancer cells enables visualization of both primary and metastatic lesions in patients<sup>3</sup>. However, while PET provides insight into tissue glucose uptake, it does not provide any further information about downstream glucose metabolism. An alternate metabolic imaging method both capable of monitoring downstream metabolism and not reliant on ionizing radiation would be preferable in many instances.

While conventional MRI is non-ionizing and provides exceptional anatomical information, it offers only limited insight with regard to metabolism. As introduced in previous chapters, CEST is an emerging suite of MRI methods capable of detecting endogenous metabolite levels in both normal and diseased tissues<sup>4</sup>. However, CEST is also limited in its ability to measure the dynamics of metabolite turnover<sup>4-6</sup>.

Spectroscopy, which is built on the same fundamental physics as magnetic resonance imaging, allows for chemically specific detection of small molecule metabolites<sup>7-9</sup>. While standard clinical MRI measures the signal generated from protons (<sup>1</sup>H) on water and fat to generate bulk structural images of the body, MRS generally suppresses these signals in order to measure much weaker signals generated from protons on less abundant molecules, including key metabolites such as N-acetyl-aspartate (NAA), choline, creatine, glutamate (Glu), glutamine (Gln),  $\gamma$ -

aminobutyric acid (GABA), and lactate (Lac). Still, a major limitation of current  $^1\text{H}$  MRS based approaches is that they only provide static measurements of metabolite concentration and as a result are unable to assess changes in tissue metabolic rates that are not reflected in a change in steady state concentration.

To date, the primary strategy to generate dynamic information using MRS has been to use exogenous (non-radioactive) isotope-labeled substrates that are administered to the patient or subject.  $^{13}\text{C}$  MRS using costly  $^{13}\text{C}$  labeled substrates like glucose and acetate has been used extensively to measure metabolic flux both in isolated cells and *in vivo* <sup>10-12</sup>. Despite this, the clinical application of  $^{13}\text{C}$  MRS has been limited owing to the requirement for additional scanner hardware. Moreover, while hyperpolarization techniques can be employed to achieve improved sensitivity of  $^{13}\text{C}$  <sup>13,14</sup>, these approaches require further specialized equipment and technical expertise. Recently, there has been growing interest in the use of deuterium ( $^2\text{H}$ ) as an alternative to  $^{13}\text{C}$  for metabolite labelling studies <sup>15-17</sup>. In deuterium MRS (DMRS), the protons on glucose or acetate are replaced by deuterium, and as these substrates are metabolized the deuterium label is transferred to the downstream metabolites which can then be detected by deuterium MRS (DMRS).

Although  $^{13}\text{C}$  MRS and DMRS offer unique solutions to measure metabolite turnover, the capability to detect any nucleus other than  $^1\text{H}$  is generally not available on clinical MRI systems<sup>18</sup>. Detection of these nuclei requires specialized coils for transmission and reception that must be designed with additional expertise or otherwise are purchased at an additional cost. Hardware availability aside, there are also inherent physical advantages of proton spectroscopy over DMRS:  $^1\text{H}$  has a gyromagnetic ratio ( $\gamma$ ) almost seven times higher than  $^2\text{H}$ . Because both the spin energy gap itself and the Larmor frequency are functions of  $\gamma$ , both the

sensitivity and the spectral resolution of the  $^1\text{H}$  spectrum are higher than for  $^2\text{H}$ . Thus, while DMRS has the advantage of very high specificity for the introduced substrate and lack of nuisance signals, it is difficult to resolve the plurality of metabolites which are generated further downstream upon absorption of glucose or acetate.

Given these limitations, we sought to develop a  $^1\text{H}$  MRS method that increases the sensitivity and versatility of MRS for measuring metabolic dynamics without the need for specialized hardware or radioactive tracers. To this end, we recently introduced quantitative exchanged-label turnover (QELT) MRS or qMRS, a method that detects deuterium labelling of metabolites by measuring the reduction in  $^1\text{H}$  MRS signal after administration of deuterium labelled substrates<sup>19</sup>. Building on our preclinical qMRS studies, here we demonstrate the potential of the analogous spectroscopic imaging technique, qCSI, for monitoring the dynamics of neural metabolism in healthy human subjects after oral ingestion of deuterated glucose. Since deuterium labelled glucose is non-toxic<sup>16,20</sup> and can be easily administered orally, this approach is safe and straightforward for use in human subjects. Given the universal availability of  $^1\text{H}$  MRS on clinical scanners and its ability to detect several biologically relevant metabolites, we envision an expansive translational potential for this technique.

## **6.2 Materials and Methods**

### ***6.2.1 Human subjects information***

This protocol was approved by the Institutional Review Board at the University of Pennsylvania, with informed consent obtained prior to the initial scan. Eight subjects participated in this study: four male and four female, ranging in age from 23-52 years, with a mean age of 32 years. Full chemical shift imaging timecourses were collected on four subjects, two of each sex. Remaining

subjects participated in SVS, single-timepoint CSI acquisitions, or non-deuterated glucose experiments.

Volunteers were scanned during two sessions on separate days: one 'baseline' measurement, and one measurement after oral deuterated glucose ingestion. For both sessions, the volunteers fasted overnight before undergoing studies in the morning. Baseline scanning sessions lasted approximately 45 minutes. In the second session, subjects were scanned for approximately two hours, beginning directly after oral ingestion 0.8g/kg of body weight of [6,6'-2H<sub>2</sub>]-glucose dissolved in water. This oral preparation was provided by the pharmacy service of the Hospital of the University of Pennsylvania, based on the self-reported body weight of each participant.

To ensure normoglycemia, blood glucose testing was performed on all subjects before the baseline session, and both before and after the glucose-ingestion session. To evaluate the choice of glucose dosage, in four subjects a full time-course of blood glucose measurements was also performed upon ingestion of an equivalent amount of non-deuterated glucose (Glucon-D, Dabur, Inc.). Testing was performed using standard home blood glucose monitoring equipment (Accu-check, Roche Diabetes). Results shown in Supplementary **Figure 6.S4** show some inter-subject variability in blood glucose levels, but with all subjects returning to baseline glucose levels within 2 hours.

### ***6.2.2. MRI acquisition methods***

MR experiments were performed on a 7T scanner (MAGNETOM Terra, Siemens Healthcare, Erlangen, Germany) equipped with a 1Tx/32Rx head coil (Nova Medical, Wilmington, MA, USA). Axial T<sub>1</sub>-weighted FLASH images were obtained to enable localization of the cortex. Following localization, spectroscopy data were acquired using custom sequences for CSI with sLASER

localization (MRSI)<sup>21,22</sup> and SVS with PRESS localization<sup>23</sup>. Localized shimming was performed to obtain water line widths of 0.08 ppm or less. Water suppression was achieved using variable pulse power and optimization relaxation (VAPOR) pulse cluster<sup>24</sup> pre-encoded to the PRESS sequence.

Specifically, SVS in two voxels and two MRSI measurements of the encompassing slab were performed in the baseline session. In the second (post-glucose) session, SVS measurements in two voxels were performed directly upon positioning the subject in the scanner (t = 20-30 mins post-ingestion), with six subsequent MRSI acquisitions (t = 50, 60, 70, 80, 90, 100 mins) and one additional pair of SVS acquisitions (t = 120 mins) at the end of the experiment. Voxel sizes of MRSI and SVS were 10 x 10 x 10mm (before interpolation) and 40 x 10 x 10 mm, respectively. Intrasubject registration between session was accomplished using an in-house co-registration program, ImScribe (available at <https://www.med.upenn.edu/cmroi/imscribe.html>), as described in previous work<sup>27</sup>.

Sequence parameters were as follows:

*SVS*: TR/TE = 3000/23 ms, spectral width = 4 kHz, averages = 64, scan time = 5 min. In each instance, an additional spectrum with 8 averages was acquired without water suppression to obtain a water reference signal for quantification and eddy current correction.

*CSI*: TR/TE = 2050/40 ms, spectral width = 4kHz with 2048 points, averages = 4, FOV = 160 x 160mm x 10 mm slice thickness on a 16 x 16 grid, interpolated to 32 x 32. The sequence incorporated elliptical weighting with Hamming-windowed spatial filtering. This resulted in a true voxel size ~2.7x larger than the acquired volume, but removed Gibbs ringing associated with the lower resolution scanning.

### 6.2.3 Quantification and data analysis

Metabolite concentrations measured by *in vivo*  $^1\text{H}$  MRS were quantified using LCModel software (v.6.3) <sup>28</sup>. Custom basis sets were simulated using specific timings and pulse shapes of the refocusing pulses in the custom sequences<sup>29,30</sup>. For the PRESS sequence, a spatial distribution of 20 x 20 locations covering the voxel were simulated and summed to take into account the effects of chemical shift artifacts caused by relatively low bandwidth refocusing pulses. In order to account for the difference in spectral patterns that occur when glutamate becomes deuterated, two additional metabolites representing single proton replacement and double proton replacement were also included. For the former, it has been noted<sup>16</sup> that replacement can occur on either the H4 or the H4' glutamate proton with equal probability. Here we have chosen to include the H4 proton replacement simulation as the spectral patterns of both are very similar for typical *in vivo* linewidths (shown in **Figure 6.S1**). For the double proton replacement case, both the H4 and H4' glutamate protons were replaced with deuterium. Exact coupling constants involving deuterium nuclei were not known, though D-H couplings are typically 1-2 Hz. In **Figure 6.S1**, we show that the spectral differences at *in vivo* linewidths are minimally dependent on D-H coupling over this range and chose 1.5 Hz for the basis set. All fits were performed over the spectral range from 0.5 to 4.2 ppm. While our previous paper presenting experimental data from rats showed changes in GABA and Gln, preliminary analysis in humans did not observe those same effects. Therefore, no deuterated versions of these metabolites were included in the basis set.

Metabolite ratios to NAA were reported as NAA does not show signal changes after deuterated glucose ingestion (see Figure 6.3). For CSI, ROIs representing primarily grey matter and primarily white matter were manually drawn on the Glu to NAA ratio map, and individual fits over the

ROIs were averaged. Representative ROIs are shown in Figure 6.2 overlaid on the baseline image. .

### 6.3 Results

The very first experiments in which we observed the qMRS effect upon subject ingestion of deuterated glucose were single voxel spectroscopy experiments at 3T and 7T<sup>31</sup>. Comparing only one pre-ingestion and one post-ingestion acquisition, we observed visually apparent decrease of the main glucose resonance at 2.3ppm in mostly gray matter voxels. An example pair of such spectra is shown in **Figure 6.1C**. We sought to extend this measurement to a form which proffers some degree of spatial and temporal resolution, and continued experiments using a semi-LASER based CSI sequence at 7T, collecting sequential post-ingestion timepoints to create CSI map timecourses which can be viewed with respect to any of the fitted resonances in the basis set. **Figure 6.1** shows spectra from selected voxels intended to be mostly gray (A) or most white (B) matter and illustrates the presence of the same decrease observed in the SVS data. Figure 1D illustrates the simulated proton resonances of deuterated glutamate species which were included in the basis set used to fit the qCSI data.

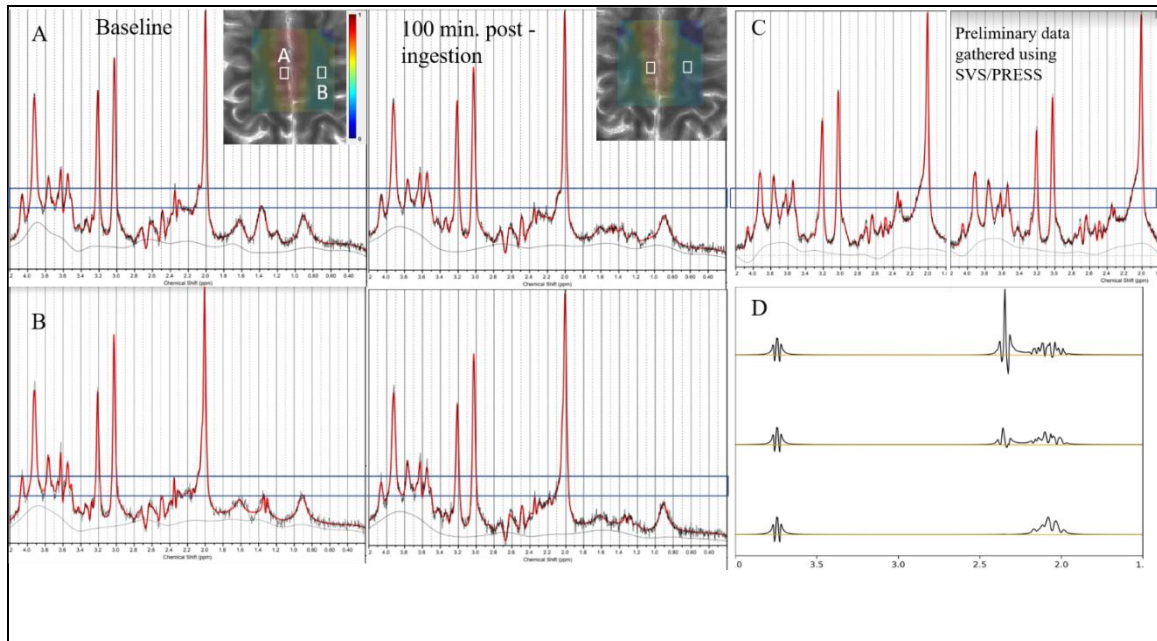


**Figure 6.1. Spectroscopic underpinnings of qCSI.** A,B) Example spectra from two CSI voxels (A,B, as shown in white boxes overlaid on image) showing decrease in main Glu resonance. C) Corresponding decrease observed in experiments with a larger SVS voxel. D) Simulations of glutamate elements in the basis set for fitting of semi-LASER data, including unlabeled Glu (top), singly-labeled  $[^2\text{D},^1\text{H}]$ -glutamate-4 (middle), and doubly-labeled  $[^2\text{D}_2]$ -glutamate-4 (bottom).

The resulting timecourses from qCSI can be visualized as in **Figure 6.2**, in which the colormap corresponds to the ratio  $[\text{Glu}]/[\text{NAA}]$  as fit in each voxel. This subject exhibits a strong decrease in the unlabeled Glu signal in the central gray matter region as well as rather dramatic decreases in certain regions of white matter. This reflects that neural glutamate present at baseline has been replaced by newly synthesized, labeled glutamate upon metabolism of the ingested glucose. Timecourses of the  $[\text{Glu}]/[\text{NAA}]$  map for the remaining subjects are available in Figure 6.S2.



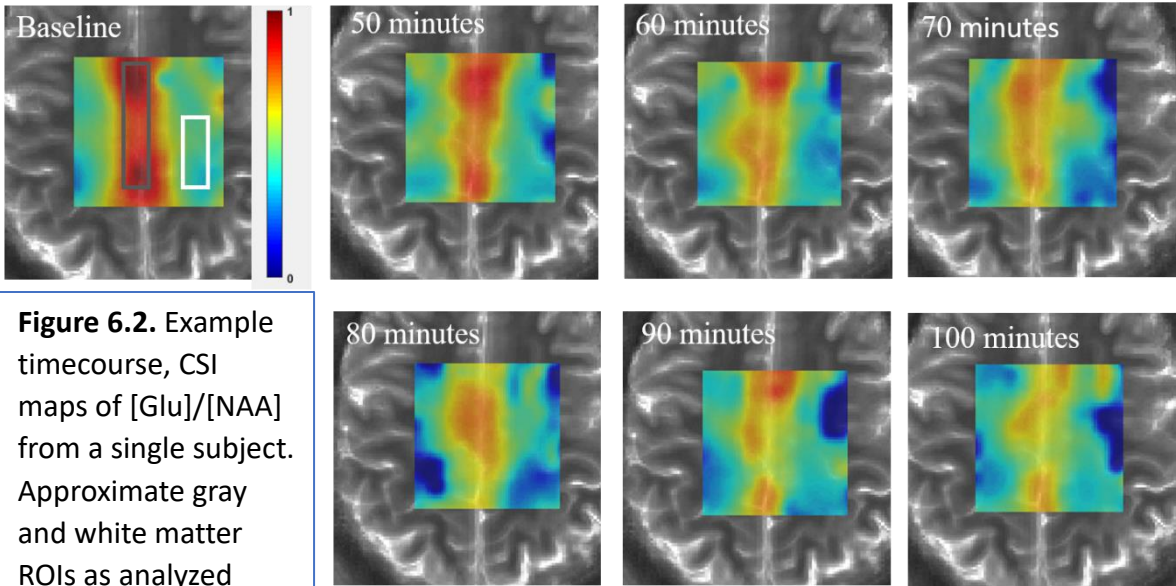


**Figure 6.2.** Example timecourse, CSI maps of [Glu]/[NAA] from a single subject. Approximate gray and white matter ROIs as analyzed further are indicated on the baseline image.

**Figure 6.3** shows data from a different subject in the form of barplots. NAA is plotted normalized to its initial value, while glutamate and derivatives are plotted as a ratio of their LC-model

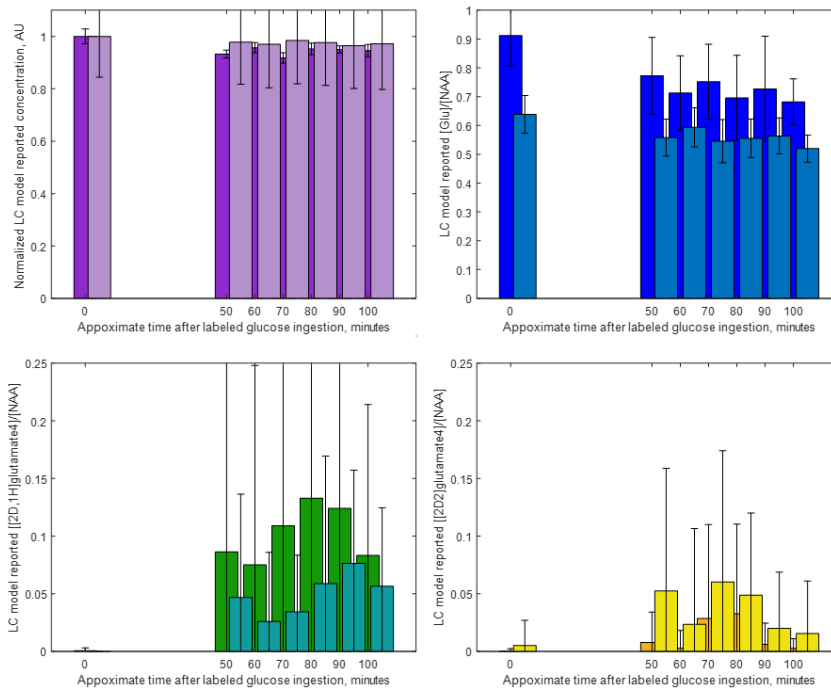
reported concentration to that of NAA. Even in individual subjects, the trend of decreasing unlabeled glutamate is robustly apparent in both gray and white matter ROIs. The appearance of the labeled derivatives was less consistent, but the appearance of singly-labeled [2D,1H]-glutamate-4 was detectable with statistical significance in both gray and white matter when all subjects' data were taken together. Barplots analogous to those in Figure 6.3 are available for all subjects in Figure 6.S3.

Figure 6.4 shows the group averages (n = 4 subjects) over time of the Glu, [2D,1H]-glutamate-4 and doubly labeled [2D2]-glutamate-4. In taking data from all subjects, nearly all timepoints show statistically significant difference from baseline with respect to measurements of unlabeled (decrease) and singly unlabeled (appearance/increase) glutamate. In gray matter, a generally monotonic trend is apparent over time, suggesting that even at this relatively long time scale, we are still capturing the dynamics of a pathway that has not reached steady state.

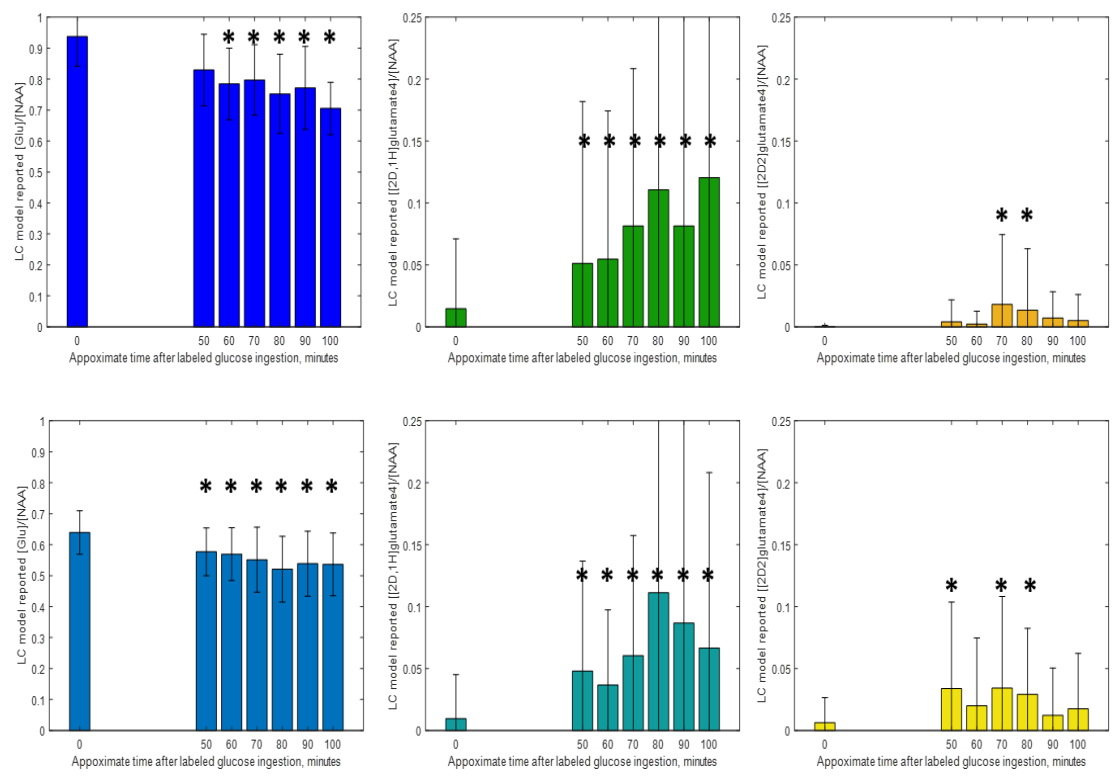
The doubly-labeled form of glutamate, as expected, appeared at a lower rate than the singly-labeled version. This quite low concentration made it difficult to detect robustly, but its appearance provides further validation that we are indeed observing changes due to downstream steps of glucose metabolism.

Tables 6.1 and 6.2 list the results (as a ratio of concentration relative to [NAA]) from all metabolites by timepoint, as well as their standard deviation and the p-value of the paired T-test which compared data from each timepoint to the baseline measurement.

**Figure 6.3.** [NAA] and ratios of glutamate varieties derived from CSI data in a single subject. In all plots, data from gray matter ROI is shown in the background, white matter ROI in foreground. Clockwise from top left: [NAA], [Glu]/[NAA], [<sup>2</sup>D,<sup>1</sup>H]-glutamate-4/[NAA], [<sup>2</sup>D<sub>2</sub>]-glutamate-4/[NAA].



**Figure 6.4.** Ratios of glutamate/NAA derived from CSI data in all subjects. Stars indicate a statistically significant difference from the baseline measurement. Top: Data from gray matter ROIs. Bottom: Data from white matter ROIs. Columns, left to right, are [Glu]/[NAA], [(<sup>2</sup>D,<sup>1</sup>H)-glutamate-4]/[NAA], [(<sup>2</sup>D<sub>2</sub>)-glutamate-4]/[NAA].



	White matter	Baseline	t = 50 min	t = 60 min	t = 70 min	t = 80 min	t = 90 min	t = 100 min
<b>Glu</b>	<i>Mean</i>	<b>0.639131</b>	<b>0.576965</b>	<b>0.569419</b>	<b>0.551451</b>	<b>0.520806</b>	<b>0.538582</b>	<b>0.536494</b>
	<i>St. Dev.</i>	0.069948	0.077164	0.085449	0.105325	0.106135	0.105107	0.101494
	<i>P-value</i>	0	1.15E-05	3.89E-06	4.97E-07	8.32E-11	1.32E-08	3.49E-09
<b>[<sup>2</sup>D,<sup>3</sup>H]-glutamate-4</b>		<b>0.00953</b>	<b>0.047959</b>	<b>0.036704</b>	<b>0.060411</b>	<b>0.111162</b>	<b>0.086635</b>	<b>0.066585</b>
		0.035522	0.088794	0.060705	0.096979	0.144996	0.172768	0.141552
		0	0.002534	0.003646	0.000246	7.63E-07	0.001063	0.003276
<b>[<sup>2</sup>D<sub>2</sub>]-glutamate-4</b>		0.006298	0.033772	0.019953	0.034171	0.029142	0.012295	0.017473
		0.020194	0.069806	0.054646	0.074007	0.053337	0.03817	0.044732
		0	0.004412	0.074408	0.006149	0.002612	0.288349	0.082959
<b>Gln</b>		0.256255	0.234369	0.227386	0.227221	0.235473	0.242184	0.265176
		0.041298	0.046887	0.055967	0.047237	0.054271	0.071213	0.068327
		0	0.008188	0.001842	0.000549	0.020956	0.191805	0.392501
<b>GABA</b>		0.060641	0.102409	0.109812	0.080157	0.117673	0.116877	0.097298
		0.030162	0.045294	0.063776	0.038913	0.069528	0.052322	0.039652
		0	3.75E-08	4.41E-07	0.002881	6.41E-08	8.23E-11	1.15E-07

Table 6.1

	Gray matter	t = 50 min	t = 60 min	t = 70 min	t = 80 min	t = 90 min	t = 100 min
	Baseline						
<b>Glu</b>	<b>0.937143</b>	<b>0.829256</b>	<b>0.784338</b>	<b>0.797078</b>	<b>0.752259</b>	<b>0.771443</b>	<b>0.705219</b>
	0.095069	0.115468	0.115445	0.113814	0.127622	0.133782	0.084542
	<b>0</b>	6.32E-10	8.19E-17	5.94E-15	2.79E-20	1.62E-16	5.77E-37
<b>[<sup>2</sup>D,<sup>1</sup>H]-glutamate-4</b>	<b>0.014591</b>	<b>0.05125</b>	<b>0.054621</b>	<b>0.081413</b>	<b>0.110647</b>	<b>0.081355</b>	<b>0.120488</b>
	0.056451	0.130687	0.119647	0.127012	0.184376	0.176343	0.141733
	<b>0</b>	0.020169	0.006502	2.11E-05	1.09E-05	0.001247	2.33E-09
<b>[<sup>2</sup>D<sub>2</sub>]-glutamate-4</b>	<b>0.000118</b>	<b>0.003962</b>	<b>0.002286</b>	<b>0.018082</b>	<b>0.01351</b>	<b>0.007192</b>	<b>0.005122</b>
	0.001074	0.017797	0.010366	0.05638	0.049504	0.021203	0.02094
	<b>0</b>	0.051161	0.059751	0.004214	0.014767	0.002791	0.031106
<b>Gln</b>	<b>0.314815</b>	<b>0.303783</b>	<b>0.289559</b>	<b>0.300469</b>	<b>0.300401</b>	<b>0.292885</b>	<b>0.303049</b>
	0.082496	0.08866	0.095685	0.095947	0.078866	0.091577	0.095838
	<b>0</b>	0.407793	0.070393	0.30317	0.251569	0.106942	0.39782
<b>GABA</b>	<b>0.129936</b>	<b>0.128</b>	<b>0.10285</b>	<b>0.124278</b>	<b>0.141418</b>	<b>0.114505</b>	<b>0.106092</b>
	0.076542	0.06451	0.05644	0.053602	0.055007	0.050979	0.054466
	<b>0</b>	0.860332	0.010324	0.581948	0.268715	0.12829	0.022003

**Table 6.2**

## 6.4 Discussion

Building on our previously proposed method for indirectly measuring  $^2\text{H}$  metabolism using  $^1\text{H}$  MRS in rats, the present work extends the method into human beings and uses CSI for greater spatial coverage. While we are primarily interested in showing comparisons of gray and white matter, CSI has the advantages of larger coverage with smaller voxel sizes compared to SVS and could potentially provide more specifically localized information. However, due to nuisance signals from skull lipids, we restricted our excited volume to a limited portion covering less than half the brain. Also, we restricted our acquisition to a single slice to keep adequate temporal resolution and to ensure more homogenous  $B_0$  and  $B_1$  fields over the VOI. This is particularly important at UHF where whole brain spectroscopic imaging is more challenging. We believe that some of the variability manifesting in the analysis presented here arises from the shortcomings in our ability to accurately draw pure gray and white matter ROIs on a map of this resolution. However, because of the coarse-grained visible differences in the map corresponding to these tissue types, we nonetheless decided to perform regional analysis in this manner.

At 7T, sequences optimized for UHF should be used that have higher bandwidths to accommodate the increased spectral dispersion and manifest greater robustness to  $B_1$  errors. (Our initial implementation of human qMRS used an unoptimized, PRESS-based SVS sequence. Because of this, quantifying small changes in overlapping metabolites was difficult even when basis set simulations took into account specific RF pulse shapes and spatial localizations.) In future improvements to the qCSI methodology, fast spectroscopic imaging techniques optimized for UHF could be used to acquire higher resolution metabolic images that allow for larger coverage and better separation of gray and white matter<sup>32,33</sup>.

As expected, average qCSI-quantified glutamate values are consistently higher in gray matter than in white matter. Our results indicate that the turnover from glucose to glutamate is also slightly higher in gray matter than in white matter, although the standard deviation is higher in our white matter measurements, making it difficult to quantify this relationship with our present results. Roughly, the labeling detected in gray matter at 100 minutes is  $\sim 20\%$ , while in white matter it is 15-20%. While there appears to be inter-subject variability on this front, this is more likely due to different degrees of partial voluming in the ROIs than to physiologic differences between healthy subjects.

As for temporal resolution, it could be argued that at such a timescale, all measurements are already of a steady state. However, the time-dependent trends visible in our gray matter data suggest that this is not the case. We would like to observe that much of the metabolic dynamics work in the literature has been done on humans or animals who are receiving an IV or similarly invasive infusion of the labeled substrate. Indeed, if this were the case, no changes would be likely to occur > 1 hour after administration. However, absorption of glucose through the digestive system presents a considerable rate-limiting step and is far from instantaneous. This is illustrated clearly in the blood glucose measurements we performed on four healthy volunteers (see SI). Thus, we don't find it inconsistent that we may be still seeing rise of the downstream deuterated glutamate species even at this time scale.

In the present work, we were not yet able to robustly measure changes in GABA or glutamine in human subjects. This could be due to the reliance on oral ingestion of deuterated glucose, as opposed to the continuous infusion used in animal experiments, or to reduced spectral sensitivity to GABA and glutamine as compared to glutamate. The use of a GABA-edited MEGA-PRESS sequence<sup>34</sup> or other specialized acquisition may improve quantification of these less salient components. Future work would also consider incorporating deuterated versions of these metabolites into the basis set.

Another spectroscopic approach for detecting metabolic dynamics using the <sup>1</sup>H signal would be to introduce glucose labeled not with deuterium, but instead with <sup>13</sup>C<sup>35-37</sup>. Once metabolized, <sup>13</sup>C would end up on the fourth carbon of glutamate. This carbon has two coupled protons whose J-coupling would then split by ~80Hz on either side of the original resonance resulting in a spectrum that exhibits only 85-90% of the original signal at 2.35 ppm (arising from protons that are coupled <sup>12</sup>C4) and about 10-15% of the signal (those coupled to <sup>13</sup>C4) would be transferred to split peaks around the center frequency. Since protons attached to <sup>13</sup>C4 labeled glutamate would be split and moved away from the glutamate proton resonance on unlabeled <sup>12</sup>C4, the main glutamate resonance intensity would be reduced in proportion to deuterium labeling, not unlike in qMRS. However, it is important to note that leveraging splitting due to J-coupling would also interfere with other resonances, making spectral quantification more difficult. <sup>13</sup>C-labeled glucose is also 4-5x more expensive than that labeled with <sup>2</sup>H. Accordingly,

from the perspective of cost and robustness, qMRS based on  $^2\text{H}$  metabolites would therefore appear to have a greater potential for clinical translation.

qMRS not only probes the kinetics of metabolic flux, but also provides information about all steady state metabolites normally accessed in an MRS acquisition, whereas in an experiment detecting  $^2\text{H}$  or  $^{13}\text{C}$ , this information would be unavailable unless a dual-tuned coil were used. Specifically, in principle qMRS presents the potential to measure labeling not only of glutamate, but of glutamine and GABA, opening the doors to quantifying rates of neuronal metabolic cycling<sup>38,39</sup>.

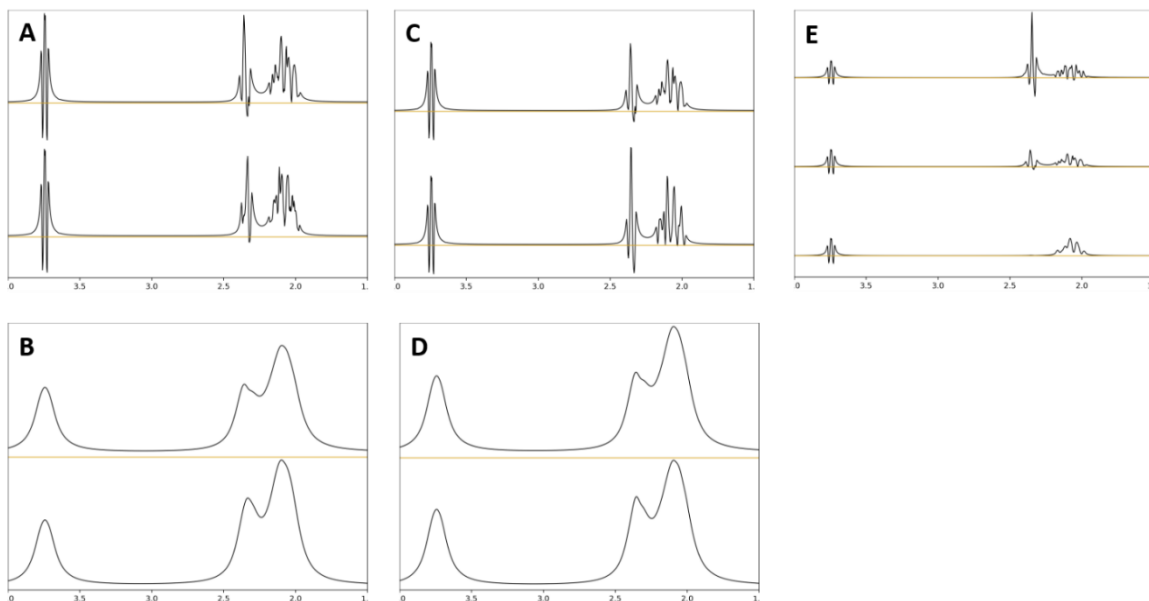
Investigators in the area of oncology may be particularly interested in monitoring lactate changes after ingestion of  $[6,6\text{-}^2\text{H}_2]$ -glucose as a measure of the Warburg effect<sup>40</sup>. Based on successful preclinical work using the qMRS lactate signal to monitor glycolytic metabolism in glioblastoma<sup>41</sup>, we are currently pursuing human studies correlating anaerobic metabolism quantified by qMRS with pathological tumor grade and prognosis.

While the feasibility studies presented in this work are performed at 7T, there is potential to extend the scope of these measurements to the much more available 3T MRI scanners. At 3T, field inhomogeneity is less of an issue, thus facilitating full brain coverage. However, in addition to a reduction in SNR, spectral resolution is compromised, making unambiguous detection of Glu more difficult, especially for an extended basis set that includes deuterated versions of metabolites. We have initiated these studies to a limited degree, and preliminary results suggest that SVS-based qMRS to detect at minimum the decrease of the main glutamate resonance is feasible at 3T<sup>31</sup>. In the realm of qCSI, sequence development is still underway to find an optimal compromise between spatial and temporal resolution at this field strength.

In summary, we demonstrated the feasibility of qCSI upon oral ingestion of deuterated glucose in human brain studies with modest –but novel for any  $^1\text{H}$ -based technique--temporal and spatial resolution. We were able to detect both the decrease in the unlabeled glutamate and the increase in the labeled derivatives by taking advantage of their specific splitting patterns in the proton spectrum. Given the centrality of glucose-to-glutamate turnover to neural metabolism, this simple experiment opens many new doors for probing neural metabolism in basic research on healthy volunteers as well as in investigations of numerous pathological conditions.

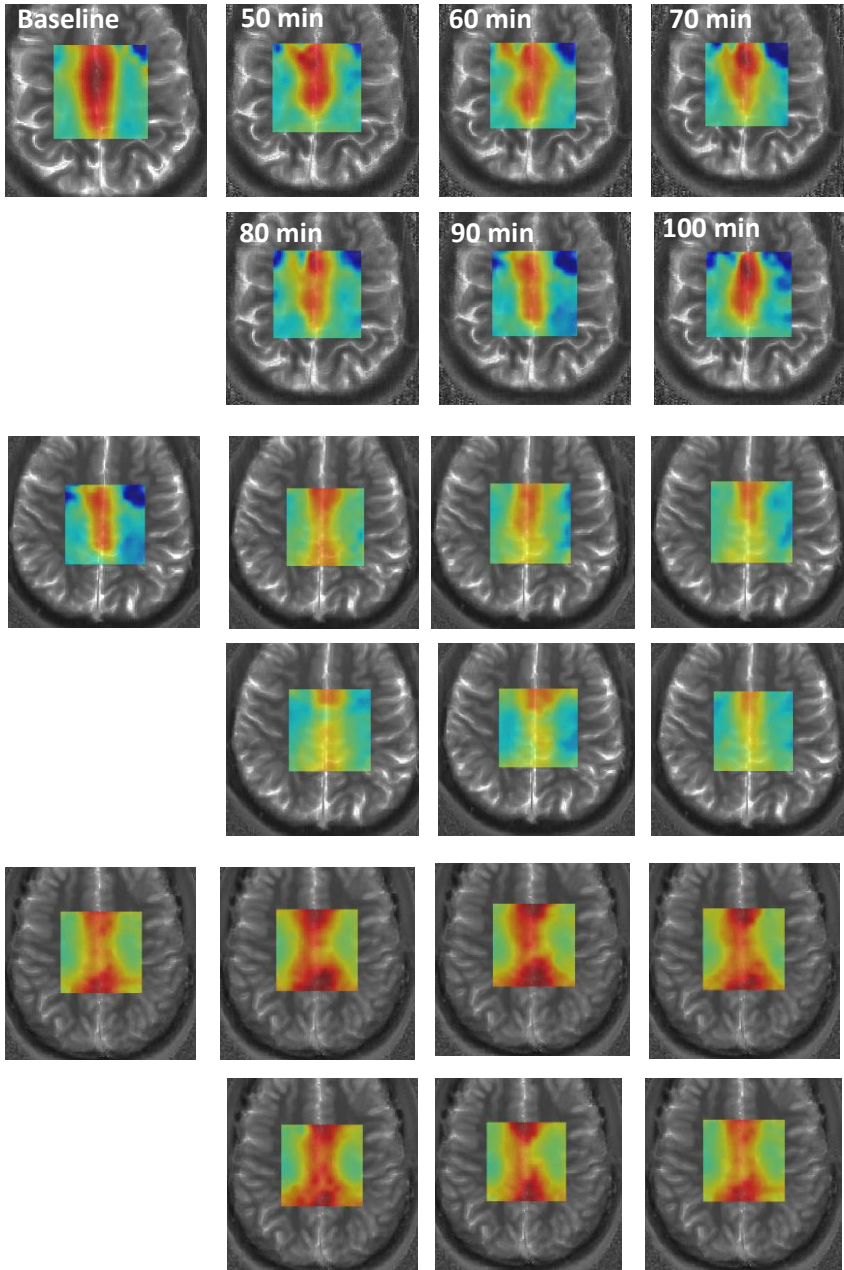


## 6.5 Supplementary Figures and Information

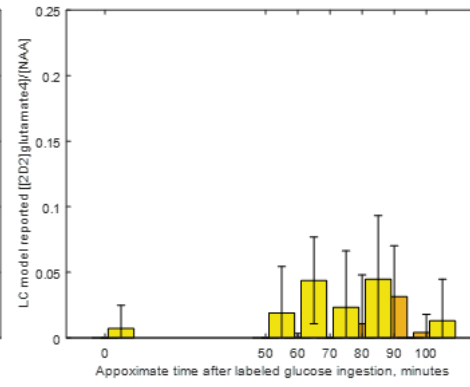
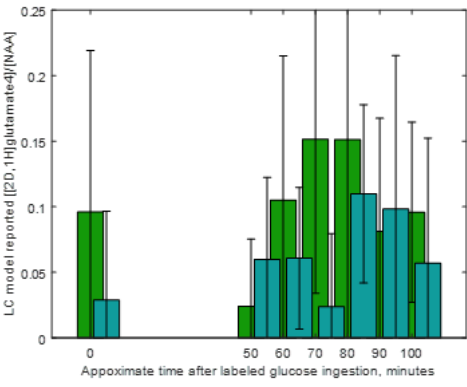
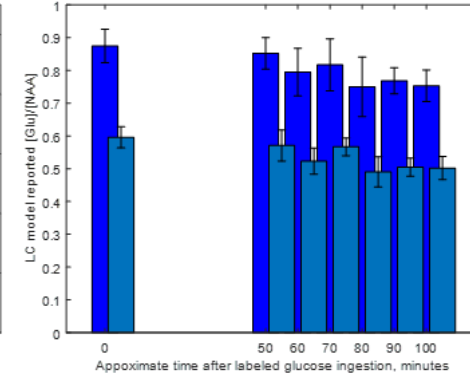
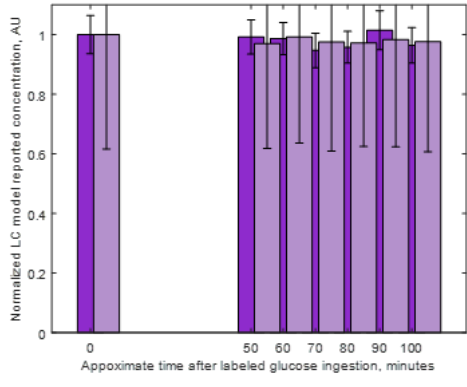
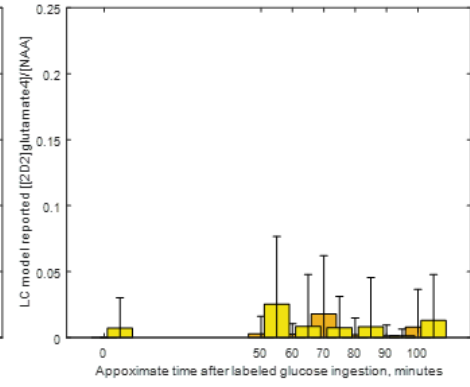
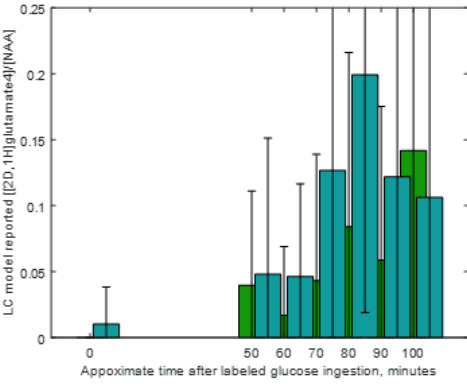
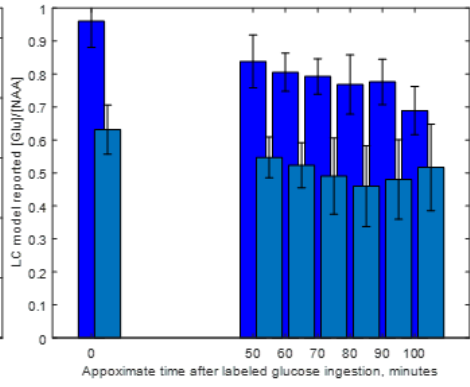
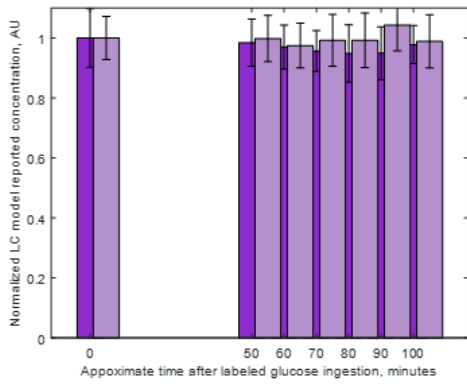


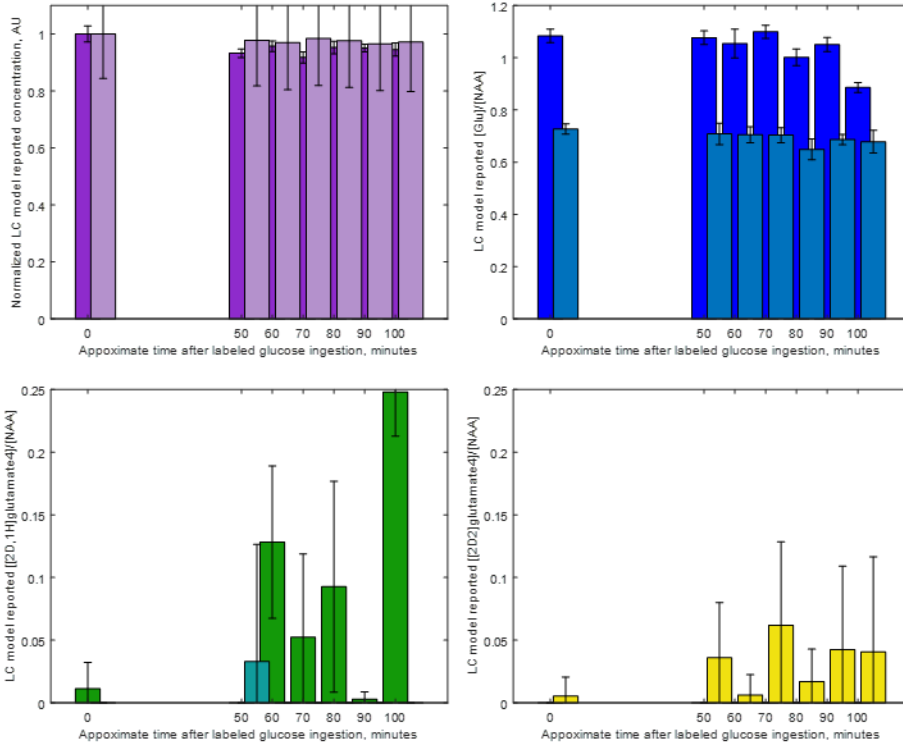
**Supplementary Figure 6.S1. Simulation of basis set glutamate metabolites. (A)** Single replacement of H with D can occur at H4 (top) or H4' (bottom). **(B)** Same as (A) with 27 Hz additional line broadening to simulate realistic in vivo conditions. **(C)** Single replacement at H4 with H-D coupling constants of 1 Hz (top) and 2 Hz (bottom). **(D)** Same as (C) with 27 Hz additional line broadening. **(E)** Glutamate elements in the basis set included normal, undeuterated (top), single proton replacement (middle), and double proton replacement (bottom). *Note that figure S1E is also included as Figure 1D in the main text.*

*Courtesy of N. Wilson*

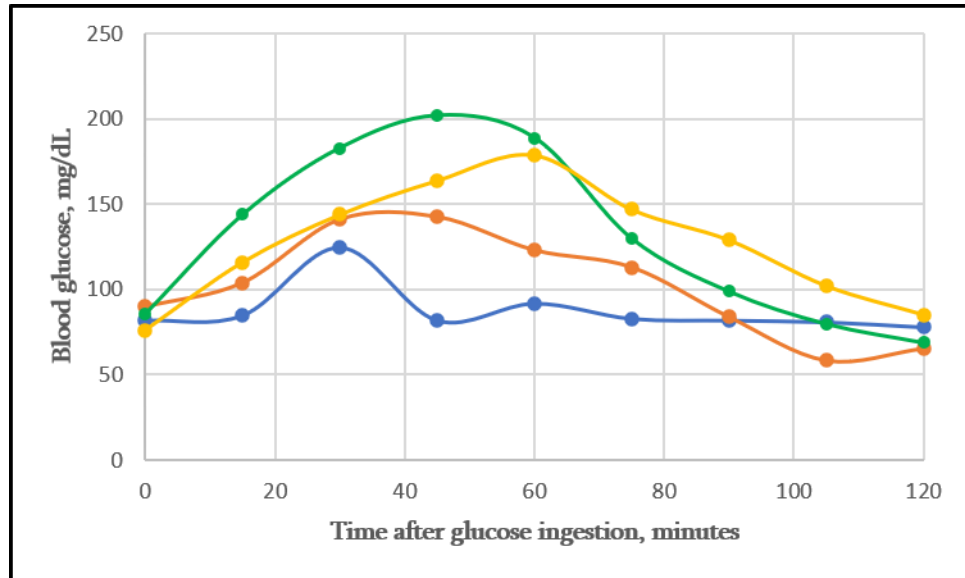


**Supplementary Figure 6.S2. Additional qCSI data sets (3 subjects) analogous to that shown in Figure 2.**

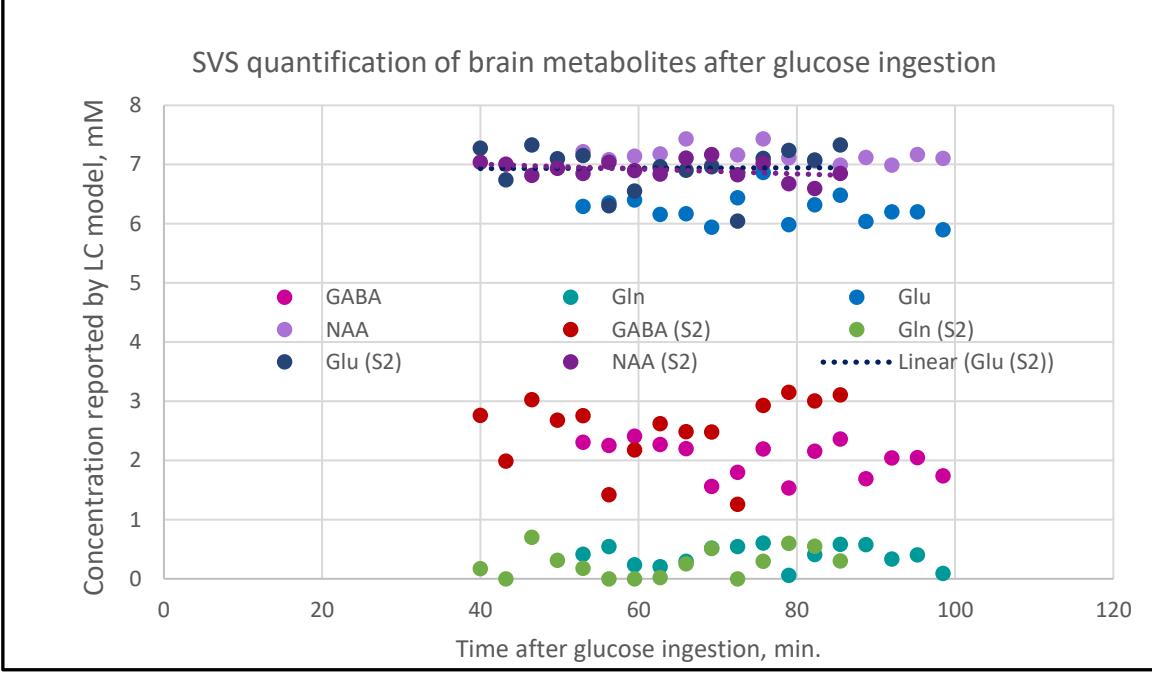




**Supplementary Figure 6.S3. Additional barplots of qCSI-quantified metabolites (3 subjects) analogous to that shown in Figure 3.**



**Supplementary Figure 6.S4. Blood glucose data** in four subjects after ingestion of 0.8g/kg of (non-deuterated) dextrose in aqueous solution. The variation present in this data would appear to reflect age, sex and body composition. All subjects were normoglycemic by 110 minutes following this “bolus” drink. **Supplementary Figure 6.S5 . SVS-quantified metabolites** upon ingestion of 0.8g/kg of non-deuterated dextrose in aqueous solution (control experiment to qMRS). Data from two subjects is plotted, as indicated in the legend (S2: Subject 2). A sample linear fit is shown to the NAA and Glu data for this subject. In contrast to qMRS with labeled glucose, this line has no slope over this time course. A white matter voxel was selected for this measurement.



## References:

1. Fuss TL, Cheng LL. Metabolic imaging in humans. *Top Magn Reson Imaging*. 2016;25(5):223-235. doi:10.1097/RMR.000000000000100
2. Kelloff GJ, Hoffman JM, Johnson B, et al. Progress and promise of FDG-PET imaging for cancer patient management and oncologic drug development. *Clin Cancer Res*. 2005;11(8):2785-2808. doi:10.1158/1078-0432.CCR-04-2626
3. Vander Heiden MG, Cantley LC, Thompson CB. Understanding the warburg effect: The metabolic requirements of cell proliferation. *Science (80- )*. 2009;324(5930):1029-1033. doi:10.1126/science.1160809
4. Van Zijl PCM, Yadav NN. Chemical exchange saturation transfer (CEST): What is in a name and what isn't? *Magn Reson Med*. 2011;65(4):927-948. doi:10.1002/mrm.22761
5. Cai K, Haris M, Singh A, et al. Magnetic resonance imaging of glutamate. *Nat Med*. 2012;18(2):302-306. doi:10.1038/nm.2615
6. Kogan F, Hariharan H, Reddy R. Chemical Exchange Saturation Transfer (CEST) Imaging: Description of Technique and Potential Clinical Applications. *Curr Radiol Rep*. 2013;1(2):102-114. doi:10.1007/s40134-013-0010-3
7. Morris PG. *Nuclear Magnetic Resonance Imaging in Medicine and Biology*. Clarendon Press; 1986.
8. Gujar SK, Maheshwari S, Bjorkman-Burtscher I, Sundgren PC. Magnetic Resonance Spectroscopy. *J Neuro-Ophthalmology*. 2005;25(3):217-226. doi:10.1097/O1.wno.0000177307.21081.81
9. Öz G, Deelchand DK, Wijnen JP, et al. Advanced single voxel <sup>1</sup>H magnetic resonance spectroscopy techniques in humans: Experts' consensus recommendations. *NMR Biomed*. Published online January 10, 2020. doi:10.1002/nbm.4236
10. Shulman RG, Rothman DL. <sup>13</sup>C NMR of Intermediary Metabolism: Implications for Systemic Physiology. *Annu Rev Physiol*. 2001;63(1):15-48. doi:10.1146/annurev.physiol.63.1.15
11. Beckmann N, Turkalj I, Seelig J, Keller U. *<sup>13</sup>C NMR for the Assessment of Human Brain Glucose Metabolism in Vivo*. Vol 30.; 1991. Accessed September 15, 2020. <https://pubs.acs.org/sharingguidelines>
12. de Graaf RA, Mason GF, Patel AB, Behar KL, Rothman DL. In vivo <sup>1</sup>H-[<sup>13</sup>C]-NMR spectroscopy of cerebral metabolism. *NMR Biomed*. 2003;16(6-7):339-357. doi:10.1002/nbm.847
13. Merritt ME, Harrison C, Storey C, Jeffrey FM, Sherry AD, Malloy CR. Hyperpolarized <sup>13</sup>C allows a direct measure of flux through a single enzyme-catalyzed step by NMR. *Proc Natl Acad Sci*. 2007;104(50).
14. Brindle KM. Imaging metabolism with hyperpolarized <sup>13</sup>C-labelled cell substrates. *J Am Chem Soc*. 2015;20:6418-6427.

15. Lu M, Zhu XH, Zhang Y, Mateescu G, Chen W. Quantitative assessment of brain glucose metabolic rates using in vivo deuterium magnetic resonance spectroscopy. *J Cereb Blood Flow Metab.* 2017;37(11):3518-3530. doi:10.1177/0271678X17706444
16. De Feyter HM, Behar KL, Corbin ZA, et al. Deuterium metabolic imaging (DMI) for MRI-based 3D mapping of metabolism in vivo. *Sci Adv.* 2018;4(8):7314-7336. doi:10.1126/sciadv.aat7314
17. Kreis F, Wright AJ, Hesse F, Fala M, Hu DE, Brindle KM. Measuring tumor glycolytic flux in vivo by using fast deuterium MRI. *Radiology.* 2020;294(2):289-296. doi:10.1148/radiol.2019191242
18. van Zijl PCM, Brindle KM. Spectroscopic measurements of metabolic fluxes. *Nat Biomed Eng.* 2020;4(3):254-256. doi:10.1038/s41551-020-0535-8
19. Rich LJ, Bagga P, Wilson NE, et al. <sup>1</sup>H magnetic resonance spectroscopy of 2H-to-<sup>1</sup>H exchange quantifies the dynamics of cellular metabolism in vivo. *Nat Biomed Eng.* 2020;4(3):335-342. doi:10.1038/s41551-019-0499-8
20. Macallan DC, Asquith B, Zhang Y, et al. Measurement of proliferation and disappearance of rapid turnover cell populations in human studies using deuterium-labeled glucose. Published online 2009. doi:10.1038/nprot.2009.117
21. Scheenen TWJ, Heerschap A, Dennis , et al. Towards <sup>1</sup>H-MRSI of the human brain at 7T with slice-selective adiabatic refocusing pulses. *Magn Reson Mater Phy.* 2008;21:95-101. doi:10.1007/s10334-007-0094-y
22. Brown TR, Kincaid BM, Ugurbil K. NMR chemical shift imaging in three dimensions. *Proc Natl Acad Sci U S A.* 1982;79(11):3523-3526. doi:10.1073/pnas.79.11.3523
23. Bottomley PA. Spatial localization in NMR spectroscopy in vivo. *Ann N Y Acad Sci.* 1987;(508):333-348.
24. Tkáč I, Gruetter R. Methodology of <sup>1</sup>H NMR spectroscopy of the human brain at very high magnetic fields. *Appl Magn Reson.* 2005;29(1):139-157. doi:10.1007/BF03166960
25. Zhu H, Barker PB. MR spectroscopy and spectroscopic imaging of the brain. *Methods Mol Biol.* 2010;711:203-226. doi:10.1007/978-1-61737-992-5\_9
26. Nanga RPR, Hariharan H, Reddy R. Fully automated macromolecule suppressed single voxel glutamate spectroscopy (FAMOUS SVGS). *J Transl Med.* 2016;14(1):1-10. doi:10.1186/s12967-016-0970-1
27. Nanga RPR, DeBrosse C, Kumar D, et al. Reproducibility of 2D GluCEST in healthy human volunteers at 7 T. *Magn Reson Med.* 2018;80(5):2033-2039. doi:10.1002/mrm.27362
28. Provencher SW. Estimation of metabolite concentrations from localized in vivo proton NMR spectra. *Magn Reson Med.* 1993;30(6):672-679. doi:10.1002/mrm.1910300604
29. Soher BJ, Semanchuk P, Todd D, Steinberg J, Young K. *VeSPA: Integrated Applications for RF Pulse Design, Spectral Simulation and MRS Data Analysis.* Vol 12.; 1994. Accessed March 31,

2021.

<http://scion.duhs.duke.edu/vespa/http://www.swig.org>. The authors acknowledge NIH funding-1R01EB008387-01A1

30. Simpson R, Devenyi GA, Jezzard P, Hennessy TJ, Near J. Advanced processing and simulation of MRS data using the FID appliance (FID-A)—An open source, MATLAB-based toolkit. *Magn Reson Med*. 2017;77(1):23-33. doi:10.1002/mrm.26091
31. Bagga P, Rich LJ, Cember ATJ, et al. Assessing gray and white matter glutamatergic turnover in human brain non-invasively using 1H MRS and deuterated glucose. *Proc Annu Meet Int Soc Magn Reson Med*. Published online 2020.
32. Moser P, Bogner W, Hingerl L, et al. Non-Cartesian GRAPPA and coil combination using interleaved calibration data – application to concentric-ring MRSI of the human brain at 7T. *Magn Reson Med*. 2019;82(5):1587-1603. doi:10.1002/mrm.27822
33. Coello E, Noeske R, Burns BL, et al. High-resolution echo-planar spectroscopic imaging at ultra-high field. *NMR Biomed*. 2018;31(11):e3950. doi:10.1002/nbm.3950
34. Mullins PG, McGonigle DJ, O’Gorman RL, et al. Current practice in the use of MEGA-PRESS spectroscopy for the detection of GABA. *Neuroimage*. 2014;86:43-52. doi:10.1016/j.neuroimage.2012.12.004
35. van Eijsden P, Behar KL, Mason GF, Braun KPJ, de Graaf RA. In vivo neurochemical profiling of rat brain by 1 H-[ 13C] NMR spectroscopy: cerebral energetics and glutamatergic/GABAergic neurotransmission. *J Neurochem*. 2010;112(1):24-33. doi:10.1111/j.1471-4159.2009.06428.x
36. de Graaf RA, Rothman DL, Behar KL. State of the art direct 13C and indirect 1H-[13C] NMR spectroscopy in vivo. A practical guide. *NMR Biomed*. 2011;24(8):958-972. doi:10.1002/nbm.1761
37. Dehghani M, Do KQ, Magistretti P, Xin L. Lactate measurement by neurochemical profiling in the dorsolateral prefrontal cortex at 7T: accuracy, precision, and relaxation times. *Magn Reson Med*. 2020;83(6):1895-1908. doi:10.1002/mrm.28066
38. Bak LK, Schousboe A, Waagepetersen HS. The glutamate/GABA-glutamine cycle: Aspects of transport, neurotransmitter homeostasis and ammonia transfer. *J Neurochem*. 2006;98(3):641-653. doi:10.1111/j.1471-4159.2006.03913.x
39. Rothman DL, Graaf RA, Hyder F, Mason GF, Behar KL, De Feyter HM. In vivo 13C and 1H-[ 13C] MRS studies of neuroenergetics and neurotransmitter cycling, applications to neurological and psychiatric disease and brain cancer. *NMR Biomed*. 2019;32(10). doi:10.1002/nbm.4172
40. Pavlova NN, Thompson CB. The Emerging Hallmarks of Cancer Metabolism. *Cell Metab*. 2016;23(1):27-47. doi:10.1016/j.cmet.2015.12.006
41. Rich LJ, Bagga P, Mizsei G, et al. Detecting glycolytic metabolism in glioblastoma using a new 1H MRS and [6,6’-2H2]glucose infusion based approach. *Proc Annu Meet Int Soc Magn Reson Med* . Published online 2020.



# Appendices

## ***Note regarding authorship of Appendix contents:***

All of the code that appears in **Appendix A**: Bloch-McConnell Simulations of the CEST experiment was written by me, **A. Cember**, with the exception as indicated of the ‘matrix exponential’ function, which is adapted from the `r8` library, and the general structure of the Matlab ‘Main’ function, which is adapted from the corresponding function written by **Dr. Hari Hariharan**. As explained in the Introductory Note to Appendix A, the remaining calculations, to whatever degree they were performed explicitly in the original Matlab version, are based off of Dr. Hariharan’s Matlab function `CEST4sim.m`, which in turn is likely inspired by the reference provided in the Appendix. The Mex-based architecture and implementation is by my own design.

In **Appendix B**, I am the author of all functions relating to  $B_1$  correction, and all ‘wrapper’ functions that are explicitly documented here. As indicated, many internally called functions which relate to CEST post-processing outside of  $B_1$  correction are previously existing, as is the GUI from which screenshots are taken to explain the steps of 3D CEST post-processing. My contribution there, outside of  $B_1$  correction, is only as the narrator. To the best of my knowledge, **Dr. Hari Hariharan**, **Dr. Anup Singh** and **Dr. Mark Elliott** are the CMROI-based contributors to this code. Of course, libraries like **spm8** and **NiftI** were developed by the wider imaging community. Specifically, as per the documentation included in these packages, SPM is developed by members and collaborators of the Wellcome Trust Centre for Neuroimaging; the author of NiftI identifies himself only as the proprietor of the email address [jimmytoolbox@gmail.com](mailto:jimmytoolbox@gmail.com).

## Appendix A: Bloch-McConnell simulations of the CEST experiment

Abby, CMROI

January 2021

### Introductory Note

The Bloch equations are a set of coupled differential equations which phenomenologically describe the dynamics, or motion, of a magnetization vector under the physical conditions of an NMR experiment. McConnell, who was interested in how the MR signal is affected by chemical exchange, realized that he could simply add terms to the Bloch equations which allowed the same mathematics to be used for his purposes. These equations which include terms representing chemical exchange are thus known as the Bloch-McConnell equations. For more about chemical exchange as a phenomenon and the classical physics treatment of NMR and MRI, please see Chapter 1 of this thesis. Like all differential equations, the Bloch-McConnell equations can be expressed in matrix form and solved numerically using the mathematics of matrices. The purpose of this Appendix is to document and explain the Matlab and C (Mex) code behind simulations of the gluCEST experiment, with explicit mention of the mathematics or physics only to the extent that it is necessary to follow along with the calculation.

This version of the simulation is based off of Hari's 'CEST4sim.m', and I believe that he based his simulations off of the theoretical treatment outlined in Woessner's 2005 paper<sup>15</sup>. The math is identical to any in that original code; my modifications were to 'translate' most of this math into the C language rather than Matlab, as this speeds up the calculation, and I wanted to do many, many of these simulations in order to study the  $B_1$  dependence of the signal. Also, the default parameter values in CEST4sim have Pool 4 representing myoinositol (MI), whereas I have modified them in an attempt to instead model the slow, 'NOE' like exchange that probably originates from cross-relaxation of the bulk water with lipids and other non-polar moieties in macromolecules.

The structure of this documentation is sort of in layers: I start with the outermost "layer" of code – the main Matlab function—and then move in to the functions and further subfunctions written in C that do the actual calculating. Eventually, we arrive at matrix operations that are general, and for which I was able to use existing code provided in Numerical Recipes (the world's most important scientific computing book) or in the widely available r8 library. If you are a CMROI user, you may not need to read beyond the explanation of the main Matlab function for your purposes. If you are someone on the internet who knows nothing about chemical exchange or MRI and just wants an instructive example of how to use MEX to integrate C code into Matlab for any kind of scientific computing purposes, then you definitely do want to keep reading. Have fun!

---

<sup>15</sup> 1. Woessner DE, Zhang S, Merritt ME, Sherry AD. Numerical solution of the Bloch equations provides insights into the optimum design of PARACEST agents for MRI. *Magn Reson Med*. 2005;53(4):790-799. doi:10.1002/mrm.20408

## Main function (Matlab)

The simulation is called by running the script `mainCalcMz_December2018edits_1.m`. In other words, this is the function that needs to be open in Matlab so that you can press “play” - you probably don't want to run this blindly by command line unless you know what you're doing, as the parameter values are set 'manually' in this script. It looks like this, with my comments from this document added in bright pink, in this font. Comments that are actually in the code are in green, as in the Matlab interface.

```
%Ha. Since we're using MATLAB, we can just pass CalcMz() these whole  
%arrays. Only then once we're in C, we'll have to pass pointers to  
the  
%inner functions.
```

If you don't understand what this comment means, that's OK – if you do, and you want to mess with the underlying C code, just heed the warning to be *\*very\** careful when passing arguments back and forth!!!

```
pathnam = '.';  
f1 = 'hanning.pta';  
fla = [pathnam filesep f1];
```

The above code is the first step to starting the simulation: it takes a file which describes the shape of the pulse. In all honesty, I have no idea what a .pta file actually contains or how to make a new one – but presumably somebody does. This is, needless to say, beyond the scope of the present document. I have never simulated any other pulse shape, but if you would like to, simply replace this file.

```
switch exist(fla)
```

This section of code is checking whether we have used that .pta file to specify the pulse shape; if we don't have one, it throws an error. It also contains code that specifies a rectangular pulse.

```
case 2  
    krect = strfind(fla, 'rect');  
    if (isempty(krect))  
        fid = fopen(fla, 'r');  
        jj = 0;  
        while 1  
            tline = fgetl(fid);  
            if ~ischar(tline), break, end  
            jj = jj+1;  
            if (jj > 8)  
                str1 = strtok(tline, ';');  
                a = sscanf(str1, '%f%f');  
                amp1(jj-8) = a(1);  
                phi(jj-8) = a(2);  
            end  
        end  
        count1 = jj-8;  
        fclose(fid);  
    else  
        amp1 = (1:100)*0.0+1.0;  
        phi = amp1-1;
```

```

        count1 = 100;
    end
    otherwise
        amp1 = [];
        phi = [];
        error(' No file selected. No data returned.\n\n');
end

% amp1 = [0.1,0.25,0.5,0.25,0.1,0.25,0.5];
% phi = [0,30,60,90,60,30,0,30,60,90];
%{0,25,50,75,100,125,150,175,200,225,250}

```

Now that we have our pulse shape defined as a vector over 100 points in “time”, we need to set the rest of the parameters. We are going to store them in a customized ‘struct’, as pairs of ‘field’ and ‘value’. The first two, amplitude and phase, are set by the .pta file read in above. The commented out lines that I was using for debugging give you an idea of their structure.

General parameters:

```

%General parameters
field1 = 'amplitude_array';    value1 = amp1;
field2 = 'phase_array';        value2 = phi;
field3 = 'count1';            value3 = count1;
field4 = 'pw1';                value4 = 800; Saturation pulse duration, in
ms
field5 = 'b1';                  value5 =
{0,10,20,30,40,50,60,70,80,90,98,126,154,182,210,238,266,294,322,350};
field6 = 'puloffsetppm';        value6 = 3.0; %%% Saturation pulse offset,
in ppm – here, you can change the ‘type’ of CEST experiment... 3.0 is for gluCEST, of course
field7 = 'pw1dc';              value7 = 99.8; Saturation pulse duty cycle
field8 = 'cf';                  value8 = 300; Saturation pulse carrier
frequency

```

Note that saturation  $B_1$  amplitude here is expressed as a vector of values, in Hz.

*IMPORTANT NOTE: If you want to run the simulation iteratively with respect to some other parameter instead of  $B_1$ , you can! You will see later on how to do this. In that case, this other parameter would be entered as a vector, and  $B_1$  would take only a single value. If you want to loop over two parameters, you will have to write this capability in yourself, but that would be straightforward.*

After this, we enter in MR-relevant properties of the components we’re interested in simulating. Each component has the following properties specified: concentration (M),  $T_1$ ,  $T_2$ , resonant frequency relative to water (‘offset ppm’), and exchange rate with bulk water. Concentration is expressed as ‘ $M_0$ ’, since what we’re basically saying is that this is the relative contribution of this set of spins to the magnetization of the sample as a whole.

Some important notes about concentrations:

--The concentration of water itself **differs between gray and white matter** of the brain  
 --The fraction of this water that is 'bound' differs between gray and white matter of the brain.  
 (--The parameter called 'bwfraction' here is not doing anything. It is vestigial, but one can enter a value there basically as a note, in order to not have to do the math when you look at these again later.)  
 --Both of these parameters may be very different for other tissues, but as long as you look them up and have a reasonable estimate there is no reason this simulation is not valid for non-brain application.  
 --**Metabolites that have multiple protons** have to be treated as [concentration normally found in vivo] x [number of protons per molecule]. This is why, for example, M<sub>0</sub> of glutamate is entered here as .036, or 36mM: that's for 12mM glutamate multiplied by the three protons on each which contribute to that <sup>1</sup>H resonance.

```

%Bulk water
field9 = 'M0w';           value9 = 77;%G:77, W:88 %%%%%%%%%%
field10 = 'T1a';          value10 = 1.7;
field11 = 'T2a';          value11 = .085; %T2 of bulk water
at 7T: 80-90ms
field12 = 'offsetappm';    value12 = 0;
field13 = 'bwfraction';    value13 = 0;%%%%%%%%%
field14 = 'M0a';          value14 = 77;%G: 66.99; W: 67.76; %
%%%%%%%%%

%Bound water: proton exchange term
field15 = 'M0bw';         value15 = 11;%G: 10.01; W: 20.24;
%% 0;%%%%%%%%%
field16 = 'T1bw';         value16 = 1;
field17 = 'T2bw';         value17 = 1e-5; %T2 of bound water:
.02 ms (also set to match exp. data)
field18 = 'offsetbwppm';   value18 = -2.4;
field19 = 'exratebw';     value19 = 20; %Literature value of
BW exchange rate is 20Hz

%Protein amides
field20 = 'M0b';          value20 = .08; %0.072; %%%%%%%%%%
protein amides
field21 = 'T1b';          value21 = 1;
field22 = 'T2b';          value22 = 0.001;
field23 = 'offsetbppm';   value23 = 3.5;
field24 = 'exrateb';      value24 = 10;

%Lipids: cross-relaxation term
field25 = 'M0c';          value25 = 1; %%%%%%%%%% New: NOE
from lipid
field26 = 'T1c';          value26 = 1; %
field27 = 'T2c';          value27 = .001; %1ms
field28 = 'offsetcppm';   value28 = -3.5; %
field29 = 'exratec';      value29 = 5; %cross-relaxation rate

%Creatine

```

```

    field30 = 'M0d';          value30 = 0.032;% 0.032;
    %%%%%%%%%%creatine
    field31 = 'T1d';          value31 = 1;
    field32 = 'T2d';          value32 = 0.01;
    field33 = 'offsetdppm';   value33 = 1.8;
    field34 = 'exrated';      value34 = 800;

    %Glutamate
    field35 = 'M0e';          value35 = 0.036;%0.036; % %%%%%%%%%%
    glutamate
    field36 = 'T1e';          value36 = 1.0;
    field37 = 'T2e';          value37 = 0.01;
    field38 = 'offseteppm';   value38 = 3.0000;
    field39 = 'exratee';      value39 = 1000; %2400

```

Before running the script, you should set these values to whatever you want. When the script runs, these are now all packaged into this struct called 'parameters'. Because this is now going to be passed to a function in C, it has to be assigned something called a pointer (ptr).

```

    parameters = struct(field1, value1, field2, value2, field3,
value3,field4, value4, field5, value5, field6, value6, field7, value7,
field8, value8,field9, value9, field10, value10, field11, value11,
field12, value12, field13,value13, field14, value14, field15, value15,
field16, value16, field17, value17,field18, value18, field19, value19,
field20, value20, field21, value21, field22,value22, field23, value23,
field24, value24, field25, value25, field26, value26,field27, value27,
field28, value28, field29, value29, field30, value30, field31,value31,
field32, value32, field33, value33, field34, value34, field35,
value35,field36, value36, field37, value37, field38, value38,field39,
value39);
    ptr2pars = StructureHandle(parameters);

```

This is just checking to make sure that you haven't accidentally told the simulation to go for longer 'time' than the definition of the pulse shape. If you haven't messed with anything, this shouldn't come up. You will just see the message that you are 'good to go'.

```

    if (parameters(1).count1 > length(amp1) || parameters(1).count1>
length(phi))
        fprintf("Error: count1 will overstep the allocated phi and amp1
arrays! Exiting without calling calculate().\n");
        return;
    else
        fprintf("Check to make sure that count1 is not greater than
array lengths-- good to go!\n");
    end

%   for i =1:11
%   CalculatedContrast = CalculateMz2(ptr2pars.structure(i));
%   fprintf("Returned from CalculateMz back to main.Calculated
Contrast = %f\n", CalculatedContrast);
%   end

```

The actual calculation is going to be done in CalculateMz3 and subsidiary functions. It will return back to you a variable called 'Calculated Contrast', which is a list of two values:  $\pm 3.0$ ppm of the Z-spectrum for each of the values of the vector-variable used as input (in my case,  $B_1$ ). The idea is that these can then easily be plotted against that independent variable vector or otherwise used conveniently.

```
CalculatedContrast = CalculateMz3(parameters);  
%7/21/2019  
Mz_pos = CalculatedContrast(1,:); Mz_neg = CalculatedContrast(2,:);
```

### Calculate Mz (C++)

CalculateMz3.cpp is a C++ file. C and C++ files are quite different from Matlab files. One important difference is that unlike in Matlab, multiple functions can be defined in a single file. They have to be declared as 'prototypes' somewhere before their actual code. The prototype gives the following information: the name of the function, the output variable of the function, and the input variable(s) of the function. I will point these out when they show up.

They also need to be 'compiled'. I am unqualified to explain what precisely this means in computer science terms, but the practical point here is that they won't 'just work when you press play' like Matlab functions – if you're using a C-based function, you have to call Matlab's function 'mex' (short for 'Matlab executable') which does some kind of special compilation which allows Matlab to interface with C. I recommend checking the Matlab documentation for the latest version of the mex compilation command, as these sometimes change between Matlab versions. \*Important\*: if you are using a Windows machine, always compile mex with the flag: `-compatibleDimArrays`

```
/*CalculateMz2.cpp  
 *THIS VERSION is different from CalculateMz in that no calls are made  
 via mexCallMatlab.  
 *Instead, it uses functions from r8lib.c, which requires that it be  
 included in the call to mex:  
 *'mex CalculateMz3.cpp r8lib.c'
```

So, before you use this program, you need to type the above line into Matlab. It compiles CalculateMz3.cpp, and also includes the C library 'r8lib'.

```
*IT WORKS, as of 9/14/2017  
*  
 *This function calculates the magnetization (and contrast in  
 magnetization  
 *arising from "+" and "-" pulses) for a given voxel. It accepts as an  
 argument  
 *a structure that contains:  
 *Input arguments:  
   field1 = 'glutamate_concentration'; value1 = {2.0, 4.0};  
   field2 = 'B1_strength';           value2 = 200;  
   field3 = 'T1_freeWater';         value3 = 1000;
```

```

    ...and so on
    *and outputs the magnetization for that voxel given a "+" pulse, a "-"
pulse
    *(away from resonance frequency, that is) and the contrast between the
two.
    *

```

Below: this is true, but ignore it. The current version of the Bloch simulations are not fully integrated with the 'virtual phantoms' code, but if you are imaginative, you can see how this would be done.

```

    *It is designed to be called as a "mex" from another function that
contains "maps"/
    *"masks"/"phantoms", or whatever you want to call them -- objects that
have
    *properties as a function of space that will generate MRI contrast.
These will
    *be in the form of structs like the one below. For simplicity, we'll
start with
    *just six ROIs, in which only one parameter is changing between them--
meaning that
    *all fields in the struct will be just single numbers, except for one
which will
    *be a vector with six elements (a la field1, currently). */

/*

    parameters = struct(field1, value1, field2, value2, field3,
value3);*/
    /*In a loop over r, Mz(r) = CalculateMz(parameters(r));*/

    /*In this way, parameters(1) will contain parameters for the ROI in
which
    *[glutamate] = 2, while parameters(2) will contain those for the
ROI in which
    *[glutamate] = 4. For now, parameters other than [glutamate] remain
the same between
    *ROIs. To access [glutamate], we ask for parameters(1).f1; to
access B1,
    *parameters(1).f2, and so on.*/

    /* Read in file to create amplitude and phase arrays*/
    /* This is done in the Matlab calling function*/

```

#include and #define statements: Needed for C functions. They tell the compiler to go look for these header (.h) files, which you need to have in the directory. The headers <named like this> are some kind of existing or standard thing. Ones <like this> were introduced by me. "Calculate2" ... "LU" stands for "lower-upper decomposition", a matrix operation that we'll need. 'Pi' is self explanatory.

```

#include <stdio.h>
#include <string.h>

```



```

#include <math.h>
#include <mex.h>
#include "LU.h"
#include "Calculate2.h" //for new version of CalculateY()
#define pi 3.14159;

```

Next, we're going to define some structs. Unlike in Matlab, where you can just tack things on, in C you need to define ahead of time everything that a struct is going to contain.

```
/*C structs*/
```

Input parameters: Basically, we'll take the corresponding struct passed from Matlab, and re-assign all the contents to this local one.

```

struct InputParameters{

    /*Things determined from reading the pulse shape file*/
    double *amp1; //I think these vectors are 0-100; if they're 0-1,
change this pointer to double.
    double *phi;
    int count1;

    /*Other pulse-related ones. Some of these may be OK as ints, not
sure at present*/
    double pw1;
    double b1;
    double puloffsetppm;
    double pwldc;
    double cf;

    /*Chemical species-specific*/
    double M0w, T1a, T2a, offsetappm, bwfraction, M0a;
    double M0bw, T1bw, T2bw, offsetbwppm, exratebw;
    double M0b, T1b, T2b, offsetbppm, exrateb;
    double M0c, T1c, T2c, offsetcppm, exratec;
    double M0d, T1d, T2d, offsetdppm, exrated;
    double M0e, T1e, T2e, offseteppm, exratee;
};

```

'Z contrast': This will hold our output: positive offset MZ,water, negative offset MZ,water, and then the negative normalized contrast between them. (Note that if you are doing the loop of simulations over offset frequency to generate a Z-spectrum, you only need to do the positive half, because the other side is done automatically.)

```

struct Zcontrast {
    double SimMza;
    double SimMzb;
    double contrastz;
};

```

Here are the prototypes, as promised. Important note: Not all of these prototypes are actually in this file, CalculateMz3.cpp – that would have just made the code too long. The first two, calculate () and MatrInv() are in CalculateMz3.ccp; CalculateY is in the header file "Calculate2.h"

which we included above. Multiple and Divide were later replaced by functions from the r8 library, and are vestigial.

```
/*Prototypes*/
void calculate (struct InputParameters *voxelPars1, struct Zcontrast
*contrast, double **pntrA, double *pntrAinvB, double **CopyOfMatrix,
double *vector, double *col, int *indx, double *Aat, double *Aate,
double *sum, double *product, double *pntrA1, double *pntrB, double
*pntrY, double *pntrY0);
void MatrInv (double **matrix, int n, double **CopyOfMatrix, double
*vector, int *indx, double *col);
void Multiply (double *pntrAinvB, double **pntrAinv, double *pntrB);
void Divide (double *pntrMz, double *pntrY0, double M0a);
void CalculateY(double *pntrY, double timeScalar, double **pntrA,
double *pntrY0, double *pntrAinvB, double *Aat, double *Aate, double
*sum, double *product);
```

Now we have to do some tricky stuff having to do with going back and forth between C and Matlab. When you call 'CalculateMz3.cpp' from Matlab, what you're actually calling is this thing called 'mexFunction'. 'Void' in C means that the function does not return anything. However, in the case of mex, this is supremely misleading, because what actually happens is that the mex Function returns the pointer to the array called "plhs". (If you don't know what a pointer is, don't worry. It's basically what it sounds like.) In the mex function, no matter what in the world it does, there are only four arguments: the contents of the input (which Matlab calls 'right hand side, as if it were an equation), an integer proclaiming how many items are in this array, and the same two things for the output.

The designation 'void' for all of the above functions may also be confusing to someone unfamiliar with C style: how can we get any output or answers if none of the functions return any arguments? In effect, the function returns the argument in the form of modifying the pointers themselves. For example, we may send MatrInv the pointer \*\*matrix full of zeros, but it gets returned to us filled with the answer to the matrix inversion problem that we gave it.

### Mex Function – still part of CalculateMz3.cpp

```
/* MEX business*/
void mexFunction(int nlhs, mxArray *plhs[], int nrhs, const mxArray
*prhs[]){
    /* mexPrintf("Inside the mex function of CalcMz2.\n");
    mexEvalString("drawnow;");*/

    /*declare local variables*/
    struct InputParameters voxelPars;
    struct InputParameters *point2pars;
    struct Zcontrast contrast;
    struct Zcontrast* ptr2contrast;
    ptr2contrast = &contrast;
    mxArray *in, *out;
    mxArray *temp;
```

```

double *output;
int nFields;
int i,j,k;

```

A note about the syntax of these declarations: the first line can be translated as “we’re declaring a struct of the type ‘Input Parameters’ which we are going to call ‘voxelPars’.” The second line means, “we’re declaring a pointer to point to a struct of the type ‘Input Parameters’; the name of this pointer is ‘point2pars’”. And so on.

The next step is to “associate the inputs”; i.e., receive this ‘rhs argument’ that was sent to the mex function into a local variable. All I do right now is simply make a copy of it, and check that the number of input fields (that big parameters struct ) is what I intend.

```

    in = mxDuplicateArray(prhs[0]); /*'in' now is a copy of the input
struct*/
    nFields = mxGetNumberOfFields(prhs[0]);
    if (nFields != 39) mexPrintf("Error: the number of fields in the
input struct is incorrect.\n");
    // if (nFields == 39) mexPrintf("The number of fields in the input
struct is correct: 39.\n");
    /* mexPrintf("Should have examined the input struct by now...\n");
mexEvalString("drawnow;");*/

    /*These calls are going to return pointers...
which means I need pointers to receive their values...(temp)
Then, I can assign the values of the struct by dereferencing the
pointer.*/

```

After that, we “associate the outputs”. We now have to do something which is required in C but not in Matlab: declare memory for the variables we need. As far as I can tell, since the mex function was already sent the input argument(s), memory sort of automatically exists for this variable. However, we need to declare memory for the output. Imagine you order something from Amazon: it already came in a box. But if you are sending something to someone else, you are responsible for procuring a box yourself. Same idea.

**\*Important\*** If you are familiar with C, you will notice that we do not use the familiar `malloc` function. MEX has its own memory allocation functions, called “`mxCreate***`”, “`mxCalloc`” and so on. See Matlab’s documentation for all the flavors of these functions. *Regular C memory allocation calls do not work in Mex!!!*

```

    //associate outputs
    // out = plhs[0] =
mxCreateDoubleMatrix(1,(mxGetDimensions(prhs[0])[1]), mxREAL); /*this
has no memory allocated for it yet*/
    /*TEST 7/21/10*/ out = plhs[0] =
mxCreateDoubleMatrix(3,(mxGetDimensions(prhs[0]) [1]), mxREAL);
    // out = plhs[0] = mxCreateDoubleScalar(0.0);
    /*TEST, used to be output = mxGetPr(out); - figured perhaps I need a
double pointer */
    output = mxGetPr(out);

```

```

/*mexPrintf("Number of dimensions has been determined as: %d.\n",
mxGetNumberOfDimensions(prhs[0]));
mexPrintf("Size of x-axis array has been determined as: %d.\n",
mxGetDimensions(prhs[0])[1]);
mexEvalString("drawnow;");*/

```

Now we're going to do a whole bunch more memory allocation for the variables we need for the calculation. There is nothing going on here outside of regular C programming. If you're not familiar with C, you can think of this as "buying the boxes" that we need to ship stuff around in, and assigning them labels.

```

/*Passed variables memory allocation*/
double **pntrA;
/*CAUTION! At different times in this function, pntrA is used to
point to matrices Aa, Ab, Ad AND their inverses*/
pntrA = (double **)mxCalloc(18, sizeof(double*));
for (i=0; i <18; i++){
    pntrA[i] = (double *) mxCalloc(18, sizeof(double));
}
double *pntrAinvB;
pntrAinvB = (double *) mxCalloc(18, sizeof(double));

/*Single dimension version of pntrA*/
double *pntrA1;
pntrA1 = (double*)mxCalloc(18*18, sizeof(double));

/*used by MatrInv()*/
double **CopyOfMatrix;
CopyOfMatrix = (double**)mxCalloc(18, sizeof(double*));
for (i=0; i<18; i++){
    CopyOfMatrix[i] = (double*)mxCalloc(18, sizeof(double));
}

double *vector;
double *col;
int *indx;
vector = (double *)mxCalloc(18, sizeof(double));
indx = (int *)mxCalloc(18, sizeof(int));
col = (double *)mxCalloc(18, sizeof(double));

/*used by CalculateY()*/
double *Aat;
Aat = (double*)mxCalloc(18*18, sizeof(double));

double *Aate;
Aate = (double*)mxCalloc(18*18, sizeof(double));

double *sum;
sum = (double*)mxCalloc(18, sizeof(double));
double *product;

```

```

product = (double*)mxCalloc(18, sizeof(double));

double *pntrB;
pntrB = (double *) mxCalloc(18, sizeof(double));

double *pntrY;
pntrY = (double *) mxCalloc(18, sizeof(double));

double *pntrY0;
pntrY0 = (double *) mxCalloc(18, sizeof(double));

```

Next, we perform the somewhat tedious operation of retrieving all of the simulation parameters from our friend 'prhs' that was holding them. The names of the first few are highlighted for visibility. Note that we keep using this function `mxGetScalar()` – this is because everything in our parameters struct is some kind of number. In the event that you have something else in there, you need to use the appropriate “get” function for that variable type.

```

for (k = 0; k < (mxGetDimensions(prhs[0])[1]); k++){
    /* mexPrintf("Looping over input values. k = %d\n",k);
    mexEvalString("drawnow;");*/

    temp = mxGetFieldByNumber(prhs[0],0,0);
    voxelPars.ampl = mxGetPr(temp);
    temp = mxGetFieldByNumber(prhs[0],0,1);
    voxelPars.phi = mxGetPr(temp);
    /* for (i=0; i<4; i++){
        mexPrintf("%f\t%f\t\n", voxelPars.ampl[i],voxelPars.phi[i]);
    }*/
    temp = mxGetFieldByNumber(prhs[0],0,2);
    voxelPars.count1 = mxGetScalar(temp);
    temp = mxGetFieldByNumber(prhs[0],0,3);
    voxelPars.pw1 = mxGetScalar(temp);
    temp = mxGetFieldByNumber(prhs[0],k,4); /*This argument must be 'k'
for B1*/
    voxelPars.b1 = mxGetScalar(temp);
    temp = mxGetFieldByNumber(prhs[0],0,5);/*This argument must be 'k'
for offset*/

```

**\*Important\*** We now interrupt this code to explain how to change what simulation parameter the series of simulations will vary. Note that this whole thing is in a loop over the indexing variable 'k'. 'k' only appears once: in whatever field you want to loop over. The two that I've ever used are B<sub>1</sub> amplitude (as the code is set up for here) and frequency offset, to create a Z-spectrum. If you want to do the latter, you would replace the 'k' in the B<sub>1</sub> line with '0' (to set it at a single value), and replace that middle 0 in the 'puloffsetppm' line here with 'k'. Of course, if you wanted to, you could simulate a surface of any number of dimensions with one press of the button by adding more layers to this loop.

```

voxelPars.puloffsetppm = mxGetScalar(temp);
temp = mxGetFieldByNumber(prhs[0],0,6);

```

```

voxelPars.pwldc = mxGetScalar(temp);
temp = mxGetFieldByNumber(prhs[0],0,7);
voxelPars.cf = mxGetScalar(temp);
temp = mxGetFieldByNumber(prhs[0],0,8);
voxelPars.M0w = mxGetScalar(temp);
temp = mxGetFieldByNumber(prhs[0],0,9);
voxelPars.T1a = mxGetScalar(temp);
temp = mxGetFieldByNumber(prhs[0],0,10);
voxelPars.T2a = mxGetScalar(temp);
temp = mxGetFieldByNumber(prhs[0],0,11);
voxelPars.offsetappm = mxGetScalar(temp);
temp = mxGetFieldByNumber(prhs[0],0,12);
voxelPars.bwfraction = mxGetScalar(temp);
temp = mxGetFieldByNumber(prhs[0],0,13);
voxelPars.M0a = mxGetScalar(temp);
temp = mxGetFieldByNumber(prhs[0],0,14);
voxelPars.M0bw = mxGetScalar(temp);
temp = mxGetFieldByNumber(prhs[0],0,15);
voxelPars.T1bw = mxGetScalar(temp);
temp = mxGetFieldByNumber(prhs[0],0,16);
voxelPars.T2bw = mxGetScalar(temp);
temp = mxGetFieldByNumber(prhs[0],0,17);
voxelPars.offsetbwppm = mxGetScalar(temp);
temp = mxGetFieldByNumber(prhs[0],0,18);
voxelPars.exratebw = mxGetScalar(temp);
temp = mxGetFieldByNumber(prhs[0],0,19);
voxelPars.M0b = mxGetScalar(temp);
temp = mxGetFieldByNumber(prhs[0],0,20);
voxelPars.T1b = mxGetScalar(temp);
temp = mxGetFieldByNumber(prhs[0],0,21);
voxelPars.T2b = mxGetScalar(temp);
temp = mxGetFieldByNumber(prhs[0],0,22);
voxelPars.offsetbppm = mxGetScalar(temp);
temp = mxGetFieldByNumber(prhs[0],0,23);
voxelPars.exrateb = mxGetScalar(temp);
temp = mxGetFieldByNumber(prhs[0],0,24);
voxelPars.M0c = mxGetScalar(temp);
temp = mxGetFieldByNumber(prhs[0],0,25);
voxelPars.T1c = mxGetScalar(temp);
temp = mxGetFieldByNumber(prhs[0],0,26);
voxelPars.T2c = mxGetScalar(temp);
temp = mxGetFieldByNumber(prhs[0],0,27);
voxelPars.offsetcppm = mxGetScalar(temp);
temp = mxGetFieldByNumber(prhs[0],0,28);
voxelPars.exratec = mxGetScalar(temp);
temp = mxGetFieldByNumber(prhs[0],0,29);
voxelPars.M0d = mxGetScalar(temp);
temp = mxGetFieldByNumber(prhs[0],0,30);
voxelPars.T1d = mxGetScalar(temp);
temp = mxGetFieldByNumber(prhs[0],0,31);
voxelPars.T2d = mxGetScalar(temp);
temp = mxGetFieldByNumber(prhs[0],0,32);
voxelPars.offsetdppm = mxGetScalar(temp);
temp = mxGetFieldByNumber(prhs[0],0,33);

```

```

voxelPars.exrated = mxGetScalar(temp);
temp = mxGetFieldByNumber(prhs[0],k,34);
voxelPars.M0e = mxGetScalar(temp);
temp = mxGetFieldByNumber(prhs[0],0,35);
voxelPars.T1e = mxGetScalar(temp);
temp = mxGetFieldByNumber(prhs[0],0,36);
voxelPars.T2e = mxGetScalar(temp);
temp = mxGetFieldByNumber(prhs[0],0,37);
voxelPars.offseteppm = mxGetScalar(temp);
temp = mxGetFieldByNumber(prhs[0],0,38);
voxelPars.exratee = mxGetScalar(temp);
/*Perfect!*/

```

Now that all of these parameters are stored in the struct called voxelPars, we have to create a pointer to that struct so that we can pass it to other functions. That's what the '&' operator is doing below.

```

point2pars = &voxelPars;

/*This is to test my matrix inversion function*/
double Test[2][2] = {{2,1},{2,2}};
double **ptr2Test;
ptr2Test = (double**)mxMalloc(2, sizeof(double*));
for (i=0; i<2; i++){
    ptr2Test[i] = (double *)mxMalloc(1, sizeof(double));
    for (j=0; j<2; j++){
        ptr2Test[i][j] = Test[i][j];
    }
}
/* mexPrintf("Test's original values are: %f, %f, %f, %f.\n",
ptr2Test[0][0], ptr2Test[0][1], ptr2Test[1][0],ptr2Test[1][1]);
MatrInv(ptr2Test,2);
mexPrintf("Test has been inverted to: %f, %f, %f, %f.\n",
ptr2Test[0][0], ptr2Test[0][1], ptr2Test[1][0],ptr2Test[1][1]);
mxFree(ptr2Test);*/

```

Above, we declared another local variable called 'contrast'. This holds the answer to our simulation. What I wrote in the comment is that we're initializing it to zero, but that's confusing, because what's actually happening right here is that we're initializing the Z magnetization of the positive and negative sides of the Z-spectrum to 1. (Since 'contrast' is the difference between them, it is indeed being initialized to zero.) This is representing the physical situation before any saturation is applied.

```

/*Initialize contrast's values to zero*/
ptr2contrast->SimMza = ptr2contrast->SimMzb = ptr2contrast->contrastz = 1.0;

```

The real math is then done by the C function `calculate()` – this current function was just a wrapper function in order to go between C and Matlab. What we want back from `calculate()` is the value of the Z magnetization at the positive and negative offsets, for every value of

whatever simulation parameter we're looping over. This is exactly what we're taking when we assign `output[ ] = ptr2contrast...` after running `calculate()`.

```
//Then I'll have to call calculate()
calculate(point2pars, ptr2contrast, pnrA, pnrAinvB,
CopyOfMatrix,vector, col, indx, Aat, Aate, sum, product, pnrA1, pnrB,
pnrY, pnrY0);

/*output = ptr2contrast->contrastz;
//mexPrintf("The contrast has been calculated as :%f.\n", ptr2contrast-
>contrastz);
/*TEST 7/21/2019*/
/*I think I have to do it this way, because I don't know how to get a
double pointer to output*/
output[3*k] = ptr2contrast->SimMza;
output[3*k+1] = ptr2contrast->SimMzb;
output[3*k+2] = ptr2contrast->contrastz;

}/// end loop over different values of the input struct
```

That is, end loop over 'k'.

Then, before leaving the mex function, we 'free' the memory that we used. I don't know exactly what happens in Matlab/mex if you fail to do this, but in principle you risk crashing your machine.

```
/*mexPrintf("About to free memory.\n");
mexEvalString("drawnow;");*/

/*Free memory
mxFree(pnrA); mxFree(pnrAinvB);*/
mxFree(CopyOfMatrix); mxFree(Aat); mxFree(Aate);
mxFree(vector);mxFree(indx);mxFree(col);
mxFree(sum); mxFree(product);
}///end mex function
```

At the end of the mex function, it will return 'output' back to Matlab for us.

Now let's see what actually happens in `Calculate()`.

**calculate()** – still part of `CalculateMz3.cpp`

```
/* Calculation: then, do the same calculation, calling LU functions to
do the matrix
* inversions and Matlab functions to do the other operations. The
calculation has two loops over time:
* one over the number of pulses, and one over time increments within
the pulse.
* It actually does two such calculations -- one for 'positive' offset
and one
```



```

    * for negative, and then calculates the difference ("contrast").*/
void calculate (struct InputParameters *voxelPars1, struct Zcontrast
*contrast, double **pntrA, double *pntrAinvB, double **CopyOfMatrix,
double *vector, double *col, int *indx, double *Aat, double *Aate,
double *sum, double *product, double *pntrA1, double *pntrB, double
*pntrY, double *pntrY0){
/*Starting here, everything we need is included in the struct
InputParameters*/
/*mexPrintf("Using CalculateMz2\n");
mexEvalString("drawnow;");*/

```

This stuff should be self explanatory by now... You'll also see that in addition to assigning local versions of these parameters, we have to do some unit conversions before actually calculating. See the comments in green.

```

/*Local variables*/
    int i, j, k, l, n1, m;
    double pwms, pwldelay;
    int npul;
    double timeStepSize;
    double W;
    double Wa, Wbw, Wb, Wc, Wd, We;
    double Cbw, Cb, Cc, Cd, Ce;
    double M0a, M0bw, M0b, M0c, M0d, M0e; //declaring these as locals
just to make life easier
    double pa, pbw, pb, pc, pd, pe;
    double Cabw, Cab, Cac, Cad, CAe;
    double k1a, k1bw, k1b, k1c, k1d, k1e;
    double k2a, k2bw, k2b, k2c, k2d, k2e;

//    double **pntrA;
//    /*CAUTION! At different times in this function, pntrA is used to
point to matrices Aa, Ab, Ad AND their inverses*/
//    pntrA = (double **)mxMalloc(18, sizeof(double*));
//    for (i=0; i <18; i++){
//        pntrA[i] = (double *) mxMalloc(18, sizeof(double));
//    }
//
//    double AdinvB[18];
//    double AinvB[18];
//    for(i=0; i<18; i++){
//        AdinvB[i] = 0.0;
//        AinvB[i] = 0.0;
//    }
//
// /*Passed variables memory allocation*/
//    double **CopyOfMatrix; /*used by MatriInv()*/
//    CopyOfMatrix = (double**)mxMalloc(18, sizeof(double*));
//    for (i=0; i<18; i++){
//        CopyOfMatrix[i] = (double*)mxMalloc(18, sizeof(double));
//    }
//
//    double *vector;

```

```

//      double *col;
//      int *indx;
//      vector = (double *)mxMalloc(18, sizeof(double));
//      indx = (int *)mxMalloc(18, sizeof(int));
//      col = (double *)mxMalloc(18, sizeof(double));
//
//      /*used by CalculateY()*/
//      double *Aat;
//      Aat = (double*)mxMalloc(18*18, sizeof(double));
//      /* for (i=0; i<18; i++){
//          Aat[i] = (double*)mxMalloc(18, sizeof(double));
//      }*/
//
//      double *Aate;
//      Aate = (double*)mxMalloc(18*18, sizeof(double));
//      /* for (i=0; i<18; i++){
//          Aate[i] = (double*)mxMalloc(18, sizeof(double));
//      } */
//
//      double *sum;
//      sum = (double*)mxMalloc(18, sizeof(double));
//      double *product;
//      product = (double*)mxMalloc(18, sizeof(double));

double W1[voxelPars1->count1]; //Now THIS might require a pointer,
since count1 is only passed in the argument struct. We'll see.
double W1x[voxelPars1->count1];
double W1y[voxelPars1->count1];
/* mexPrintf("Declared all local variables in calculate().\n");
mexEvalString("drawnow;");*/

/*Fill local variables with values from input struct voxelPars*/

pwms = voxelPars1->pw1dc;
pwldelay = 100-voxelPars1->pw1dc;
npul = (int)voxelPars1->pw1/100;
timeStepSize=0.001*(pwms/voxelPars1->count1);
/* mexPrintf("Count1 has been set equal to: %d; npul has been set
equal to:%d.\n", voxelPars1->count1, npul);
mexEvalString("drawnow;");*/

/*Determine offset frequency of the metabolites in Hz (?)*/
Wa = voxelPars1->offsetappm * voxelPars1->cf * 2 * pi;
// mexPrintf("Wa has been set to: %f.\n", Wa);
Wbw = voxelPars1->offsetbwppm * voxelPars1->cf * 2 * pi;
// mexPrintf("Wbw has been set to: %f.\n", Wbw);
Wb = voxelPars1->offsetbppm * voxelPars1->cf * 2 * pi;
// mexPrintf("Wb has been set to: %f.\n", Wb);
Wc = voxelPars1->offsetcppm * voxelPars1->cf * 2 * pi;
// mexPrintf("Wc has been set to: %f.\n", Wc);
Wd = voxelPars1->offsetdppm * voxelPars1->cf * 2 * pi;
// mexPrintf("Wd has been set to: %f.\n", Wd);
We = voxelPars1->offseteppm * voxelPars1->cf * 2 * pi;
// mexPrintf("We has been set to: %f.\n", We);

```

```

/* Set "absolute" rates of proton exchange from each metabolite --
"bw" is bound water*/
Cbw = voxelPars1->exratebw; // taub is in Hz units
Cb = voxelPars1->exrateb; // taub is in Hz units
Cc = voxelPars1->exratec; // taub is in Hz units
Cd = voxelPars1->exrated; // taub is in Hz units
Ce = voxelPars1->exratee; // taub is in Hz units

/*Move M0 values from voxelPars into local bins*/
/*M0a = M0w * (1-bwfraction);
M0bw = M0w * bwfraction;*/
/* M0a = voxelPars.M0a;
M0bw = voxelPars.M0bw;*/
M0a = voxelPars1->M0a;
M0bw = voxelPars1->M0bw;
M0b = voxelPars1->M0b;
M0c = voxelPars1->M0c;
M0d = voxelPars1->M0d;
M0e = voxelPars1->M0e;

/*Determine fraction of the total proton signal coming from each
metabolite*/
pa = M0a / (M0a+M0bw+M0b+M0c+M0d+M0e);
pbw = M0bw / (M0a+M0bw+M0b+M0c+M0d+M0e);
pb = M0b / (M0a+M0bw+M0b+M0c+M0d+M0e);
pc = M0c / (M0a+M0bw+M0b+M0c+M0d+M0e);
pd = M0d / (M0a+M0bw+M0b+M0c+M0d+M0e);
pe = M0e / (M0a+M0bw+M0b+M0c+M0d+M0e);

/*Calculate exchange rate between "a" (bulk water) and each
metabolite*/
Cabw=voxelPars1->exratebw*pbw;
Cab=voxelPars1->exrateb*pb;
Cac=voxelPars1->exratec*pc;
Cad=voxelPars1->exrated*pd;
Cae=voxelPars1->exratee*pe;

/*Determine total decay rate constants from T1 and T2 decay and
chemical exchange*/
k1a=1/voxelPars1->T1a+Cabw+Cab+Cac+Cad+Cae; k2a=1/voxelPars1->
T2a+Cabw+Cab+Cac+Cad+Cae;
k1bw=1/voxelPars1->T1bw+Cbw; k2bw=1/voxelPars1->T2bw+Cbw;
k1b=1/voxelPars1->T1b+Cb; k2b=1/voxelPars1->T2b+Cb;
k1c=1/voxelPars1->T1c+Cc; k2c=1/voxelPars1->T2c+Cc;
k1d=1/voxelPars1->T1d+Cd; k2d=1/voxelPars1->T2d+Cd;
k1e=1/voxelPars1->T1e+Ce; k2e=1/voxelPars1->T2e+Ce;

/*Define bulk (ALL spins) magnetization vector B, which starts out
composed only of z components*/
/*And Y, which will hold our calculated signal vectors*/

```

```

    double B[] = {(M0a/voxelPars1->T1a),0,0,(M0bw/voxelPars1->T1bw),0,0,(M0b/voxelPars1->T1b),0,0,(M0c/voxelPars1->T1c),0,0,(M0d/voxelPars1->T1d),0,0,(M0e/voxelPars1->T1e),0,0};
    double Y0[] = {M0a,0,0,M0bw,0,0,M0b,0,0,M0c,0,0,M0d,0,0,M0e,0,0};
    double Y[18] = {0,0,0,0,0,0,0,0,0,0,0,0,0,0,0,0,0,0};

    /*double *pntrB;
    pntrB = (double *) mxCalloc(18, sizeof(double));

    double *pntrY;
    pntrY = (double *) mxCalloc(18, sizeof(double));

    double *pntrY0;
    pntrY0 = (double *) mxCalloc(18, sizeof(double));*/

    double *pntrMz;
    /* mexPrintf("Did all of the arithmetic using values from voxelPars.\n");
    mexEvalString("drawnow;");*/

```

Now we define the matrices describing the Bloch-McConnell equations themselves. This is obviously a little too small to read, but see Chapter 1b of this thesis for closer examination of these matrices and the equations that they represent. First, the 'pulse off' matrix,  $A_d$ . This matrix is static once we have defined all of the input parameters to the simulation.

```

    /*Define matrix Ad, which describes evolution of the magnetization during periods with no pulse (decay)*/
    double Ad [18][18] = {
        {-1.0*k1a, 0, 0, Cbw, 0, 0, Cb, 0, 0, Cc, 0, 0, Cd, 0, 0, Ce, 0, 0},
        // Mza
        {0, -1.0*k2a, Wa, 0, Cbw, 0, 0, Cb, 0, 0, Cc, 0, 0, Cd, 0, 0, Ce, 0},
        // Mya
        {0, -1.0*Wa, -1.0*k2a, 0, 0, Cbw, 0, 0, Cb, 0, 0, Cc, 0, 0, Cd, 0, 0, Ce},
        // Mxa
        {Cbw, 0, 0, -1.0*k1bw, 0, 0, 0, 0, 0, 0, 0, 0, 0, 0, 0, 0, 0},
        // Mzb
        {0, Cabw, 0, 0, -1.0*k2bw, Wbw, 0, 0, 0, 0, 0, 0, 0, 0, 0, 0, 0}, //
        // Myb
        {0, 0, Cabw, 0, -1.0*Wbw, -1.0*k2bw, 0, 0, 0, 0, 0, 0, 0, 0, 0, 0, 0},
        // Mxb
        {Cab, 0, 0, 0, 0, 0, -1.0*k1b, 0, 0, 0, 0, 0, 0, 0, 0, 0, 0}, //
        // Mzb
        {0, Cab, 0, 0, 0, 0, 0, -1.0*k2b, Wb, 0, 0, 0, 0, 0, 0, 0, 0},
        // Myb
        {0, 0, Cab, 0, 0, 0, 0, -1.0*Wb, -1.0*k2b, 0, 0, 0, 0, 0, 0, 0, 0},
        // Mxb
        {Cac, 0, 0, 0, 0, 0, 0, 0, 0, -1.0*k1c, 0, 0, 0, 0, 0, 0, 0}, //
        // Mzc
        {0, Cac, 0, 0, 0, 0, 0, 0, 0, 0, -1.0*k2c, Wc, 0, 0, 0, 0, 0}, //
        // Myc
        {0, 0, Cac, 0, 0, 0, 0, 0, 0, -1.0*Wc, -1.0*k2c, 0, 0, 0, 0, 0, 0},
        // Mxc
        {Cad, 0, 0, 0, 0, 0, 0, 0, 0, 0, 0, -1.0*k1d, 0, 0, 0, 0, 0},
        // Mzd
        {0, Cad, 0, 0, 0, 0, 0, 0, 0, 0, 0, 0, -1.0*k2d, Wd, 0, 0},
        // Myd
        {0, 0, Cad, 0, 0, 0, 0, 0, 0, 0, 0, 0, -1.0*Wd, -1.0*k2d, 0, 0},
        // Mxd
        {Cae, 0, 0, 0, 0, 0, 0, 0, 0, 0, 0, 0, 0, 0, -1.0*k1e, 0},
        // Mze
        {0, Cae, 0, 0, 0, 0, 0, 0, 0, 0, 0, 0, 0, 0, 0, -1.0*k2e, We},
        // Mye
        {0, 0, Cae, 0, 0, 0, 0, 0, 0, 0, 0, 0, 0, 0, -1.0*We, -1.0*k2e}
        // Mxe
    };

    /*Define matrix Aa, which describes the evolution of the magnetization during the pulse for the "positive offset" calculation.
    *The relevant elements with W get updated within the loop*/

```

As I wrote above, the other matrix is 'pulse on', so its elements change as a function of whatever the pulse is doing at that instant in time (i.e., that index of the vector representing time, which the loop is over). There are actually two copies of this matrix, labeled  $A_a$  and  $A_b$ , to represent the saturation pulse being at the positive offset or negative offset. They are actually "the same" if you look at this code closely, but note that the value of 'W' which they are filled with changes, gaining a negative sign before filling the second matrix  $A_b$ .

```
/*First we're going to do the "experiment" with the positive offset
frequency*/
```

```
W = voxelPars1->puloffsetppm * voxelPars1->cf *2.0*pi;
// mexPrintf("W of the positive offset experiment has been set to:
%f.\n", W);
// mexPrintf("W-Wa equals: %f. Wa-W equals:%f\n", W-Wa, Wa-W);
```

```
double Aa[18][18] = {
{-1.0*kia, Wix[0], Wiy[0], Cbw, 0, 0, Cb, 0, 0, Cc, 0, 0, Cd, 0, 0, Ce, 0, 0 }, // Mza
{-1.0*Wix[0], -1.0*k2a, Wa-W, 0, 0, Cbw, 0, 0, Cb, 0, 0, Cc, 0, 0, Cd, 0, 0, Ce, 0 }, // Mya
{ Wiy[0], W-Wa, -1.0*k2a, 0, 0, Cbw, 0, 0, Cb, 0, 0, Cc, 0, 0, Cd, 0, 0, Ce, 0 }, // Mxa
{ Cabw, 0, 0, -1.0*k1bw, Wix[0], Wiy[0], 0, 0, 0, 0, 0, 0, 0, 0, 0, 0, 0 }, // Mzb
{ 0, Cabw, 0, -1.0*Wix[0], -1.0*k2bw, Wb-W, 0, 0, 0, 0, 0, 0, 0, 0, 0, 0, 0 }, // Myb
{ 0, 0, Cabw, Wiy[0], W-Wb, -1.0*k2bw, 0, 0, 0, 0, 0, 0, 0, 0, 0, 0, 0 }, // Mxb
{ Cab, 0, 0, 0, 0, 0, -1.0*k1b, Wix[0], Wiy[0], 0, 0, 0, 0, 0, 0, 0, 0 }, // Mzb
{ 0, Cab, 0, 0, 0, 0, -1.0*Wix[0], -1.0*k2b, Wb-W, 0, 0, 0, 0, 0, 0, 0, 0 }, // Myb
{ 0, 0, Cab, 0, 0, 0, 0, Wiy[0], W-Wb, -1.0*k2b, 0, 0, 0, 0, 0, 0, 0 }, // Mxb
{ Cac, 0, 0, 0, 0, 0, 0, 0, 0, -1.0*k1c, Wix[0], Wiy[0], 0, 0, 0, 0, 0 }, // Mzc
{ Cac, 0, 0, 0, 0, 0, 0, 0, 0, -1.0*Wix[0], -1.0*k2c, Wc-W, 0, 0, 0, 0, 0 }, // Myc
{ 0, 0, Cac, 0, 0, 0, 0, 0, 0, 0, Wiy[0], W-Wc, -1.0*k2c, 0, 0, 0, 0, 0 }, // Mxc
{ Cad, 0, 0, 0, 0, 0, 0, 0, 0, 0, 0, -1.0*k1d, Wix[0], Wiy[0], 0, 0, 0 }, // Mzd
{ 0, Cad, 0, 0, 0, 0, 0, 0, 0, 0, -1.0*Wix[0], -1.0*k2d, Wd-W, 0, 0, 0, 0, 0 }, // Myd
{ 0, 0, Cad, 0, 0, 0, 0, 0, 0, 0, 0, Wiy[0], W-Wd, -1.0*k2d, 0, 0, 0, 0 }, // Mxd
{ Cae, 0, 0, 0, 0, 0, 0, 0, 0, 0, 0, 0, -1.0*k1e, Wix[0], Wiy[0], 0, 0 }, // Mze
{ 0, Cae, 0, 0, 0, 0, 0, 0, 0, 0, 0, 0, -1.0*Wix[0], -1.0*k2e, We-W, 0, 0 }, // Mye
{ 0, 0, Cae, 0, 0, 0, 0, 0, 0, 0, 0, 0, 0, Wiy[0], W-We, -1.0*k2e } // Mxe
};
```

```
// mexPrintf("Element [2][1] of [Aa] has been set equal to:
%f.\n", Aa[2][1]);
```

```
/*Then we're going to the the "negative offset" experiment.*/
```

```
W = -(voxelPars1->puloffsetppm) * voxelPars1->cf *2.0*pi;
// mexPrintf("W of the negative offset experiment has been set
to: %f.\n", W);
// mexPrintf("W-Wa equals: %f. Wa-W equals: %f\n", W-Wa, Wa-W);
```

```
/*Define matrix Ab (same as Aa), which describes the
evolution of the magnetization during the pulse for the "negative
offset" calculation.
```

```
*The relevant elements get updated within the loop*/
```

```
double Ab[18][18] = {
{-1.0*kia, Wix[0], Wiy[0], Cbw, 0, 0, Cb, 0, 0, Cc, 0, 0, Cd, 0, 0, Ce, 0, 0 }, // Mza
{-1.0*Wix[0], -1.0*k2a, Wa-W, 0, 0, Cbw, 0, 0, Cb, 0, 0, Cc, 0, 0, Cd, 0, 0, Ce, 0 }, // Mya
{ Wiy[0], W-Wa, -1.0*k2a, 0, 0, Cbw, 0, 0, Cb, 0, 0, Cc, 0, 0, Cd, 0, 0, Ce, 0 }, // Mxa
{ Cabw, 0, 0, -1.0*k1bw, Wix[0], Wiy[0], 0, 0, 0, 0, 0, 0, 0, 0, 0, 0, 0 }, // Mzb
{ 0, Cabw, 0, -1.0*Wix[0], -1.0*k2bw, Wb-W, 0, 0, 0, 0, 0, 0, 0, 0, 0, 0, 0 }, // Myb
{ 0, 0, Cabw, Wiy[0], W-Wb, -1.0*k2bw, 0, 0, 0, 0, 0, 0, 0, 0, 0, 0, 0 }, // Mxb
{ Cab, 0, 0, 0, 0, 0, -1.0*k1b, Wix[0], Wiy[0], 0, 0, 0, 0, 0, 0, 0, 0 }, // Mzb
{ 0, Cab, 0, 0, 0, 0, -1.0*Wix[0], -1.0*k2b, Wb-W, 0, 0, 0, 0, 0, 0, 0, 0 }, // Myb
{ 0, 0, Cab, 0, 0, 0, 0, Wiy[0], W-Wb, -1.0*k2b, 0, 0, 0, 0, 0, 0, 0 }, // Mxb
{ Cac, 0, 0, 0, 0, 0, 0, 0, 0, -1.0*k1c, Wix[0], Wiy[0], 0, 0, 0, 0, 0 }, // Mzc
{ 0, Cac, 0, 0, 0, 0, 0, 0, 0, -1.0*Wix[0], -1.0*k2c, Wc-W, 0, 0, 0, 0, 0 }, // Myc
{ 0, 0, Cac, 0, 0, 0, 0, 0, 0, 0, Wiy[0], W-Wc, -1.0*k2c, 0, 0, 0, 0, 0 }, // Mxc
{ Cad, 0, 0, 0, 0, 0, 0, 0, 0, 0, 0, -1.0*k1d, Wix[0], Wiy[0], 0, 0, 0 }, // Mzd
{ 0, Cad, 0, 0, 0, 0, 0, 0, 0, 0, -1.0*Wix[0], -1.0*k2d, Wd-W, 0, 0, 0, 0, 0 }, // Myd
{ 0, 0, Cad, 0, 0, 0, 0, 0, 0, 0, 0, Wiy[0], W-Wd, -1.0*k2d, 0, 0, 0, 0 }, // Mxd
{ Cae, 0, 0, 0, 0, 0, 0, 0, 0, 0, 0, 0, -1.0*k1e, Wix[0], Wiy[0], 0, 0 }, // Mze
{ 0, Cae, 0, 0, 0, 0, 0, 0, 0, 0, 0, 0, -1.0*Wix[0], -1.0*k2e, We-W, 0, 0 }, // Mye
{ 0, 0, Cae, 0, 0, 0, 0, 0, 0, 0, 0, 0, 0, Wiy[0], W-We, -1.0*k2e } // Mxe
};
```

```
/* mexPrintf("Initialized our three big matrices!\n");
mexEvalString("drawnow;");*/
```

In order to solve the system of differential equations, we'll need to use the inverse of matrix  $A_d$ , so we're calculating it ahead of time. This is done by a separate function, `MatrInv`, which will be

defined below. Note that the function `r8mat_mm` is a matrix multiplication function from the `r8` library.

```

/*Calculate inverse of Ad, for use in solution to Bloch equation;
determine its action on B, store in vector AdinvB. */
for (i=0; i<18; i++){
    for(j=0; j<18; j++){
        pntrA[i][j] = Ad[i][j];
        CopyOfMatrix[i][j] = pntrA[i][j]; /* 9/5/17*/
    }
}

MatrInv(pntrA, 18, CopyOfMatrix, vector, indx, col);

for (i=0; i<18; i++){
    pntrB[i] = B[i];
}

/*pntrA is already pointing to Adinv, but needs to be 1d for
MM()*/
for (i=0; i<18; i++){
    for(l=0; l<18; l++){
        pntrA1[i*18+l] = pntrA[i][l];
    }
}
r8mat_mm(18,18,1, pntrA1, pntrB, pntrAinvB);

/*Dereference pointer to store result*/
for (i=0; i<18; i++){
    AdinvB[i] = pntrAinvB[i];
}

/*Set the RF pulse vector W1.*/
for (i=0; i<voxelPars1->count1; i++){
    W1[i] = voxelPars1->ampl[i]*voxelPars1->b1*2*pi;
}

/*First we're going to do the "experiment" with the positive
offset frequency*/
for (n1=0; n1< npul; n1++){ //loop over number of pulses
    for (j=0; j< voxelPars1->count1; j++){ //loop over time
        increments within each pulse

                /*Define x and y components of the (circularly polarized)
RF pulse*/
                /* W1x = W1(j-1)*cos(phi(j-1)); W1y = W1(j-1)*sin(phi(j-1));
*/
                W1x[j] = W1[j-1]*cos(voxelPars1->phi[j-1]);
                W1y[j] = W1[j-1]*sin(voxelPars1->phi[j-1]);

```

These lines below update the values of Aa in accordance with the pulse vector. The line with the asterisks is what makes this the positive offset run and not the negative one (by setting pntrA to point to matrix Aa as opposed to matrix Ab). Otherwise, the two blocks of code are identical.

```

        /*Update relevant elements of Aa with new values of W1x and
W1y*/
    for (i=0; i<6; i++){
        k = i*3;
        Aa[k][k+1] = W1x[j];
        Aa[k][k+2] = W1y[j];
        Aa[k+1][k] = -W1x[j];
        Aa[k+2][k] = W1y[j];
    }

    /*Invert A and determine its action on B*/
    for (i=0; i<18; i++){
        for(m=0; m<18; m++){
            pntrA[i][m] = Aa[i][m]; *****
            CopyOfMatrix[i][m] = pntrA[i][m]; /* 9/11/17*/
        }
    }
    MatrInv(pntrA,18, CopyOfMatrix, vector, indx, col);
    /*pntrA is now pointing to Ainv*/

    for (i=0; i<18; i++){
        pntrB[i] = B[i];
    }

    /*pntrA is already pointing to Aainv, but needs to be 1d
for MM()*/
    for (i=0; i<18; i++){
        for(l=0; l<18; l++){
            pntrA1[i*18+l] = pntrA[i][l];
        }
    }

    r8mat_mm(18,18,1, pntrA1, pntrB, pntrAinvB);

    for (i=0; i<18; i++){ /*Dereference pointer to store
result*/
        AinvB[i] = pntrAinvB[i];
    }

    /*Use AinvB in the solution for the Bloch equation, for
Y(t) after this very small dt*/
    /* [Y=expm(timeStepSize*Aa)*(Y0+AinvB)-AinvB] using:
void CalculateY(double *pntrY, double timeScalar, double
**pntrA, double *pntrY0, double *pntrAinvB);*/

    /* mexPrintf("AinvB = %f ,%f ,%f ,%f ...\\n", AinvB[0],
AinvB[3], AinvB[6], AinvB[9]);

```

```

        mexPrintf("Y0 = %f ,%f, %f, %f ... \n", Y0[0], Y0[3],
Y0[6], Y0[9]);
        mexPrintf("Y = %f ,%f, %f, %f ... \n", Y[0], Y[3], Y[6],
Y[9]);*/

/*Assign pointers--pntrA is already pointing to matrix Aa*/
for (i=0; i<18; i++){
    pntrY[i] = Y[i];
    pntrY0[i] = Y0[i];
    pntrAinvB[i] = AinvB[i];
    for(m=0; m<18; m++){
        pntrA[i][m] = Aa[i][m];
    }
}

```

CalculateY is yet another subfunction which does the rest of the math once we have already done the step of calculating the matrix inverse and its action on the magnetization vector B. First, it is called with 'AinvB' set for one of the positive offset "pulse on" matrix. It will be documented next.

```

/*Call function, pass pointer arguments*/
CalculateY(pntrY,timeStepSize,pntrA,pntrY0,pntrAinvB, Aat,
Aate, sum, product);

/*Dereference pointer to store result*/
for (i=0; i<18; i++){
    Y[i] = pntrY[i];
}
// mexPrintf("Y = %f ,%f, %f, %f ... \n", Y[0], Y[3], Y[6],
Y[9]);
/*Set this solution Y as Y0, the ansatz for the next
iteration*/
for (i=0; i< 18; i++){
    Y0[i] = Y[i];
}
// mexPrintf("Finished this iteration of CalculateY.j = %d.
Y[0] = %f, M0a = %f.\n", j, Y[0], M0a);
} //end loop over time increments within one pulse

```

The duty cycle (i.e. the time that the pulse is actually on) of our experiments is not 100%. So, next we call CalculateY again with AinvB set to describe the action of that 'decay' matrix instead.

```

/*Use AdinvB to calculate the evolution of the magnetization
during the time between pulses*/
/* [Y=expm(pwldelay*0.001*Ad)*(Y0+AdinvB)-AdinvB] using:
void CalculateY(double *pntrY, double timeScalar, double
**pntrA, double *pntrY0, double *pntrAinvB);*/

/*Assign pointers*/
for (i=0; i<18; i++){
    pntrY[i] = Y[i];
    pntrY0[i] = Y0[i];
    pntrAinvB[i] = AdinvB[i];
}

```



```

    for(j=0; j<18; j++){
        ptrA[i][j] = Ad[i][j];
    }
}

/*Call function, pass pointers*/
// mexPrintf("Upcoming call to CalculateY is for
relaxation.\n");
CalculateY(ptrY, pwlDelay*0.001, ptrA, ptrY0, ptrAinvB, Aat,
Aate, sum, product);

/*Dereference pointer to store result*/
for (i=0; i<18; i++){
    Y[i] = ptrY[i];
    // if(n1 == (npul-1)) mexPrintf("Y[i] = %f.\n", Y[i]);
}

/*Zero Mx and MY for all six species before next pulse-- EDITED
9/13/17*/
for (i=0; i<6;i++){
    Y[(i)*3 + 1] = 0.0;
    Y[(i)*3 + 2] = 0.0;
}

for (i=0; i< 18; i++){
    Y0[i] = Y[i];
    // if(n1 == (npul-1)) mexPrintf("Y[i] = %f.\n", Y[i]);
}
// mexPrintf("Y[0] after pulse %d = %f\n", n1,Y[0]);
} //end loop over pulses

```

This is the end of the 'positive offset' experiments. The answer (that is, the values of Mz after the saturation pulse for pulses of all B<sub>1</sub> values -- or whatever the variable parameter is) is assigned to the variable contrast.SimMza. After the 'negative offset' experiments, we will store the vector of answers in contrast. SimMzb.

```

/*Store the results of the "+" simulation in SimMza.*/
contrast->SimMza = Y[0]/M0a;
/* mexPrintf("After SimA. Y[0] = %f, M0a = %f.\n", Y[0], M0a);*/

////////////////////////////////////Repeat everything for
negative offset experiment

/*Now we're going to the the "negative offset" experiment.*/
/* W = -(voxelPars.puloffsetppm) * voxelPars.cf *2.0*pi;*/
/*double Y0[] =
{M0a,0,0,M0bw,0,0,M0b,0,0,M0c,0,0,M0d,0,0,M0e,0,0};*/
for (i=0; i<18; i++){
    if (i ==0) Y0[i] = M0a;
    else if (i ==3) Y0[i] = M0bw;
    else if (i ==6) Y0[i] = M0b;
    else if (i ==9) Y0[i] = M0c;

```

```

        else if (i ==12) Y0[i] = M0d;
        else if (i ==15) Y0[i] = M0e;
        else Y[i] = 0;
    }

    for (n1=0; n1< npul; n1++){ //loop over number of pulses
        for (j=0; j< voxelPars1->count1; j++){ //loop over time
            increments within each pulse

                /*Define x and y components of the (circularly polarized)
RF pulse*/
                /* W1x = W1(j-1)*cos(phi(j-1)); W1y = W1(j-1)*sin(phi(j-1));
*/
                W1x[j] = W1[j-1]*cos(voxelPars1->phi[j-1]);
                W1y[j] = W1[j-1]*sin(voxelPars1->phi[j-1]);
                // mexPrintf("W1x = %f, W1y = %f, j = %d.\n", W1x[j],
W1y[j], j);

                /*Update relevant elements of Ab with new values of W1x and
W1y*/
                for (i=0; i<6; i++){
                    k = i*3;
                    Ab[k][k+1] = W1x[j];
                    Ab[k][k+2] = W1y[j];
                    Ab[k+1][k] = -W1x[j];
                    Ab[k+2][k] = W1y[j];
                    //mexPrintf("Inside loop to reassign W1[k]. W1x[k] =
%f.\n", W1x[k]);
                }

                /*Invert A and determine its action on B*/
                /* AinvB = LUAug4(Ab)*B;*/

                for (i=0; i<18; i++){
                    for(m=0; m<18; m++){
                        pntrA[i][m] = Ab[i][m]; *****
                        CopyOfMatrix[i][m] = pntrA[i][m]; /* 9/11/17*/
                    }
                }

                MatrInv(pntrA, 18, CopyOfMatrix, vector, indx, col);

                // mexPrintf("Calculated inverse of [Ab].\n");

                /*pntrA is already pointing to Ainv*/
                for (i=0; i<18; i++){
                    for(l=0; l<18; l++){
                        pntrA1[i*18+l] = pntrA[i][l];
                    }
                }

                for (i=0; i<18; i++) pntrB[i] = B[i];

```

```

r8mat_mm(18,18,1, pnrA1, pnrB, pnrAinvB);

/*Dereference pointer to store result*/
for (i=0; i<18; i++){
    AinvB[i] = pnrAinvB[i];
}

/*Use AinvB in the solution for the Bloch equation, for
Y(t) after this very small dt*/
/*[Y=expm(timeStepSize*Ab)*(Y0+AinvB)-AinvB] using:
void CalculateY(double *pntrY, double timeScalar, double
**pntrA, double *pntrY0, double *pntrAinvB);*/

/*Assign pointers*/
for (i=0; i<18; i++){
    pnrY[i] = Y[i];
    pnrY0[i] = Y0[i];
    pnrAinvB[i] = AinvB[i];
    for(m=0; m<18; m++){
        pnrA[i][m] = Ab[i][m];
    }
}

/*Call function, pass pointer arguments*/
CalculateY(pnrY,timeStepSize,pnrA,pnrY0,pnrAinvB, Aat,
Aate, sum, product);

/*Dereference pointer to store result*/
for (i=0; i<18; i++){
    Y[i] = pnrY[i];
}

/*Set this solution Y as Y0, the ansatz for the next
iteration*/
for (i=0; i< 18; i++){
    Y0[i] = Y[i];
}

} //end loop over time increments within one pulse

/*Y=expm(pwldelay*0.001*Ad)*(Y0+AdinvB)-AdinvB;
void CalculateY(double *pntrY, double timeScalar, double
**pntrA, double *pntrY0, double *pntrAinvB);*/

/*Assign pointers*/
for (i=0; i<18; i++){
    pnrY[i] = Y[i];
    pnrY0[i] = Y0[i];
    pnrAinvB[i] = AdinvB[i];
    for(j=0; j<18; j++){
        pnrA[i][j] = Ad[i][j];

```

```

    }
}

// mexPrintf("Upcoming call to CalculateY is for
relaxation.\n");
CalculateY(pntrY, pwldelay*0.001, pntrA, pntrY0, pntrAinvB, Aat,
Aate, sum, product);
for (i=0; i<18; i++){ /*Dereference pointer to store result*/
    Y[i] = pntrY[i];
    //if(n1 == (npul-1)) mexPrintf("Y[i] = %f.\n", Y[i]);
}

/*Zero Mx and MY for all six species before next pulse-- EDITED
9/13/17*/
for (i=0; i<6;i++){
    Y[(i)*3 + 1] = 0.0;
    Y[(i)*3 + 2] = 0.0;
}
for (i=0; i< 18; i++){
    Y0[i] = Y[i];
    //if(n1 == (npul-1)) mexPrintf("Y[i] = %f.\n", Y[i]);
}
//mexPrintf("Y[0] after pulse %d = %f\n", n1,Y[0]);
} //end loop over pulses

/*Store the results of the "+" simulation in SimMza.*/
contrast->SimMzb = Y[0]/M0a;
/* mexPrintf("After SimB. Y[0] = %f, M0a = %f.\n", Y[0], M0a);*/

```

Now that we've done both offsets, before we return our answer to the main mex function, we're going to calculate one more thing: the negative-normalized asymmetry as a percent, giving us what we usually report as the gluCEST value.

```

/*Calculate contrast between "+" and "-" experiments*/
contrast->contrastz = 100 * (contrast->SimMzb - contrast-
>SimMza)/contrast->SimMzb;
// mexPrintf("pw1 was set equal to: %f.\n", voxelPars.pw1);
// mexPrintf(" %f\t %f\n", contrast->SimMza, contrast->SimMzb);

/* Output arguments: ....
*...I guess they should just be SimMza1, SimMzb, and contrastz.
--remember that if the pointers are assigned properly, you won't need
to explicitly
return anything! */
/* mxFree(CopyOfMatrix); mxFree(Aat); mxFree(Aate);
mxFree(vector); mxFree(indx); mxFree(col);
mxFree(sum); mxFree(product);*/

//mexPrintf("Reached end of calculate(). Contrastz has been calculated
as: %f .Going back to mex function.\n", contrast->contrastz);
return;

```

```
}
```

Ok, at long last, this is the end of calculate().

### Matrix inversion – still part of CalculateMz3.cpp

Here's the matrix inversion function. This is basically taken from Numerical Recipes.

```
/*Adapted from wrapper function of LUAug4.cpp*/
void MatrInv(double **matrix, int n, double **CopyOfMatrix, double
*vector, int *indx, double *col){
    /* mexPrintf("Inside MatrInv().\n");
    mexPrintf("The first square of matrix is: %f, %f, %f, %f.\n",
matrix[0][0],matrix[0][1],matrix[1][0],matrix[1][1]);
    mexEvalString("drawnow;");*/
    //for our friends *indx and *vector
    /* double *vector;
    int *indx;
    double *col;*/
    int i,j;

    /*Create copy of matrix to send to internal functions
    double **CopyOfMatrix;
    CopyOfMatrix = (double**)mxMalloc(n, sizeof(double*));
    for (i=0; i<n; i++){
        CopyOfMatrix[i] = (double*)mxMalloc(n, sizeof(double));
        for (j=0; j<n; j++){
            CopyOfMatrix[i][j] = matrix[i][j];
        }
    }*/
    /* for (j=0; j<n; j++){
        CopyOfMatrix[i][j] = matrix[i][j];
    }*/

    /* vector = (double *)mxMalloc(n, sizeof(double));
    indx = (int *)mxMalloc(n, sizeof(int));
    col = (double *)mxMalloc(n, sizeof(double));*/

    double holder;
    int d = 0;
    // mexPrintf("Inside MatrInv(). Declared local variables. \n");
    // mexEvalString("drawnow;");
    //then we send everything to ludcmp, which returns c as its
decomposition
    ludcmp(CopyOfMatrix, n, indx, vector, d);
    // mexPrintf("Inside MatrInv(). Returned from ludcmp.\n");
    // mexEvalString("drawnow;");
    for (j=0; j<n;j++){
        for (i=0; i<n; i++){
            col[i] = 0.0;
        }
        col[j]=1.0;
        //This constructs the necessary column of the identity matrix to
send to lubksb()
```

```

        lubksb(CopyOfMatrix, n ,indx, col);
        // mexPrintf("Inside MatrInv(). Returned from one call of
bksb.\n");
        // mexEvalString("drawnow;");

        //the key output we care about from here is actually "col"
        for (i=0; i<n; i++){
            // mexPrintf("Col[i] = %f.\n", col[i]);
            holder =(double)col[i];
            matrix[j][i] = holder; //Now "matrix" will hold the inverse
of the "matrix" that was sent...
        }
        /* mexPrintf("Filled 'matrix'. Returning now for safety.\n");
mexEvalString("drawnow;");
return;*/
    }
    /* mexPrintf("Done with loops in MatrInv().\n");
mexEvalString("drawnow;");*/
    /* mxFree(vector);mxFree(indx);mxFree(col);*/
    /* mxFree(CopyOfMatrix);*/
    return;
}
}

```

## Calculate2.h

This header file contains the function that *actually* does the numerical solving, which I've divided into five steps, or 'functions'. It uses one more function defined in a separate header, `matrix_exponential`, which will follow. As mentioned before, I ended up not using my own `Multiply and Divide`, so they are actually not defined here.

```

#include <stdio.h>
#include <string.h>
#include "matrix_exponential.h"

void CalculateY(double *pntrY, double timeScalar, double **pntrA,
double *pntrY0, double *pntrAinvB, double *Aat, double *Aate, double
*sum, double *product);
void MatrInv (double **matrix, int n, double **CopyOfMatrix, double
*vector, int *indx, double *col);
void Multiply (double *pntrAinvB, double **pntrAinv, double *pntrB);
void Divide (double *pntrMz, double *pntrY0, double M0a);

```

**CalculateY()** --in Calculate2.h, called by Calculate()

```

void CalculateY(double *pntrY, double timeScalar, double **pntrA,
double *pntrY0, double *pntrAinvB, double *Aat, double *Aate, double
*sum, double *product){

    int i,j;
    char *title;

    /*declare pointers to mxArrays*/

```

```

mxArray *input1, *input2, *output;
mxArray *ppRHS[2];

/*First function: Add Y0 to AinvB*/
for (i=0; i<18; i++){
    sum[i] = pntrY0[i]+pntrAinvB[i];
}

/*Second function: Multiply timeScalar by A*/
for (i=0; i<18; i++){
    for (j=0; j<18; j++){
        Aat[i*18+j] = pntrA[j][i]*timeScalar;
    }
}
/*    mexPrintf("About to display output (2): Aat. \n");
title = "Aat";
r8mat_print(18,18,Aat,title);    */

/*Third function: Find matrix exponential of Aat*/
Aate = r8mat_expml(18, Aat);

/* mexPrintf("About to display output (3): Aate. \n");
title = "Aaate";
r8mat_print(18,18,Aate,title);    */

/*Fourth function: multiply Aate and sum*/
r8mat_mm(18,18,1, Aate, sum, product);

/* mexPrintf("About to display output (4): product. \n");
title = "Product";
r8mat_print(18,1,product,title);    */

/*Fifth function: Subtract AinvB from product*/
for (i=0; i<18; i++){
    pntrY[i]= product[i]-pntrAinvB[i];
}

/*    mexPrintf("About to display output (5): Y. \n");
title = "Y (result)";
r8mat_print(18,1,pntrY,title);    */
}
matrix_exponential.h

```

This is copied and pasted from a multi-function C file from the r8 library.

```

#include <stdlib.h>
#include <stdio.h>
#include "r8lib.h"

```

```

/*
  Complex functions.

double complex *c8mat_expml ( int n, double complex a[] );
/*
  Real functions. A.C: I'm only going to use r8mat_expml, matrix
  exponentiation by Pade approximation.
*/
double *r8mat_expml ( int n, double *a );
double *r8mat_expml2 ( int n, double a[] );
double *r8mat_expml3 ( int n, double a[] );

double *r8mat_expml ( int n, double *a )
{
  /*mexPrintf("Are we there yet??");
  char *title = "matrixSent2Exp";
  r8mat_print(18,18,a,title);*/

  double *a2;
  double a_norm;
  double c;
  double *d;
  double *e;
  int ee;
  int k;
  const double one = 1.0;
  int p;
  const int q = 6;
  int s;
  double t;
  double *x;

  a2 = r8mat_copy_new ( n, n, a );
  /* mexPrintf("n is %d. First element of a2 is: %f\n",n, a2[0]);*/

  a_norm = r8mat_norm_li ( n, n, a2 );

  ee = ( int ) ( r8_log_2 ( a_norm ) ) + 1;

  s = i4_max ( 0, ee + 1 );

  t = 1.0 / pow ( 2.0, s );

  r8mat_scale ( n, n, t, a2 );

  x = r8mat_copy_new ( n, n, a2 );

  c = 0.5;

  e = r8mat_identity_new ( n );

  r8mat_add ( n, n, one, e, c, a2, e );

```



```

d = r8mat_identity_new ( n );

r8mat_add ( n, n, one, d, -c, a2, d );

p = 1;

for ( k = 2; k <= q; k++ )
{
    c = c * ( double ) ( q - k + 1 ) / ( double ) ( k * ( 2 * q - k + 1
) );

    r8mat_mm ( n, n, n, a2, x, x );

    r8mat_add ( n, n, c, x, one, e, e );

    if ( p )
    {
        r8mat_add ( n, n, c, x, one, d, d );
    }
    else
    {
        r8mat_add ( n, n, -c, x, one, d, d );
    }

    p = !p;
}
/*
E -> inverse(D) * E
*/
r8mat_minvm ( n, n, d, e, e );
/*
E -> E^(2*S)
*/
for ( k = 1; k <= s; k++ )
{
    r8mat_mm ( n, n, n, e, e, e );
}

free ( a2 );
free ( d );
free ( x );
/* mexPrintf("At the end of exmp. e[0] = %f; e[1] = %f\n", e[0],
e[1]);*/
return e;
}

```

## Appendix B: GluCEST post-processing in Matlab

Abby, CMROI

January 2021

### Introductory Note

The purpose of this documentation is to explain in an accessible, informal, hands-on way how to do the post-processing and analysis of human brain gluCEST data, including some things that I developed while working in our lab. This includes:

- How to collect and fit B1 calibration data as in Cember et al 2021 [done]
- How to use the resulting 'surfaces' in post-processing of 2D [done] and 3D gluCEST data
- How the rest of the post-processing works (i.e., what is this code doing, anyway?)
- How to create DICOMs and NIFTIs from the resulting CEST maps [done]
- How to do automatic segmentation of brain anatomy using Freesurfer and the Segmentation Service in ITK-SNAP
- How to do ROI-based analysis of your CEST data based on the results of these segmentations

Currently, I do post-processing of 2D CEST data in a command-line based function that I wrote myself, but use Hari's GUI-based post-processing for 3D data. Most of the underlying code –and everything that happens after we get the CEST map– is the same.

**Important note:** ALL AUTOMATIC SEGMENTATIONS REQUIRE A FULL-BRAIN T1 IMAGE. If you do not acquire this on your subjects, you can generate CEST maps of your slice or slab, but cannot do any of the other analysis that I describe here. ALWAYS COLLECT A FULL-BRAIN T1 STRUCTURAL IMAGE.

All of the code described here already exists. However, **this document is designed so that, if desired, you can copy and paste Matlab code from this word document into Matlab to create your own version of these scripts and functions.**

Let's start with walking through using my code to process 2D CEST data, as this will serve as an overview and provide context before we dive into everything else.

**Important note on compiling mex files:** Some of the steps in CEST post-processing (e.g.  $B_0$  correction) and also in ' $B_1$  fitting' as described here make use of mex files. Unlike regular Matlab .m files, mex files need to be compiled before they can run. If someone gave you a bunch of code, it's likely that the compiled version of the mex file already exists, and you don't need to worry about this. However, if someone with a Windows machine gave you code, and you have a Mac – or vice versa—you might need to. For every file that ends with ".c" or ".cpp", you need to have a corresponding one that ends with ".mexw64" for Windows or something else (I'm not sure what the extension is) on Mac. Compiling is as simple as typing: `mex filename.cpp`

However, if you're on Windows, I highly recommending including this flag:

```
mex filename.cpp -compatibleDimArrays
```

I'm not 100% how to tell when this will and won't be needed, but if you don't use it, you can cause a memory leak during the conversion between Matlab dim variable types and C int. Matlab will crash and you will have no idea why.

### Post-processing of 2D CEST data: Getting from scanner data to a CEST map DICOM or NIFTI

If you have gotten your data off of the scanner, it will already be sorted into folders based on the sequence. If you got your data off of the Linux machine known affectionately as Pedro (and the RTEXTORT folder), the dicoms will be unsorted. You will need to begin by running the function `cdsort3d.m`.

Almost all of our in-house code requires a library of functions contained in a folder labeled "**COMMON**". It has to be on the path in order for all downstream functions to work. ('cdsort' is in this folder.)

To do post-processing of GluCEST data, use the folder called "**Code for using Abby's  $B_1$  correction**".

Begin by running the main function – right now, it's called `MAINFunction_CorrectUsingFittingGear319A`. I will call it 'Main' for short from here on. It does not require any input arguments.

```
function processed = MAINFunction_CorrectUsingFittingGear319A()  
%Changed Fitting Gear to 319A, 10/11/2020  
    load('FittingGear_319A');  
    DataStruct = ReadNewData();  
    DataStruct = NewDataToDataStruct(DataStruct);  
    DataStruct = CreateMasks(DataStruct, FittingGear_319A);  
    DataStruct = CorrectB1_F(DataStruct, FittingGear_319A);  
    processed = DataStruct;  
end
```

The first thing that this function will do is prompt you to **read in all of the data** from their original dicom folders. If you look at the code, you will see that this is being accomplished by the function `ReadNewData()`, which in turn calls several functions which begin with the word 'Read'. B0 correction and other things are accomplished here.

The next function that Main will call is called `NewDatatoDataStuct()`. This is a wrapper function for internal use, and does not require you to do anything.

Next, `CreateMasks()` will **sort the pixels into T<sub>1</sub> bins**. This sorting is done based on bin bounds defined in the file called "FittingGear". It will show you a color-coded T<sub>1</sub> map as output so that you can visualize the sorting.

Lastly, the **B<sub>1</sub> correction** will be performed – also in accordance with "FittingGear", which specifies the correction surfaces. This function will prompt you to enter the nominal B1 value in Hz: for our CEST sequences, this is 210 Hz.

**NOTE:** *If you generate new and improved correction surfaces (collecting and fitting more data, for example, or using a different sequence), only the "FittingGear" .mat file needs to be replaced; it is modular. However, if the functional form itself changes (and not just the parameter values or T<sub>1</sub> bins), then the function called "evaluate...m" also needs to be replaced.*

When you're done, the struct which internally is called 'processed' will be returned as 'ans', unless you gave it a name when you called the function. For example, you could type:

```
SubjectAC = MAINFunction_CorrectUsingFittingGear319A()
```

And then when this function is finished running, a variable called 'SubjectAC' will exist in the workspace, which holds the data you just read in, and all of the outputs: T1 map, B1 map, etc. Of course, it has the final CEST map: this will be in:

```
SubjectAC.B1correctedCEST_normNeg
```

I generally save this single-subject struct as a .mat file, and call it something like 'SubjectAC\_date\_ProcessedData.m'. However, if you're processing the data from many related subjects at the same time, you can save all of the structs into a single .mat file. Just make sure to save the workspace after each data set that you process! Occasionally, something may cause Matlab to crash, and you don't want to have to load all of this stuff over again!

At this point, you probably want to **generate a DICOM and/or NIFTI from the final CEST map**. To do this, you can use the script `WriteDicomNiftiCESTmap.m`. (You can always do this later by reloading the 'ProcessedData'.m files.) When you press 'Play/Run' on this function, it will ask you what struct you want the DICOM for. You should type the name of the struct exactly as it appears in the workspace, e.g.: SubjectAC.

It will also ask you to choose where you would like them saved, and then for a series number (which can be totally arbitrary) and a file name/description.

```
DataName = input('Which DataStruct do you need a dicom for?');

str1 = sprintf('Please choose where you would like to save the
dicoms. ');
pathname1 = uigetdir([DataName.refpath filesep '..'],str1); % file
chooser
outfolder = pathname1;
new_series = input(' Type in a new dicom series number between 500-999
: ');
new_description = input('Please type a description for these files
(dicom and nifti) (e.g. CEST map)', 's');

%%%
%Create Dicom from CEST map in Data Struct
%I think I need to actually create the dicoms in a folder that is on
the
%path for this function, otherwise dicom2nifti won't be able to find
%them...
[CESTdicom, outfolder1] = dicom_create_Abby(DataName.dicomhdr,
DataName.B1correctedCEST_normNeg, outfolder,new_series,
new_description,1);
addpath(outfolder1);
outfile = strcat(new_description, '.nii');

%Convert Dicom to Nifti
files=dir(CESTdicom);
names{1} = files(1).name;
dicom_spm2nifti(names,outfile); %8/14/2018
%vol = dicom_spm2nifti(infiles,outfile).'outfile' has to be a string
that
%includes a file extension.

%Edit nifti to be "three dimensional"
fixNIFTI(outfile);
```

The function will then also create a NIFTI from this DICOM. This whole process requires two libraries to be in the Matlab path: **spm8**, and **NiftI** (in addition to **COMMON**). You'll see that at the end of the script WriteDicomNiftiCESTmap.m, a function is called called fixNIFTI(). This is a workaround to force the viewing program ITK-SNAP to treat a 2D image as if it is a 3D image, thus orienting it properly in 3D space. The load\_untouch\_nii() and save\_untouch\_nii() functions called here are part of the NiftI library.

```
function fixNIFTI(filename)
    %This will load an object of type 'nii'
    current_NIFTI = load_untouch_nii(filename);
    %This changes the variable
    current_NIFTI.hdr.dime.dim(1) = 3;
    %This saves the object 'nii' with given file name
```

```
    save_untouch_nii(current_NIFTI, filename);  
end
```

The CEST NiFTI will be created in whatever the current Matlab directory is – which is probably not where you want it to be stored indefinitely. I just immediately cut and paste it from there to wherever the rest of the data is for that subject.

At this point, you can load your CEST DICOM or NIFTI to ITK-SNAP or another viewing program and look at it as if you would any other image. Later on, I'll talk about what to actually do with these files in terms of analysis.

### **Fitting calibration data to produce the correction surfaces defined in “FittingGear\*\*\*.mat”**

#### **Creating “Fitting Gear” Structs**

Suppose we have collected B1 calibration data at B1 strengths ....[50,90,130,170,210,250]

Calibration data is read in by ReadCalibrationData.m:

This function reads in all of the data needed from a B1 calibration data set, but does NOT do any of the fitting. The next step in the process is to run versions of sort\*() and fit\*() for the data set.

The user will see the following instruction, to which we respond with the B1 strengths mentioned above:

```
Please enter the nominal B1 strengths at which data were  
collected. (Use square brackets)  
[50, 90, 130, 170, 210, 250]
```

```
Type in the required CEST offset value in ppm :  
(For gluCEST) 3.0
```

Note that if you've already loaded some of the data into a Matlab struct, you can send this struct as an input argument to ReadCalibrationData, so that you don't have to go through the process of loading it again. The default situation coded here is that it assumes that a previously loaded struct contains a B1 map and a defined ROI, but not the CEST data. You can change these assumptions (and, consequently), the steps that are skipped, by altering the values of these Boolean variables inside the code.

```
if isstruct(CurrentStruct)  
%If we sent an input argument, it means that we've already loaded this  
stuff  
    haveCEST = 0;  
    haveB1 = 1;  
    haveROI = 1;  
else  
    haveCEST = 0;
```

```

        haveB1 = 0;
        haveROI = 0;
end

```

The user will then be asked to select the T1 images, to draw an ROI of none yet exists, the CEST images *for the first B1 point* and WASSR images. The code will calculate the B0 map and do a B0 correction on the positive and negative offset CEST images for this B1 point. This process will be repeated until all the data of all B1 points has been loaded and B0-corrected. Then, the user will select the B1 map images, and the code will calculate the B1 map.

The new 'StructCalibration' will then be returned from ReadCalibrationData.m

**Setting the intervals for T1 bins:** If for some reason one wants to re-determine the intervals for T1 binning (for example, for collecting several new data sets which are on different slices – or even, to use something entirely different as the 'Index Image'), then this function can take up to three different Index Images (eg. T1 maps), ask the user how many evenly-populated (e.g. T1) bins they'd like to sort the data into, and it will figure out what the intervals should be.

```

function [NumMasks, Intervals] = setMaskIntervals(GoodIndexImage1,
GoodIndexImage2, GoodIndexImage3, LB, UB)
%Figure out how many useable pixels we have
    if (~GoodIndexImage2)
        %We only have one input T1 image
        GoodIndexImage = GoodIndexImage1;
    else
        %We have at least two input T1 images
        if (~GoodIndexImage3)
            GoodIndexImage = [reshape(GoodIndexImage1,1, []),
reshape(GoodIndexImage2, 1, [])];
        else
            %We have three input T1 images
            GoodIndexImage = [reshape(GoodIndexImage1,1, []),
reshape(GoodIndexImage2, 1, []), reshape(GoodIndexImage3, 1, [])];
        end
    end

    end
    AllValues = sort(GoodIndexImage(:));

    AllValues = AllValues(AllValues > LB); %Set min pixel value for
binning
    AllValues = AllValues(AllValues < UB); %Set max pixel value " " "
    NumGoodPixels = numel(AllValues);

    %Then, divide that number by whatever the user enters as the
%number of masks.variable: NumMasks
    MasksPrompt = 'Please enter the number of masks to divide the data
into\n';
    NumMasks = input(MasksPrompt);
    MaskPopulation = int64(NumGoodPixels/NumMasks);

    Intervals = zeros(2,NumMasks);

```

```

    %--Then, we want to to figure out the ranges in mask values that
    correspond
    %to those numbers. variable: 2xNumMasks array which holds start and
    end
    %values for each mask. ImageDims(2) x NumMasks array which holds
    the masks
    maskIndex = 1;
    Intervals(1,maskIndex)= AllValues(1);%lower bound of first mask
    % Intervals(1,maskIndex) = 1000; %9/17/2018 --just kidding, see
    above
    Intervals(2,maskIndex)= AllValues(MaskPopulation); %upper bound

    for maskIndex = 2:NumMasks-1
        Intervals(1,maskIndex) = AllValues(MaskPopulation*(maskIndex-
1)+1);
        Intervals(2,maskIndex) = AllValues(MaskPopulation*(maskIndex));
    end

    maskIndex = NumMasks;
    Intervals(1,maskIndex) = AllValues(MaskPopulation*(maskIndex-1)+1);
    Intervals(2,maskIndex) = AllValues(NumGoodPixels);

end

```

The next step is to **sort the pixels** in each data set into T1 bins, and then to fit the resulting clumps of pixels to our functional form. Assuming the intervals have been defined (either from an existing FittingGear struct, or as re-determined by the above function) , then we can call:

```

[sorted] = sortIntoBins(StructCalibration, NumMasks, Intervals)
StructCalibration.sorted = sorted

```

Where 'sorted' is basically a discretized T1 map, with each pixel holding the T1 bin number. It is used in the function `defineUseable( )` to weed out pixels

I haven't written functions for these, **just scripts which can be used as templates** for any further use. For example, in this case I was using a data set which I named 'TFL' (as it was the first collected with this sequence )contained in a 'StructCalibration' variable which I had named 'TestStructDelta' :

```

np = ones(1,26); %this index is for the CEST values vectors
TestStructDelta = defineUseable(TestStructDelta, 0, .2, 0.1, 1.5);
for i = 1:240
    for j = 1:180
        if (TestStructDelta.useable(i,j))
            bin = TestStructDelta.sorted(i,j);
            for m = 1:6 %loop over nominal B1 values
                PosValsByBin_TFL(bin,np(bin)) =
TestStructDelta.CESTposImages(i,j,m);
                NegValsByBin_TFL(bin,np(bin)) =
TestStructDelta.CESTnegImages(i,j,m);
            end
        end
    end
end

```



```

        BlvalsByBin_TFL(bin,np(bin)) =
TestStructDelta.Blmap(i,j) * TestStructDelta.Blvals(m);
        np(bin) = np(bin) + 1;
    end
end
end
end
npTFL = np;

```

Basically, what we've done here is **sorted all of the CEST values and absolute (nominal \* B1 map) B1 values into vectors**. The length of these vectors is tabulated by the tally 'np', which stands for 'number of points'. Basically, 'np' in each bin index is going to correspond to the number of 'useable' pixels in that bin in that dataset, as defined by this first function called by the script:

### Define useable pixels of data set:

```

%Define useable area of calibration images
%Requirements:
% 1)B1 map value has to have a certain value
% 2)T1 value has to fall into range of bins
% 3)Data has to be "good" (if using 'CheckData')
% 4)CEST signal has to be within certain bounds
%Update, 8/29/2019: Now takes Blthreshold as an input argument
%Update, 9/14/2019: CEST threshold now has to be met for more points
%Update, 9/17/2019: Re-introduce "GoodYesNo".

%Note, 11/6/2020: CheckData and its internal function RightShape (which
return the element
%'CalibrationStruct.GoodYesNo' which is refences above) were
%originally meant for use in pixel-by-pixel fitting; they should not
really be necessary now that pixels in one bin are being fit all at
once. However,
%in some cases where data is excessively noisy, its use may help to
exclude
%problematic pixels.

function StructCalibration = defineUseable3(StructCalibration,
CEST_LB,CEST_UB, B1_LB, B1_UB)

%     Blthreshold = 0.8; %%%%%%%%%%

    useable = StructCalibration.roiMask;
    useable(StructCalibration.Blmap > B1_LB) = 1;
    useable(StructCalibration.Blmap < B1_LB) = 0;
    useable(StructCalibration.Blmap > B1_UB) = 1;

    useable = useable .* StructCalibration.sorted;
    %useable = useable .* StructCalibration.GoodYesNo;
    %9/17/2019
    useable(StructCalibration.sorted <0) = 0;

```

```

    %useable = useable .* StructCalibration.GoodYesNo;

    useable(StructCalibration.CESTposImages(:,:,1) < CEST_LB) = 0;
%    useable(StructCalibration.CESTposImages(:,:,2) < CEST_LB * 0.5)
= 0;
    useable(StructCalibration.CESTposImages(:,:,1) > CEST_UB) = 0;
%    useable(StructCalibration.CESTposImages(:,:,2) > CEST_UB) = 0;
% (above) lower bound for first B1 point, Struct 1. Make this 100
for
% prepTFL dataset, 1500 for TLE dataset -- still using as on
7/9/19
    StructCalibration.useable = useable;
end

```

Now that we have PosValsByBin\_DataSet, NegValsByBin\_DataSet and B1valsByBin\_Data, we're ready to fit these things to Equation [1].

```

vars = {'lengthCurrent', 'yfitN', 'yfitP', 'resnormN', 'resnormP',
'residualN', 'residualP', 'exitflagN', 'exitflagP', 'An', 'Ap', 'Cn',
'Cp', 'Dn', 'Ep', 'En', 'Ep'};
clear(vars{:})
E = E_TFL_test;
for i = 1:26
    %NewSimpleArray = SimpleArray(SimpleArray ~= 0)
    %July 16th, 2019: new E bounds
    B1valsCurrent = B1valsByBin_TFL(i,:); NegValsCurrent =
NegValsByBin_TFL(i,:); PosValsCurrent = PosValsByBin_TFL(i,:);
    B1valsCurrent = B1valsCurrent(B1valsCurrent ~= 0);NegValsCurrent =
NegValsCurrent(NegValsCurrent ~= 0);PosValsCurrent =
PosValsCurrent(PosValsCurrent ~= 0);
    lengthCurrent(i,:) = size(B1valsCurrent);

    [yfitN(i,1:lengthCurrent(i,2)),resnormN(i),residualN(i,1:lengthCurrent(
i,2)),exitflagN(i),An(i),Cn(i),Dn(i),En(i)] =
curvefit_Abby_6(B1valsCurrent,NegValsCurrent,E(i));

    [yfitP(i,1:lengthCurrent(i,2)),resnormP(i),residualP(i,1:lengthCurrent(
i,2)),exitflagP(i),Ap(i),Cp(i),Dp(i),Ep(i)] =
curvefit_Abby_6(B1valsCurrent,PosValsCurrent,En(i));
end

for i = 1:26
    FitPars4Average(1,i) = An(i);
    FitPars4Average(2,i) = Cn(i);
    FitPars4Average(3,i) = Dn(i);
    FitPars4Average(4,i) = En(i);

    FitPars4Average(5,i) = Ap(i);
    FitPars4Average(6,i) = Cp(i);
    FitPars4Average(7,i) = Dp(i);

```

```

    FitPars4Average(8,i) = Ep(i);
end

%ResultsTFL =
[yfitP(i,1:lengthCurrent(i,2)),resnormP(i),residualP(i,1:lengthCurrent(
i,2)),exitflagP(i)];
% residualP_TFL = residualP; resnormP_TFL = resnormP;
% residualN_TFL = residualN; resnormN_TFL = resnormN;
% yfitN_TFL = yfitN; yfitP_TFL = yfitP;
% lengthCurrentTFL = lengthCurrent;
% FitPars4Average_TFL = FitPars4Average;

FitTFL.residualP = residualP; FitTFL.resnormP = resnormP;
FitTFL.residualN = residualN; FitTFL.resnormN = resnormN;
FitTFL.yfitN = yfitN; FitTFL.yfitP = yfitP;
FitTFL.lengthCurrent = lengthCurrent;
FitTFL.FitPars4Average = FitPars4Average;

%%%%%%%%%%%%%%%%%%%%%%%%%%%%%%%%%%%%%%%%%%%%%%%%%%%%%%%%%%%%%%%%%%%%%%%%
figure, imagesc(FitTFL.FitPars4Average)
colormap('hsv'), caxis([-3e-4 3e-4])

```

After we've generated these 'Fit\*\*\*' structs for every data set, we'll take a **weighted average of the results** to form the final correction surface. An algebraic description of this math (rather than computer code) is provided in my B<sub>1</sub> correction paper<sup>16</sup>. The steps we're doing below are: 1) counting the number of points in each vector 2) dividing the residual norm vector for each fit by the value of the scaling parameter, E (representing M<sub>0</sub>) for each fit 3) further dividing this result by the number of points in that vector -- since either larger E or a larger number of points will automatically result in the residual norm being larger, which does not reflect the fit being worse. This is being done for all three data sets (A, B, C) for both the positive and negative offset fits. (In the following code, you might want to replace labels 'A' 'B' and 'C' with more descriptive names of the data set e.g., the initials of the subject they were created from).

```

%Calculate residual norms normalized by E and by number of data points
NumberOfPoints_A = length(B1valsByBin_A);
NumberOfPoints_B = length(B1valsByBin_B);
NumberOfPoints_C = length(B1valsByBin_C);

resnormP_A_NormE = FittingResultsStructA.resnormP ./
FittingResultsStructA.FitPars4Average(4,:).^2;
resnormP_B_NormE = FittingResultsStructC.resnormP ./
FittingResultsStructC.FitPars4Average(4,:).^2;

```

---

<sup>16</sup> Cember ATJ, Hariharan H, Kumar D, Nanga RPR, Reddy R. Improved method for post-processing correction of B<sub>1</sub> inhomogeneity in glutamate weighted CEST images of the human brain. *NMR Biomed.* 2021;in press.

```

resnormP_C_NormE = FittingResultsStructB.resnormP ./
FittingResultsStructB.FitPars4Average(4,:).^2;

resnormP_A_NormENP = resnormP_A_NormE ./ NumberOfPoints_A;
resnormP_B_NormENP = resnormP_B_NormE ./ NumberOfPoints_B;
resnormP_C_NormENP = resnormP_C_NormE ./ NumberOfPoints_C;

resnormN_A_NormE = FittingResultsStructA.resnormN ./
FittingResultsStructA.FitPars4Average(4,:).^2;
resnormN_B_NormE = FittingResultsStructC.resnormN ./
FittingResultsStructC.FitPars4Average(4,:).^2;
resnormN_C_NormE = FittingResultsStructB.resnormN ./
FittingResultsStructB.FitPars4Average(4,:).^2;

resnormN_A_NormENP = resnormN_A_NormE ./ NumberOfPoints_A;
resnormN_B_NormENP = resnormN_B_NormE ./ NumberOfPoints_B;
resnormN_C_NormENP = resnormN_C_NormE ./ NumberOfPoints_C;

%Then, we initialize the matrix that will be our 'final product':
ParameterValue = ones(8,26);

% %To use three data sets

for i = 1:26
%This is a loop over T1 bins
    %First we want to examine the value of resnorm_ENP of each data
    set,and
    %take its reciprocal
    A0 = 1/resnormP_A_NormENP(i); B0 = 1/resnormP_TLE_NormENP(i); C0 =
1/resnormP_TFL_NormENP(i);
    Sum = A0+B0+C0;
    Coefficient = 1/Sum;
    A1 = A0*Coefficient; B1 = B0*Coefficient; C1 = C0*Coefficient;
    for p = 5:7
    %This is a loop over fitting parameters
        ParameterValue(p,i) = A1*FitA.FitPars4Average(p,i)+
B1*FitB.FitPars4Average(p,i)+C1*FitC.FitPars4Average(p,i);
    end

    %Paramters 1-3 hold negative offset values
    %Parameters 5-7 hold positive offset values
    %Parameters 4 and 8 are E i.e. M0, the scaling parameter

    A0 = 1/resnormN_A_NormENP(i); B0 = 1/resnormN_TLE_NormENP(i); C0 =
1/resnormN_TFL_NormENP(i);
    Sum = A0+B0+C0;
    Coefficient = 1/Sum;
    A1 = A0*Coefficient; B1 = B0*Coefficient; C1 = C0*Coefficient;

    for p = 1:3
        ParameterValue(p,i) = A1*FitA.FitPars4Average(p,i)+
B1*FitB.FitPars4Average(p,i)+ C1*FitC.FitPars4Average(p,i);
    end
end

```

```
end
```

Now that we've filled this matrix called 'ParameterValue', we're going to evaluate Equation 1 to make surfaces described by these parameters, **smooth** that surface, and then **refit** it to Equation 1 to get our final 'Correction Surfaces'.

```
for i = 1:26
    %ParameterValue(4,i) = 1; ParameterValue(8,i) = 1;
    surfaceP(i,:) = evaluateJanuary2019(ParameterValue(:,i),1);
    surfaceN(i,:) = evaluateJanuary2019(ParameterValue(:,i),-1);
end

%Now smooth the surface, with some degree of Gaussian filtering
SmoothSurfaceP = im_filtNew(surfaceP,5);
SmoothSurfaceN = im_filtNew(surfaceN,5);

%Or no filtering
% SmoothSurfaceP = surfaceP;
% SmoothSurfaceN = surfaceN;

FittedSurfaceP = zeros(26,51);
FittedSurfaceN = zeros(26,51);

x = [0:5:250];
for i = 1:26
    [FittedSurfaceP(i,:),~,~,~,Ap(i),Cp(i),Dp(i),Ep(i)] =
    curvefit_Abby_6(x, SmoothSurfaceP(i,:), 1);
    [FittedSurfaceN(i,:),~,~,~,An(i),Cn(i),Dn(i),En(i)] =
    curvefit_Abby_6(x, SmoothSurfaceN(i,:), 1);
end

for i = 1:26
    FitPars4Average(1,i) = An(i);
    FitPars4Average(2,i) = Cn(i);
    FitPars4Average(3,i) = Dn(i);
    FitPars4Average(4,i) = En(i);

    FitPars4Average(5,i) = Ap(i);
    FitPars4Average(6,i) = Cp(i);
    FitPars4Average(7,i) = Dp(i);
    FitPars4Average(8,i) = Ep(i);
end

FittedSurfaceParameters = FitPars4Average;
figure, imagesc(FittedSurfaceParameters)
caxis([-3e-4 3e-4]), colormap('hsv'), colorbar

%Use smoothed, fitted surface to create Fitting Gear
FittingGearNew.NumMasks = 26;
```

```
FittingGearNew.intervals = IntervalsA_B_C;
FittingGearNew.FitPars4Average = transpose(FittedSurfaceParameters);
FittingGearNew.averagesPos = SmoothSurfaceP;
FittingGearNew.averagesNeg = SmoothSurfaceN;
```

### **End of ‘Creating Fitting Gear Structs’**

We’ve now generated a ‘FittingGear’ struct of the kind used by the B1 correction code described above. Note that my code (`MAINFunction_CorrectUsingFittingGear319A.m`) can only handle 2D CEST data. For processing 3D CEST data, we need to use Hari’s GUI-based code, `CEST3DB1NEW.m`.

### **Evaluate() and CurveFit()**

However, before we move on, we need to take a look at the key subfunctions from above process: `evaluateJanuary2019()` and `curvefit_Abby_6()`. These are the functions that actually define the functional form, a.k.a Equation 1. For outdated reasons, the variables here are designated with the letters {B,C,D} instead of their current form of Greek letters. Evaluate() does just what it sounds like: it simply takes the values that you want to plug in for each variable and evaluates the expression. It’s used to generate curves or surfaces (which are families of curves) from parameter values.

```
function curve = evaluateJanuary2019(parameters, offset)
%Now with an extra parameter for scaling instead of sending normalized
%data.
Bn = parameters(1); Cn = parameters(2); Dn = parameters(3); En =
parameters(4);
Bp = parameters(5); Cp = parameters(6); Dp = parameters(7); Ep =
parameters(8);
x = [0:5:250];
curveN = En*(1+(Bn*x.^2 ./ (Cn*x.^2 +1)) - Dn*x.^2);
curveP = Ep*(1+(Bp*x.^2 ./ (Cp*x.^2 +1)) - Dp*x.^2);
if (offset == 1)
    curve = curveP;
end
if (offset == -1)
    curve = curveN;
end
end
```

The opposite is done by `curve_fit_Abby_6()` – it takes data which is assumed to fall along a curve, and fits it to generate parameter values. What’s a little bit confusing here is that the real fitting is done by `lsqcurvefit()` (LSQ stands for “least squares”), which is a built-in Matlab function. The reason we need our own function as a “wrapper” is because we’re defining some customized functional form. If we wanted to use one of the built-in options, like a regular linear fit, we wouldn’t need to do this. Something very tricky happens when we actually call `lsqcurvefit()`: as one of the input arguments, we actually send it a handle to another function, called `composite()`. That’s where our customized functional form is defined – we specify the

initial guess for the parameters in `curve_fit_Abby_6()`, but the definition of their actual 'role' doesn't show up until `composite()`.

```
function [yfit, resnorm, residual, exitflag, B, C, D, E] = curvefit_Abby_6(x,
yin, E)
%Note: while we retain the option to send E as an input argument, right
now
%this has no functionality. E will be fit separately for each pixel's
%positive and negative offset curve.

%plot(x, yin, 'or','markerFaceColor', 'r')

np = length(x); %number of points
if (length (yin) ~= np)
    error('curvefit_Abby: x and y array sizes do not match')
end
if ( size(x,1) == size(yin,1) )
    y = double(yin);
else
    y = double(yin)';
end

pars = double(4);
lb = double(4);
ub = double(4);
%
% %fill pars with initial guess values%%%%%%%%%%%%%%%%%%%%%%%%%%%%%%%%%%%%%%%%
% from simulation of CEST with MT and DS:
% B
%   -0.1135   * 1.9837 e-4 = -2.25e-5
% C
%
%   0.0932   * 1.9837 e-4 = 1.85e-5
% D
%   -0.0040 * 1.9837 e-4 = 8e-7

pars(1) = -2.25e-5; %A (called B in this function)
pars(2) = 1.85e-5;% %C
pars(3) = 6e-7; %D -- had been 8e-7
pars(4) = 2000; %E
lb(1) = -1e-3;
lb(2) = 1e-7;
ub(1) = 1;
ub(2) = 1;%1;
lb(3) = 6e-7;%-1;
ub(3) = 6e-7;%1e-5
if (E) %The intention here is that if E is predetermined and sent to
the function, then we want to freeze it at that value.
    pars(4) = E;
    lb(4) = E;
    ub(4) = E;
else
    lb(4) = -100;%-100;
```

```

    ub(4) = 3500;%10000;
end

%Took these options from Hari:
oldoptions = optimoptions('lsqcurvefit');
%options = optimoptions(oldoptions, 'TolFun', 1e-18,'TolX', 1e-
18,'MaxFunEval',20000,'MaxIter', 12000 );
%Above: current code. Below: experimentation on 8/6/2018
% options = optimoptions(oldoptions, 'TolFun', 1e-5,'TolX', 1e-
5,'MaxFunEval',1000,'MaxIter', 1000 );
options = optimoptions(oldoptions, 'TolFun', 1e-12,'TolX', 1e-
12,'MaxFunEval',1000,'MaxIter', 10000 );

[ip, resnorm, residual, exitflag,~,~,~] =
lsqcurvefit(@composite,pars,x,y,lb,ub,options);
%[ip, resnorm, ~, ~,~,~,~] =
lsqcurvefit(@composite,pars,x,y,lb,ub,options);
%This 'pars' will become 'ip' used by composite; x will be sent as x.
% Fitted parameters are returned back in ip.

% ...

%Refill arrays A, B, C and D to return
%Initialize and refill yfit to return
yfit = x*0;

B = ip(1);
C = ip(2);
D = ip(3);
E = ip(4);

% yfit = yfit + ((1.0)./(A*x.^2 +1)) + (B*x.^2 ./ (C*x.^2 +1)) -
D*x.^2;
%yfit = yfit + E*((1.0)./(A*x.^2 +1)) + (B*x.^2 ./ (C*x.^2 +1)) -
D*x.^2);
yfit = yfit + E*(1 + (B*x.^2 ./ (C*x.^2 +1)) - D*x.^2);
%disp(transpose(yfit));-- Useful if you want to copy into an Excel
sheet
end

function yfit = composite(ip,x)

    yfit = x*0; %This initializes the result by creating a vector the
same size as x, but of all zeros.

    %Assign parameters from argument vector
    b = ip(1);
    c = ip(2);
    d = ip(3);

```



```

e = ip(4);

%define functional form
% yfit = yfit + ((1.0)./(a*x.^2 +1)) + (b*x.^2 ./ (c*x.^2 +1)) -
d*x.^2;
%yfit = yfit + e*((1.0)./(a*x.^2 +1)) + (b*x.^2 ./ (c*x.^2 +1))
- d*x.^2);
yfit = yfit + e*(1+ (b*x.^2 ./ (c*x.^2 +1)) - d*x.^2);
end

```

### **Post-processing of 3D CEST data**

This GUI works as do previous versions of Hari’s GUI for post-processing of CEST data (my intention is that the individual functions will be documented in more detail elsewhere). The feature that has been added to incorporate my  $B_1$  correction is the option ‘NEWB1’ in the menu that appears when one clicks the button “Calculate  $B_1$  corrected CEST”. This correction relies upon two things: that you have loaded the  $T_1$  map (MP2RAGE) instead of an MT image, and the presence of a file in the directory called “NewgluCESTB1Cal.mat”. This .mat file holds information analogous to that in a ‘FittingGear’ struct. Multiple versions of this file can be saved in the directory; only the one with this *exact* file name will be used (unless you edit the code to do otherwise).

The contents of this .mat file are:

```

--a double (regular number) called ‘NumMasks’
--a 2 x 26 double (vector) called ‘Intervals’
--a 26 x 8 double (vector) called ‘B1FitPars’

```

One can take a FittingGear struct and generate the variables needed in this .mat file by simply doing the following:

```

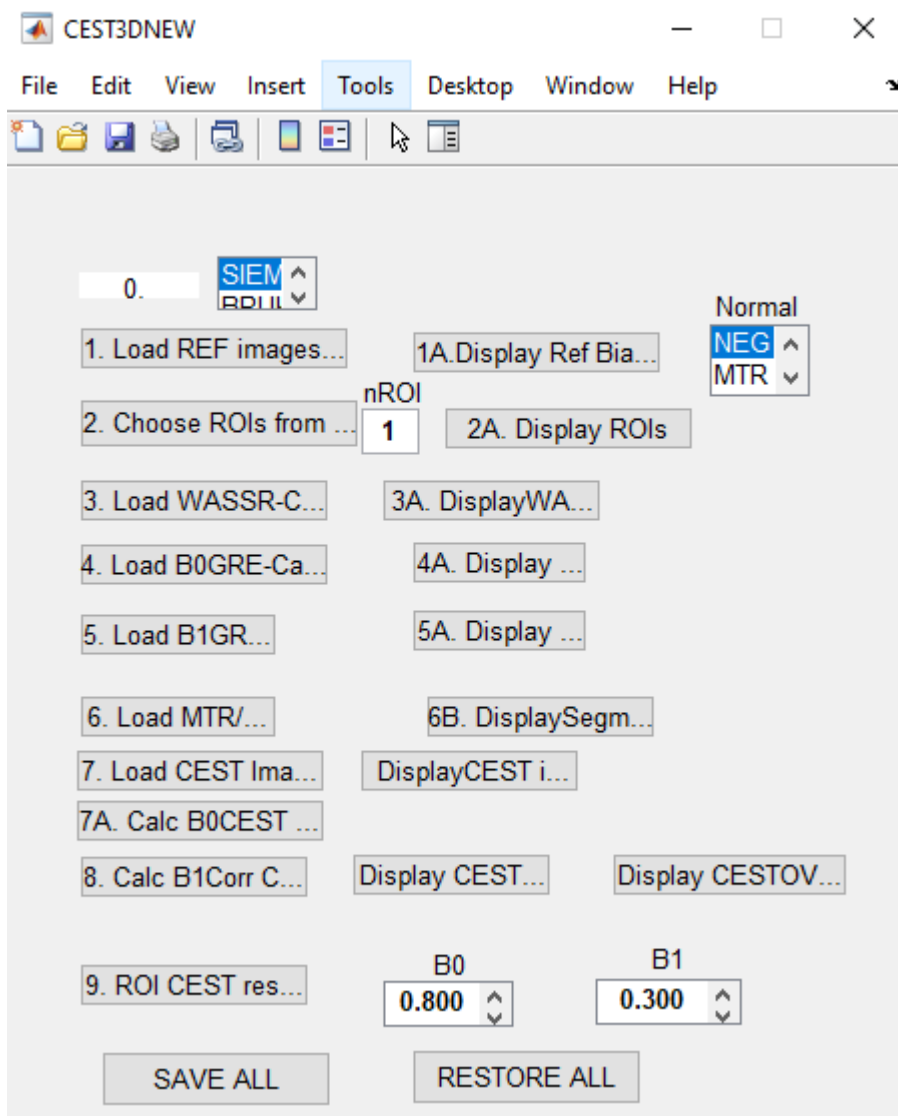
Intervals = FittingGear_319A.intervals;
B1FitPars = FittingGear_319A.FitPars4Average;
NumMasks = FittingGear_318A.NumMasks;

```

Then, save the three variables into a .mat file and give it the file name “NewgluCESTB1Cal.mat”. I would recommend that you save it with some designation indicating which FittingGear it came from, and then make a copy which has the default “...Cal.mat” name when you actually want to run it inside CEST3DB1NEW.

One useful thing to note before getting started is that, unlike the 2D post-processing pipeline in which we had to create Dicoms and NIFTIs as a separate step, this GUI should do it for you automatically – both for the final CEST maps and the images comprising intermediate steps. The NIFTIs will be in the same newly created directory that the Dicoms are in.

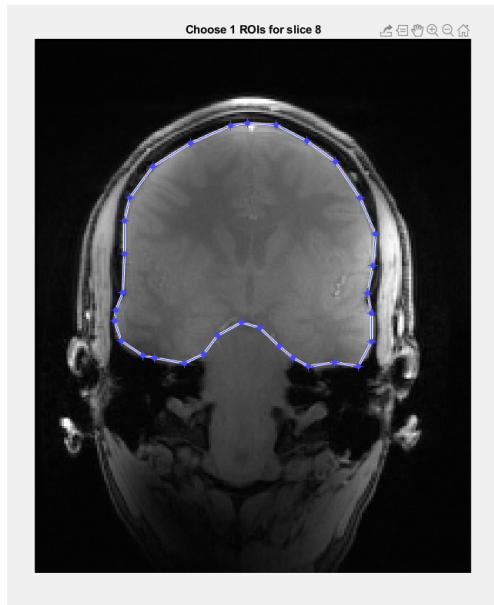
We can walk through the whole process with some screenshots:



When you press “run” (green “play” button) or type ‘CEST3DNEW’ into the command line, this GUI should appear. Frustratingly, on Windows at least, it is scrunched like this and cannot be expanded. The first thing to notice is that there are two “menus” where our selection is highlighted in blue: We have chosen “Siemens” data instead of “Bruker” (which is the animal scanner), and “Neg” instead of “MTR”. This second designation is a choice of how to

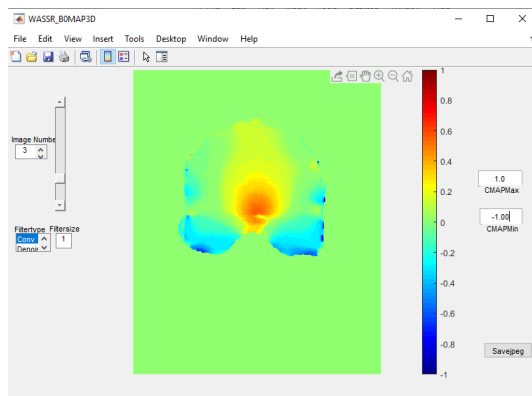
normalize the CEST asymmetry data. I would say that negative normalization is the default. There may, however, be instances where you want to normalize by the 0 ppm image of the MTR acquisition, which is why this option is here.

The first thing you will want to do – provided you already have the data sorted into directories; if not, run `cdsort3d` – is click the button ‘1. Load REF images’. When prompted, you should choose the “NONE” images for the CEST acquisition. For the prep-TFL based 3D gluCEST sequence, I think the none image is just called `_sat_hippo`, or something similar. A window will appear where these are visible. If you don’t see the slice you think you are processing data for, stop now, figure out what’s wrong, and start over. After you close this window, if you want to see the **references images** at any later time, click button 1A. (This is the function of all of the other ‘A’ buttons: they just let you display something again that you already calculated and might have closed.)



The next step is to **choose the ROI**. This GUI is assuming that you want to do this manually. If you have an ROI as an output from some other program (like an automatic segmentation), then you will need to either a) not use this GUI or b) feed the GUI your pre-existing ROI matrix. I will try to address how to do this later. When you click button 2, you will be asked a) whether you want an ROI (I think the alternative is that it does the processing on the whole image, but you shouldn't do this, because it will waste computational time calculating on empty space) b) whether you want them to be defined separately for each slice and c) and which tool to use. The best selection for the latter is "Poly", which allows you to define a polygon with as many sides (and therefore, whatever arbitrary shape) you want

by clicking with the mouse each time you want one line segment to end and another to begin. In the picture here, I chose to draw an ROI that's "Common for all slices", so it gave me the middle slice of the reference image to draw on: Slice 8. Every blue circle is where I clicked the



mouse to "cut out" the brain mask. To complete ROI selection, double click somewhere inside the polygon. I always choose the "Display ROI" to be the same as the "Processing ROI". Because drawing manual ROIs is tedious, I highly recommend that you click "Save All" after you have drawn the ROI. If Matlab crashes or anything else goes wrong in later steps, you don't want to have to do this over again.

Next we're going to **load the WASSR scan** and calculate the **B<sub>0</sub> map**. Note that there are actually

options for B<sub>0</sub> mapping: WASSR or Field Mapping, which is the option presented by button 4. So, you will only every use one of these two buttons to process the data for a particular experiment. (For clarification, the WASSR scan itself does not automatically generate a B<sub>0</sub> map – as in, that's not what you see on the scanner or in these images. The B<sub>0</sub> map has to be calculated from the WASSR acquisitions, which have a structure similar to the CEST acquisition: we collected several images with saturation at different offsets. If you want to understand the general idea of how this works, you can read the original paper.<sup>17</sup>) Calculating the B<sub>0</sub> map the most computationally intensive step of the CEST post-processing. If anything is wrong, Matlab

<sup>17</sup> Kim M, Gillen J, Landman BA, Zhou J, Van Zijl PCM. Water saturation shift referencing (WASSR) for chemical exchange saturation transfer (CEST) experiments. Magn Reson Med. 2009;61(6):1441-1450. doi:10.1002/mrm.21873

may crash during this step, hence my earlier recommendation. If this keeps happening, try recompiling the  $B_0$  correction related mex files with the compiler flag that I mentioned at the beginning.

...

*Please note that this documentation is a work in progress, as of April 2021 when this thesis was submitted. If you have found this thesis online at a later date and are seeking the contents listed below as “Coming soon”, please search for Abigail Cember on LinkedIn, ResearchGate, GitHub or on the website of the Center for Advanced Metabolic Imaging in Precision Medicine, U. Penn., where a final version of this documentation as well as updates to the code it describes will be provided in the future.*

**Coming soon:**

*--The rest of 3D gluCEST processing*

*--How to run segmentation on Freesurfer for cortical gray matter or in ITK-SNAP for the medial temporal lobe*

*--How to respace the Freesurfer segmentation so that you can overlay it with your original T1 and CEST maps*

*--How to take these segmentations and reslice them using c3d*

*--How to use Istat, either in the GUI or in command line, to get regional averages of gluCEST or any other map type*

*--How to use the resliced NIFTIs and CEST maps to generate histograms and other types of visualizations that I like in Matlab (back to code written by Abby)*

*--How to run T-tests on your CEST data for statistical significance*

*Сама наука не простоит минуты без красоты.*

*Ф.М. Достоевский*